NTNU – Trondheim
Norwegian University of
Science and Technology

Ballistic Perforation of Surface Hardened Mild Steel Plates

Erlend Orthe
Henrik Thorsen

Master of Science in Engineering and ICT

Submission date:	June 2014
Supervisor:	Tore Børvik, KT
Co-supervisor:	Jens Kristian Holmen, KT Odd Sture Hopperstad, KT

Norwegian University of Science and Technology
Department of Structural Engineering

Department of Structural Engineering
Faculty of Engineering Science and Technology
NTNU- Norwegian University of Science and Technology

ACCESSIBILITY

OPEN

MASTER'S THESIS 2014

SUBJECT AREA: Computational Mechanics	DATE: 10 June 2014	NO. OF PAGES: 203 20 +158 + 25

TITLE:

Ballistic Perforation of Surface Hardened Mild Steel Plates

BY:

Erlend Orthe
Henrik Thorsen

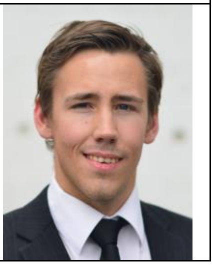

SUMMARY:

The main objective with this thesis was to investigate experimentally and numerically the effect surface hardening has on the ballistic properties of monolithic and laminated mild steel plates. 300x300 mm^2 plates of thicknesses 12 mm, 6 mm, and 4 mm were made from a low carbon structural steel (NVE36) and combined in such a way that the total thickness always was 12 mm. Some of the plates were then surface hardened by the Kverneland Group to obtain different hardness profiles; (1) as-received, (2) very hard surface with a soft core and (3) very hard surface with a hard core.

Ballistic impact tests were performed at SIMLab, NTNU, using 7.62 mm AP bullets. From these tests, the Recht-Ipson model was used to obtain ballistic limit curves for all layered/hardened configurations. The experiments showed that surface hardening had a positive effect on the ballistic resistance compared to the as-received material, while lamination did not seem to influence the results significantly. The surface hardened plates suffered from radial cracks and fragmentation during penetration, while the as-received material failed by ductile hole growth.

Material properties were obtained by conducting tensile tests and microhardness measurements. The material tests revealed that the plates had not been hardened to their expected hardness profiles. This affected the comparison between a soft core and a hard core configuration. The modified Johnson-Cook constitutive relation and the Cockcroft-Latham fracture criterion were chosen to represent the material behaviour. Identification of material constants was done by direct calibration in combination with Bridgman's analysis, and by inverse modelling using LS-OPT.

Numerical simulations of the impact tests were conducted in IMPETUS Afea Solver with higher order 3D volume elements. Surface hardened plates were modelled with a varying yield stress over the thickness by use of scaling factors obtained from the material tests. The numerical results were finally compared with the experimental findings. IMPETUS was able to describe the main trends from the experiment and the numerical results were conservative for all the analyses.

Additionally, a numerical case study was performed with nominal hardness profiles. The study showed that nominal hard core plates performed better than nominal soft core plates, while layering did not seem to affect the result significantly.

RESPONSIBLE TEACHER:	Professor Tore Børvik.
SUPERVISORS:	Professor Tore Børvik, PhD candidate Jens Kristian Holmen and Professor Odd Sture Hopperstad.
CARRIED OUT AT:	SIMLab, The Department of Structural Engineering, NTNU.

Institutt for konstruksjonsteknikk
Fakultet for ingeniørvitenskap og teknologi
NTNU- Norges teknisk- naturvitenskapelige universitet

TILGJENGELIGHET

ÅPEN

MASTEROPPGAVE 2014

FAGOMRÅDE:	DATO:	ANTALL SIDER: 203
Beregningsmekanikk	10. juni 2014	20 +158 + 25

TITTEL:

Ballistisk Perforering av Settherdede Lavfaste Stålplater

UTFØRT AV:

Erlend Orthe
Henrik Thorsen

SAMMENDRAG:
Hensikten med denne oppgaven var å undersøke eksperimentelt og numerisk hvordan settherding påvirker de ballistiske egenskapene til monolittiske og laminerte lavfaste stålplater. 300x300 mm^2 plater med tykkelse 12 mm, 6 mm, og 4 mm ble maskinert fra et lavkarbon konstruksjonsstål (NVE36) og kombinert slik at den totale tykkelsen ble 12 mm. De fleste platene ble settherdet av Kverneland Group for å oppnå forskjellige hardhetsprofiler; (1) uherdet, (2) veldig hard overflate med myk kjerne og (3) veldig hard overflate med hard kjerne.

Ballistiske tester har blitt utført ved SIMLAB, NTNU, hvor 7.62 mm AP kuler ble brukt. Fra disse testene ble Recht-Ipson modellen benyttet til å etablere ballistiske grensekurver for alle kombinasjoner av laminering og settherding. Testene viste at settherding hadde en positiv effekt på den ballistiske motstanden, sammenlignet med det uherdede materialet. Laminering, derimot, så ikke ut til å gi noen stor forskjell. De settherdede platene fremviste radielle sprekker og fragmentering, mens duktil hullutvidelse ble observert hos det uherdede materialet.

Materialegenskaper til de ulike platene ble funnet ved hjelp av strekktester og mikrohardhetsmålinger. Materialtestene avslørte videre at platene ikke hadde blitt settherdet til deres forventede verdier. Dette påvirket sammenligningen mellom myk og hard kjerne. En modifisert versjon av Johnson-Cook sin konstitutive relasjon og Cockcroft-Latham sitt bruddkriterium ble valgt for å representere materialegenskapene. Identifikasjon av materialkonstanter ble utført ved både direkte kalibrering og ved inversmodellering med LS-OPT.

Numeriske simuleringer av de eksperimentelle forsøkene ble utført i IMPETUS Afea Solver med høyere ordens 3D volumelementer. De settherdede platene ble modellert med en varierende flytespenning over tykkelsen ved hjelp av skaleringsfaktorer som ble funnet fra materialtestene. De numeriske resultatene ble deretter sammenlignet med de eksperimentelle. IMPETUS var i stand til å predikere hovedtrendene fra eksperimentene og de numeriske resultatene var konservative for alle analyser.

I tillegg ble et numerisk studie med nominelle hardhetsprofiler utført. Dette studiet viste at plater med nominell hard kjerne presterte bedre enn de med nominell myk kjerne. Laminering så derimot ikke ut til å påvirke resultatet betydelig.

FAGLÆRER:	Professor Tore Børvik.
VEILEDERE:	Professor Tore Børvik, PhD kandidat Jens Kristian Holmen og Professor Odd Sture Hopperstad.
UTFØRT VED:	SIMLab, Institutt for konstruksjonsteknikk, NTNU.

Department of Structural Engineering
FACULTY OF ENGINEERING SCIENCE AND TECHNOLOGY
NTNU - Norwegian University of Science and Technology

MASTER'S THESIS 2014

for
Erlend Orthe and Henrik Thorsen

Ballistic perforation of surface hardened mild steel plates

The main objective of the research project is to investigate experimentally and numerically the effect surface hardening has on the ballistic properties of monolithic and laminated mild steel plates. The main topics in the research project will be as follows;

1. 300 x 300 mm^2 plates of thicknesses 12 mm, 6 mm, and 4 mm are made from low carbon structural steel (NVE36).
2. Most of the plates are surface hardened by the Kverneland Group to obtain different hardness profiles throughout the plates: (1) as received, (2) very hard surface with a soft core and (3) very hard surface with a hard core.
3. A literature survey is done to understand the mechanisms of phase transformation and surface hardening of steel plates.
4. Ballistic tests are performed using 7.62 mm AP bullets to determine the ballistic properties with regards to hardness profile and plate layering.
5. Material testing is required to obtain the mechanical properties of the specimens with transformed microstructure due to the surface hardening. This includes hardness testing and uniaxial stress testing.
6. A constitutive relation and a failure criterion need to be chosen and calibrated based on the material tests.
7. Numerical simulations of the impact tests using IMPETUS Afea Solver are carried out. The numerical results are compared to the experimental findings.

Supervisors: Tore Børvik, Jens Kristian Holmen and Odd Sture Hopperstad (NTNU)

The thesis must be written according to current requirements and submitted to Department of Structural Engineering, NTNU, no later than June 10th, 2014.

NTNU, January 14th, 2014

Tore Børvik
Professor

Acknowledgements

This thesis has been written for the Structural Impact Laboratory (SIMLab) at the Norwegian University of Science and Technology (NTNU) during the spring of 2014. The thesis is a requirement for the degree of Master of Science in Engineering and ICT, with specialization in Computational Mechanics.

We would like to thank our main supervisors Professor Tore Børvik and PhDc Jens Kristian Holmen for guidance and valuable insight on the subject at hand, and for proofreading parts of this thesis. They were available to us at all times, and we are very grateful for that. Also, thanks to Professor Jan Ketil Solberg for offering us better understanding on subjects regarding metallurgy and surface hardening.

Furthermore, we would like to thank our supervisor Professor Odd Sture Hopperstad, and PhDc Lars Edvard Dæhli for teaching us more about triaxiality and plasticity via the course TKT4135 *Materials Mechanics* at NTNU.

Also, thanks to Senior Engineer Trond Auestad for valuable assistance with the ballistic experiments, Engineer Tore Andre Kristensen at SINTEF for conducting tensile tests, and Senior Engineer Trygve Lindahl Schanche for conducting microhardness measurements.

Furthermore, thanks to Dr. Lars Olovsson for answering our questions regarding IMPETUS Afea Solver throughout the semester, and Dr. Torodd Berstad for providing computer-solutions when encountering difficulties in LS-DYNA, LS-OPT, and usable solvers at NTNU.

Lastly, we would like to thank Espen Skogsrud and Torjus Sandviken who has endured our many discussions in the office, in combination with heavy coffee consumption.

Working on this thesis has enabled us to employ the knowledge acquired during our time at NTNU, as well as gaining further understanding in the areas of material mechanics, both macro- and microscopic behaviour, and ballistic impact problems.

Trondheim, 10.06.2014.

Erlend Orthe | Henrik Thorsen

Erlend Orthe | Henrik Thorsen

Abstract

The main objective with this thesis was to investigate experimentally and numerically the effect surface hardening has on the ballistic properties of monolithic and laminated mild steel plates. 300x300 mm^2 plates of thicknesses 12 mm, 6 mm, and 4 mm were made from a low carbon structural steel (NVE36) and combined in such a way that the total thickness always was 12 mm. Some of the plates were then surface hardened by the Kverneland Group to obtain different hardness profiles; (1) as-received, (2) very hard surface with a soft core and (3) very hard surface with a hard core.

Ballistic impact tests were performed at SIMLab, NTNU, using 7.62 mm AP bullets. From these tests, the Recht-Ipson model was used to obtain ballistic limit curves for all layered/hardened configurations. The experiments showed that surface hardening had a positive effect on the ballistic resistance compared to the as-received material, while lamination did not seem to influence the results significantly. The surface hardened plates suffered from radial cracks and fragmentation during penetration, while the as-received material failed by ductile hole growth.

Material properties were obtained by conducting tensile tests and microhardness measurements. The material tests revealed that the plates had not been hardened to their expected hardness profiles. This affected the comparison between a soft core and a hard core configuration. The modified Johnson-Cook constitutive relation and the Cockcroft-Latham fracture criterion were chosen to represent the material behaviour. Identification of material constants was done by direct calibration in combination with Bridgman's analysis, and by inverse modelling using LS-OPT.

Numerical simulations of the impact tests were conducted in IMPETUS Afea Solver with higher order 3D volume elements. Surface hardened plates were modelled with a varying yield stress over the thickness by use of scaling factors obtained from the material tests. The numerical results were finally compared with the experimental findings. IMPETUS was able to describe the main trends from the experiment and the numerical results were conservative for all the analyses.

Additionally, a numerical case study was performed with nominal hardness profiles. The study showed that nominal hard core plates performed better than nominal soft core plates, while layering did not seem to affect the result significantly.

Contents

Nomenclature

Afea	Advanced Finite Element Analysis
AP	Armour-Piercing
APM2	One type of AP bullet
CC	Circumferential Cracks
CCT	Continuous Cooling Transformation
CDM	Central Difference Method
CET	Cavity Expansion Theory
CL	Cockcroft-Latham fracture criterion
CPU, GPU	Central processing unit and graphics processing unit
D1, D2	Direction 1, Direction 2
DHG	Ductile Hole Growth
EOS	Equation of state
F	Fragmentation
FE	Finite Element
FEM	Finite Element Method
JC	Johnson-Cook constitutive relation
MJC	Modified Johnson-Cook constitutive relation
MSE	Mean Square Error
NFEM	Nonlinear Finite Element Method
NTNU	Norwegian University of Science and Technology
P1,P2,P3	Plate 1, Plate 2 and Plate 3

PM	Pinhole model
RC	Radial Cracks
SIMLab	Structural IMpact Laboratory
SMM	SIMLab Metal Model
UH, SC, HC	Unhardened (as-received), soft core and hard core configurations
UH1, UH2	Unhardened (as-received) direction 1 and direction 2
α_T	Thermal expansion coefficient
$\alpha(z)$	Scaling factor over thickness, z
α-iron	Ferrite
γ-iron	Austenite
ΔK	Change in kinetic energy
ΔT	Change in temperature
Δt_{cr}	Critical time step
Δt_{erode}	Time erosion
$\Delta\varepsilon_{erode}$	Deviatoric geometric strain increment
ΔU	Change in potential
ε	Total strain
$\varepsilon^e, \varepsilon^p$	Elastic and plastic strain
$\varepsilon_e, \varepsilon_A, \varepsilon_G, \varepsilon_l$	Engineering, Almansi, Green and logarithmic strain
ε_f	Strain at failure
ε_u	Strain at σ_u
$\dot{\varepsilon}_0$	Reference strain rate
θ_{Ri}	Used in SMM where $\theta_{Ri} = C_i Q_{Ri}$
λ	Distance between particles
μ_σ	Lode parameter
ν	Poisson's ratio
ρ	Mass density
σ	Stress

σ_{eq}, φ	Equivalent stress
σ_0	Initial yield stress
$\sigma_{0.2}$	0.2 % Offset yield stress
σ_Y	Flow stress
σ_e, σ_t	Engineering stress and true stress
σ_f	Stress at failure
$\sigma^{'}$	Deviatoric stress
σ_H	Hydrostatic stress
σ^*	Triaxiality. σ_H/σ_{eq}
$\sigma_1, \sigma_2, \sigma_3$	Principal stress where $\sigma_1 > \sigma_2 > \sigma_3$
σ_u	Ultimate tensile strength
τ_f	Critical shear stress value
τ_{max}	Maximum shear stress
χ	Taylor-Quinney coefficient.
C_{ijkl}	4th order tensor of elastic constants
$\{\dot{\mathbf{D}}\}, \{\ddot{\mathbf{D}}\}$	Velocity and acceleration
$[\mathbf{M}], [\mathbf{M}]$	Mass and daming matrix
$\mathbf{p}$	Linear momentum
$\{\mathbf{R}\}^{int}, \{\mathbf{R}\}^{ext}$	Internal and external forces
3x4 mm target	Triple layered/laminated plates with total thickness 12 mm
2x6 mm target	Double layered/laminated plates with total thickness 12 mm
12 mm target	Monolithic plate with thickness 12 mm
A_0, A	Initial and current area
A_3, A_{cm}	Phase and temperature boundaries
a	Radius of the crack
A,B,n	Material constants for Power hardening law
A, C_i, Q_i	Material constant for Voce hardening law
a, p	Recht-Ipson constants

a/R	Ratio between the cross-section and the radius of the curvature
bcc	Body-centred-cubic crystal structure
c_d	Dilatational wave speed in the material
C,m	Strain rate hardening and thermal softening constants for MJC
CO, CO_2	Carbon monoxide and carbon dioxide
C_p	Specific heat parameter
D_0, D_x, D_y	Initial diameter, current diameter in x and y direction
D	Damage parameter
d	Closest distance from the integration point to the crack-tip
d_p	Diameter of projectile
E	Young's modulus
$f(\sigma, R)$	Yield function
f	Scaling function for node splitting in IMPETUS Afea Solver
F	Applied force
fcc	Face-centred-cubic crystal structure
Fe_3C	Cementite
G_I	Strain energy release rate
h_t	Initial thickness of target
Halo	Circumferential crack surrounding an exit hole
HV	Vickers Hardness
$HV_{0.2}$	Vickers Hardness measured with a 0.2 kg diamond shaped indenter
$HV_{12,c}$	Average Vickers hardness in core of monolithic plates
I	Impulse
K_I	Stress intensity factor
L_0, L	Initial and current length
L_e	Characteristic length of the smallest element in a FEM analysis
l_p	initial length of projectile
m	The mass

m_p	Projectile mass
m_{pl}	Plug mass
M_s, M_f	Start and final temperature for martensitic transformation
p	Plastic true strain
$\dot{p}_0$	Reference plastic strain rate
$\dot{p}$	Plastic strain rate
Q	Heat added to the system
r	Strain ratio. Equals unity for isotropy
R	Isotropic hardening variable
S0	The Voce constant used in LS-OPT. See A
T, T_r, T_m	Material, room and melting temperature
V	Volume of a body
v_{bl}	Ballistic limit velocity
v_i	Initial/impact/striking/incoming velocity
v_r	Residual/outgoing velocity
W	Work done by the system
W_{cr}	Critical value in CL fracture criterion
W_{free}	Inelastic energy loss
W_n	Additionally energy dissipation

Chapter 1

Introduction

Different materials have been investigated for protection against small-arms bullets, however steel is still the dominating material in the design of protective structures. This is due to its high strength and high ductility. Thin plates of ultra-high-strength steel is advantageous when it comes to civil and military armours because it offers excellent load carrying capability and great impact resistance for a low cost, compared to other alloys [12]. Recent studies have suggested that ordinary structural steel, when diffusing carbon atoms into the surface, may provide correspondingly good, or even better, ballistic properties than high-strength steels [54].

Previous research by SIMLab and the Department of Materials Science and Engineering at NTNU investigated procedures for obtaining different hardness profiles providing protection against ballistic impacts. Lou et al. [54] surface hardened 12 mm NVE36 steel plates, with a nominal yield stress of 355 MPa. This steel grade was chosen due to its low-strength/low-cost in combination with its high-ductility. The goal was to increase the surface strength, but maintain a ductile core. Thus, combine the high-strength properties with plastic dissipation from the ductility. The study showed that when surface hardening this low-strength steel, they were able to obtain a higher ballistic resistance than a Hardox 400 wear steel with a yield stress of about 1200 MPa.

The ballistic perforation resistance of layered target plates has been investigated for a long time. By layering thinner plates, more global deformation may occur which absorbs considerable amounts of the projectiles energy during impact. An interesting idea is to combine multi-layering with surface hardening. Coucheron [24] investigated this combination using NVE36 steel. He obtained a higher resistance when layering two 6 mm plates than a monolithic 12 mm thick plate. However, the research on ballistic properties of multi-layering combined with surface hardening is limited.

This thesis will investigate, both experimentally and numerically, the effect surface hardening has on the ballistic perforation resistance of monolithic and laminated NVE36 steel plates.

A short overview of each chapter is given below.

Chapter 2 - Theory: Theory relevant to this thesis. This includes an introduction to impact dynamics, mechanics of materials, microstructure and phase transformation of steel, the surface hardening process and an overview of some previous work on the subject.

Chapter 3 - Target Materials: A presentation of the target materials and how they were obtained. Results from performed tensile tests and microhardness measurements conducted on the investigated material are provided and discussed.

Chapter 4 - Ballistic Impact Experiments: Description and procedure of the ballistic impact experiments conducted on the target materials. Results from the experiments are presented and discussed.

Chapter 5 - Identification of Material Constants: Material models are calibrated based on results from conducted tensile tests. First, identification of material constants are obtained by direct calibration. Then, an inverse modelling approach was performed by utilizing the optimization tool LS-OPT in combination with LS-DYNA. Scaling factors for modelling a varying yield stress over the thickness are presented.

Chapter 6 - Numerical Design: Numerical base models of monolithic configurations are established using IMPETUS Afea Solver. A sensitivity study is conducted on the base models.

Chapter 7 - Numerical Results: Based on the results from Chapter 6, a numerical model is established for all target configurations. Numerical simulations are run and compared with the ballistic experiments, followed by discussion of the results.

Chapter 8 - Numerical Case Study: Nominal Surface Hardening: A numerical case study where nominal hardness profiles are implemented in IMPETUS is conducted. The numerical results are presented and discussed.

Chapter 9 - Concluding Remarks: Summary of results and conclusions.

Chapter 10 - Further Work: Suggestions for further work in this research area are presented.

Chapter 2

Theory

In this chapter, relevant theoretical background for this thesis will be presented. This involves an introduction to impact dynamics and macro- and microscopic view of mechanics of materials. Furthermore, a very short description of relevant fracture mechanisms and general numerics will be explained. Additionally, since a nonlinear finite element method (NFEM) has been applied, the basic theory will be briefly presented. Lastly, an overview of some of the previous work on the subject will be given.

2.1 Impact and Penetration Dynamics

Structural impact is defined as the collision between two or more solid objects, where the interaction between the bodies may be elastic, plastic or fluid, or any combination of these [9]. The impact process has two features which distinguishes it from other disciplines of classical mechanics which operates under quasi-static conditions. Firstly, the importance of inertia effects and, secondly, the role of stress-wave propagation. The former phenomenon comes in to play in the governing equations which are based on fundamental conservation laws of mechanics and physics. The role of stress wave propagation is important in the analysis of the problem since most impact events are highly transient phenomena where no steady-state conditions may occur. Also, the impacted material may introduce strain rate effects, thermal softening and hydrodynamic material behaviour which is not observed in quasi-statically loaded materials.

Most of the work in the field of impact dynamics regarding stress wave propagation, ballistic modelling and numerical simulations are based on three fundamental conservation laws; conservation of mass, conservation of linear momentum, and conservation of energy [69]. These laws are expressed as:

Conservation of mass: $m = \int_V \rho dV = \text{constant}$

Conservation of linear momentum: $\mathbf{p} = \int_V \mathbf{v} \rho dV = \text{constant}$

Conservation of energy: $\Delta K + \Delta U = Q + W$

where m is mass, ρ is mass density, V is volume of the body, $\mathbf{p}$ is linear momentum, and $\mathbf{v}$ is velocity of the body. Furthermore, ΔK is the change in kinetic energy, ΔU is change in potential energy, Q is heat added to the system and W is the work done by the system. Conservation of linear momentum is closely related to the impulse-momentum law which states that the impulse, I, imparted to a body is equal to its change in momentum.

Based on these fundamental principles one can create simplified analytical models which help predict the outcome of an impact process. One of them, the Recht-Ipson model [64], will be elaborated later in this thesis.

2.1.1 Terminology

Some basic and relevant definitions used in structural impact dynamics are presented in the following section.

Ballistics is defined as the art of accelerating bodies by use of some kind of engine [9]. One can divide the science of ballistics into three main research areas:

- *Interior ballistics*: Study of the motion and forces on an object when still inside the launcher.
- *Exterior ballistics*: Study of an object during free flight.
- *Terminal ballistics*: Study of the interaction between an object and the target during impact.

This thesis focuses on terminal ballistics which is the area of interest in *fortification*. Fortifications are structures used for additional strengthening [9].

Projectiles are items that can be launched [70]. They can be categorized as soft, semi-hard or hard depending on deformation during impact. Also, projectiles can be characterized according to initial geometry, material density and flight orientation. Examples of projectile nose shapes include flat-ended, ogival, hemispherical, and conical. These are depicted in Figure 2.1.

The *target* is defined as any moving or stationary object struck by the projectile. Similarly to the projectile, the target can be categorized according to certain characteristics like geometry and material properties. Typically, the target is classified by its thickness. Backman and Goldsmith [5] divided the target thickness into four categories:

- *Semi-infinite*: When there is no influence of the distal boundary on the penetration process.
- *Thick*: If there is influence of the distal boundary on the penetration process only after substantial travel into the target.
- *Intermediate*: When the rear surface exerts considerable influence on the deformation process during nearly all of the projectile motion.
- *Thin*: If the stress and deformation gradient throughout the thickness does not exists.

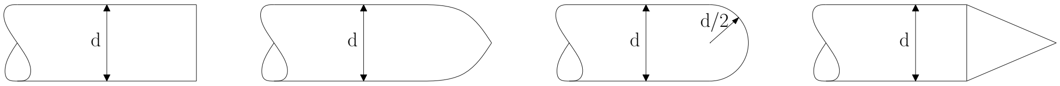

(a) Flat-ended. (b) Ogival. (c) Hemispherical. (d) Conical.

Figure 2.1: Different projectile nose shapes.

The target structures in the present study are different compositions of structural steel plates. They are either monolithic or layered/laminated plates with the same total thickness and weight. The layered plates are in contact with each other. Figure 2.2 displays a simple overview of these compositions.

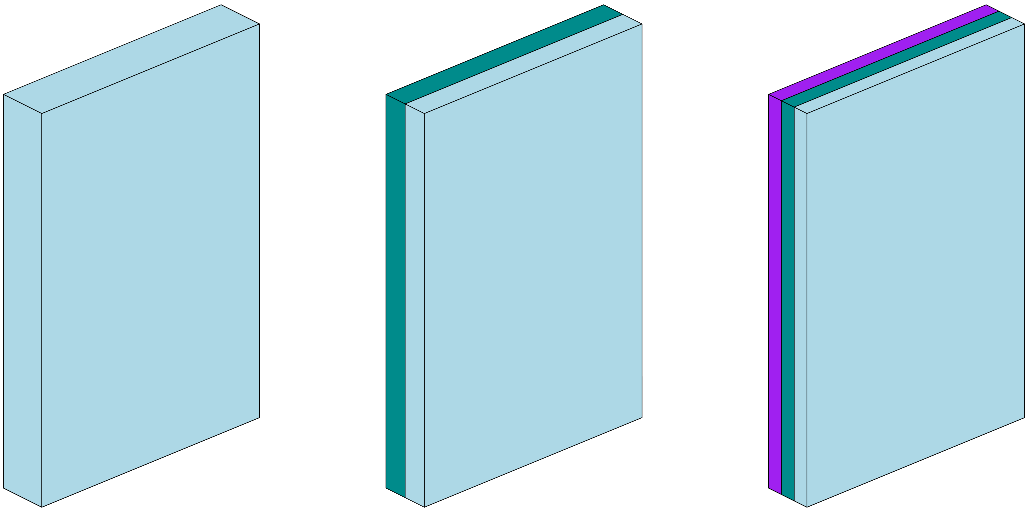

(a) Monolithic. (b) Double layered. (c) Triple layered.

Figure 2.2: Layering of target plates.

Penetration is the entry of a projectile into any region of the target [9]. We define the incoming velocity of the projectile as the impact, or initial, velocity, v_i. If the projectile perforates the target, the outgoing velocity is denoted as residual velocity, v_r. According to Backman and Goldsmith [5] the penetration process can be divided into three categories:

- *Perforation*: Projectile passes through the target resulting in a finite residual velocity.
- *Embedment*: Projectile stops during impact with target.
- *Ricochet*: Projectile is deflected from target without being stopped.

One of the most predominant factors influencing the target response is the impact velocity. The impact velocity can be classified into certain velocity ranges, or regimes; *low velocity regime* (0-50 m/s), *sub-ordnance velocity regime* (50-500 m/s), *ordnance velocity regime* (500-1500 m/s), *ultra-ordnance velocity regime* (1500-3000 m/s), *hypervelocity regime* (> 3000 m/s). This thesis deals with velocities in the ordnance velocity regime, which is a typical range for military applications. Most of the kinetic energy is converted into plastic work and the response area in the target is typically 2-3 projectile diameters from impact zone, i.e. hardly any global deformation in the target is observed [9].

The *ballistic limit velocity*, v_{bl}, describes the greatest velocity the projectile can have without perforating the target structure [22]. If the impact velocity is increased above this limit, the projectile will have a residual velocity. The *ballistic limit curve* describes the residual velocity as a function of impact velocity (Figure 2.3). It is often compared to the *ballistic limit line* which is the curve for a target with zero thickness, i.e. the impact velocity equals the residual velocity.

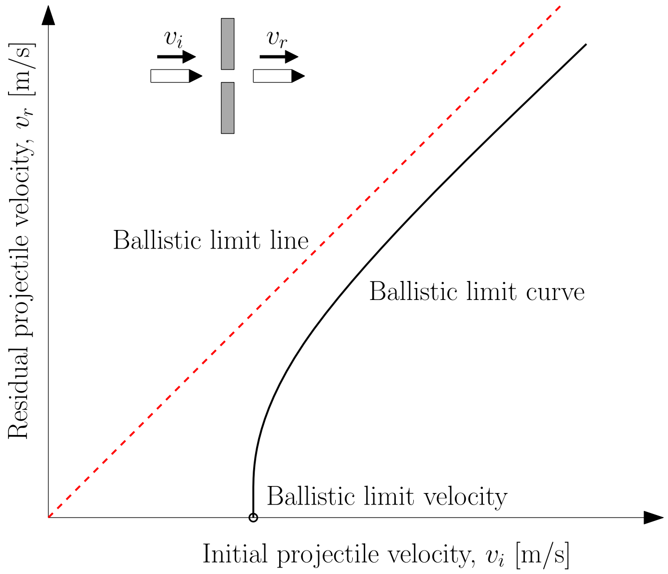

Figure 2.3: Ballistic limit curve.

2.1.2 Target Response and Impact Characteristics

There are several ways the impacted target can fail with multiple factors contributing to that effect. Besides the impact velocity, other important parameters include; material properties, projectile shape and trajectory, target support and relative dimensions of projectile and target. Target response is commonly divided into non-failure modes and failure modes. *Non-failure modes* consist of two types of transverse displacement due to plastic deformation; bulging and dishing. *Bulging* is a local phenomenon in which the target deforms to the shape of the projectile nose, while *dishing* is introduced by global bending. Very thick target plates may exhibit cratering as well. This thesis is more concerned with the failure modes. The most relevant perforating failure modes for thin and/or intermediate targets are illustrated in Figure 2.4. Also, a short description is provided. Even if one of the modes dominates the failure process, they will often be accompanied by several other modes.

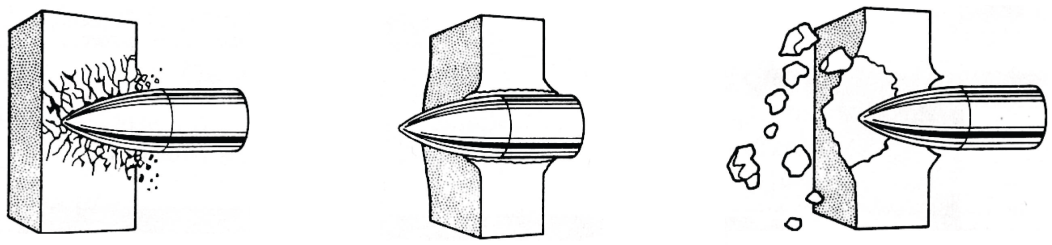

(a) Brittle fracture. (b) Ductile hole growth. (c) Fragmentation.

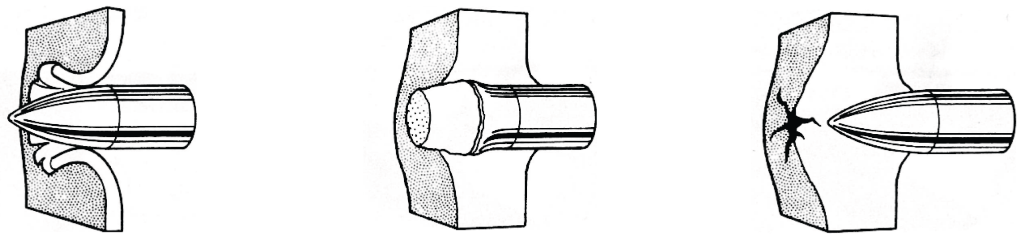

(d) Petaling. (e) Plugging. (f) Radial fracture.

Figure 2.4: Failure modes in impacted plates [5].

- *Radial fracture*: Arises from the compressive wave that propagates away from the impact point in the target. This builds up a large circumferential tensile stress wave. If the tensile strength of the target is smaller than this stress, radial cracks may occur, and can also be accompanied by circumferential cracks.
- *Plugging*: A failure mode typical for blunt projectiles. During impact, a zone with a high shear gradient will be established in the vicinity of the projectiles periphery.

This adiabatic shearing process causes a plug to be pushed out of the target approximately equal to the projectiles diameter. At high deformation rates, plastic work is converted into heat causing reduced shear capacity.

- *Fragmentation*: Can occur at high impact velocities, especially for thin and/or brittle materials.
- *Ductile hole growth*: Occurs in ductile materials impacted by conical or ogival projectiles. Material is pushed away in the radial direction as the projectile perforates the target. This causes the impact hole to increase in size and the target is thickened in the area around the edge of the hole.
- *Petaling*: Generated by high radial and circumferential tensile stresses after passage of the initial stress wave occurring near the tip of the projectile. Bending moments are created as the projectile pushes the target material forward. This failure mode is most apparent for thin plates struck by ogival or conical projectiles at relatively low velocities or by blunt projectiles near the ballistic limit. Due to inhomogeneities or weaknesses in the material the tensile strength will eventually be exceeded as the projectile deforms the bulge on the back of the plate. Ultimately, a star-shaped crack is formed around the tip of the projectile. The petals are created by the continuing forward motion of the projectile.

The projectiles kinetic energy is dissipated into a number of complex mechanisms during impact. These include elastic vibrations, local and global plastic deformations, fracture, and friction between projectile and the target. There are several ways of analysing impact problems. These include empirical, analytical and numerical methods, e.g. NFEM. However, all these analysis strategies are approximated in nature, meaning they all are based on simplified assumptions. One example of an analytical method is the Cavity Expansion Theory (CET), first introduced by R. Hill [37].

2.1.3 Simplified Methods - The Recht-Ipson Model

In 1963, Recht and Ipson [64] developed a simple analytical model for the ballistic curve based on the basic conservations laws of momentum and energy stated earlier. A short derivation of this useful expression follows. They first considered a blunt projectile impacting a thin plate, i.e.

$$\frac{h_t}{l_p} < \frac{1}{2} \qquad \text{and} \qquad \frac{h_t}{d_p} < \frac{1}{2}$$

where h_t is initial thickness of target, l_p and d_p is the length and diameter of the projectile, respectively. This results in failure by plugging where the plug has the same diameter and assumed equal residual velocity as the perforating projectile. The projectile mass is denoted m_p, and the plug mass, m_{pl}. If the projectile and the plug collided in free space, the conservation of momentum law yields

$$\mathbf{p}_{in} = \mathbf{p}_{out}$$

$$m_p v_i = (m_p + m_{pl}) v_r$$

and the residual velocity becomes

$$v_r = \left(\frac{m_p}{m_p + m_{pl}} \right) v_i \tag{2.1}$$

Considering the energy balance of this free impact, the incoming kinetic energy from the projectile must equal the outgoing kinetic energy from the projectile and the plug, as well as any inelastic energy loss, W_{free}, from heat and deformation occurring during the impact. Hence,

$$\frac{1}{2} m_p v_i^2 = \frac{1}{2} (m_{pl} + m_p) v_r^2 + W_{free}$$

and

$$W_{free} = \frac{1}{2} (m_{pl} + m_p) v_r^2 - \frac{1}{2} m_p v_i^2$$

By inserting Eq. 2.1 into the above expression, an equation for the additional loss from the free collision is found.

$$W_{free} = \frac{1}{2} m_p \left[\frac{m_{pl}}{m_p + m_{pl}} \right] v_i^2 \tag{2.2}$$

When including the target plate in the equations, the work required to push out the plug has to be included. This work will mainly be due to shear forces, denoted W_n. Now, an expression for the total energy balance is obtained.

$$\frac{1}{2} m_p v_i^2 = \frac{1}{2} (m_{pl} + m_p) v_r^2 + W_{free} + W_n \tag{2.3}$$

Assuming the residual velocity is zero and impact velocity equals the ballistic limit velocity, the energy balance in Eq. 2.3 yields

$$W_n = \frac{1}{2} m_p \left[\frac{m_p}{m_p + m_{pl}} \right] v_{bl}^2 \tag{2.4}$$

By inserting the energy contributions from Eq. 2.2 and Eq. 2.4 into Eq. 2.3, an expression for the residual velocity becomes

$$v_r = \left[\frac{m_p}{m_p + m_{pl}} \right] (v_i^2 - v_{bl}^2)^{\frac{1}{2}} \tag{2.5}$$

Later, Recht and Ipson considered a projectile with an ogival or conical nose. They then assumed a failure mode where no plugging occurred. Thus, only the plastic dissipation from the target, W, is included, generating the following energy balance

$$\frac{1}{2}m_p v_i^2 = \frac{1}{2}m_p v_r^2 + W \tag{2.6}$$

Applying the same procedure as for Eq. 2.4, an expression for the additional work, W, is obtained.

$$W = \frac{1}{2}m_p v_{bl}^2$$

Solving for this new constant, the residual velocity based on a conical or ogival projectile yields

$$v_r = (v_i^2 - v_{bl}^2)^{\frac{1}{2}} \tag{2.7}$$

The residual velocity, from Eq. 2.7, does not rely on the mass of the projectile. Also, Eq. 2.7 and Eq. 2.5 are almost the same except for the first mass term. The Recht-Ipson model is only approximate and assumes ideal conditions, and also assumes that the penetrating work is constant when initial velocity is larger than the ballistic limit, which is not always true.

Lambert and Jonas [70] reviewed these equations and discovered an empirical model which generalized the expression into

$$v_r = a(v_i^p - v_{bl}^p)^{\frac{1}{p}} \tag{2.8}$$

Where a, p and v_{bl} are empirical constants which has to be determined experimentally. Assuming ductile hole growth as failure mode, then $a = \left[\frac{m_p}{m_p + m_{pl}}\right] = 1$.

2.2 Mechanics of Materials

This section provides a presentation of the theory necessary to establish a material model. An isotropic constitutive relation has been employed in order to represent the elastic-plastic material behaviour. When the material enters the plastic domain, it has been shown a nonlinear and history-dependent relationship between stress and strain [43]. In addition, a fracture criterion has been included.

Applying tensor notation, the strain tensor can be divided into a recoverable (elastic) part and a non-recoverable (plastic) part.

$$\varepsilon_{ij} = \varepsilon_{ij}^e + \varepsilon_{ij}^p, \qquad i, j = 1, 2, 3 \tag{2.9}$$

The stress tensor can be related to the elastic strain by the generalized Hooke's law.

$$\sigma_{ij} = C_{ijkl}\varepsilon_{kl}^e = C_{ijkl}(\varepsilon_{kl} - \varepsilon_{kl}^p), \qquad i, j, k, l = 1, 2, 3 \tag{2.10}$$

where C_{ijkl} is the 4th order tensor of elastic constants. In one dimension, this equals Young's Modulus, E.

When entering the plastic domain, a yield function must be defined, expressed as

$$f(\sigma, R) = \varphi(\sigma) - \sigma_Y(R) \leq 0$$

where $\sigma_{eq} = \varphi(\sigma)$ is the equivalent stress and $\sigma_Y = \sigma_0 + R$ is the flow stress. Furthermore, σ_0 is the initial yield stress and R is the isotropic hardening variable. When $f(\sigma, R) < 0$, the behaviour is elastic and for $f(\sigma, R) = 0$ the material yields.

The stress component can be divided into a deviatoric and a hydrostatic part

$$\sigma_{ij} = \sigma_{ij}^{'} + \sigma_H \quad , \quad \sigma_H = \frac{1}{3}(\sigma_1 + \sigma_2 + \sigma_3) \tag{2.11}$$

where $\sigma_{ij}^{'}$ is the deviatoric stress tensor and σ_H is the hydrostatic part.

The von Mises yield criterion (J2 flow rule) is applied, i.e. σ_{eq} is expressed as

$$\sigma_{eq} = \sqrt{3J_2} = \sqrt{\frac{3}{2}\sigma_{ij}^{'}\sigma_{ij}^{'}} \tag{2.12}$$

In terms of the principal stresses, i.e. σ_1, σ_2, σ_3, the von Mises yield criterion becomes

$$f(\sigma_1, \sigma_2, \sigma_3) = \sqrt{\frac{3}{2}\sigma_{ij}^{'}\sigma_{ij}^{'}} - \sigma_Y = \sqrt{\frac{1}{2}((\sigma_1 - \sigma_2)^2 + (\sigma_2 - \sigma_3)^2 + (\sigma_3 - \sigma_1)^2)} - \sigma_Y = 0$$

The yield criterion only depends on a deviatoric stress state, which is common for metals and alloys. This is because the plastic deformation is created by plastic slip, which is a shear-driven deformation mode [43].

In order to predict the strain and stress in a material, different measures must be considered. This will be presented in the following sections. Also, further derivation on the subject will be with respect to one dimension.

2.2.1 Strain Measures

For impact problems, large strains are inevitable and it is therefore important to obtain a good strain measure for nonlinear geometry. However, for small deformations the engineering strain is often used. This measure refers to the initial configuration of the geometry and assumes infinitesimal strains. It is given as

$$\varepsilon_e = \frac{L - L_0}{L_0}$$

where L_0 and L is initial and current length, respectively.

For nonlinear behaviour, many different strain measures have been introduced over the years. In order to choose a good strain measure, some requirements must be fulfilled:

- The strain must give infinitesimal strains when linearised (should tend towards the engineering strain for small deformations).
- The strain should tend to $-\infty$ in "full compression" and ∞ for "infinite stretching".
- The strain must predict zero strain for rigid body translations and rotations.

Proposed strain measures include the Almansi strain, the Green strain and the logarithmic strain

$$\varepsilon_A = \frac{L^2 - L_0^2}{2L^2} \quad , \quad \varepsilon_G = \frac{L^2 - L_0^2}{2L_0^2} \quad , \quad \varepsilon_l = \ln \frac{L}{L_0}$$

The logarithmic strain, i.e. true strain, is simply derived by changing the nominal length to the deformed configuration, i.e.

$$d\varepsilon_l = \frac{L - L_0}{L} = \frac{dL}{L}, \quad \varepsilon_l = \int_{L_0}^{L} \frac{dL}{L} = \ln \frac{L}{L_0} = \ln(1 + \varepsilon_e) \tag{2.13}$$

The logarithmic strain measure is the only measurement that fulfils the aforementioned requirements for large strains, and this will be adopted.

2.2.2 Stress Measures

The engineering stress is defined for the initial configuration

$$\sigma_e = \frac{F}{A_0}$$

where F is the applied force, and A_0 is the initial area.

For geometrical nonlinearities, the true stress, or Cauchy stress, may be introduced. This stress measure takes the deformed configuration, A, into account, i.e.

$$\sigma_t = \frac{F}{A}$$

Since the theory of plasticity assumes constant volume [43], the following relation is obtained

$$AL = A_0 L_0 \quad \Longrightarrow \quad \frac{A_0}{A} = \frac{L}{L_0}$$

Thus, true stress can be expressed as a function of the engineering values

$$\sigma_t = \frac{F}{A} = \frac{F}{A_0}\frac{L}{L_0} = \sigma_e(1+\varepsilon_e) \tag{2.14}$$

2.2.3 Equivalent Stress vs. Equivalent Plastic Strain

From performed tension tests, force vs. displacement curves are obtained. In these tests, described in Chapter 3, a laser measured the true diameter of the tensile specimen in two perpendicular directions, D_x and D_y. The initial and current cross sectional area of the cylindrical tensile specimen is then,

$$A_0 = \frac{\pi D_0^2}{4} \quad \text{and,} \quad A = \frac{\pi D_x D_y}{4}$$

respectively, where D_0 is initial diameter of the tensile specimen. An explicit expression of the logarithmic strain is then obtained

$$\varepsilon_l = \ln\frac{L}{L_0} = \ln\frac{A_0}{A} = \ln\left(\frac{D_0^2}{D_x D_y}\right)$$

The tensile specimen experiences a uniaxial stress state until diffuse necking occurs. Before this point, the measured stress component, $\sigma_t = \sigma_1$, equals the equivalent stress. Note, the principal stress, σ_1, is the longitudinal stress in a uniaxial tension test. Diffuse necking is defined as an instability, and occurs when the applied force reaches its maximum, i.e. $dF = 0$.

Thus, from Eq. 2.14, we obtain

$$F = \sigma_t A$$

$$dF = \sigma_t dA + A d\sigma_t = 0$$

and

$$-\frac{dA}{A} = \frac{d\sigma_t}{\sigma_t}$$

Furthermore, the constant volume relation gives

$$\frac{dL}{L} = -\frac{dA}{A} = d\varepsilon_l$$

From these equations, an expression may be obtained which shows that diffuse necking occurs when the slope of the true stress vs. logarithmic strain curve equals the true stress itself, i.e.

$$\frac{d\sigma_t}{d\varepsilon_l} = \sigma_t \tag{2.15}$$

This is also known as the Considère criterion [43].

After diffuse necking, the specimen will be introduced to a complex triaxial stress state and σ_t does not longer equal the equivalent stress. This is due to the geometrical discontinuity, a notch, that diffuse necking creates. Under tension this notch produces radial and transverse stresses [27]. These stresses increase the value of the longitudinal stress, σ_1. Bridgman [8] came up with a mathematical correction which compensated for the introduced transverse stresses.

His analysis gives an approximation for what the uniaxial flow stress would have been in the tension test if necking had not introduced triaxial stresses [27]:

$$\sigma_{eq} = \frac{\sigma_t}{(1 + 2R/a)[\ln(1 + a/2R))]} \tag{2.16}$$

The Bridgman correction is based on the following assumptions; (i) strains remain constant across the neck, (ii) the neck geometry is approximated by the arc of a circle, (iii) the cross section remains circular through the neck, and (iv) that the von Mises yield criterion applies [27].

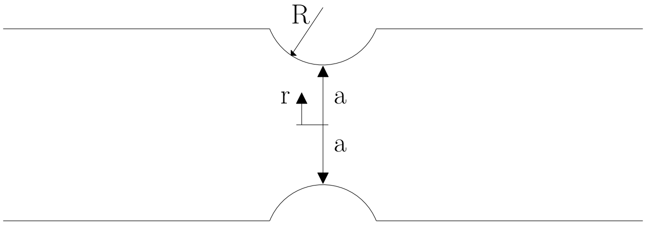

Figure 2.5: Sketch of a notch in diffuse necking.

Note that Eq. 2.16 is a function of the ratio a/R. This ratio describes the relation between the radius of the current cross section, a, and the radius of the curvature, R, of the necking geometry (Figure 2.5). Le Roy et al. [50] proposed an empirical expression for this ratio

$$\frac{a}{R} = 1.1(\varepsilon^p - \varepsilon_u), \qquad \varepsilon^p > \varepsilon_u \tag{2.17}$$

where ε_u is plastic strain at necking. Furthermore, the plastic strain is obtained by extracting the elastic part, i.e.

$$\varepsilon^p = \varepsilon_l - \frac{\sigma_t}{E}$$

In uniaxial tension test it should be noted that the equivalent plastic strain equals the plastic strain i.e. $p = \varepsilon^p$.

2.2.4 Johnson-Cook Material Model

In order to model the impact problem, a constitutive relation should include the following features:

- Strain hardening
- Strain rate hardening
- Temperature softening

In 1983, Johnson and Cook [45] presented a thermoviscoplastic material model which accommodates the aforementioned factors. The Johnson-Cook (JC) model is given as

$$\sigma_{eq} = [A + Bp^n]\left[1 + C\ln\frac{\dot{p}}{\dot{p}_0}\right]\left[1 - \left(\frac{T - T_r}{T_m - T_r}\right)^m\right] \tag{2.18}$$

where

A, B, C, n, m	material constants
p	equivalent plastic strain
$\dot{p}$	plastic strain rate
$\dot{p}_0$	reference plastic strain rate
T	material temperature
T_r	room temperature
T_m	material's melting temperature

The material temperature will be changed during loading. Since the impact process is a fast transient problem, adiabatic heating may be assumed [11]. The change in temperature can be expressed as

$$\Delta T = \int_0^p \chi \frac{\sigma_{eq}dp}{\rho C_p} \tag{2.19}$$

where

ρ	material density
C_p	specific heat parameter
χ	Taylor-Quinney coefficient

The Taylor-Quinney coefficient represents the fraction of plastic work converted into heat, and a typical value is χ=0.9 for metals [38].

It may be seen that if the strain rate is less than the reference value, the logarithmic term gives a negative value which may cause trouble. Therefore, a modified Johnson-Cook (MJC) material model was proposed [14], given as

$$\sigma_{eq} = [A + Bp^n]\left[1 + \frac{\dot{p}}{\dot{p}_0}\right]^C \left[1 - \left(\frac{T - T_r}{T_m - T_r}\right)^m\right] \tag{2.20}$$

The original JC uses a Power law to describe the material strain hardening (first term in Eq. 2.18). A different isotropic strain hardening law may be introduced instead. The Voce hardening law is given as

$$\sigma_{eq} = \sigma_0 + R(p) = A + \sum_{i=1}^{n} Q_i(1 - e^{-C_i p}) \tag{2.21}$$

where A, Q_i, C_i are material constants calibrated from a tension test. This thesis uses $n = 3$ in order to represent a material exhibiting a yield plateau. More about this in Chapter 3. Note that A does not necessarily coincide with the real yield stress. This is only a numerical value in order to represent the best curve fit.

Combining the MJC and the Voce hardening law gives the final expression for representing the equvalent stress

$$\sigma_{eq} = \left[A + \sum_{i=1}^{n} Q_i(1 - e^{-C_i p})\right]\left[1 + \frac{\dot{p}}{\dot{p}_0}\right]^C \left[1 - \left(\frac{T - T_r}{T_m - T_r}\right)^m\right] \tag{2.22}$$

2.2.5 Ductile Fracture Criterion - Cockcroft-Latham

Besides a constitutive relation, it is required to include a fracture criterion in ballistic impact. Ductile fracture may occur by one of the two following fracture modes [44]:

- **(i)** Void nucleation, growth and coalescence in the bulk of the material.
- **(ii)** Emergence of localized shear bands in which voids nucleate, grow and coalesce under extreme shear strains.

Cockcroft and Latham [19] suggested that cracking in metalworking is associated with induced tensile stresses. Furthermore, ductile fracture mode (i) is highly dependent on the stress triaxiality [63]. A well known fracture criterion that includes this is the Cockcroft-Latham (CL) fracture criterion, given as

$$W = \int_0^{\varepsilon_f} \langle \sigma_1 \rangle \, dp \leq W_{cr} \tag{2.23}$$

where

$$\langle \sigma_1 \rangle = \begin{cases} \sigma_1 & \text{if } \sigma_1 > 0 \\ 0 & \text{if } \sigma_1 \leq 0 \end{cases}$$

and W is the ”plastic work” per unit volume. The quotation marks are used because the real plastic work is calculated with respect to equivalent stress and not principal stress. Furthermore, ε_f is the strain at failure and W_{cr} is the critical ”plastic work”. The criterion can also be expressed in terms of a damage parameter, D.

$$D = \frac{W}{W_{cr}} \leq 1.0$$

The CL criterion is used since it depends on the easily obtained (from a tension test) principal stress component, σ_1, which depends on the stress triaxiality. Furthermore, Kane et al. [46] showed that the one parameter CL-criterion gives equally good results as more advanced failure criteria in simulations of perforation of steel plates under various stress states.

The Lode parameter [44] may be expressed as

$$\mu_\sigma = \frac{2\sigma_2 - \sigma_1 - \sigma_3}{\sigma_3 - \sigma_1} \tag{2.24}$$

where σ_2 and σ_3 are principal stresses perpendicular to σ_1.

Triaxiality is another non-dimensional variable defined as the ratio between the hydrostatic and the equivalent stress, i.e.

$$\sigma^* = \frac{\sigma_H}{\sigma_{eq}} = \frac{\frac{1}{3}(\sigma_1 + \sigma_2 + \sigma_3)}{\sigma_{eq}} \tag{2.25}$$

The triaxiality characterizes the stress field and is shown to be one of the more important parameters defining the ductility of a metal [44].

From Eq. 2.24, different values for the most important stress states are obtained:

$$\mu_\sigma = \begin{cases} +1 & \text{Axisymmetric tension, } \sigma_2 = \sigma_3 \\ 0 & \text{Pure shear} \\ -1 & \text{Bisymmetric tension, } \sigma_1 = \sigma_2 \end{cases}$$

By including the von Mises criterion, the hydrostatic stress, and the Lode parameter, the principal stress can be expressed as

$$\sigma_1 = \left(\sigma^* + \frac{3 + \mu_\sigma}{3\sqrt{3 + \mu_\sigma^2}} \right) \sigma_{eq} \tag{2.26}$$

This equation illustrates that σ_1 depends on the triaxiality and the Lode parameter. Thus, the CL criterion can be expressed as

$$W = \int_0^{\varepsilon_f} \left(\sigma^* + \frac{3+\mu_\sigma}{3\sqrt{3+\mu_\sigma^2}} \right) \sigma_{eq} dp \leq W_{cr}$$

In the CL criterion, $\langle \sigma_1 \rangle$ cannot be less than zero, indicating that the criterion does not predict ductile fracture for negative principal stresses. This is reasonable to assume since there will be no nucleation, growth and coalescence of voids during super imposed compression.

From Eq. 2.26 it is clear that σ_1 becomes zero when

$$\sigma^* = -\frac{3+\mu_\sigma}{3\sqrt{3+\mu_\sigma^2}}$$

leading to an infinite fracture strain for

$$\sigma^* = \begin{cases} -\frac{2}{3} & \text{for } \mu_\sigma = +1 \\ -\frac{1}{\sqrt{3}} & \text{for } \mu_\sigma = 0 \\ -\frac{1}{3} & \text{for } \mu_\sigma = -1 \end{cases}$$

Since the tension test produces an axisymmetric stress state, i.e. $\mu_\sigma = +1$, an expression for the triaxiality with respect to the true stress and the equivalent stress may be obtained:

$$\sigma^* = \frac{\sigma_1}{\sigma_{eq}} - \frac{2}{3} \tag{2.27}$$

By combining Eq. 2.27 and Eq. 2.25, the following relation yields

$$\frac{\sigma_1}{\sigma_{eq}} - \frac{2}{3} = \frac{\frac{1}{3}(\sigma_1 + \sigma_2 + \sigma_3)}{\sigma_{eq}}$$

Furthermore, since $\sigma_2 = \sigma_3$, an explicit expression for the two other principal stresses is acquired

$$\sigma_2 = \sigma_3 = \sigma_1 - \sigma_{eq} \tag{2.28}$$

Hence, all principal stresses, triaxiality, and hydrostatic stress for the specimen may be found. The last expression only applies for the uniaxial tension test, and not necessarily for an impact problem.

Furthermore, ductile fracture mode (ii) may be modelled with the maximum shear stress criterion, showed in Eq. 2.29. This criterion is independent of the stress triaxiality, but depends on the Lode parameter [44].

$$\tau_{max} = max\left\{\left|\frac{\sigma_1 - \sigma_2}{2}\right|, \left|\frac{\sigma_2 - \sigma_3}{2}\right|, \left|\frac{\sigma_3 - \sigma_1}{2}\right|\right\} = \tau_f \tag{2.29}$$

where τ_{max} is maximum shear stress and τ_f is a critical shear value.

2.3 Numerical Methods

2.3.1 Nonlinear Finite Element Method

The impact process is a highly nonlinear event which includes; intricate contacts, large deformations, and material nonlinearities. This complex problem can be analysed numerically, preferably by a nonlinear finite element method. The general dynamic equilibrium equation states:

$$[\mathbf{M}]\{\ddot{\mathbf{D}}\} + [\mathbf{C}]\{\dot{\mathbf{D}}\} + \{\mathbf{R}\}^{int} = \{\mathbf{R}\}^{ext} \tag{2.30}$$

where

$[\mathbf{M}]$	mass matrix
$\{\ddot{\mathbf{D}}\}$	acceleration
$[\mathbf{C}]$	damping matrix
$\{\dot{\mathbf{D}}\}$	velocity
$\{\mathbf{R}\}^{int}$	internal forces
$\{\mathbf{R}\}^{ext}$	external forces

Explicit time integration is best suited for high speed nonlinear problems [57].

2.3.2 Explicit Time Integration

Explicit methods are preferable for solving contact and wave propagation problems created by impact loads since no equilibrium iterations are necessary [21]. An implicit method, however, would fail to solve this problem when fracture is considered. This is because implicit methods are based on solving equilibrium equations which may not be in balance at fracture [10].

The explicit method is a direct integration scheme which refers to calculation of response history using step-by-step integration in time [21]. Thus, the dynamic equilibrium equation at the nth time step becomes

$$[\mathbf{M}]\{\ddot{\mathbf{D}}\}_n + [\mathbf{C}]\{\dot{\mathbf{D}}\}_n + \{\mathbf{R}\}^{int}_n = \{\mathbf{R}\}^{ext}_n \tag{2.31}$$

Furthermore, an explicit scheme calculates a predicted value at future time step $n+1$, based on known conditions at one or more preceding time steps.

A well known explicit integration scheme is the classical Central Difference Method (CDM). This method is often used as a base algorithm in modern finite element software with different modifications such as the half-step method. The CDM is based on a 1st order Taylor series expansion, and the method is conditionally stable. Small time steps are required and, assuming zero damping, the critical time step is given as

$$\Delta t_{cr} = \frac{L_e}{c_d}, \quad c_d = \sqrt{\frac{E}{\rho}}$$

where

Δt_{cr}	critical time step
L_e	characteristic length of the smallest element
c_d	dilatational wave speed in the material
E	Young's modulus

More about explicit methods can be found in Cook et al. [21].

2.3.3 Method of Least Squares

Throughout this study many optimizations have been applied to different parameters, e.g. material calibration and ballistic curves. For these parameters, the method of Least Squares has been used. This method attempts to approximate a solution for overdetermined systems, which are systems containing more equations than unknowns. The method seeks to find a solution that minimizes the sum of squares for the errors made by one given equation, $f(x)$, i.e. minimizing the expression

$$S = \sqrt{\sum_{i=0}^{N} (y_i^2 - f(x_i)^2)}$$

where $f(x_i)$ is the predicted value, and y_i the actual value of the dependent variable, x_i.

For the ballistic curves, the built-in Solver-function in Microsoft Office Excel 2010 was used. MATLAB was applied, with the Levenberg-Marquardt algorithm, when calibrating the material data from the tension tests.

2.4 Brittle Fracture Criterion

Brittle fracture modes may be divided into three different linearly independent modes, as displayed in Figure 2.6.

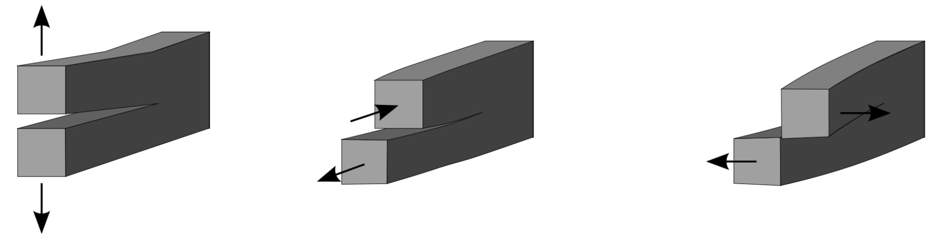

(a) Mode I: Opening. (b) Mode II: In-plane shear. (c) Mode III: Out-of-plane shear.

Figure 2.6: Different fracture modes [76].

The stress intensity factor, K, is used to predict the stress intensity at the tip of a crack. This theoretical construct is useful for providing a failure criterion for brittle materials, which applies to the surface of surface hardened steel (see Section 2.6).

For mode I, the stress intensity factor, K_I, is

$$\mathrm{K}_I = \sigma\sqrt{\pi a}$$

where σ is the normal stress and a is the radius of the crack.

When applying node splitting in the IMPETUS Afea Solver, see section below, a measure of the fracture toughness may be given. This is expressed by the strain energy release rate, G_I, which is directly related to K_I through [27]

$$G_I = \frac{{K_I}^2}{E} \tag{2.32}$$

More detailed description on this topic can be found in literature, e.g. in Anderson [3] and François et al. [31].

2.5 IMPETUS Afea Software

IMPETUS Afea Solver (Advanced Finite Element Analysis) is a software package for nonlinear computational mechanics [74]. The package includes different solver modules and a post processor. This thesis applies the Finite Element (FE) module which is a nonlinear explicit finite element code. Its primary purpose is to predict large deformations of structures exposed to extreme loading conditions [74].

IMPETUS Afea Solver utilizes the graphic processing unit (GPU) to allow a considerable speed up of the numerical calculations. The solver applies only volume elements with one contact algorithm (penalty), and uses Lagrangian formulation of motion. In addition to linear elements, IMPETUS Afea includes higher order elements with no zero-energy-modes. These are suitable for extreme deformations. In this thesis, a combination of linear and cubic elements has been employed, more about this in Chapter 6. Figure 2.7 shows how the 64-node cubic hexahedron elements is built up. An additional reason for using IMPETUS was the option of applying node splitting.

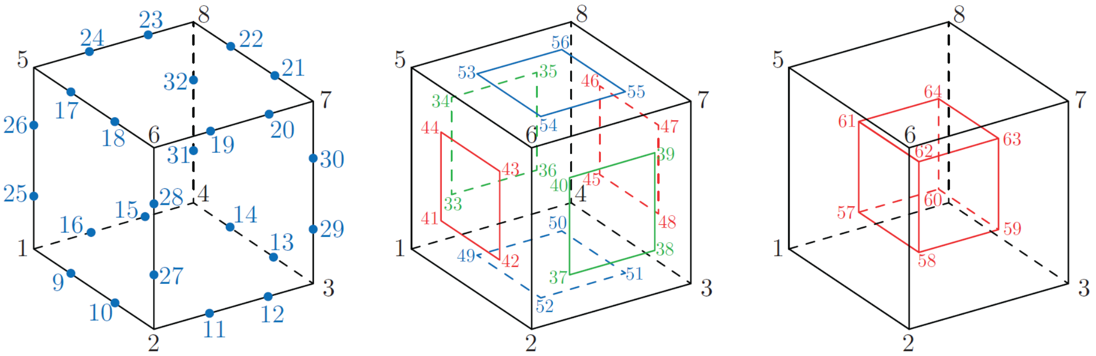

Figure 2.7: High-order element: 64-node cubic hexahedron [61].

2.5.1 Node splitting in IMPETUS

Node splitting is a numerical failure/damage modelling technique which can be used in IMPETUS Afea. It is a feature allowing crack propagation and fragmentation to occur without removing elements. The technique is implemented with respect to mode I fracture. Node splitting is desirable as the surface hardened plates exhibited cracking and fragmentation in this study. Kjølseth and Karlsen [47] have given a description of the node splitting technique. Another damage formulation is element erosion. Here, elements lose their deviatoric properties, but are still able to take hydrostatic stresses when reaching the CL-criterion until a critical time step is reached [41].

Node splitting in IMPETUS Afea includes a scaling function, f, in combination with the CL criterion, see Eq. 2.33. This, in order to include plastic localization over a spatial distance much smaller than the element size [34]. The criterion is calculated in the integration points closest to the crack-tip, and reads

$$f * W \geq W_{cr} \tag{2.33}$$

The function $f \geq 1$ can be described as

$$f \propto \sqrt{\frac{d * W_{cr}}{G_I}}$$

where d is the closest distance from the integration point to the crack-tip, while W_{cr} and G_I are material parameters described earlier. For low G_I values the scaling function increases, thus reaching W_{cr} sooner and crack propagation occurs faster. However, when G_I is set to zero, the scaling function is not applied and crack propagation is driven by W_{cr} [60].

Node splitting is shown to be more computationally expensive than failure modelling by element erosion. When the material cracks, additional contact surfaces and nodes appear, thereby increasing the computation time [60]. Furthermore, the direction of the crack propagation is mesh sensitive [33].

2.6 Microstructure

The mechanical behaviour of a material is closely dependent on its microstructure. Within the same aggregate state, e.g. solid, liquid, and gas, matter may appear in multiple phases. For solids, the difference between the phases depends on their atomic arrangement, or crystal structure (see Section 2.6.1). Steel is an alloy of iron with a carbon amount of up to 2 wt. % [67]. Additional alloying elements contributing to different qualities of the steel are also present. During the process of making steel, from raw iron ore to the finished product of structural steel, different temperature ranges are involved. This range of temperatures, as well as the carbon content, influences how the steel is structured and will be discussed in the following section.

2.6.1 Crystal structure

Like most metals, iron is made up of small crystals [26]. The crystals are an assembly of atoms packed together in regular three-dimensional patterns held jointly by covalent and metallic bonds [26]. Materials will seek a crystal structure which gives minimum energy, and depends on temperature. The most prominent crystal structures, described by a unit cell, for steel are face-centred-cubic (fcc) and body-centred-cubic (bcc). The difference between the two structures can be seen in Figure 2.8. The fcc structure consists of iron atoms placed in the corners of a cube, as well as an atom at the centre of the cube faces. Similarly, the bcc has atoms in each corner, but instead of atoms at the cube faces, it has one atom at the centre of the cube. Carbon atoms are dissolved in the interstitial space between the iron atoms.

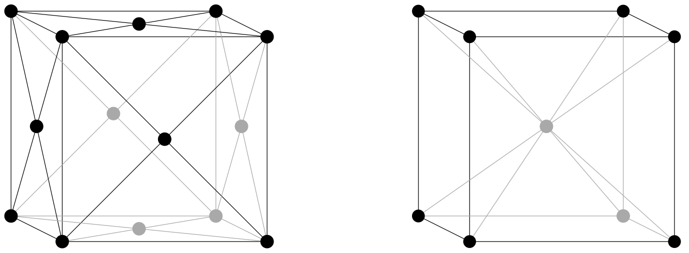
(a) Face-centred-cubic. (b) Body-centred-cubic.

Figure 2.8: Crystal structures.

Crystals are seldom perfect. They have different kinds of defects formed during growth or subsequent handling which influence the mechanical behaviour of the material. The most prominent defects or faults which weakens the crystal lattice are known as *dislocations*. Dislocations allow the crystal to slip and deform plastically. By subjecting the crystal to shear stress above some critical value, the atoms in the crystal will re-arrange and move through the crystal without affecting the main lattice structure [37], see Figure 2.9. The slip occurs in the crystallographic plane with the greatest atomic density. This movement of dislocations causes irreversible plastic strains. While increasing the applied stress, additional dislocations are created with different slip directions. This increased dislocation density causes blockage and the load has to be raised to cause further deformation. This is known as work hardening, or strain hardening. More information about this can be found in Dieter [27].

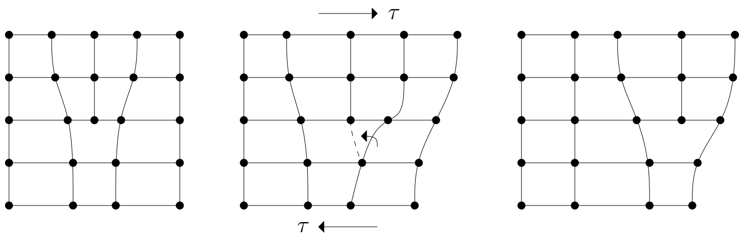

Figure 2.9: Motion of an edge dislocation adapted from Dey [26].

2.6.2 Phase-diagram

The microstructure of steel can be described by an iron-carbon phase diagram (Figure 2.10). However, it will be used in its metastable form, Fe-Fe_3C. This is because the stable form of carbon, graphite, forms during very slow cooling. Under normal conditions carbon precipitates as Fe_3C, or cementite, and it is therefore practical to use the metastable system. The phase diagram describes how the microstructure of steel changes with respect to temperature and amount of carbon. These variables determine which phase, i.e. crystal structure, the iron-carbon alloy is in, and thereby its mechanical properties and physical characteristics. Materials that can appear in multiple crystal structures are called allotropic materials [26].

At relatively low temperatures, iron exists in a stable bcc structure called *ferrite* (α-iron). This is a very soft and ductile phase, which can only dissolve small amounts of carbon (max 0.025 % C) [67]. When considering only iron, i.e. 0 % C, and the temperature is increased above about 910 °C, ferrite transforms to *austenite*, or γ-iron. Austenite can contain up to 2 % carbon. Like ferrite, this is a very ductile and soft phase, but the crystal structure has changed from bcc to fcc. The austenite phase is bounded from below by the phase/temperature boundaries, A_3 and A_{cm}. The maximum carbon content in the austenite phase reflects the upper limit for carbon content of steel. At higher values, we get cast iron [67]. If the steel contains less than 0.8 % C (hypoeutectoid steel [67]) and the temperature drops below the austenite phase boundaries, grains of ferrite start to form [4]. As more and more grains are forming, there becomes an excess of carbon in the austenite. The excess carbon can be precipitated as cementite. *Cementite* has an orthorhombic structure and is very hard and brittle [67]. When cooled further, a blend of strips of ferrite and cementite is obtained in a single grain. This structure is called pearlite. *Pearlite* has mechanical behaviour in between that of ferrite and cementite. For steel with carbon content above 0.8 %, i.e. hypereutectoid steel, the cooled structure will take form of both pearlite and cementite.

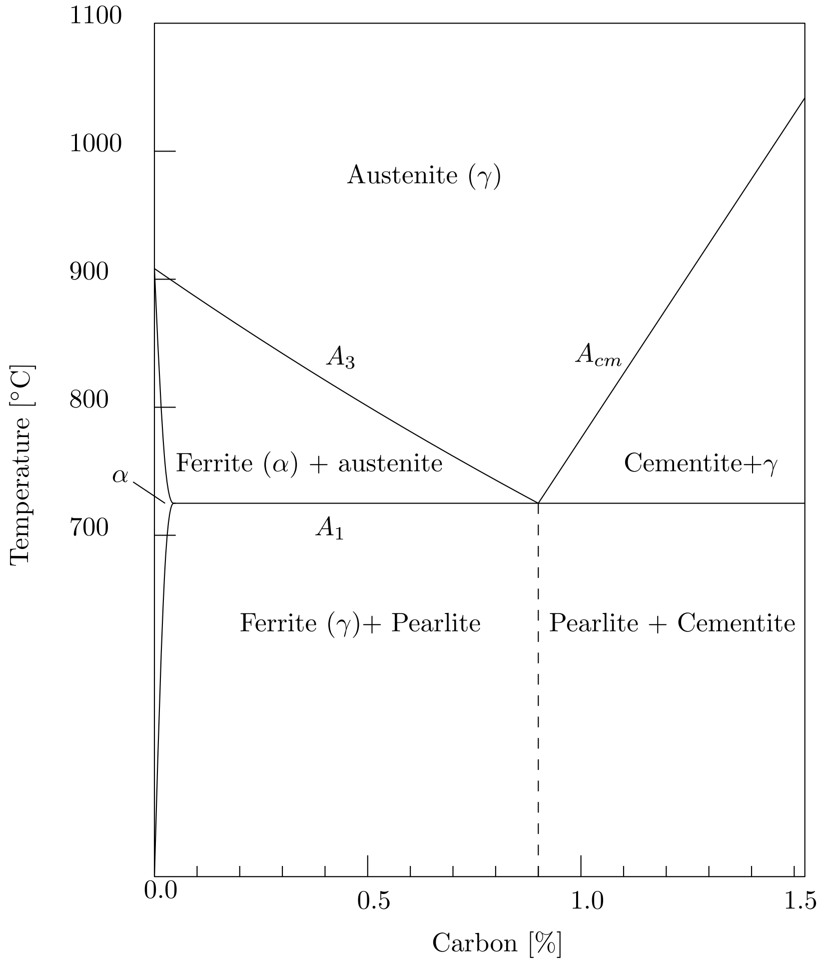

Figure 2.10: Phase-diagram. Adapted from Larsen [48].

The crystal structures so far forms at relatively low cooling rates. At higher cooling rates the precipitation and growth of ferrite and pearlite is limited [67]. When cooled from the austenite temperature area at a faster cooling rate than previously assumed, a structure called *bainite* may form. This is a microstructure which consists of needles, or plates, which nucleates from the austenite grain boundaries [67].

When cooled even more rapidly from a stable austenite phase, a martensitic transformation occurs and the austenite changes to a microstructure called *martensite* [30]. In contrast to the previously described phase transformations, a martensitic transformation is a phase change in which there is no carbon diffusion [30]. Since no carbon diffusion occurs, martensite becomes over-saturated with carbon which creates a structure that is very hard and brittle [4]. The martensite structure is similar to a ferrite structure, but instead it has a body-centred-tetragonal arrangement. This means that it changes from an fcc structure to a bcc structure which is slightly elongated in one of its dimensions

(Figure 2.11(a)). The crosses in the figure represent possible placements of carbon atoms. This distorted structure has the appearance of fine needles [26] and dislocations find it hard to move through such a strained structure, thereby increasing its hardness [4]. The distortion implies a slight volume change which causes internal stresses to appear [67]. These stresses may be alleviated by tempering.

The rapid cooling process which transforms austenite into martensite is considered a purely athermal transformation [30]. This means that the transformation is independent of time and can be described by its start temperature, M_s, and its final temperature, M_f. Solberg [67] gave an empirical equation for the start temperature, see Eq. 2.34. Martensite is the hardest microstructure in steel and is used to harden steel [67]. Hardness is a measure of a materials ability to resists indentation (see Section 3.5). The hardness is highly dependent on the carbon content. This can be visualized by the graph in Figure 2.11(b) adapted from Ashby and Jones [4]. When cooling from M_s to M_f, austenite transforms gradually to martensite, and unless the steel is cooled continuously to M_f temperature it will contain some retained austenite which is soft. However, the martensitic transformation is very rapid and occurs at a speed of sound in the material, around 10^3 m/s [30].

$$M_s = 539 - 423 \cdot (\%\text{C}) - 30.4 \cdot (\%\text{Mn}) - 17.7 \cdot (\%\text{Ni}) - 12.1 \cdot (\%\text{Cr}) - 7.5 \cdot (\%\text{Mo}) \tag{2.34}$$

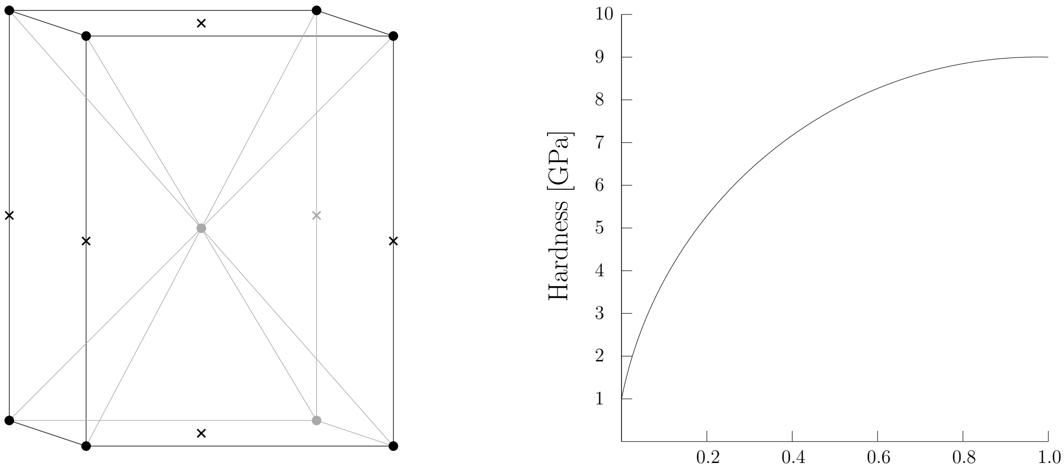

(a) Martensite crystal structure.

(b) Hardness of martensite as function of carbon.

Figure 2.11: Martensite structure and hardness of martensite as function of carbon content. Adapted from Ashby and Jones [4].

2.7 Structural steel - NVE36

The present study applies different hardness profiles of hot rolled NVE36 low strength structural steel plates. Structural steel typically has a ferrite/pearlite structure with maximum 30 % pearlite [67]. The hardened plates have been subjected to surface hardening, and a description of the most essential heat treatments and strengthening mechanism will be investigated in this section.

2.7.1 Strengthening mechanisms

Several ways exist to increase the resistance that occurs during dislocation motion. These strengthening mechanisms introduce barriers in the crystal lattice, which the dislocation interacts with.

Grain boundary strengthening utilizes the fact that a smaller grain size increases strength. Grain boundaries acts as barriers for dislocation to move through. Hall and Petch showed a relation between the strength of the material as a function of the grain size [67]. This relation states that smaller grain size increases the yield stress [27]. *Solid solution strengthening* involves making the material impure. The introduced solute atoms may either take the place of the solvent atoms, i.e. substitutional solid solution, or occupy the interstitial positions in the lattice. Either way, the solute atoms roughens up the slip planes causing increased dislocation resistance. *Precipitation strengthening* is a process in which fine particles causes obstruction of the dislocation movement. This is achieved by first heating the material to a soluble temperature followed by quenching and reheating. A better description of the process will be done in later sections.

In addition to the aforementioned strengthening mechanism, this thesis will focus on martensite strengthening and surface hardening. This involves a martensitic transformation which has been described earlier. In the following section, the process of achieving this will be covered.

2.7.2 Heat treatment

As discussed earlier, change in temperature and carbon content are variables which can drastically change the microstructure and properties of steel. Heat treatment encompasses a range of different processes aimed to change the mechanical behaviour of a material. This study investigates surface hardened structural NVE36 steel, and therefore the most essential heat treatment processes will be described.

Surface hardening

The ability for steel to transform from an austenite phase to a martensitic structure is called hardenability [67]. Surface hardening is a hardening process which strengthens the surface of a metal object while the underlying metal underneath remains soft and ductile. In short, surface hardening involves heating the metal to the austenite phase and infusing carbon into the surface of the steel through a process called carburization. Next, depending on the hardening method, the metal is subject to slow cooling or quenching. Quenching causes a martensitic transformation to occur, making the surface both hard and brittle while the core remains in a ferritic and/or pearlite structure. To alleviate the brittleness it is necessary to reheat the steel in a heat treatment called *tempering*.

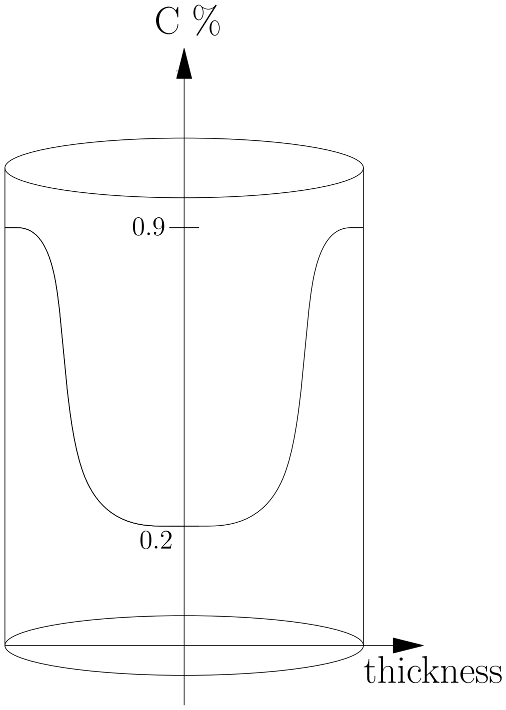

Figure 2.12: Carbon profile through a surface hardened steel material. Adapted from Solberg [67].

Carburization

Carburization is a diffusion-controlled heat treatment process in which steel absorbs carbon by being subjected to a carbon-rich environment at high temperatures (850-950°C) for a certain period of time. By heating the steel to this temperature range, i.e. above critical temperature A_3, it transforms to austenite and enables it to absorb carbon, which diffuses into the material [67]. Different kinds of carbon sources can be used [67]:

- *Gas*: Subjecting the material in a gas atmosphere consisting of CO/CO2 blend or hydrocarbon gas such as methane, ethane, propane, etc.
- *Liquid*: Sodium bath consisting of sodium carbonates
- *Solid* or *packing*: Packing the metal in 60 % coal and 40 % carbonate.

When using a gas mix of CO and CO2 as a hardening agent, the following reaction occurs at the surface of the steel

$$2\text{CO} \rightarrow \text{CO}_2 + \text{C(absorbed in surface)} \tag{2.35}$$

Too much carbon absorbed in the surface may cause the M_f temperature to be too low, and thereby causing soft retained austenite to remain in the surface after hardening. Therefore, the carburizing process is controlled such that the surface contains approximately 0.85-0.95 % carbon [67].

Quenching

In order to transform the crystal structure in the surface of the material, from austenite in the carburization process into martensite, rapid cooling, or quenching, is necessary. How fast it should be cooled depends on multiple factors. Amongst them are the amount of alloying elements and carbon in the metal, as well as the size of the particular material. Figure 2.13 displays a simplified Continuous Cooling Transformation (CCT) diagram. This diagram shows what phase changes occur during cooling of a carburized steel plate. The CCT-diagram at the left applies for the core (c) where there is less carbon than on the surface (see Figure 2.12). Following its cooling path, all of the austenite has transformed into ferrite and pearlite at temperature, T_c. However, due to higher amount of diffused carbon, the surface (s) will still be austenitic. This can be seen in the CCT-diagram to the right. Note that the phase-”noses” are shifted to the right and downwards. This is because carbon increases hardenability and greatly influences the temperature at which martensitic transformation occurs, see Eq. 2.34. Also, it has been assumed that the surface contains 0.8 %, i.e. it is eutectoid. Consequentially, there is no ferrite ”nose”. Additionally, this amount of carbon in the surface causes M_f to be at sub-zero temperatures. Thus, some retained austenite in the surface could be expected, unless ice water is used [67] as quenching agent. Therefore, to obtain a martensitic structure in the surface, quenching should be done directly after reaching T_c temperature in the core. The cooling path would then, ideally, not trespass the other phase-”noses” and obtain the desired martensite structure.

Remark, the given CCT-diagrams are only meant to display the principal of quenching. They are not necessarily correct in terms of proportion and scaling.

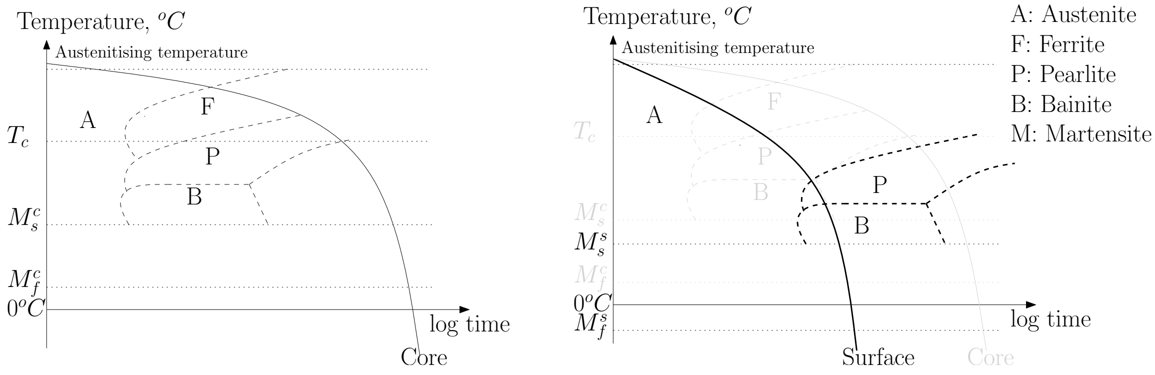

(a) CCT-diagram for core.

(b) CCT-diagram for surface.

Figure 2.13: Simplified CCT-diagram adapted from Solberg [66].

There are different ways to harden a material. One way is to quench the metal directly after carburization, followed by tempering (Direct Harden). This method gives rather coarse and brittle martensite due to austenite grain growth occurring at the carburization temperature. Another way is to slowly cool the material after carburization and then reheat the material to austenite temperature in the surface followed by quenching and tempering. This causes austenite grain size refinement and consequently a finer and less brittle martensite, which also will be somewhat stronger given by the Hall-Petch relation (grain size strengthening). See Solberg [67] for other methods. Figure 2.14 shows the surface hardening steps for the latter method.

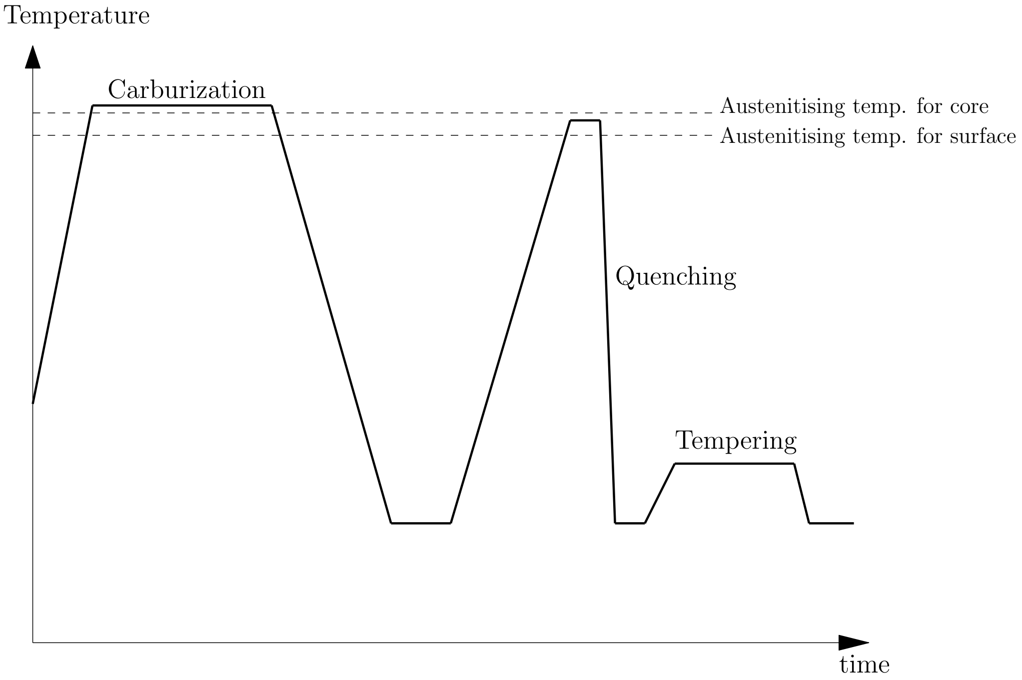

Figure 2.14: Case-hardening process. Adapted from Solberg [67].

Tempering

After quenching, a martensitic transformation has occurred. As described before, martensite is a very brittle phase which causes internal stresses to appear. To alleviate the brittleness, reheating the material to a temperature below A_1 allows carbon to diffuse from the over-saturated bcc structure. This enables the structure to deform plastically thereby releasing some of its internal stresses. Consequentially, a decrease in material hardness occurs, but its toughness increases [67].

The tempering temperature depends on the combination of desirable strength and toughness. For any given strength-toughness combination, the tempering temperature increases with amount of carbon and alloying elements [67]. Typical range is between 150-700°C [67]. During tempering, the over-saturated martensite precipitates the carbon as carbides. The more carbon trapped in the martensite structure, the more carbide precipitates. This causes the distance, λ, between particles to be reduced. As a result, precipitation hardening occurs which reduces the strength loss caused by the tempering process. The increase in strength from precipitation hardening is proportional to $1/\lambda$ [27].

Decarburization

By subjecting the hardened steel to an environment containing oxygen and hydrogen above tempering temperature, the carbon in the surface may diffuse out of the material. This may cause a reduction in the hardness at the surface.

2.8 State of the Art

In this section, previous work relevant to this thesis will be presented and discussed.

2.8.1 Heat Threated Steel Plates

There has been some previous work with respect to the ballistic resistance of surface hardened steel. Lou et al. [54] investigated the ballistic protection of monolithic 12 mm thick NVE36 steel plates which were surface hardened using a self-protective diffusion paste during carburization. 7.62 mm APM2 bullets were used to impact the plates. The experiments showed that unhardened 12 mm plates had a ballistic limit of 592 m/s while surface hardened 12 mm plates had a ballistic limit of 766 m/s, i.e. an increase of about 30 %. It should be noted that the hardening process produced steel with a martensitic core structure, i.e. a hard core. Also, in an unpublished study by Lou et al. [53] they investigated layered 2x6 mm NVE36 steel plates with the same heat treatment. This resulted in a ballistic limit velocity of 810 m/s, i.e. better than monolithic plates.

Coucheron [24] also conducted a study on the ballistic performance of surface hardened NVE36 steel plates. He investigated procedures to obtain a ferrit/pearlite microstructure in the core and martensite in the surface, as opposed to the hard core obtained by Lou et al. Coucheron examined monolithic 12 mm plates as well as layered configurations of 2x6 mm, and 3x4 mm plates[1]. However, only the monolithic plate obtained the wanted ferrit/pearlite core structure, i.e. a soft core. The study found that 12 mm plates with a ferrite/pearlite core had a ballistic limit of 684 m/s, i.e. lower than the hard core 12 mm plate from Lou et al. Additionally, Coucheron observed that double layered plates with hard core performed better than monolithic hard core plates from Lou et al. However, 3x4 mm plates lowered the ballistic perforation resistance.

In his project thesis, Coucheron [23] investigated the ballistic resistance of layered 4x3 mm surface hardened NVE36 steel plates. Gas was used as carburization agent. The results yielded only a 3 % increase in ballistic resistance over the unhardened 12 mm monolithic plate obtained from Lou et al.

Larsen [49] tried to surface harden a 12 mm thick abrasion resistant Hardox 450 steel in his project thesis. The study showed only minor ballistic resistance improvement over the unhardened steel, and therefore it was not recommended to surface hardened said steel.

A study by Børvik et al. [12] showed that the perforation resistance increases almost linearly with material strength. The study investigated five different steel grades; Weldox 500E, Weldox 700E, Hardox 400, Domex Protect 500, and Armox 560T; and subjected them to both 7.62 mm Ball bullets and 7.62 mm AP bullets in the ordnance velocity regime. It was found that material strength is a much more important feature than

---

[1] 4x3 mm was also surface hardened, but no ballistic tests were performed

ductility with respect to small-arms protection. This was also found by Holmen et al. [41] where four different heat treated AA6070 aluminium alloys were investigated.

2.8.2 Monolithic vs. Layered Plates

Flores-Johnson et al. [28] did a numerical investigation on the ballistic performance of monolithic, double and triple layered metallic plates made of either steel (Weldox 700E) or aluminium (Al 7075-T651) or a combination of these. The projectile used in the simulations was a 7.62 mm APM2 bullet in the velocity range 775-950 m/s, and the numerical models were developed using the explicit finite element code LS-DYNA. The study showed that monolithic plates performed better than triple layered plates, but the difference between monolithic and double layered was not significant. This was also found experimentally by Børvik et al. [12] using Weldox 700E steel . However, Flores et al. observed that above striking velocities of 850 m/s, 12 mm monolithic plates presented slightly better performance of 2x6 mm in contact.

A study conducted by Dey et al. [25] on the ballistic resistance of Weldox 700E steel in the sub-ordnance velocity regime, showed that monolithic 12 mm plate had better ballistic performance compared to 2x6 mm plates for ogival projectiles. However, the opposite effect was found when using blunt projectiles. The blunt projectiles gave a different failure mode when layering; global deformation and membrane stretching, while monolithic plates failed by plugging.

Zukas and Scheffler [71] conducted a numerical investigation on the impact effects in monolithic and multi-layered steel plates using both Lagrangian and Eulerian wave propagation codes. The plates were impacted by 65 mm long hemispherical nosed rods with diameter of 13 mm and impact velocity of 1164 m/s. They concluded that layering dramatically weakens thin and intermediate targets, see Figure 2.15. The weakening effect was attributed to the reduced bending stiffness in the structure. Radin and Goldsmith [62] performed several experimental tests on layered and monolithic aluminium plates with varying thickness using both conical and blunt projectiles. They found that the monolithic plates had better ballistic resistance than layered plates of same thickness, and credited this to the higher bending resistance of the former. This was also found experimentally by Gupta and Madhu [36] who impacted both mild steel, RHA steel, and aluminium plates by jacketed hard-core ogival projectiles in the range 800-880 m/s. A later experimental and numerical study of the behaviour of thin aluminium plates of different thickness under impact of hemispherical, ogival, and flat steel projectiles by Gupta et al. [35] found similar results. The double layered configurations were comparable with monolithic plates in terms of ballistic resistance, but when increasing the number of layers the monolithic plates offered better resistance.

Nixdorff [59] analytically studied the variation in the ballistic limit velocity with the number of plate layers while holding the total plate thickness constant. He found that for targets subdivided into n layers of equal thickness, that the ballistic limit was lower

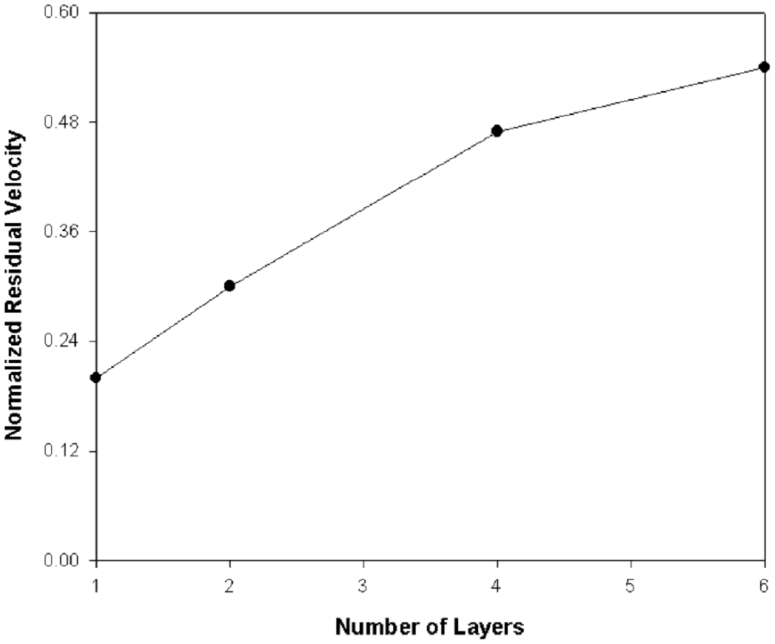

Figure 2.15: Variation of normalized residual velocity (v_r/v_i) with target layering. Taken from Zukas and Scheffler [71].

than a monolithic plate of same total thickness. This became globally more apparent as the number n of subdivisions was raised keeping the total thickness constant. In a recent paper, Ben-Dor et al. [6] presented a mathematical proof of the conjecture that layering does not improve ballistic properties of ductile shields against high-speed sharp nosed impactors. On the basis of semi-empirical model [65], the proof showed that when the dimensionless thickness (ratio of thickness to diameter of impactor) of monolithic shield and the thickness of the layers lie in the range 1/3 to 1, layering does not affect ballistic properties of the shield. Otherwise, monolithic plates are superior over layered plates with same total thickness. This was also confirmed by comparing with experiments or numerical results [7].

Almohandes et al. [1] investigated experimentally the effects of layered mild steel plates (1-8 mm thickness) with respect to ballistic resistance impacted by 7.62 mm standard bullets. The study observed that single steel plates are more effective than layered plates of equal thickness both in contact or spaced by an air gap. Additionally, the investigation found that ballistic resistance of layered steel plates decrease as the number of layers increase. The results from the experiments have been in good agreement with an analytical model based on conservation laws developed by Liang et al. [51].

Corran et al. [20] investigated experimentally the ballistic properties of layered steel and aluminium in the sub-ordnance regime. They found that double/triple layering shield performed better than monolithic plates above a certain critical thickness (4-6 mm), see Figure 2.16. Marom and Bodner [56] also found that multi layered beams were more effective against perforation than monolithic beams. A 0.22 inch lead bullet with velocity of 375 m/s was used in the study.

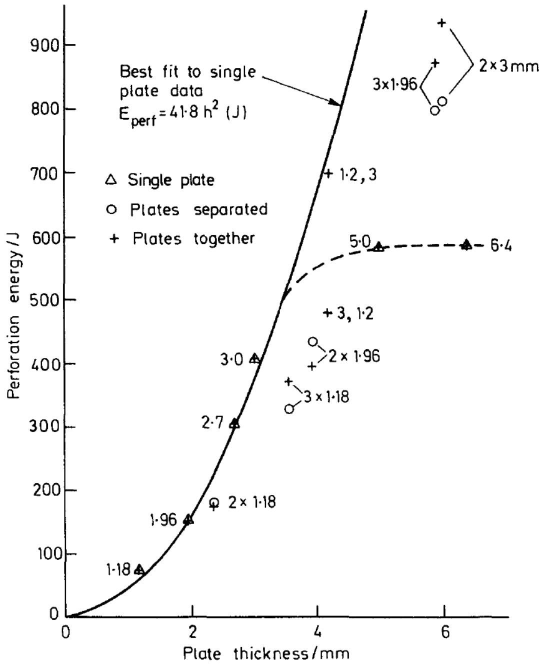

Figure 2.16: Drop in resistance for monolithic plates . Adapted from Corran et al. [20].

Based on the above papers, it may be concluded that the data on ballistic resistance of laminated plates is limited and, somewhat, contradictory. However, the main trends appears to be that when untreated, layering has a negative effect on the ballistic resistance when ogival or conical projectiles are used. Furthermore, surface hardening of mild steel seems to give a positive effect on the ballistic perforation resistance.

Chapter 3

Target Materials

This chapter investigates the microstructure of the material and how it was obtained. Additionally, a description of the material tensile tests and hardness measurements will be presented.

3.1 Target Configurations

This study investigates the ballistic perforation resistance of hot rolled NVE36 structural steel plates. The chemical components are tabulated in Table 3.4. Three layer configurations were considered; 12 mm monolithic, 2x6 mm double layered, and 3x4 mm triple layered (Figure 3.1). Furthermore, three heat treatment configurations were studied. Firstly, the base material which was untreated (unhardened) had a constant hardness over the thickness. Secondly, two other configurations were surface hardened to obtain a hardness profile over the thickness. Hence, there are a total of 9 configurations (Table 3.1). The different hardening types will be referred to as the as-received, or unhardened, configuration (UH), soft core configuration (SC), and the hard core (HC) configuration.

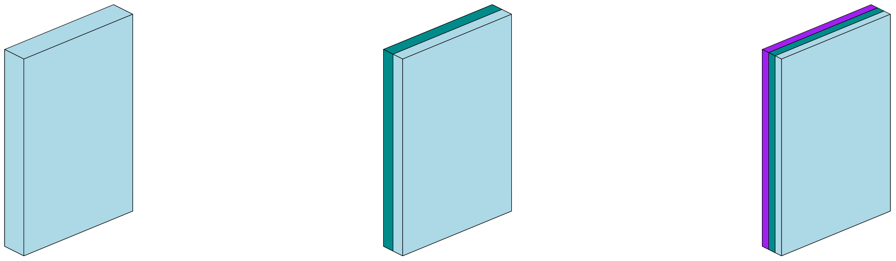

(a) Monolithic (b) Double layered (c) Triple layered

Figure 3.1: Target plate configurations.

Table 3.1: The 9 target configurations.

Layer config. [mm]	Hardening config.	Notation
12	As-received	Plate 1, Plate 2, Plate 3
	Soft core	Plate 1, Plate 2, Plate 3
	Hard core	Plate 1, Plate 2, Plate 3
2x6	As-received	Plate 1 (frontplate), Plate 2 (rearplate)
	Soft core	Plate 1 (frontplate), Plate 2 (rearplate)
	Hard core	Plate 1 (frontplate), Plate 2 (rearplate)
3x4	As-received	Plate 1 (frontplate), Plate 2 (midplate), Plate 3 (rearplate)
	Soft core	Plate 1 (frontplate), Plate 2 (midplate), Plate 3 (rearplate)
	Hard core	Plate 1 (frontplate), Plate 2 (midplate), Plate 3 (rearplate)

The following tests were performed to obtain material properties

- **Tension tests**: Conducted on tensile specimens cut out from a separate plate (Plate 3) for the monolithic configuration for each heat treatment. Separate meaning no ballistic tests were conducted on these plates.
- **Microhardness**: Conducted on each heat treatment for
  - **(i)** Monolithic (12 mm): Plate 1[1]
  - **(ii)** Double layered (2x6 mm): Plate 1 and Plate 2
  - **(iii)** Triple layered (3x4 mm): Plate 1, Plate 2, and Plate 3

3.2 Material Processing

The surface hardening procedure was performed by Dr. Fredrik Haakonsen at Kverneland Group. A more in depth description of the different heat treatment elements in this procedure is described in Section 2.7.2. First, the plates were subject to carburization in a pit furnace at 920°C for 4 hours for the 4 mm plates, and 6 hours for the 6 mm plates and 12 mm plates. Then, the plates were air cooled back to room temperature before they were hardened in a LAC PK 180/12 muffle furnace at 920°C. The procedure required that the plates were through hot for 10 minutes during reheating. This resulted in the following holding times: 20 min, 30 min and 45 min for the 4 mm, 6 mm and 12 mm plates, respectively. Next, the plates intended to get a hard core were instantly quenched in a 10 % NaOH solution, while the plates intended to have a soft core were air cooled for a certain time depending on thickness, before quenched in NaOH solution. Finally, the plates were tempered in a LAC KNC/V 1000/65 furnace at 245°C for 2 hours. A summary of the surface hardening process is given in Table 3.2.

---

[1] Plate 2 and Plate 3 were also tested. However, only for additional measurements. See Appendix E.

Table 3.2: Details of the surface hardening process for all treated plates.

	Thickness[mm]	Carburizing	Cooling	Reheating	Cooling	Tempering
SC	12	6 h at 920°C	Air cooling	45 min at 920 °C	Air cool for 95 s then solution quench	2 h at 245 °C
	6	6 h at 920°C	Air cooling	30 min at 920 °C	Air cool for 60 s then solution quench	2 h at 245 °C
	4	4 h at 920°C	Air cooling	20 min at 920 °C	Air cool for 33 s then solution quench	2 h at 245 °C
HC	12	6 h at 920°C	Air cooling	45 min at 920 °C	Solution quench	2 h at 245 °C
	6	6 h at 920°C	Air cooling	30 min at 920 °C	Solution quench	2 h at 245 °C
	4	4 h at 920°C	Air cooling	20 min at 920 °C	Solution quench	2 h at 245 °C

Figure 3.2 displays a schematic of what the hardness should be through the thickness of the profile as a result of the surface hardening process. In addition, the intended microstructures are given. Note that the curve is only descriptive, meaning the purpose of the figure is only to display the major difference between hard core and soft core. Table 3.3 shows the nominal core values.

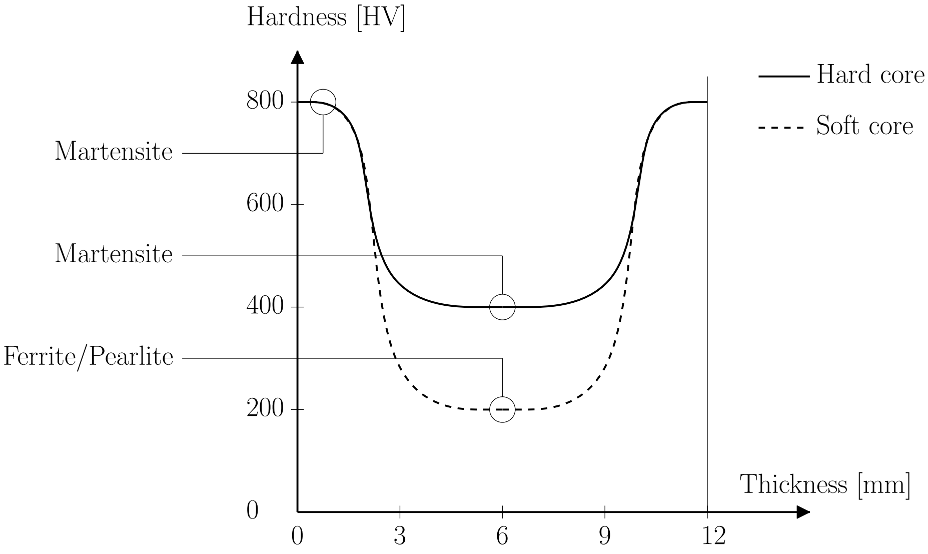

Figure 3.2: Nominal hardness throughout thickness.

Table 3.3: Nominal Vickers hardness($HV_{0.2}$) of core.

	As-received	Soft core	Hard core
$HV_{0.2}$	200	200	400

Table 3.4: Chemical composition of as-received NVE36 steel plates.

	C	Si	Mn	S	P	Al	Nb	Cr	Ni	Cu	Mo	V	Ti
4 mm	0.15	0.26	1.48	0.006	0.018	0.036	0.023	0.03	0.01	0.04	0.004	0.003	0.015
6 mm	0.15	0.26	1.48	0.006	0.018	0.036	0.023	0.03	0.01	0.04	0.004	0.003	0.015
12 mm	0.15	0.35	1.50	0.010	0.007	0.044	0.037	0.019	0.019	0.044	0.001	0.002	0.002

3.3 Tensile Tests - Experimental Work

The tensile tests were carried out at NTNU (Norwegian University of Science and Technology) by SINTEF (The Foundation for Scientific and Industrial Research). Each tensile test was conducted at room temperature (T=293 K). The tensile specimens had circular cross sections and can be seen in Figure 3.3 together with the tensile machine. A more detailed description of the specimens geometry can be seen in Figure 3.4. Also, the specimens were screw threaded for easy and rigid mounting.

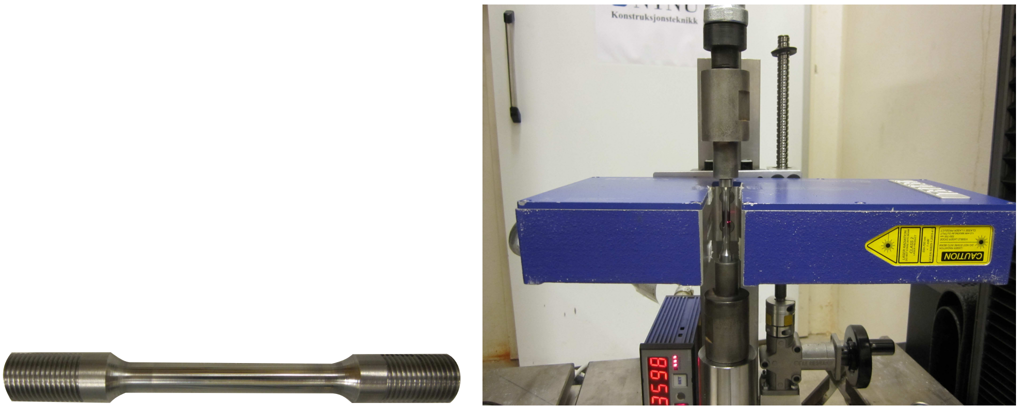

(a) Tensile specimen.

(b) Tensile machine equipped with laser scan micrometer.

Figure 3.3: Tensile test at NTNU.

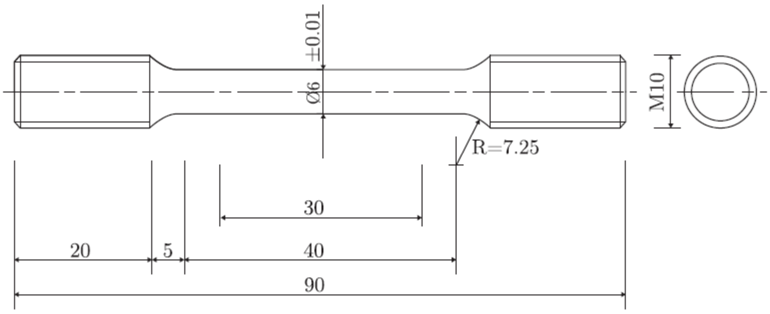

Figure 3.4: Tensile specimen geometry (dimensions in mm).

Three tensile tests were conducted for each heat treatment. However, in the unhardened plate, three specimens were cut out from two perpendicular directions (D1 and D2). Hence, six tensile tests were conducted for the unhardened material. This was done to reveal any anisotropy.

The tensile specimens from the unhardened configuration were mounted in a Zwick/Roell Z030 - 30kN test machine, while the soft core and hard core configurations were mounted in an Instron 100 kN test machine. All the tensile specimens were cut out from the core of the 12 mm plates. Each device loaded the specimen with a speed of 1.2 mm/min, i.e. a strain rate of 0.0005 s^{-1}. An XLS 13XY- Laser Scan Micrometer measured continuously the diameter reduction in two perpendicular directions during loading. The laser was placed on a mobile frame which ensured that measurements were taken at the point of necking. Beforehand, the specimens were given a slightly smaller diameter near the centre of the gauge region which the laser searched for prior to each test. This ensured that necking occurred near the centre of each specimen.

Note, the tensile specimens were cut out from separate plates than those used in the ballistic experiments described in Section 4.1.

3.4 Tensile Tests - Experimental Results

The following true stress-strain curves were obtained from the tension test for the unhardened material.

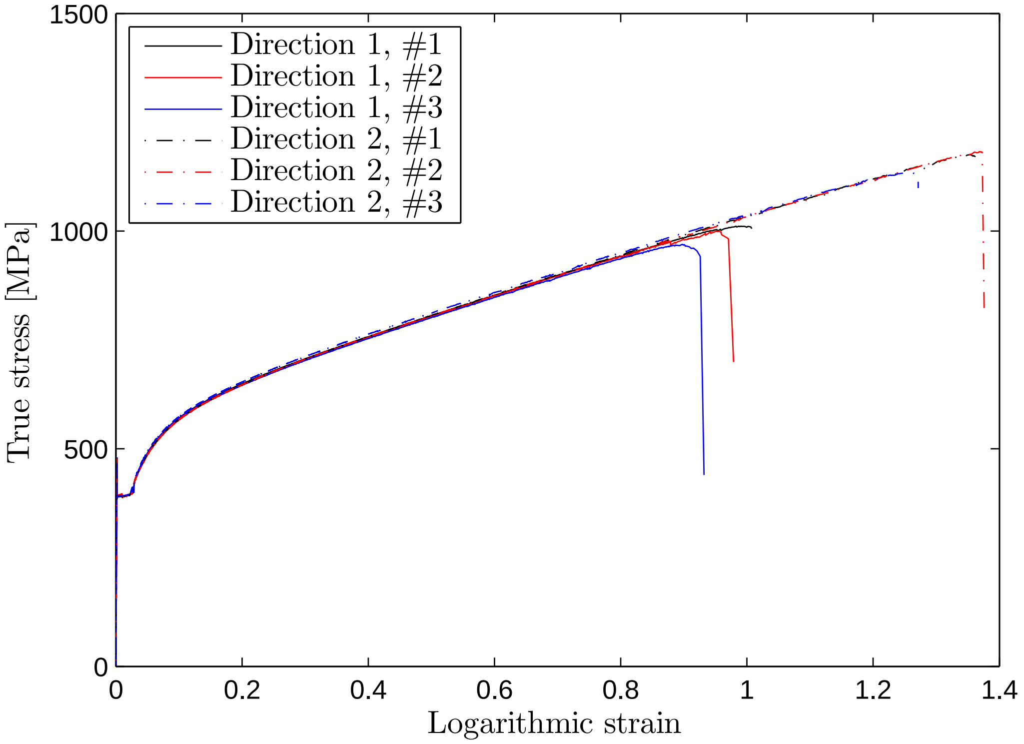

Figure 3.5: Stress-strain curves for unhardened material.

From Figure 3.5 we observe that the yield stress and strain hardening of the two perpendicular directions almost coincide. However, when it comes to the logarithmic strain and true stress at failure, we notice a large difference. This indicates that the material is more ductile in direction 2, and an anisotropic failure criterion could have been introduced. Fourmeau [29] proposed such a criterion, however, this criterion needs more validation and did not influence the failure significantly. Hence, this will not be investigated in this thesis. Furthermore, the unhardened material exhibits a yield plateau which is commonly seen for mild steels. Figure 3.6 shows a closer look at this plateau.

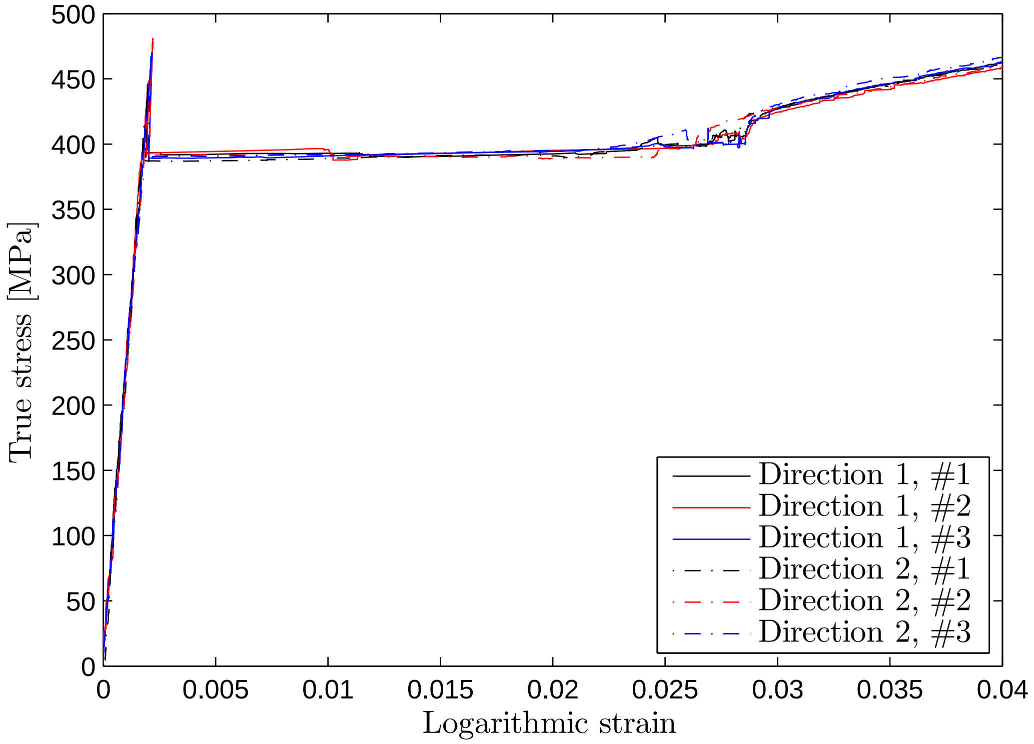

Figure 3.6: Yield plateau and linear elastic zone for the unhardened configuration.

Hot rolled steel is considered an isotropic material [48]. However, since the laser measured the diameter continuously in two perpendicular direction during testing, an investigation to this conjecture was done. The strain ratio, r, is defined as $r = \frac{\ln(D_y/D_0)}{\ln(D_x/D_0)}$, and should be equal to unity for isotropic materials. The following ratios were obtained[2].

Table 3.5: Calculated r-values for as-received material.

D1, #1	D1, #2	D1, #3	D2, #1	D2, #2	D2, #3
0.95	0.97	0.95	0.94	0.94	0.94

Since the r-ratio is close to unity and the stress-strain curve in each perpendicular direction almost coincides, isotropy appears to be a valid assumption.

---

[2] Last 20 data points before fracture used for each ratio.

Furthermore, an investigating of the elastic properties such as the Young's Modulus (E), Poisson's ratio (ν), and the lower yield stress (σ_0) was conducted. By averaging over all the different tensile tests, the values given in Table 3.6 are obtained.

Table 3.6: Measured and nominal ([54], [73]) values of elastic properties for as-received NVE36.

	σ_0 [MPa]	E [MPa]	ν
Measured	391.23	212 379	0.331
Nominal	355	210 000	0.303

The calculated Young's Modulus and Poisson's ratio are in good agreement with the nominal values for steel. This shows that the laser performs accurate measurements. The measured values will be used as material input for the later numerical analysis.

Figure 3.7 displays the true stress-strain curves obtained for all hardening configurations. However, only a representative curve from each configuration is shown. Appendix G displays all the curves for the soft core and hard core material.

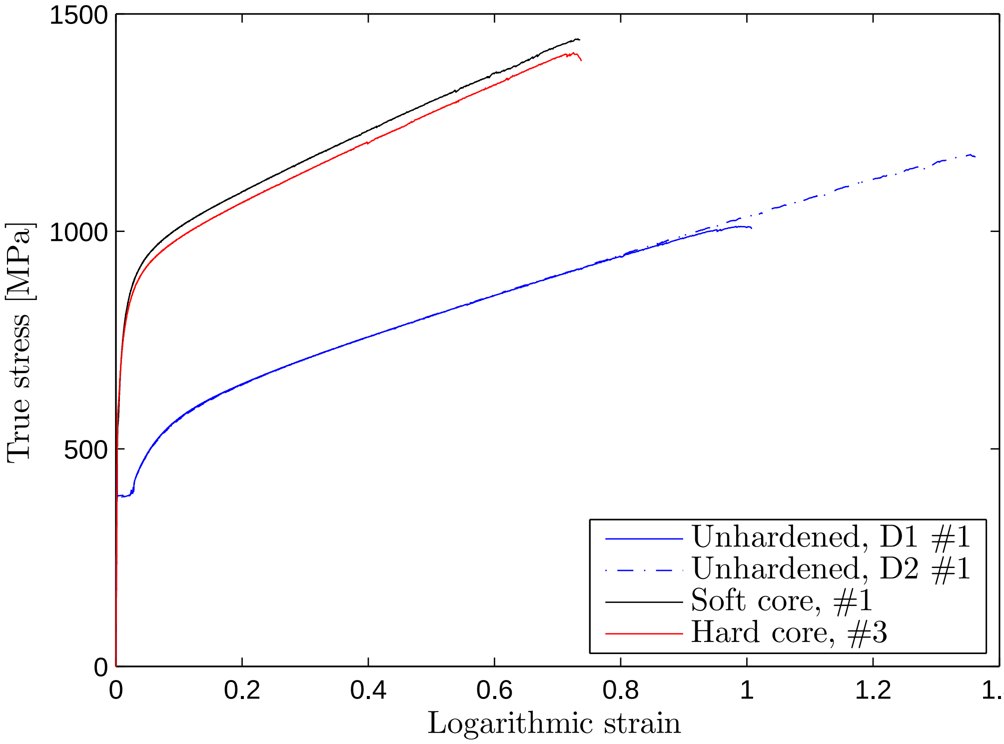

Figure 3.7: All representative stress-strain curves.

Table 3.7 displays calculated stress and strain values from Figure 3.7. We observe that the soft core exhibits a slightly higher tensile strength than the hard core. This is contrary to the intended behaviour, where the hard core should have been stronger than the soft core.

Table 3.7: Calculated stress values from soft core and hard core plates.

	$\sigma_{0.2}$ [MPa]	σ_u [MPa]	ε_u	σ_f [MPa]	ε_f
As-received D1, #1	391.0	531.36	0.211	1011.28	0.978
As-received D2, #1	385.8	530.05	0.219	1176.37	1.349
Soft Core, #1	585	912.69	0.103	1442.60	0.725
Hard Core, #3	617	890.18	0.103	1410.66	0.719

where

$\sigma_{0.2}$	0.2% offset engineering yield stress
σ_u	ultimate engineering tensile strength
ε_u	strain at σ_u
σ_f	engineering stress at failure
ε_f	engineering strain at failure

Note that the 0.2 % offset yield stress is obtained from Sintef and not calculated by the authors.

Furthermore, the calculated critical values in the CL criterion, based on the true stress-strain curves, are given in Table 3.8.

Table 3.8: Critical values for CL criterion based on true stress-strain curves.

Material	W_{cr} [MPa]
As-received, Direction 1	791
As-received, Direction 2	1187
Soft core	871
Hard core	857

The unhardened material gives a very large span in the critical value. This is due to the difference in failure strain for direction 1 and 2, as previously mentioned. How this affects the ballistic response numerically will be investigated in Chapter 6.

3.5 Microhardness - Experimental Work

Since the soft core and the hard core material configurations were surface hardened, an important factor for this study was the microhardness over the plate thickness. Senior engineer Trygve Lindahl Schanche at NTNU performed the necessary microhardness measurements. Only target plates subjected to ballistic experiments (Section 4.1) were investigated. For the unhardened material, only Plate 1 for each layer configuration was analysed. Figure 3.8 shows which part of the plate was sent to microhardness analysis (Sample). This sample is also viewed in Figure 3.9(a).

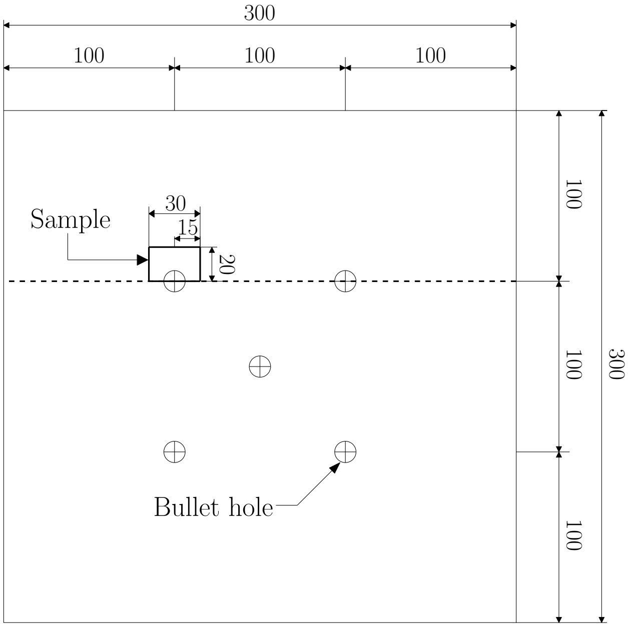

Figure 3.8: Sample of target plate sent to microhardness analysis. Measurements in mm.

Vickers hardness ($HV_{0.2}$) was used to determine the hardness of the material. Before the measurements, each sample was sanded by P1200(FEPA) grit size over the thickness to ensure an even surface. The hardness was measured using a Leica VMHT MOT microhardness measuring device. A 0.2 kg diamond shaped indenter was pressed on the material surface and the load was held constant for approximately 15 seconds (Figure 3.9(b)). This was done over a path across the thickness (Figure 3.9(a)). Then, by measuring the average of the diagonals of the indentation left by the indenter in the material surface, one can evaluate the hardness of the material [27]. Vickers hardness is defined as the load divided by the surface area of the indentation [27].

The indentation was done at approximately every 80 μm from the edge. As the values started to stabilize, i.e. in the core, the indentation distance was increased. Due to corrosion of some of the plates, measuring on the edge of the plate thickness was difficult and therefore the outermost measurement was moved some distance inward. More information about the process can be found in [52].

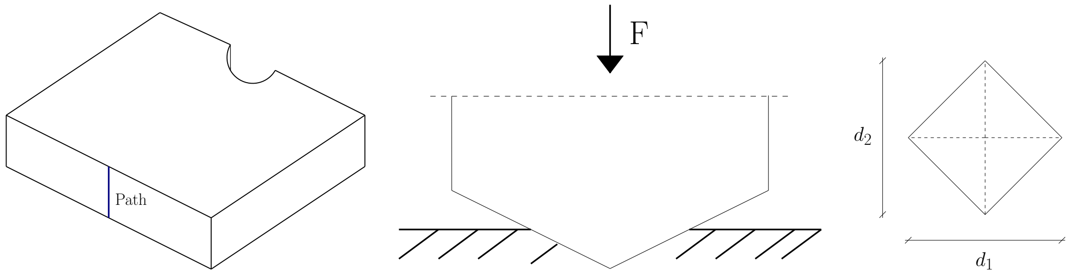

(a) Measuring path over thickness in sample. (b) Vickers process. (c) Indentation in material.

Figure 3.9: Hardness measuring.

There is a relation between the ultimate tensile strength and the material hardness, where $\sigma_u \approx 3HV$ [30]. Furthermore, a relationship between the ultimate tensile strength and the yield strength has shown to be $\sigma_u = 1.2\sigma_0$ [10]. Thus, finding the hardness over the thickness allows an estimate of the varying yield stress to be calculated. Alternatively, these relations may be obtained from the actual experimental tests performed on the material. The latter approach is conducted in Section 5.4. In Section 3.6.1 - 3.6.3 all measurements of the microhardness over the thickness are plotted.

3.6 Microhardness - Experimental Results

The measured microhardness in Vickers, $\mathrm{HV}_{0.2}$, for the different layer and hardening configurations will be presented in the following sections. A discussion on the results will be done in Section 3.8. The average hardnss values were measured where the core hardness was somewhat stable, e.g. in the region 3-9 mm for monolithic plates.

3.6.1 12 mm Plates

From Figure 3.10(b), it is apparent that the soft core configuration have not been hardened with the intended value of 200 $\mathrm{HV}_{0.2}$ in the core. Instead, it has been hardened to a hardness approximately 50 % higher. Contrary, the hard core is not hardened enough. Thus, the soft core and the hard core configurations exhibit almost the same core hardness. Also, notice how the core values in the soft core Plate 1 varies. This might be because of uncertainty in the measurements.

Table 3.9 displays the different average core hardness values for each material configuration.

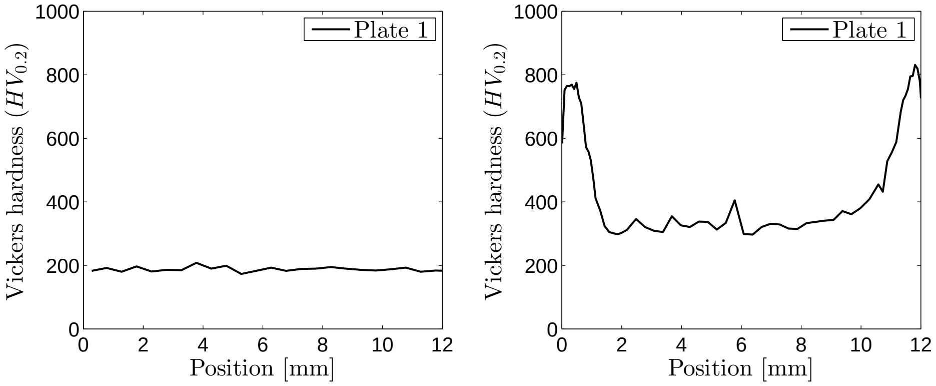

(a) As-received.

(b) Soft core.

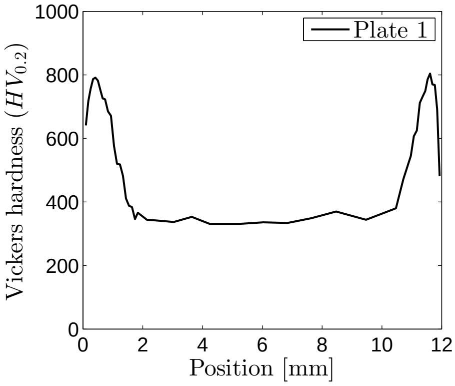

(c) Hard core.

Figure 3.10: Microhardness over the thickness for 12 mm plates.

Note that the soft core shows a lower core hardness than the hard core. However, a higher tensile strength was observed in the tension tests. The reason for this is that different plates were used for each material test. Appendix E shows that the soft core hardness in Plate 3 is higher than the hard core hardness in Plate 3. This indicates that the results are, in fact, consistent. However, since the hardness measurements obtained for Plate 3 arrived close to the deadline, these values have not been used in this thesis.

Table 3.9: Average hardness for plate cores ($HV_{0.2}$) of the 12 mm plate.

	Plate 1
As-received	189.83
Soft core	328.10
Hard core	338.71

3.6.2 2x6 mm Plates

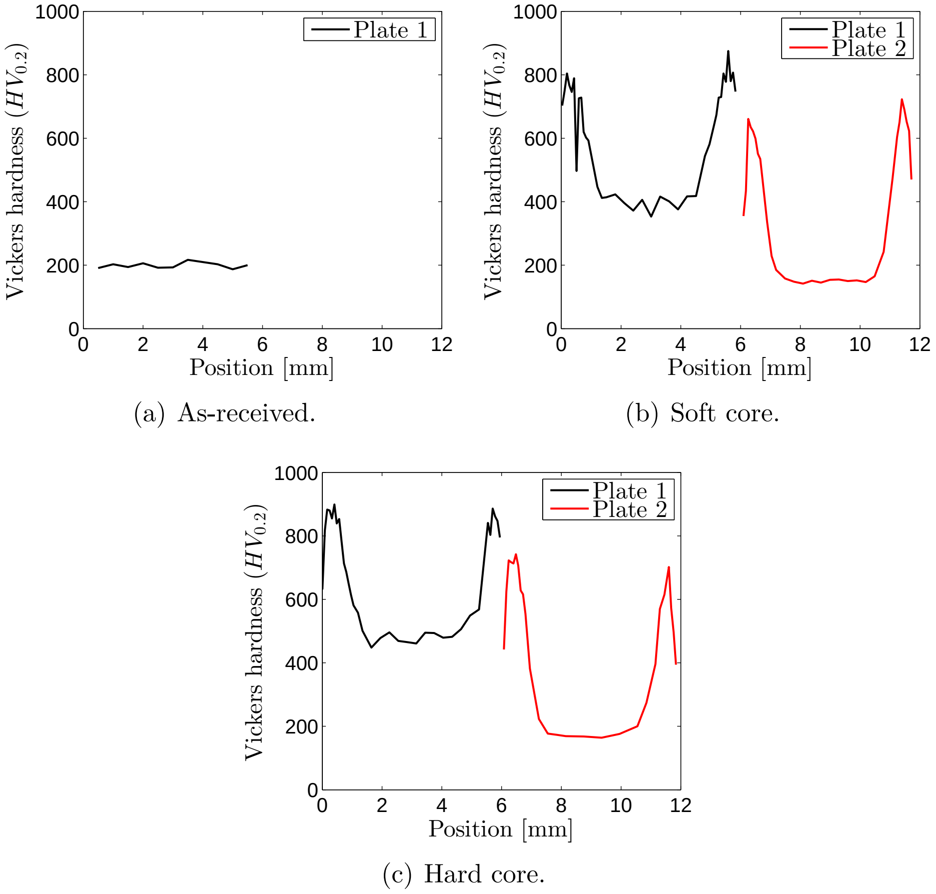

(a) As-received.

(b) Soft core.

(c) Hard core.

Figure 3.11: Microhardness over thickness for 2x6 mm plates.

From Figure 3.11(b) and 3.11(c), we observe that something went wrong for the hardened plates. Both configurations shows major differences between Plate 1 and Plate 2. However, the reason for this is unknown. It may be that the plates were wrongly hardened, or a mix up occurred when labelling the plates before the authors received them. Also, notice that core hardness in Plate 2 is less than the as-received material. Furthermore, the hard core configuration have slightly higher hardness than the soft core plates. Table 3.10 displays the average core hardness for the different configurations. In addition, both surfaces of the hard core front plate exhibits a hardness of approximately 900 $HV_{0.2}$.

Table 3.10: Average hardness for plate cores ($HV_{0.2}$) of the 2x6 mm plates.

	Plate 1	Plate 2
As-received	199.63	N/A
Soft core	400.33	151.54
Hard core	481.17	171.17

3.6.3 3x4 mm Plates

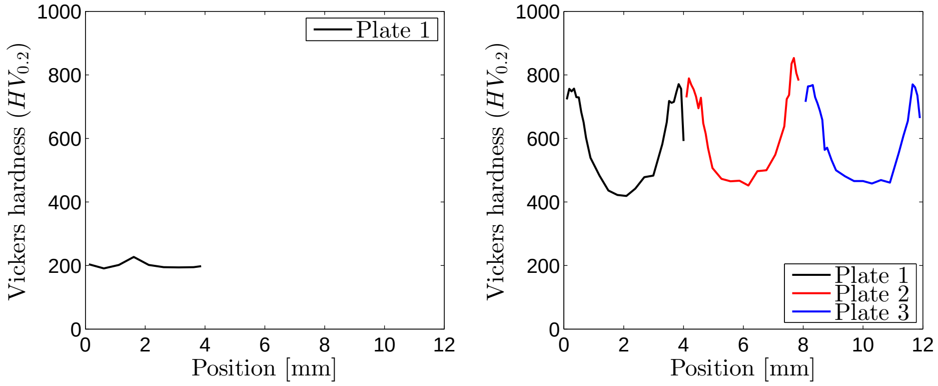

(a) As-received. (b) Soft core.

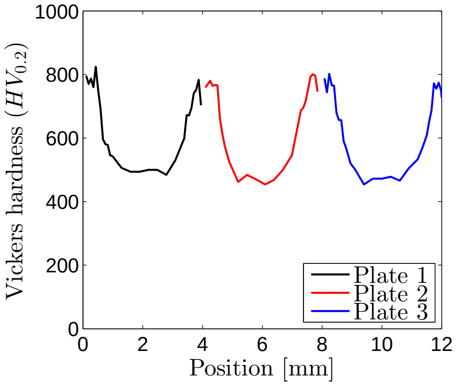

(c) Hard core.

Figure 3.12: Microhardness over thickness for 3x4 mm plates.

All the hardened plates shows a similar core hardness between each plate. However, they all exhibit a much higher hardness than intended. This applies especially for the soft core plates. The average core hardness is shown in Table 3.11.

Table 3.11: Average hardness for plate cores ($HV_{0.2}$) of the 3x4 mm plates.

	Plate 1	Plate 2	Plate 3
As-received	200.89	N/A	N/A
Soft core	451.86	480.14	471.57
Hard core	503.00	488.75	485.25

3.7 Investigation of Microstructure

This section presents photographs of the materials' microstructure. The pictures were taken using a Leica MEF4M light microscope. Figures will indicate where the photos are taken by referring to the hardness profiles from the previous sections. Only representative photographs are presented, and all photos are in the same scale.

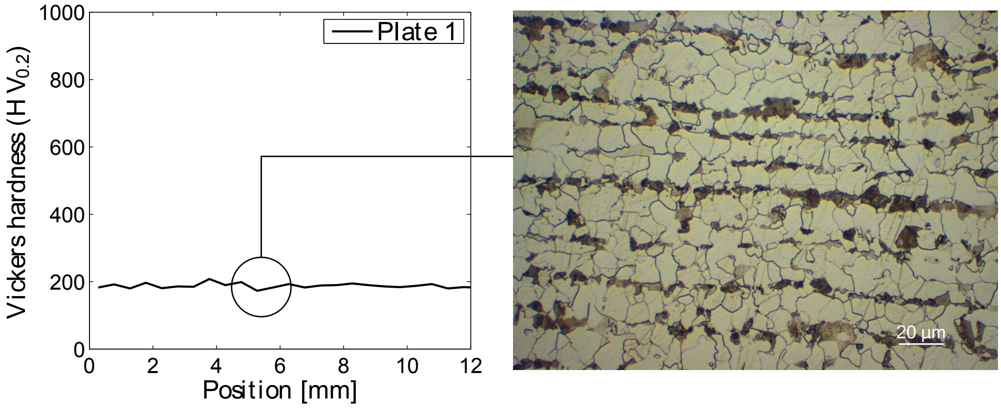

Figure 3.13: 12 mm as-received.

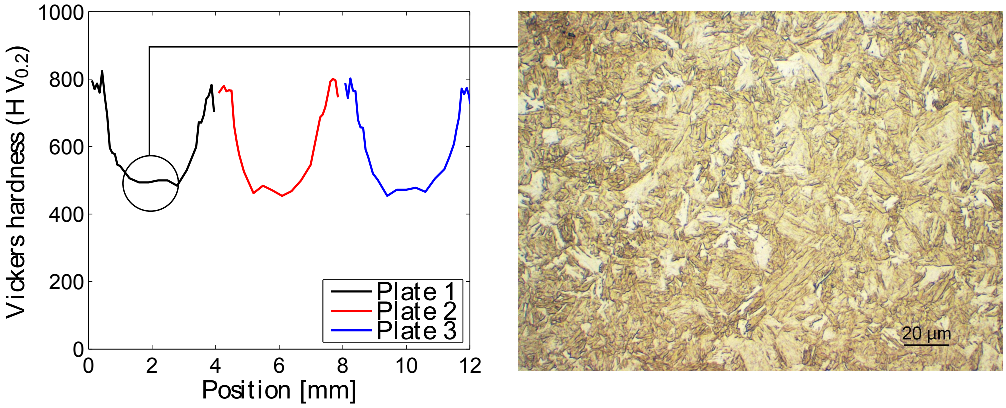

Figure 3.14: 3x4 mm hard core.

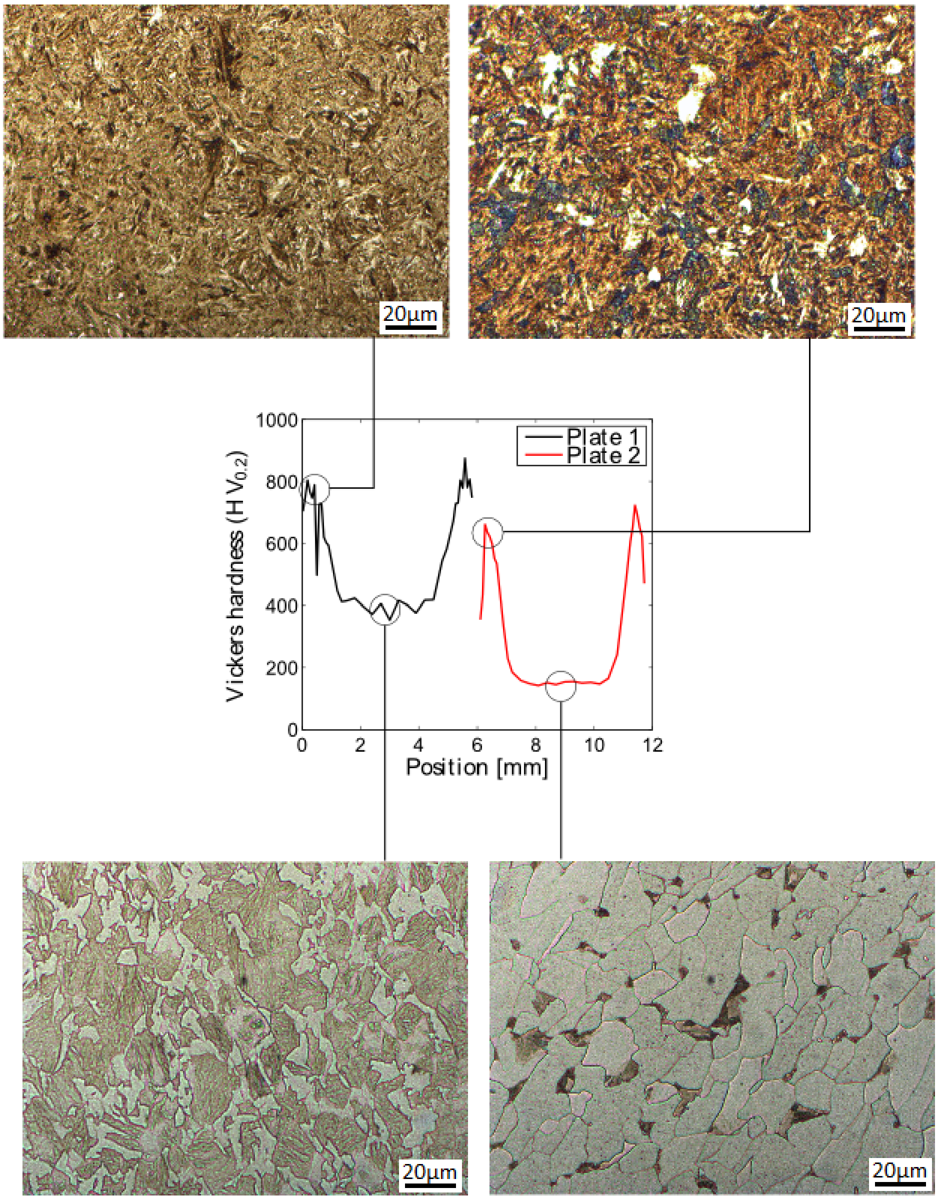

Figure 3.15: 2x6 mm soft core.

The photographs are supplementary to the hardness profiles. They reveal that the monolithic as-received plate has a ferrite/pearlite microstructure, while the triple layered hard core has a mostly martensitic structure. This is apparent by the needle like structure in Figure 3.14. Furthermore, the photos confirms the major difference between Plate 1 and Plate 2 of the double layered soft core configuration. The core of Plate 1 consists of ferrite and martensite, while the core of Plate 2 consists of mostly ferrite and some pearlite. Only the surface of the 2x6 soft core plates are presented as all the configurations had similar hardness in this area. A martensitic structure has been obtained here. However, the surface of Plate 2 has some white spots. These may be ferrite or retained austenite.

It is difficult to know the difference, but there exists methods to confirm what these are [66]. Also, the reduced hardness at the surface may be the result of decarburization.

3.8 Summary and Discussion

A short summary, discussion, and remarks related to the material investigation described in the previous sections will be presented in the following.

- The tension tests were only conducted on separate 12 mm plates (Plate 3) which were not subjected to ballistic experiments. However, the used microhardness measurements were conducted on the plates which the ballistic tests were performed on.
- Table 3.7 from Section 3.4 showed that the soft core material displayed a higher tensile strength than the hard core material. This was not the wanted behaviour since the soft core was intended a soft and ductile core, similar to the as-received material.
- The heat treated double layered configuration exhibited major differences between each plate. Plate 1 had a much harder core than Plate 2, which looked like a soft core (Figure 3.11(b) and Figure 3.11(c)). The reason for this is not known. Either something went wrong in the hardening process, or a mix up between soft core and hard core has occurred when marking the plates. Either way, the measured hardness profiles were used in the numerical analyses.
- The triple layered configurations exhibited a consistent hardness profile in each plate. However, the hardened plates displayed a harder core than intended. This applies especially for the soft core configuration.
- The obtained hardness measurements between the different layer configurations showed that nominal core values have not been fulfilled. The triple layered plates are harder than the double layered plates[3] which are harder than the monolithic plates.
- Again, it is not necessarily a correlation between the obtained results from tension tests and the hardness tests. E.g. the soft core exhibited higher tensile strength than hard core, but had lower hardness. This is because different plates were used in each test.

Thus, in this thesis, it is apparent that the hardening process is a non-deterministic and uncertain procedure since the hardness varies and the nominal requirements have not been satisfied.

---

[3] Only for Plate 1, see Figure 3.11(b) and 3.11(c).

Chapter 4

Ballistic Impact Experiments

This chapter contains a presentation of the ballistic experiments conducted on the target materials described in Chapter 3. The objective of the experiment was to determine the ballistic limit velocity and the ballistic limit curve for the different target configurations (Table. 4.1).

Table 4.1: Target configurations.

Layer configuration	Case	Heat treatment	Number of tests
12 mm	#1	As received	10
	#2	Soft core	17
	#3	Hard core	10
2x6 mm	#4	As received	9
	#5	Soft core	6
	#6	Hard core	8
3x4 mm	#7	As received	8
	#8	Soft core	8
	#9	Hard core	9
Total			85

4.1 Experimental Work

The experiments were conducted in a ballistic rig at SIMLab, NTNU. The rig consists of a 7.62 x 63 mm smooth-bored Mauser gun with a barrel length of 1 meter located inside a 16 m^3 impact chamber (Figure 4.1). The Mauser fired the projectiles using a remote trigger from a safe distance. In order to guarantee a well-defined impact point for each shot, the gun was mounted in a rigid rack. Each test was filmed by a high-speed camera (Figure 4.4(c)) with a frame rate of 75 000 fps, which was triggered when the bullet passed through a metal sheet placed in front of the muzzle of the barrel (Figure 4.4(d)).

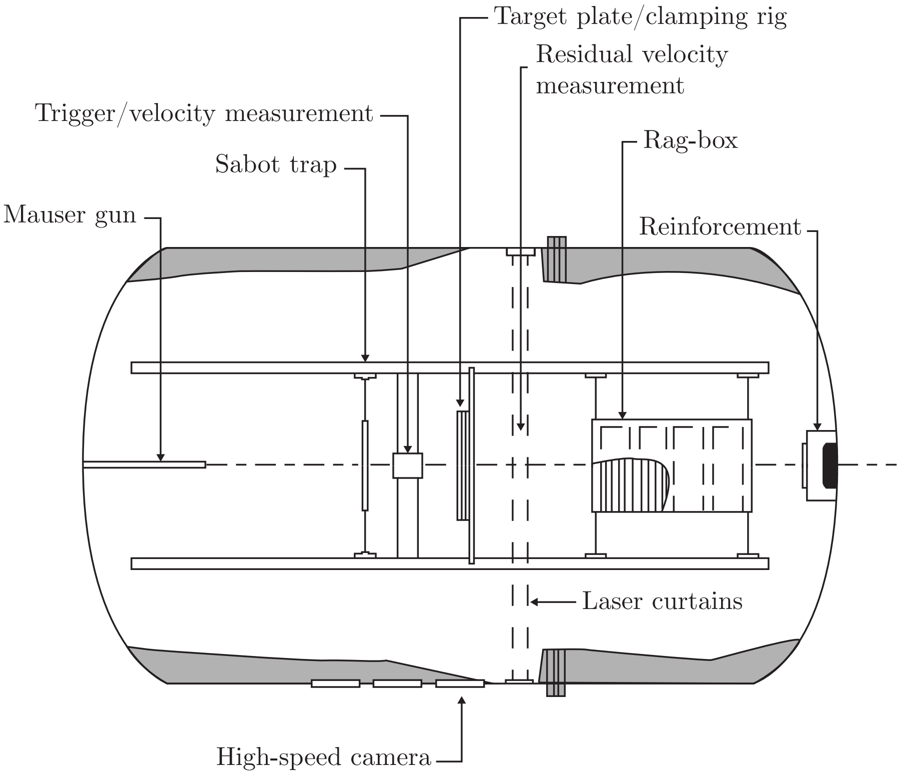

Figure 4.1: Schematic of experimental set-up, adapted from Holmen and Johnsen [40] and Børvik et al. [16].

The projectile used was a 7.62 mm APM2 bullet with a total mass of 10.5 ± 0.25 g. An APM2 bullet consists of a brass jacket, an end cap, a lead tip, and a 5± 0.25 g ogive-nose hard steel core. Figure 4.2 shows the dimensions and various parts of the projectile. Table 4.2 displays the projectile's material constants taken from Børvik et al. [18], while more information can be found in Børvik et al. [12].

Table 4.2: Material constants for whole APM2 7.62 mm bullet.

Material	ρ [kg/m^3]	E [MPa]	ν	α_T [1/K]	C_p [J/kgK]	χ
Steel core	7850	210000	0.30	1.2E-5	910	0.9
Lead filling	10660	10000[1]	0.42	2.9E-5	124	0.9
Brass jacket	8520	115000	0.31	1.9E-5	385	0.9

where α_T is the material's thermal expansion coefficient. The other material constants were presented in Chapter 2.

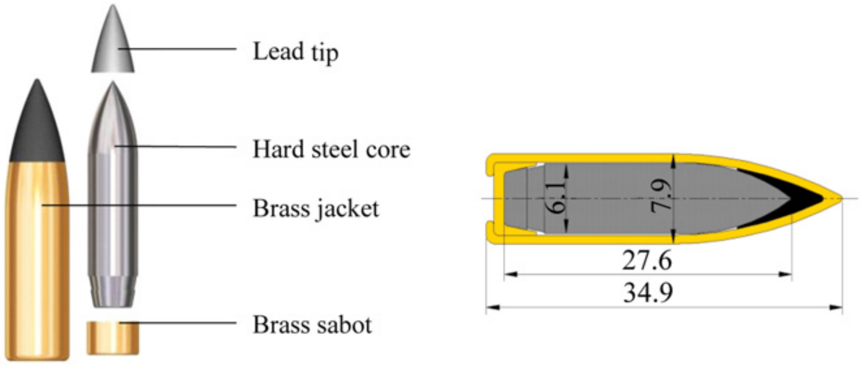

Figure 4.2: Schematic and geometry of the 7.62 mm bullet (dimensions in mm) [41].

Square target plates with dimension 300 x 300 mm^2 were clamped to a frame by two transverse beams and adjusted to the desired point of impact (Figure 4.4(a)). Hence, a fixed boundary condition for the plates horizontal sides were provided while the vertical sides remained free. Even though the boundary conditions in the experiments were well-defined, they cannot be considered fully clamped. Børvik et al. [12] argues that boundary conditions are of minor importance during such high-velocity impacts when the in-plane distance between single shots and the boundary is several projectile diameters. Initially, the in-plane distance between single shots and the boundaries of the plate were minimum 100 mm. However, since more shots were required to gather sufficient data, extra shots were fired in closer proximity to one another (Figure 4.3). Since the impact velocity was typically between 650 m/s - 900 m/s hardly any global deformation was present, thereby enabling the possibility to fire projectiles closer to one another without influencing the response. This has also been done in previous work by Holmen and Johnsen [40].

---

[1] Wrong Young's modulus in [18].

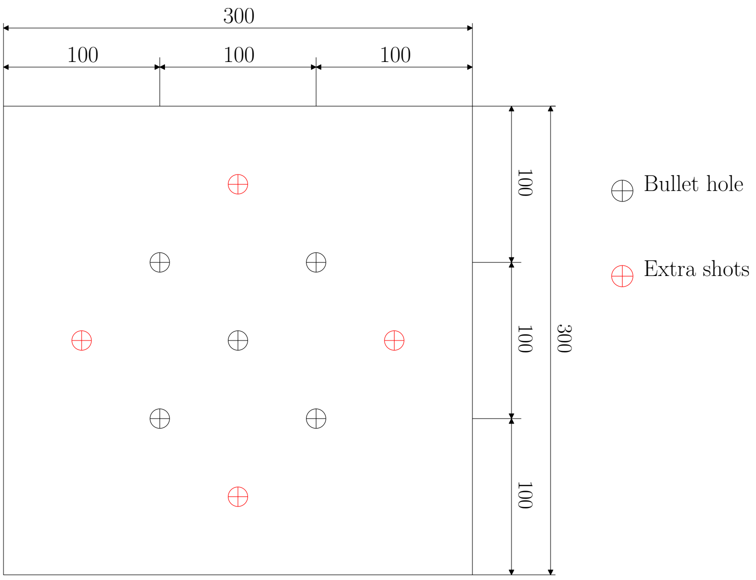

Figure 4.3: Target plate impact locations (dimensions in mm).

Some of the target plates had deformed during surface hardening, especially the thinner configurations (Figure 4.4(b)). This made it sometimes difficult to establish contact between the plates when layering. Therefore, additional clamps were used to force the plates together while fixing them to the rig. Even though the clamps helped, some of the plates had undesirable space between them. This is commented in the tabulated results in following sections. Also, special attention was given when tightening the deformed plates in fear of causing cracks in the hardened surface.

Before each shot, the amount of ammunition was adjusted so that the projectiles impacted the targets at various velocities. The quantity of gunpowder used was in accordance with previously obtained adjustment graphs which related the amount of powder in the cartridge with the measured muzzle speed of the bullet. However, a spread (± 20 m/s) in initial velocity was observed even for projectiles with equal amount of powder in their cartridges. This uncertainty sometimes caused difficulties in determining the ballistic limit velocities for different target configurations and several tests had to be executed.

(a) Target plates clamped to rigid frame by transverse beams.

(b) Deformation due to surface hardening.

(c) High-speed camera operating at 75 000 fps.

(d) Camera trigger mechanism.

Figure 4.4: Pictures taken during the experimental work.

4.2 Experimental Results

The results from the ballistic experiments will be presented in this section. First, the effect of hardening will be investigated in each layer configuration. Then, a comparison between monolithic and laminated configurations with the same heat treatment will be examined.

For all configurations, a ballistic limit curve was obtained using a least square fit based on the Recht-Ipson model described in Section 2.1.3. Furthermore, since the plates mainly failed by ductile hole growth with limited plugging, the Recht-Ipson parameter, a, was set equal to unity. However, fragments were sometimes ejected on the front and rear side of the hardened plates. The Recht-Ipson parameter, p, and v_{bl} was fitted to the test data.

Pictures of all entry and exit holes can be found in Appendix A.

4.2.1 12 mm Plates

Tabulated results from the ballistic experiments are summarized in Table 4.3.

Table 4.3: Tabulated results - 12 mm plates.

Hardening config.	Test	Gunpowder [grain]	v_i [m/s]	v_r [m/s]	Comment
As-received	1	Full	859.50	676.60	OK
	2	41.00	745.10	500.60	OK
	3	27.00	466.90	0.00	Projectile split in two
	4	37.00	685.40	389.80	OK
	5	33.00	635.20	260.60	OK
	6	31.00	-	-	No measurements
	7	31.00	544.20	0.00	OK
	8	32.00	559.60	0.00	OK
	9	33.20	593.30	108.30	OK
	10	33.00	578.30	0.00	OK
Soft core	1	Full	884.40	469.00	OK
	2	45.00	796.00	291.90	OK
	3	41.00	760.60	0.00	OK
	4	42.00	725.20	0.00	OK
	5	42.50	793.50	283.00	OK
	6	41.50	771.40	316.00	Projectile split in two
	7	41.50	773.90	268.50	Projectile split in two
	8	41.00	742.90	200.30	OK
	9	40.00	745.10	57.50	OK
	10	47.00	851.20	515.30	Projectile split in two
	11	40.50	733.70	0.00	Projectile split during handling
	12	41.00	741.10	0.00	OK
	13	41.50	773.00	197.30	OK
	14	41.00	770.50	284.40	OK
	15	40.50	739.80	252.40	OK
	16	40.00	706.70	0.00	OK
	17	40.00	720.00	97.90	OK
Hard core	1	Full	914.80	563.00	OK
	2	45.00	788.60	307.60	OK
	3	40.00	734.10	0.00	OK
	4	40.50	742.90	63.40	OK
	5	41.00	747.30	0.00	OK
	6	42.00	764.00	216.70	Projectile split in two
	7	41.50	756.20	197.50	Projectile split in two
	8	47.00	851.20	412.70	Projectile split in two
	9	41.00	748.40	170.80	Projectile split in two
	10	45.00	824.50	362.20	OK

4.2.1.1 As-received

The dominant failure mode for the as-received 12 mm plates was ductile hole growth. This can be seen by investigating the impacted plates and bullet holes in Appendix A. The exit holes of each shot shows that the material has been pushed aside by the projectile, thereby thickening the plate in vicinity of the exit hole. This is as expected since the unhardened NVE36 material is a mild steel type which has high ductility. This was verified by the tensile tests. Additionally, no fragmentation occurs as the plate has uniform hardness with no brittle surface of martensite. A representative test is shown in Figure 4.5.

Furthermore, notice how the brass jacket of the projectile is peeled off during the penetration process. However, sometimes the jacket is embedded in the indentation of the entry hole. Cross section of test number 2 revealed that the brass jacket caused a crater in the entry hole (Figure 4.5(d)).

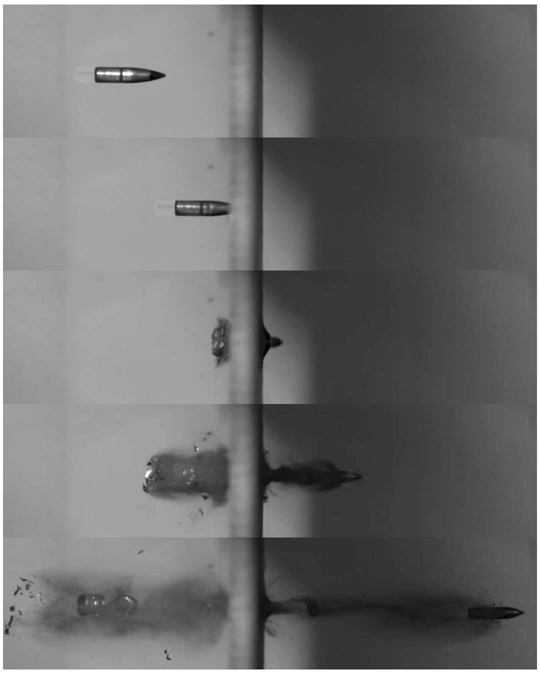

(a) Time-lapse.

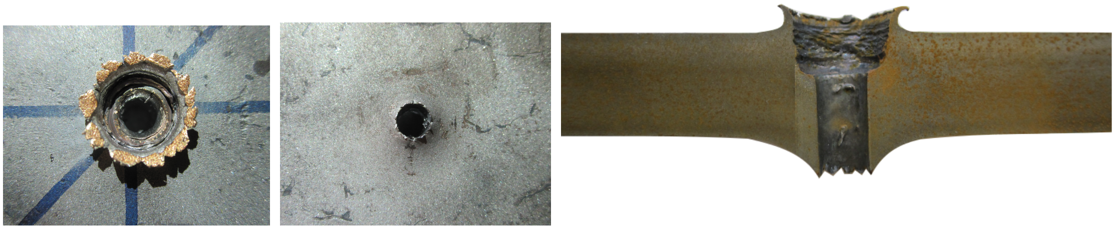

(b) Entry hole. (c) Exit hole. (d) Cross section.

Figure 4.5: Test no. 2 for unhardened 12 mm plate. v_i=745.10 m/s, v_r=500.60 m/s.

4.2.1.2 Soft Core

The 12 mm soft core plates failed by a combination of multiple modes. In addition to ductile hole growth, fragmentation has occurred at the exit holes of some of the tests (Figure 4.6). The fragmentation occurred in the carburized layer. Furthermore, radial cracks developed in close proximity around the exit hole. Similar observations were made by Lou et al. [54] and Coucheron [24]. It is likely that the appearance of the two latter modes occurs as a consequence of the brittleness of the material surface. Additionally, the projectile split in two in several tests. This contributed to the observed spread in experimental results since half of the bullet had a higher v_r than the other half.

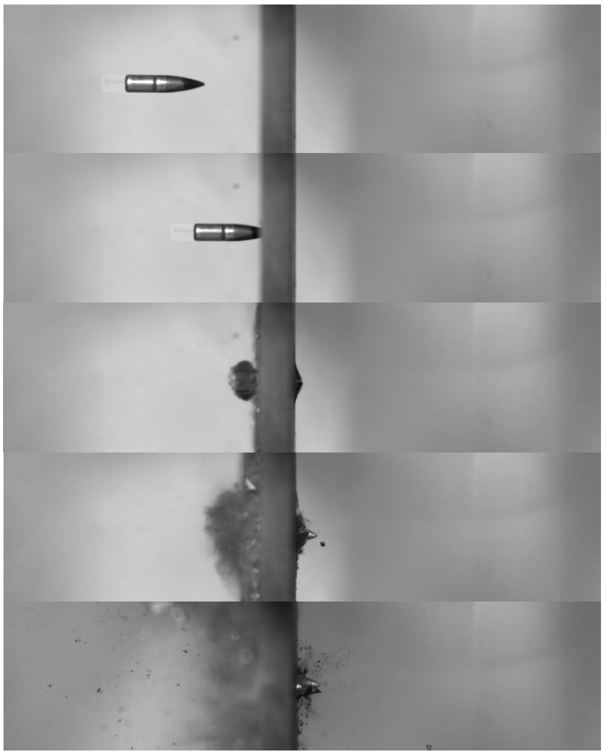

(a) Time-lapse.

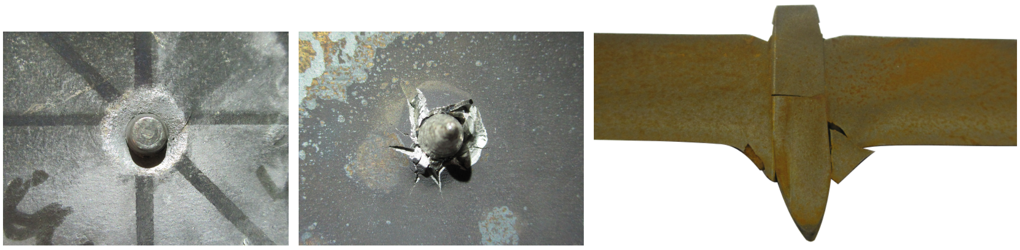

(b) Entry hole. (c) Exit hole. (d) Cross section.

Figure 4.6: Test no. 3 for soft core 12 mm plate. v_i=760.60 m/s, v_r=0.00 m/s.

4.2.1.3 Hard Core

The 12 mm hard core plates displayed much of the same ballistic response as the soft core plates. This includes ductile hole growth, fragmentation, and radial cracks. Based on the similar material properties, found in Chapter 3, this is as expected. Furthermore, in 4 of the 10 shots fired on this configuration, the projectile split in two pieces. However, no noticeable difference in both target response and residual velocity compared to other shots was observed. In some of the tests, parts of the bullet remained in the target, while the rest of the bullet perforated the plate. Figure 4.7 displays images from test no. 2.

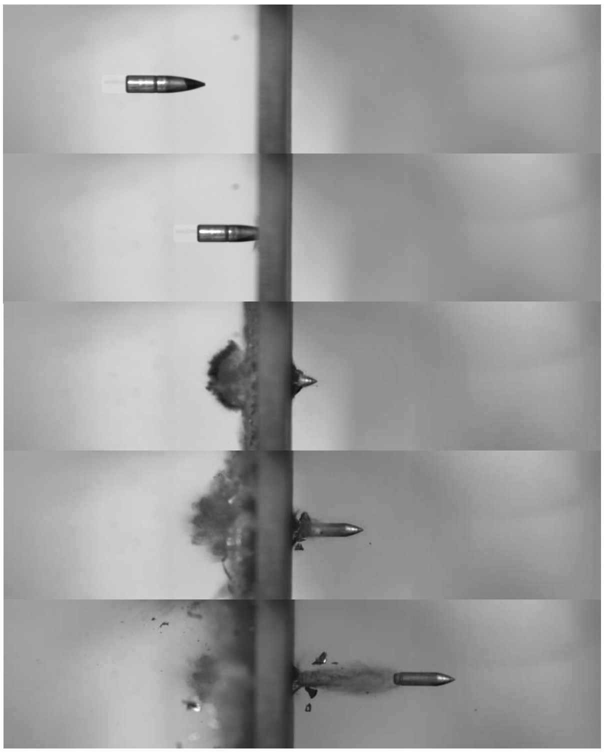

(a) Time-lapse.

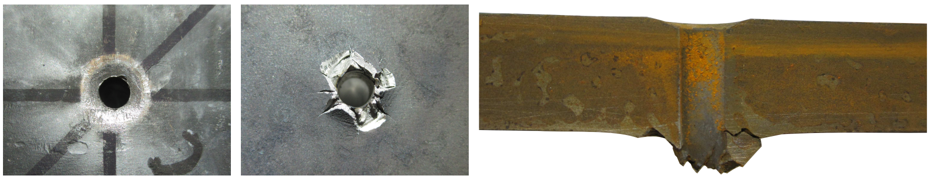

(b) Entry hole. (c) Exit hole. (d) Cross section.

Figure 4.7: Test no. 2 for hard core 12 mm plate. v_i=788.60 m/s, v_r=307.60 m/s.

4.2.1.4 Ballistic Limit Curve

By fitting the ballistic results to the Recht-Ipson model, the parameters in Table 4.4 were obtained. The resulting ballistic limit curves are given in Figure 4.8.

Table 4.4: Recht-Ipson parameters for 12 mm plates.

Heat treatment	v_{bl} [m/s]	a	p
As-received	587.50	1.00	2.21
Soft core	720.00	1.00	1.88
Hard core	737.40	1.00	2.06

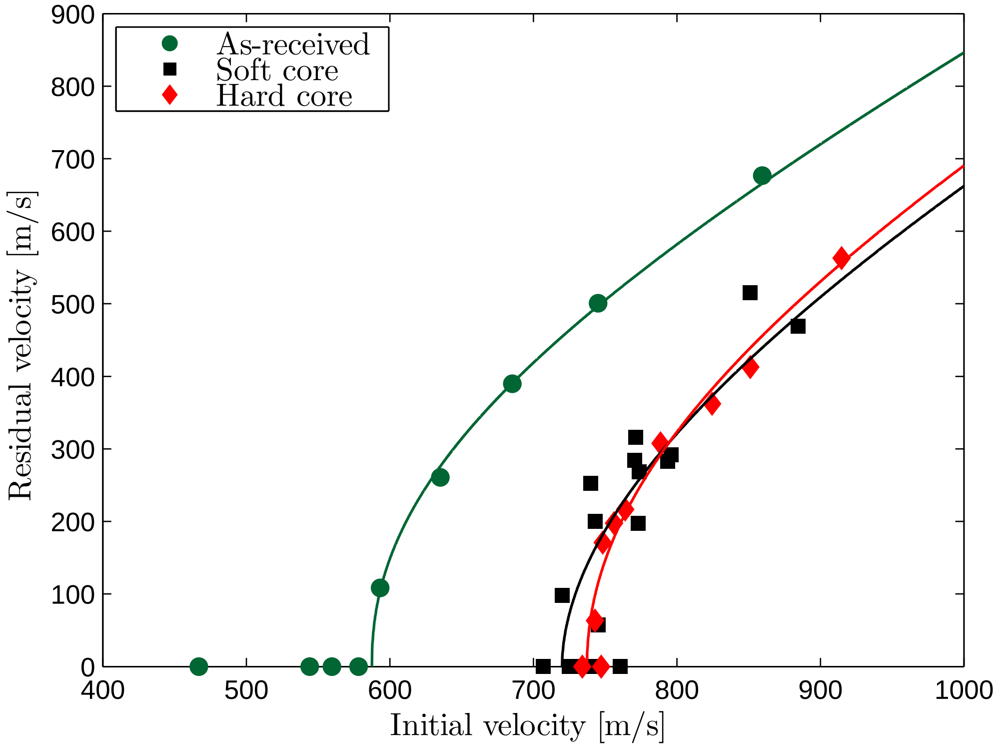

Figure 4.8: Ballistic velocity curve for 12 mm plates.

The curves suggest that hardening has a positive effect on the ballistic resistance. The hard core and soft core configuration gives an increase of 25.5% and 22.6%, respectively, in the ballistic limit velocity compared to the unhardened material. Furthermore, the hard core has a 2.4% higher ballistic limit velocity than soft core. Otherwise, the curves are very alike. This could be explained by the similar material behaviour, shown in Chapter 3. However, due to the spread in the soft core tests, the ballistic limit curve is somewhat uncertain. Furthermore, Lou et al. [54] obtained a ballistic limit velocity of 592 m/s for monolithic unhardened 12 mm plates, i.e. very similar to the results in this study. Coucheron [24] obtained a ballistic limit velocity of 684 m/s for a surface hardened

12 mm soft core plate. Hence, a difference of 5.3% compared to the soft core in this thesis. However, the plate in Coucheron's study had a core (approximately 250 $HV_{0.2}$) consisting of ferrite and pearlite, while the soft core plates in this study had a harder core of martensitic/ferrite structure.

4.2.2 2x6 mm Plates

Tabulated results from the ballistics experiments are give in Table 4.5.

Table 4.5: Tabulated results - 2x6 mm plates.

Hardening config.	Test	Gunpowder [grain]	v_i [m/s]	v_r [m/s]	Comment
As-received	1	Full	903.70	732.10	OK
	2	37.00	685.40	378.30	OK
	3	33.00	589.60	0.00	OK
	4	34.00	617.20	194.60	OK
	5	33.50	591.40	0.00	OK
	6	33.60	622.80	202.70	Projectile split in two
	7	33.50	608.00	162.90	OK
	8	33.20	597.00	115.70	OK
	9	45.00	807.3	606.3	OK
Soft core	1	Full	914.80	627.90	Projectile split in two
	2	45.00	760.60	357.40	OK
	3	38.00	681.00	0.00	OK
	4	39.00	697.50	0.00	OK
	5	39.50	736.30	299.50	OK
	6	39.00	713.30	195.80	OK
Hard core	1	Full	892.70	539.10	OK
	2	45.00	798.40	394.30	OK
	3	40.00	727.40	127.50	OK
	4	39.00	711.90	0.00	OK
	5	42.00	767.20	332.80	OK
	6	41.00	763.10	232.60	OK
	7	40.50	753.30	184.00	Projectile split in three
	8	40.20	711.60	0.00	OK

4.2.2.1 As-received

The 2x6 mm unhardened plates failed by ductile hole growth. No fragmentation occurred, as can be seen in the projectiles' entry and exit holes in Appendix A. Hence, the visual examination exhibits similar results as the monolithic unhardened plates. This is as expected due to their ductile behaviour. However, the double layered plates displayed more global deformation than the monolithic configuration.

Furthermore, the brass jacket was peeled off and embedded in the entry hole of the shots with the highest velocities(> 685 m/s). However, for lower velocities, the jacket was removed entirely and only the steel core remained of the projectile. Figure 4.9 shows this behaviour. Furthermore, notice the gap between the plates in Figure 4.9(d). Visual inspection along the edges prior to the test showed that they were in contact. Therefore, it is not known if the gap was created during impact or was present all along.

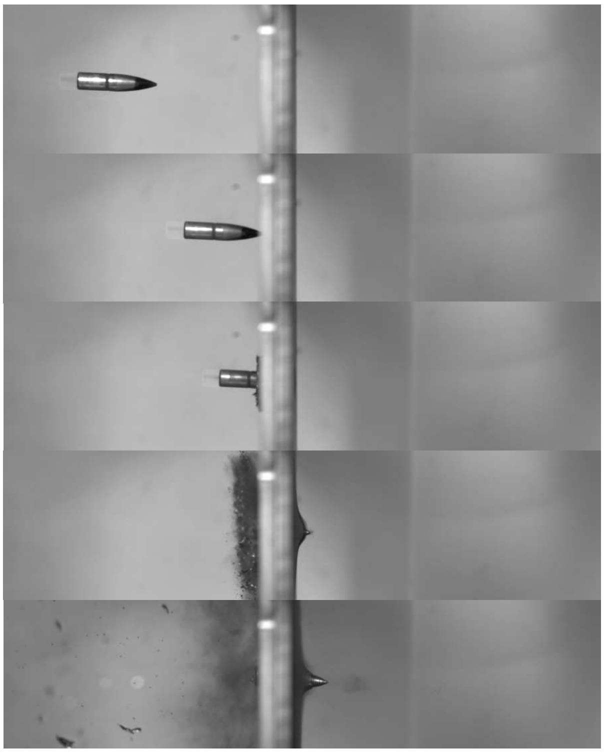

(a) Time-lapse.

(b) Entry hole. (c) Exit hole. (d) Cross section.

Figure 4.9: Test no. 3 for unhardened 2x6 mm plate. v_i=589.60 m/s, v_r=0.00 m/s.

4.2.2.2 Soft Core

The double layered soft core plates experienced failure by ductile hole growth and radial cracks. Also, fragmentation at the front plate was observed. Except from Test no. 1, none of the tests exhibited fragmentation of the back plate. This seems to be in good agreement with the measured hardness profiles found in Section 3.6.2, where the back plate showed overall lower hardness than the front plate. Furthermore, delamination of the brittle carburized layer occurred at test no. 1 (the highest impact velocity) in the front plate. Additionally, the brass jacket has peeled completely off due to the hardened front plate for all velocities. Figure 4.10 displays test no. 3.

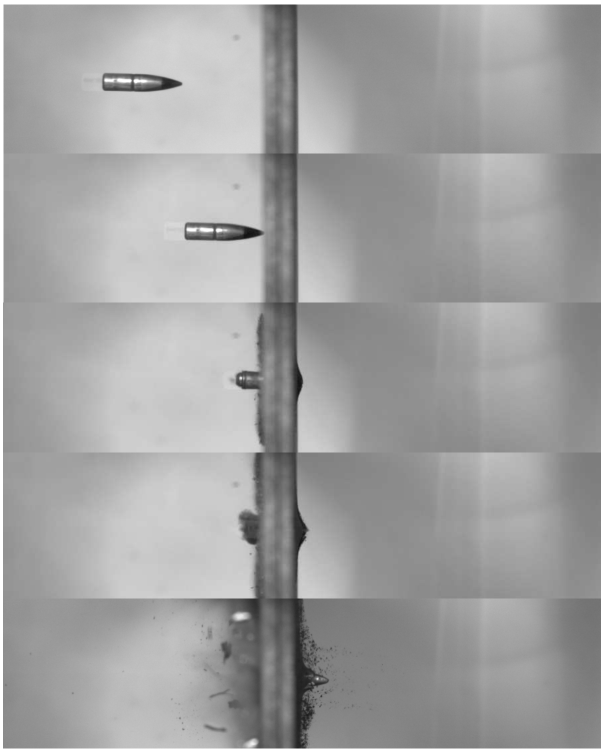

(a) Time-lapse.

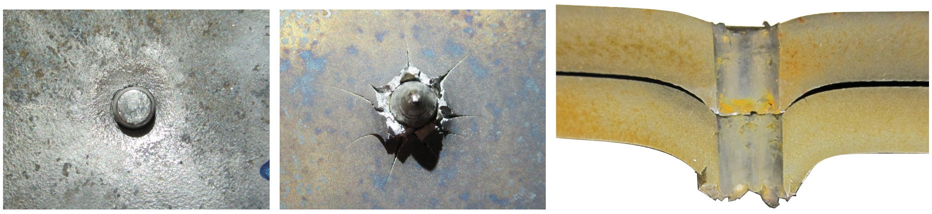

(b) Entry hole. (c) Exit hole. (d) Cross section[2].

Figure 4.10: Test no. 3 for soft core 2x6 mm plate. v_i=681.00 m/s, v_r=0.00 m/s.

---

[2] Bullet removed during cutting of plates

4.2.2.3 Hard Core

The double layered hard core plates displayed the same failure modes as the soft core configuration. Meaning ductile hole growth, radial fracture and fragmentation of the front plate. The back plate did not display as much fragmentation. This may be explained by the results found in Section 3.6.2, where the back plate of the double layered hard core had almost similar core hardness as the back plate of the soft core. The radial cracks occurs due to the brittle surface. Furthermore, delamination occurred in the vicinity of the entry hole in some of the tests. In Figure 4.11 one can see the front surface layer of the brittle martensite which was removed during penetration. Especially the shots at the highest velocities displayed most fragmentation of the brittle front surface. This might be because of the high surface hardness found in Section 3.6.2.

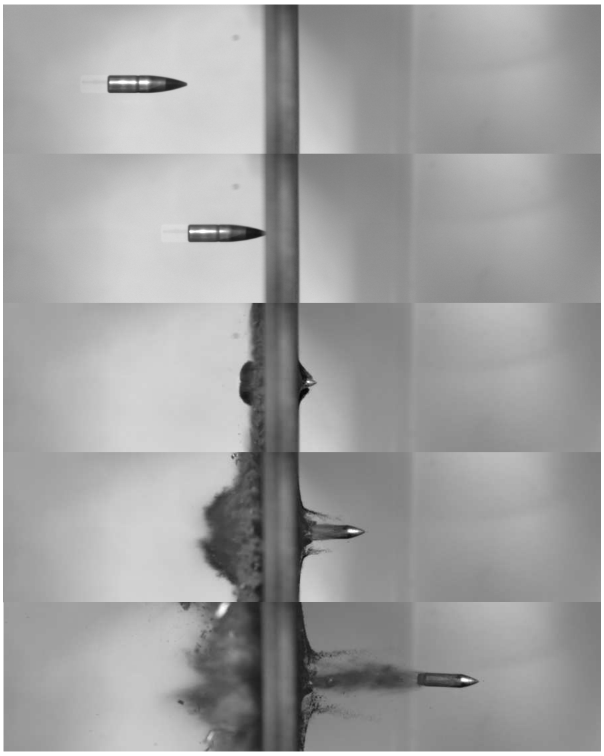

(a) Time-lapse.

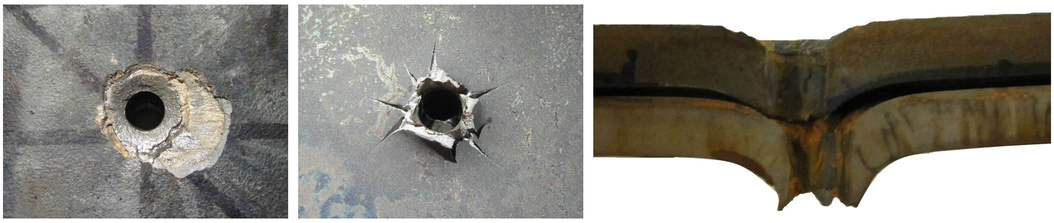

(b) Entry hole. (c) Exit hole. (d) Cross section.

Figure 4.11: Test no. 1 for hard core 2x6 mm plate. v_i=892.70 m/s, v_r=539.10 m/s.

4.2.2.4 Ballistic Limit Curve

By fitting the ballistic results to the Recht-Ipson model, the parameters in 4.6 were obtained. The resulting ballistic limit curves are given in Figure 4.12.

Table 4.6: Recht-Ipson parameters for 2x6 mm plates.

Heat treatment	v_{bl} [m/s]	a	p
As received	591.50	1.00	2.21
Soft core	697.80	1.00	2.26
Hard core	718.50	1.00	2.17

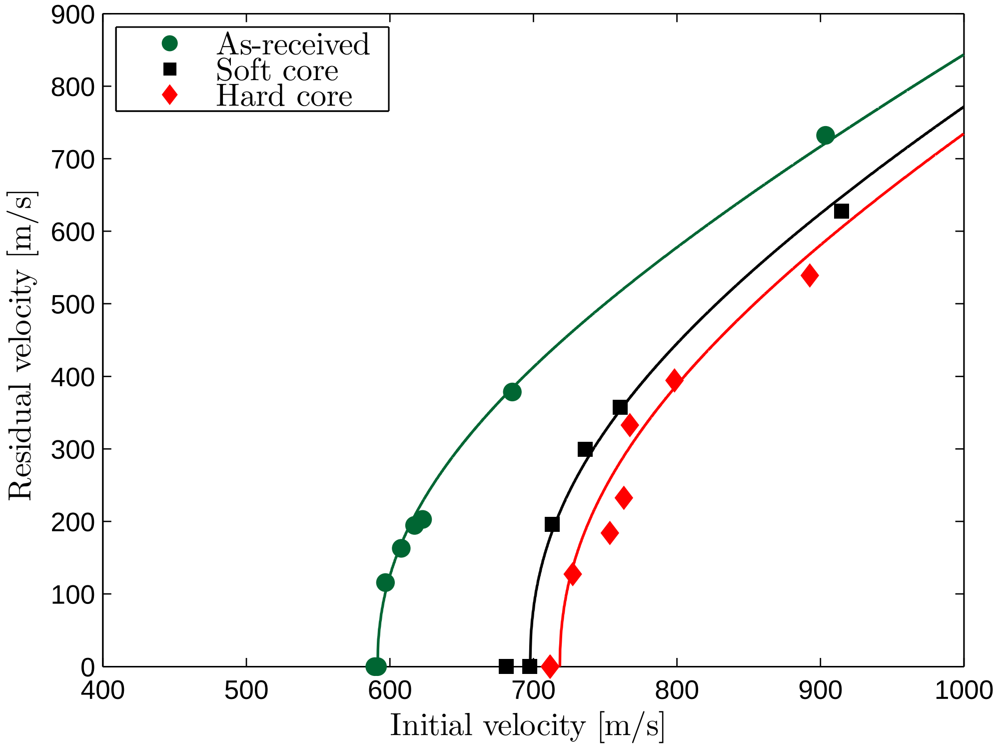

Figure 4.12: Ballistic velocity curve for 2x6 mm plates.

The ballistic limit curves for the 2x6 mm plates shows many of the same tendencies as for the monolithic plates. That is, hardening has a positive effect on the ballistic limit velocity and increases the perforation resistance. The hard core and soft core configuration increases the ballistic limit velocity by 21.5% and 18.0%, respectively.

Furthermore, the hard core configuration exhibits 3.0% higher ballistic limit velocity than the soft core. This is in accordance with obtained hardness measurements from Section 3.6.2, where the front plate of the hard core configuration was harder than soft core.

4.2.3 3x4 mm Plates

Tabulated results from the ballistics experiments are give in Table 4.7.

Table 4.7: Tabulated results - 3x4 mm plates.

Hardening config.	Test	Gunpowder [grain]	v_i [m/s]	v_r [m/s]	Comment
As-received	1	Full	906.50	756.70	OK
	2	37.00	703.10	445.40	OK
	3	34.00	628.30	320.10	OK
	4	32.00	567.50	0.00	OK
	5	33.00	620.90	309.50	OK
	6	32.50[3]	680.60	450.00	OK
	7	32.50	570.80	0.00	OK
	8	33.00	592.60	216.40	OK
Soft core	1	Full	916.00	550.90	Halo created
	2	45.00	805.80	392.10	Halo removal
	3	40.00	738.50	239.10	OK
	4	38.50	727.20	0.00	Plate crack
	5	40.00	729.60	250.00	OK
	6	40.50	755.30	312.30	OK
	7	39.00	722.20	83.00	Halo removal
	8	38.50	677.30	0.00	Plate crack
Hard core	1	Full	892.70	556.40	OK
	2	45.00	815.30	433.90	OK
	3	39.00	714.20	101.70	OK
	4	38.50	717.30	0.00	OK
	5	39.00	713.60	171.70	Small gap
	6	40.50	744.20	250.00	OK
	7	38.50	715.50	173.00	Small gap. Halo created
	8	38.30	711.60	83.90	OK
	9	38.00	681.90	0.00	OK

4.2.3.1 As-received

The unhardened 3x4 mm plates failed by ductile hole growth. As with the other unhardened configurations, the brass jacket peeled off during impact. Part of the jacket was crumbled and can be seen embedded on the front of the plate in some of the tests (see Appendix A). In other shots pieces of the jacket can be seen inside the bullet hole (Figure 4.13).

From the cross section, in Figure 4.13, it appears that the unhardened 3x4 mm configuration experiences more global deformation than the unhardened 2x6 mm and 12 mm plates. This was also noticed by Dey et al. [25], where layered thin plates were compared with

---

[3] Possible measurement mistake in gunpowder amount.

monolithic. This effect might be due to the lower bending stiffness lamination introduces, as suggested by Zukas and Scheffler [71]. Furthermore, notice that the front plate does not deform as much as the two other plates.

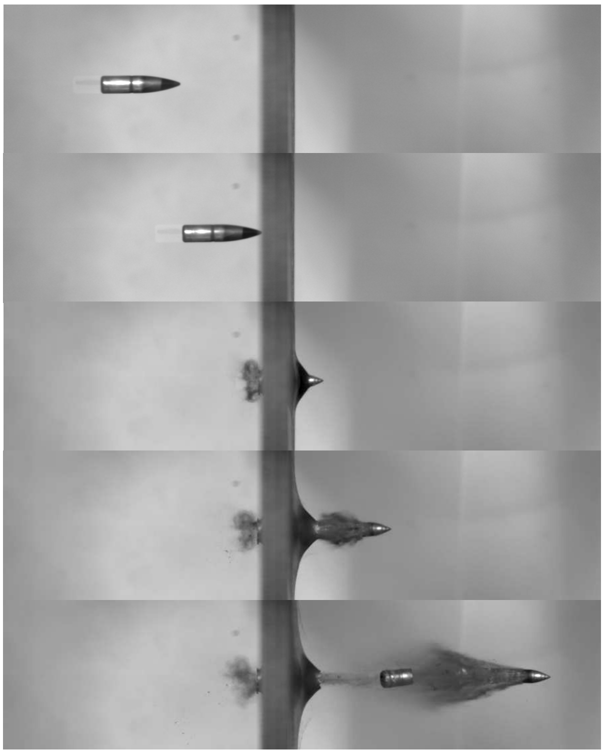

(a) Time-lapse.

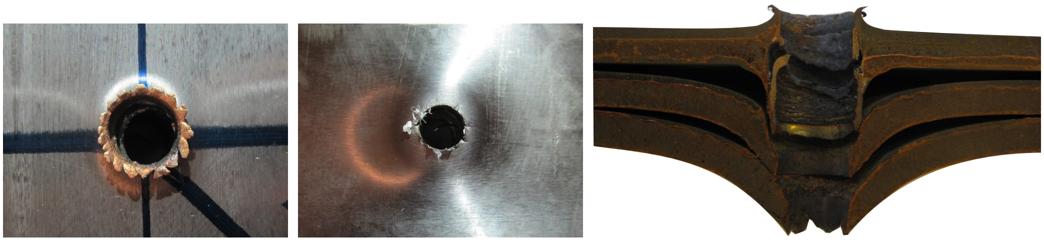

(b) Entry hole. (c) Exit hole. (d) Cross section.

Figure 4.13: Test no. 1 for unhardened 3x4 mm plates. v_i=906.50 m/s, v_r=756.70 m/s.

4.2.3.2 Soft Core

The soft core configuration failed by multiple modes. The plates suffered from both radial and circumferential cracks. Fragmentation was also observed. Figure 4.14 shows this brittle behaviour. Notice the "halo" (circumferential crack) surrounding the exit hole. Ductile hole growth was also seen. In test no. 1 the projectile impacted the target with a small impact angle causing a change in flight direction after perforation. However, it does not seem to influence the results significantly.

Furthermore, the brass jacket was completely removed during all the tests. Additionally, the soft core configuration experienced less global deformation than the unhardened plates.

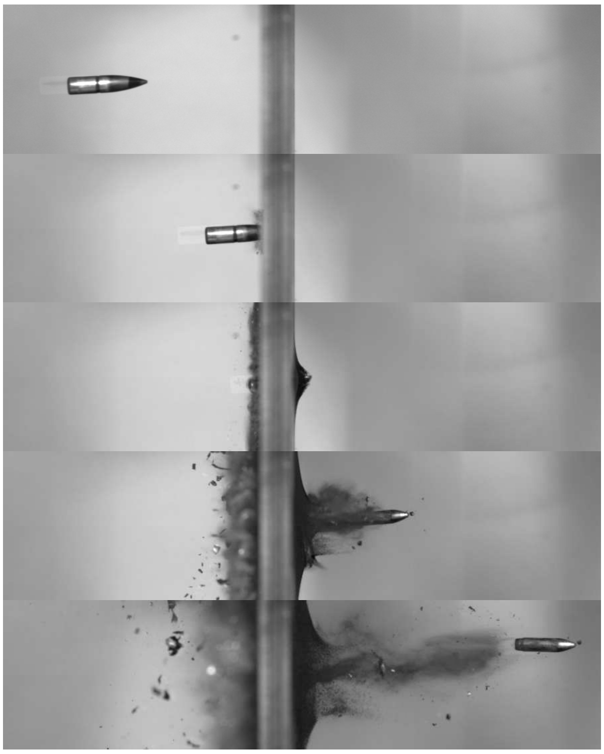

(a) Time-lapse.

(b) Entry hole. (c) Exit hole. (d) Cross section.

Figure 4.14: Test no. 1 for soft core 3x4 mm plate. v_i=916.00 m/s, v_r=550.90 m/s.

Severe circumferential cracks caused a large circular piece of the back plate (a halo) to be removed during perforation in shot 2 and 7, see Figure 4.15. The same phenomenon was observed in Coucheron [24].

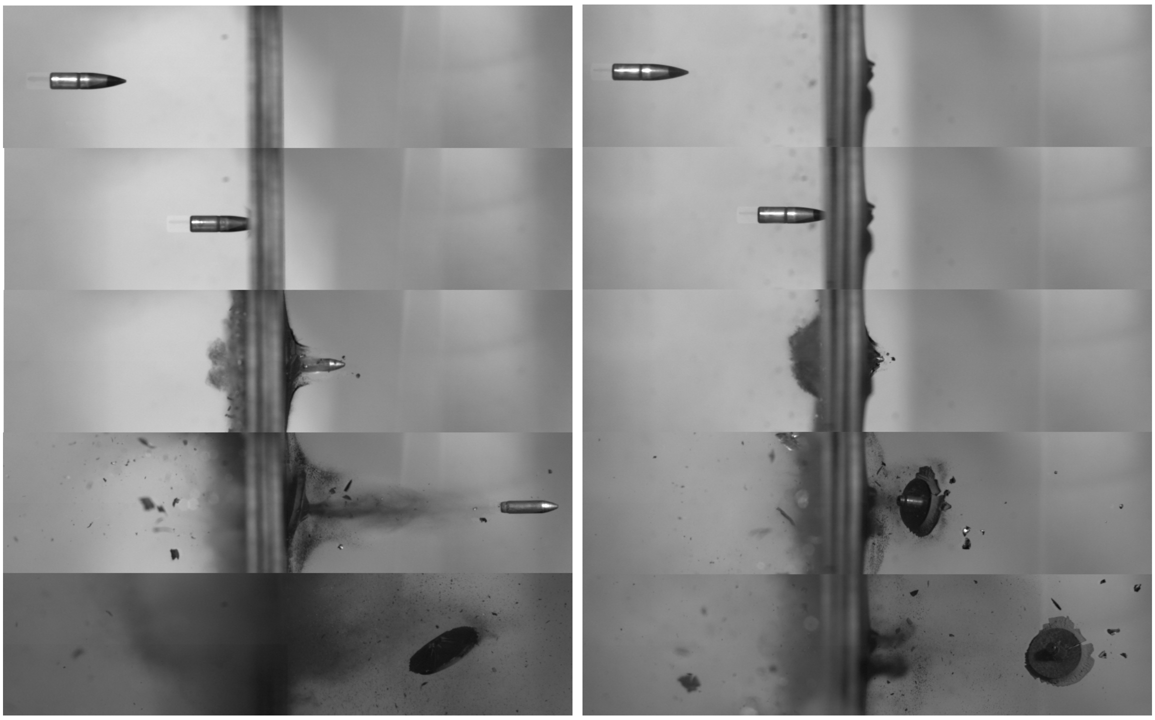

(a) Test no. 2: Time-lapse.

(b) Test no. 7: Time-lapse.

(c) Test no. 2: Back plate halo.

(d) Test no. 7: Back plate halo.

Figure 4.15: Halo created in 3x4 mm soft core back plates.

4.2.3.3 Hard Core

From Figure 4.16, and the figures in Appendix A, we observe that the hard core 3x4 mm plates suffers from ductile hole growth, radial cracks and fragmentation. This is similar to the soft core behaviour. Furthermore, the brass jacket peels completely off and is removed in all the tests. Additionally, the hard core configuration did not experience as much global deformation as the unhardened plates. In the time-lapse for test no. 3, a change in flight direction was also observed. This might be because of pre deformations of the hardened plates as described earlier.

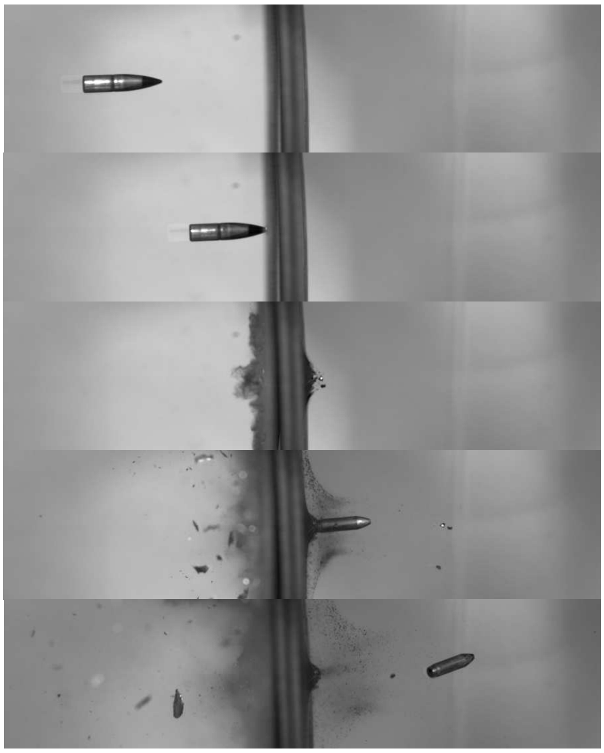

(a) Time-lapse.

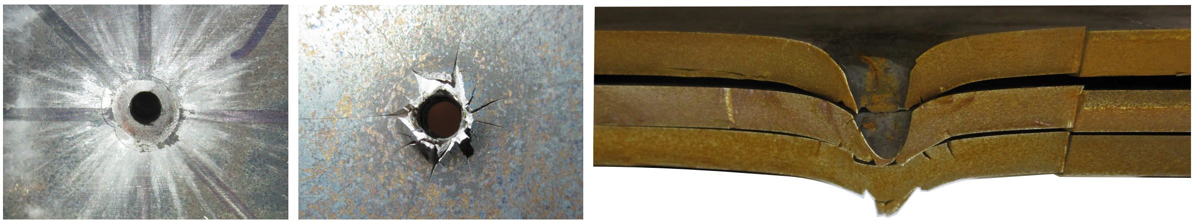

(b) Entry hole. (c) Exit hole. (d) Cross section[4].

Figure 4.16: Test no. 3 for hard core 3x4 mm plate. v_i=714.20 m/s, v_r=101.70 m/s.

---

[4] The cross section cut missed the hole somewhat. The bullet perforated the target.

4.2.3.4 Ballistic Limit Curve

By fitting the ballistic results to the Recht-Ipson model, the parameters in Table 4.8 were obtained. The resulting ballistic limit curves are given in Figure 4.17.

Table 4.8: Recht-Ipson parameters for 3x4 mm plates.

Heat treatment	v_{bl} [m/s]	a	p
As received	570.80	1.00	2.36
Soft core	706.10	1.00	2.03
Hard core	703.20	1.00	2.06

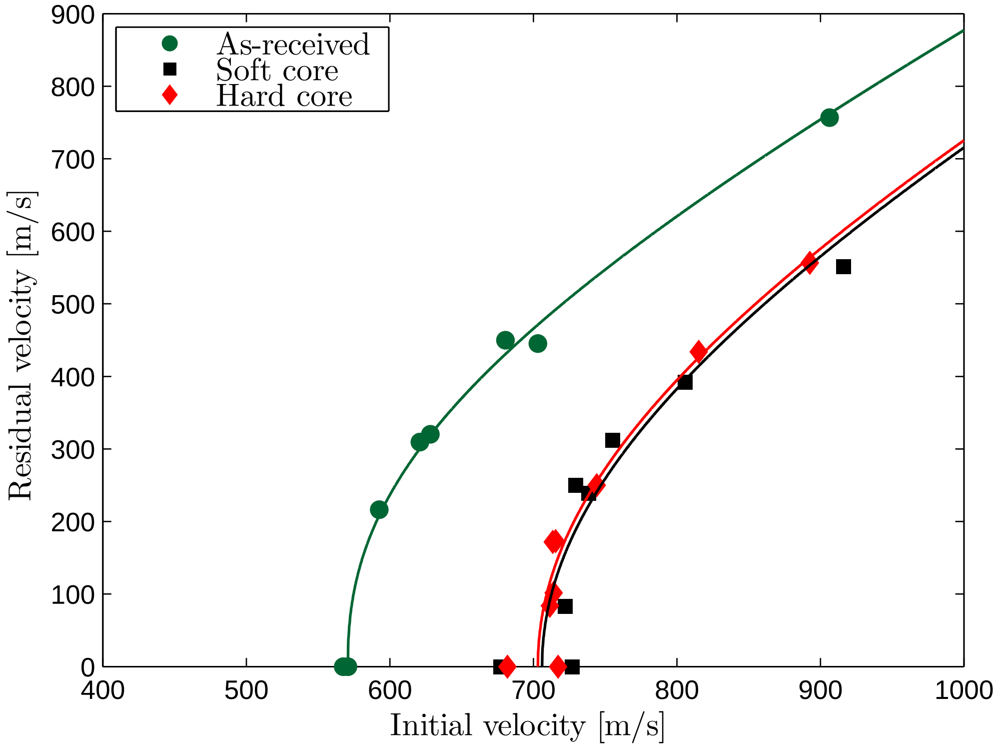

Figure 4.17: Ballistic velocity curve for 3x4 mm plates.

As with the other plate configurations, heat treatment increases the perforation resistance of the 3x4 mm plates. Soft core and hard core configurations gives an 23.7% and 23.2% increase in ballistic limit velocity, respectively. Hard core has a 0.4% lower ballistic limit velocity than soft core, however, the difference is negligible because of spread in the experimental data. This similarity is as expected since the material hardness, found in Section 3.6.3, was similar.

4.2.4 Monolithic vs. Layered Plates

The following section will give a concise comparison and investigation of the effects of laminating plates against a pure monolithic configuration. However, it is important to keep in mind (from the material investigation) that only the unhardened material exhibited the same hardness for all layer configurations. The soft core and hard core plates showed different hardness profiles for each lamination.

4.2.4.1 As-received

The ballistic limit curves for the unhardened configurations in Figure 4.18 suggests that laminating has no clear positive effect on the ballistic limit velocity. This is in agreement with earlier studies described in Section 2.8. The 3x4 mm configuration displays somewhat lower perforation resistance. However, the double layered configuration has almost identical curve as the monolithic. It should be noted that the material investigations in Section 3.6 showed that the 2x6 mm unhardened plates are approximately 5% harder than the monolithic 12 mm. This is seen in Table 3.9 and 3.10.

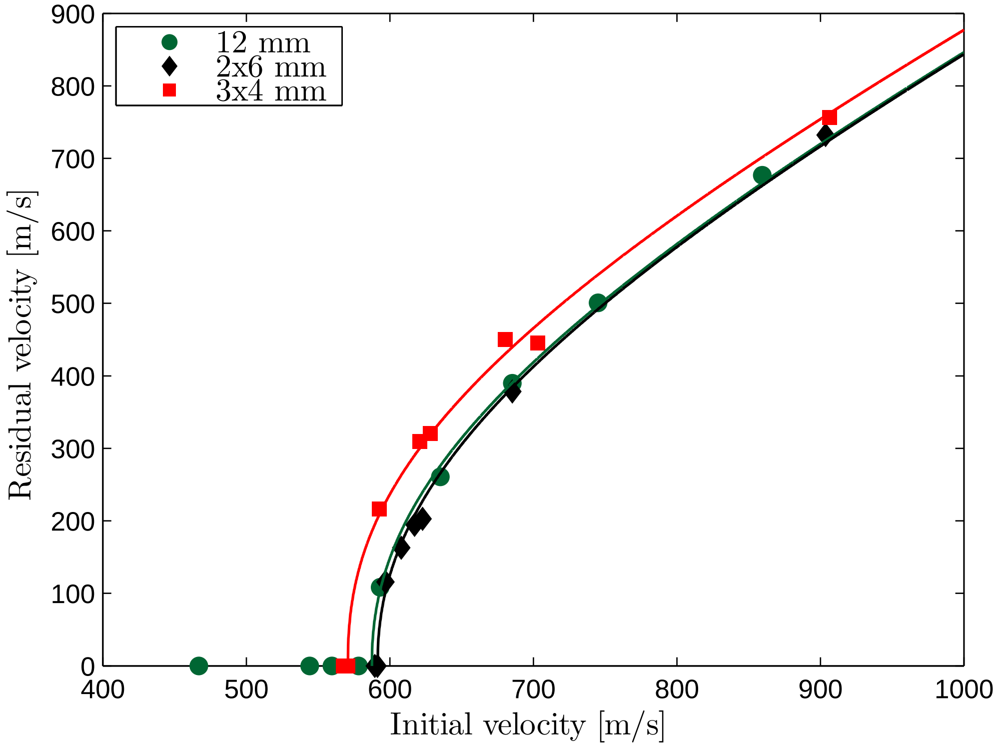

Figure 4.18: Ballistic velocity curve for all unhardened configurations.

Based on the cross sections shown in Figure 4.19, the layered configurations seem to exhibit more global deformation than the monolithic. This was also observed by Dey et al. [26] when applying ogival projectiles. Note that the initial velocities in the figure differ from each other. However, the monolithic plate has the lowest initial velocity and still exhibit noticeable less global deformation. Hence, the observation is valid.

(a) 12 mm Test no. 3. $v_i = 466.90$ m/s.

(b) 2x6 mm Test no. 3. $v_i = 589.60$ m/s.

(c) 4x4 mm Test no. 7. $v_i = 570.80$ m/s.

Figure 4.19: Deformation for different layer configurations in as-received target. $v_r =$ 0 m/s for all tests.

4.2.4.2 Soft Core

Figure 4.20 shows that the soft core monolithic configuration has a higher ballistic limit velocity than the other layered configurations. However, the results are somewhat uncertain due to the large spread in ballistic data. The triple layered configuration displays a slightly higher perforation resistance than the double layered plates. However, the material investigation found that the 3x4 mm plates were harder than the 2x6 mm configuration (Table 3.10 and Table 3.11), suggesting that the increased hardness counteracts the lower bending stiffness of the thinner plates.

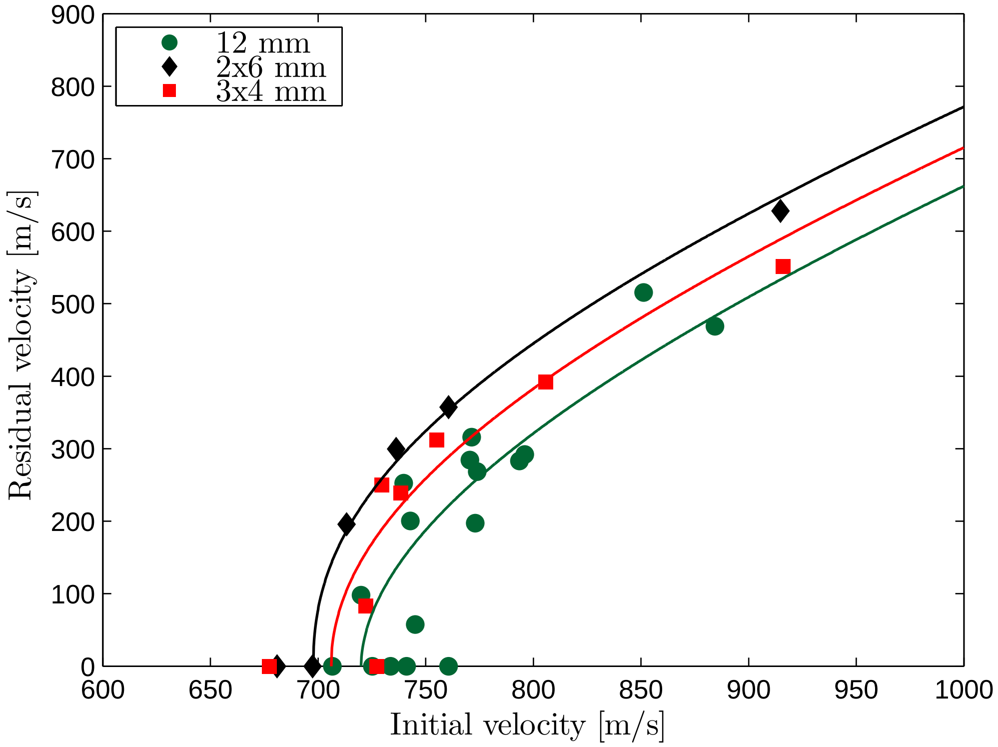

Figure 4.20: Ballistic velocity curve for all soft core configurations.

4.2.4.3 Hard Core

Figure 4.21 shows that the monolithic hard core plates have a higher ballistic limit velocity than the layered configurations. This is in contrast with Coucheron [24] and Lou et al. [53], who found a better ballistic resistance for the 2x6 mm hardened plates. However, this contrast may be explained by the low core hardness discovered in the back plate used in this thesis (See Section 3.6.2).

Furthermore, the triple layered configuration shows a lower ballistic limit velocity than the 2x6 mm plates. This is in contrast to the soft core results.

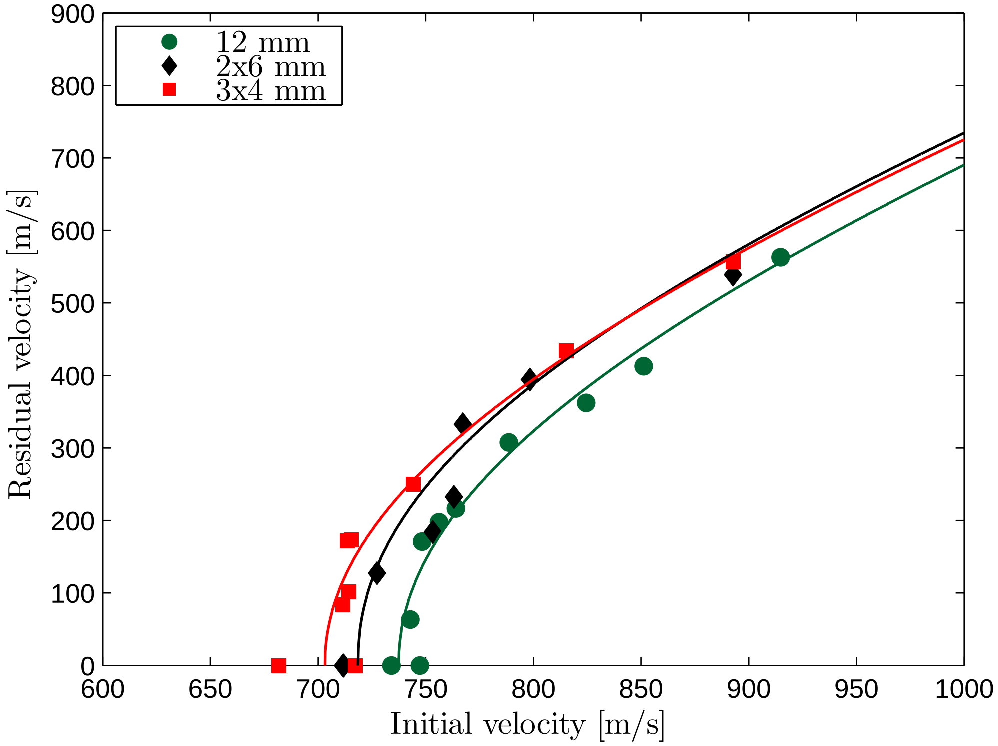

Figure 4.21: Ballistic velocity curve for all hard core configurations.

4.3 Summary and Discussion

A short summary and discussion of the observations and results presented in this section will be given. The following notation for the failure modes will be applied

RC	Radial Cracks	see Figure 2.4(f)
DHG	Ductile Hole Growth	see Figure 2.4(b)
F	Fragmentation	see Figure 2.4(c)
CC	Circumferential Cracks	-

Table 4.9 gives a summary of the ballistic limit velocity obtained in the different heat treated plates within each thickness configuration. Additionally, the relative difference between the hardened configurations with respect to the unhardened is presented.

Table 4.9: Summary - heat treatment in each plate configuration.

Thickness [mm]	Heat treatment	v_{bl} [m/s]	Rel. diff.	Failure modes
12	As-received	587.50	-	DHG
	Soft core	720.00	+22.6%	RC, F, DHG
	Hard core	737.40	+25.5%	RC, F, DHG
2x6	As-received	591.50	-	DHG
	Soft core	697.80	+18.0%	RC, F, DHG
	Hard core	718.50	+21.5%	RC, F, DHG
3x4	As-received	570.80	-	DHG
	Soft core	706.10	+23.7%	RC, CC, F, DHG
	Hard core	703.20	+23.2%	RC, F, DHG

Table 4.10 summarizes and compares monolithic vs. layered plates for each heat treatment configuration.

Table 4.10: Summary - plate layering in each heat treatment.

Heat treatment	Thickness [mm]	v_{bl} [m/s]	Rel. diff.	Failure modes
As-received	12	587.50	-	DHG
	2x6	591.50	+0.7%	DHG
	3x4	570.80	-2.8%	DHG
Soft core	12	720.00	-	RC, F, DHG
	2x6	697.80	-3.1%	RC, F, DHG
	3x4	706.10	-1.9%	RC, CC, F, DHG
Hard core	12	737.40	-	RC, F, DHG
	2x6	718.50	-2.6%	RC, F, DHG
	3x4	703.20	-4.6%	RC, F, DHG

Other observations from the ballistic experiments are listed below.

- Surface hardened plates showed an increase between 18-26% in the ballistic limit velocity compared to the unhardened (as-received) plates.
- Fragmentation and radial cracks occurred for the surface hardened target plates, but not for the unhardened plates.
- Hardened plates experienced less global deformation than unhardened.
- Hardened plates were sometimes subjected to delamination of the brittle martensitic surface layer. Especially the entry hole of 2x6 mm hard core at higher velocities.
- No significant difference (within 3%) between soft core and hard core plates in terms of ballistic limit velocities for all configurations.
- Back plates (i.e. Plate 2) for the double layered soft core and hard core configurations were not subjected to fragmentation. The hardness of these plates was less than the unhardened material.
- Hardened plates tended to destroy the entire brass jacket without embedment. Embedment was observed for the unhardened plates.
- Lamination did not increase the overall ballistic limit velocity.
- The double and triple layered plates were hardened more than the monolithic, but did not provide a better ballistic limit velocity. Hence, if hardened with nominal values, these laminations would most likely not provide a better overall ballistic limit velocity compared with the monolithic.
- Lamination of plates caused more global deformation than monolithic.

It is, however, important to remember that these observations are based on experimental data which contains large spreads. This concerns especially the hardened plates. Therefore, it is difficult to draw conclusions between the soft core and hard core configurations.

Chapter 5

Identification of Material Constants

Based on the true stress-strain curves obtained from the tensile tests described in Chapter 3, a material model will be calibrated for the NVE36 material. The MJC model was chosen as a constitutive relation, and will be calibrated using two approaches: (i) Direct calibration and (ii) inverse modelling using LS-DYNA.

5.1 Direct Calibration

In order to directly calibrate the MJC constitutive relation, a MATLAB script shown in Appendix D, was applied. The procedure was as follows

(i) Strain at necking was obtained by employing the Considère criterion (Eq. 2.15).

(ii) Due to necking, the equivalent stress was calculated using the Bridgman correction (Eq. 2.16) with the Le Roy a/R ratio (Eq. 2.17).

(iii) Voce law (Eq. 2.21), was used to calibrate the equivalent stress.

The results are shown in Figures 5.1 - 5.4. A three term Voce law was used to calibrate the material constants. This was done to better capture the yield plateau in the unhardened material. The obtained Voce parameters are given in Table 5.1.

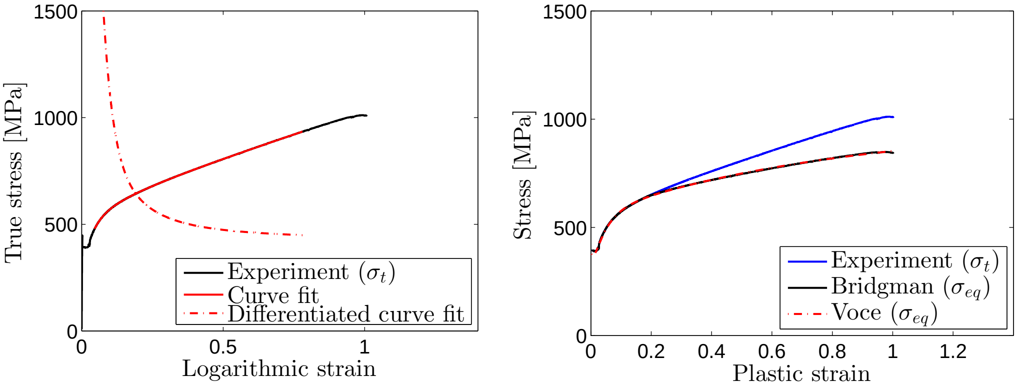

(a) Necking cross point. (b) Bridgman correction.

Figure 5.1: As-received direction 1.

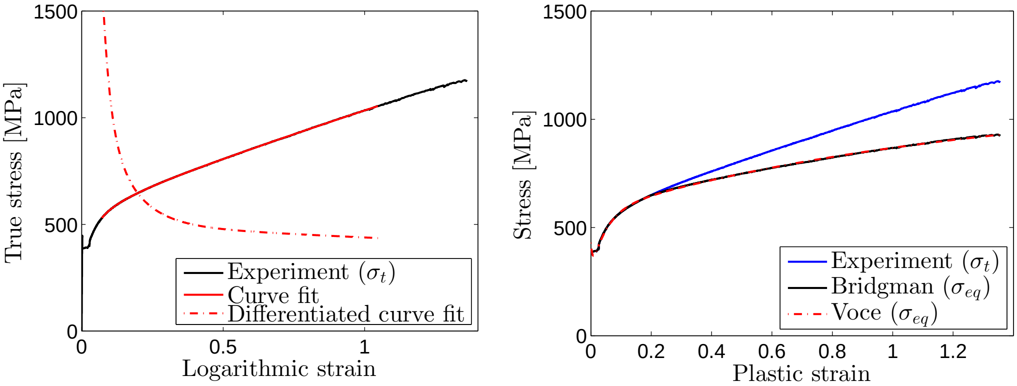

(a) Necking cross point. (b) Bridgman correction.

Figure 5.2: As-received direction 2.

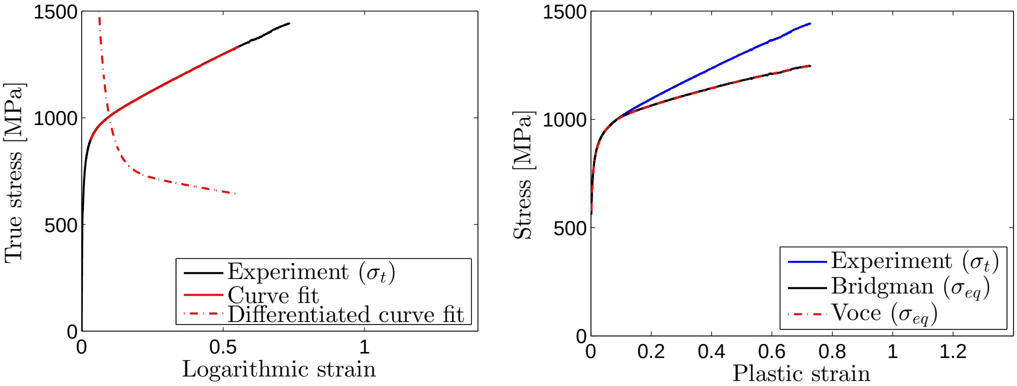

(a) Necking cross point. (b) Bridgman correction.

Figure 5.3: Soft core.

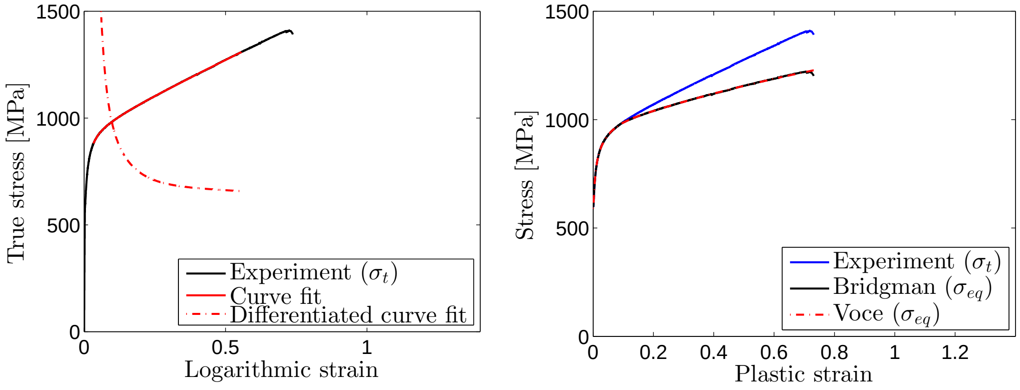

(a) Necking cross point.
(b) Bridgman correction.

Figure 5.4: Hard core.

Table 5.1: Obtained Voce parameters from direct calibration.

	A [MPa]	Q_1 [MPa]	C_1	Q_2 [MPa]	C_2	Q_3 [MPa]	C_3
As-received, Direction 1	520.45	414.42	1.25	281.85	22.53	-245.53	173.46
As-received, Direction 2	429.55	543.84	0.79	281.01	19.74	-138.97	174.62
Soft core	487.39	581.94	0.90	272.11	206.80	208.67	32.41
Hard core	551.32	639.74	0.79	209.24	163.41	186.21	29.44

The Voce parameters are in descending order, i.e. $Q_1 > Q_2 > Q_3$. Term 1 in Voce law is the classic strain hardening introduced by Voce in 1948 [68]. The second term is included to round of the first peak in the stress-strain curve, and to improve the convergence of a FEM solution [55]. The third term is only a phenomenological way to include the static strain aging coming from our unhardened material, i.e the yield plateau [55].

Furthermore, since only quasi-static tension tests were performed, the strain rate hardening (C) and temperature softening (m) were not calibrated. Instead, these were found in literature. Constants calibrated for the Weldox 460 E steel in Børvik et al. [15] were used. The different parameters are presented in Table 5.2.

Table 5.2: Strain rate hardening and temperature softening parameters for MJC.

	C	m
As-received	0.0114	0.94

5.2 Inverse Modeling - Calibrating in LS-OPT

The Bridgman correction and the Le Roy a/R ratio, are only approximate solutions with many assumptions. Hence, it might be interesting to look at another way of obtaining the equivalent stress. LS-OPT is an optimization tool which interacts with the FEM program LS-DYNA. An axisymmetric finite element model of the tensile specimen was generated in LS-DYNA on which several numerical tensile tests were run in sequential order. In each analysis, input material parameters are changed and, hence, different responses are obtained. Herein, the material parameters are the constants in Voce law. The idea is, by successively comparing the responses to a given target curve, the response with the best fit has the best material-input parameters.

The target curve was the true stress-strain obtained from the tensile tests. The tensile specimen was modelled in LS-DYNA using volume weighted solid elements, i.e. element formulation 15, with element size in the necking region as specified in Figure 5.5. A closer view of the necking region can be seen in Figure 5.8. The numerical model was axisymmetric to reduce the analysis time, and no fracture criterion was specified. The material parameters obtained from the direct calibration were used as an initial guess. Upon reading the keyword file (input), LS-OPT runs several iterations while changing the desired parameters, i.e. Voce parameters, to obtain a solution with the smallest mean square error (MSE) between target curve and the computed true stress-strain curve. The middle node of the model was moved a slight distance inwards (0.005 mm) to force necking to occur at this location.

All the analyses were run on the computer cluster, Snurre, at NTNU. The cluster contains 12 CPUs à 2.4 GHz. By applying the cluster LS-OPT was able to run multiple jobs within each iteration making the process much faster compared to personal computers.

Figure 5.5: Tensile specimen in LS-OPT: Element size in necking region 0.3 x 0.15 mm.

5.2.1 SIMLab Metal Model

Since a three-term Voce hardening law was applied for the NVE36 steel material, the material card *MAT_107 in LS-DYNA could not be used (restricted to only two Voce terms for MJC). Instead, SIMLab Metal Model (SMM) was applied, which allows three Voce terms. The Voce hardening law is implemented by SIMLab in the following manner [42]

$$R = \sum_{i=1}^{3} R_i = \sum_{i=1}^{3} Q_{Ri}(1 - \exp(-\frac{\theta_{Ri}}{Q_{Ri}}p)) \tag{5.1}$$

where the relation between θ_{Ri} and C_i parameter in Voce is, $\theta_{Ri} = C_i Q_{Ri}$.

5.2.2 Results

For the unhardened material a true stress-strain curve was optimized both with and without a yield plateau. The intention behind this was to perform a parameter study in Chapter 6 to investigate how this affects the ballistic response numerically. Direction 1 (UH1) was used as target curve for the optimization with yield plateau, and direction 2 (UH2) for optimization without yield plateau. This choice was arbitrary as the stress-strain curves in the different directions were similar except the strain at failure. In order to capture the yield plateau, the yield stress parameter (A) was locked in the material card in LS-DYNA. Hence, only Q_{Ri} and θ_{Ri} had to be fitted.

LS-OPT had difficulty optimizing the curve with the yield plateau. Even though necking had been forced by moving the middle node slightly inwards, several of the iterations had the model neck at different locations. Since optimization was based on information (displacement) from the middle node, the ”most optimized” curve from LS-OPT was not usable. Yet, by moving the middle node even more inwards the problem remained. Therefore, a more or less manual approach was applied. By going through all the jobs from each iterations and picking the ones were the above problem was not an issue, an optimized curve was selected. This was not as time consuming as one might think, since the jobs which were up for the picking were the ones where the stress-strain curves were monotonically increasing. For the unhardened material with yield plateau this optimized curve was job 2 in the 18th iteration.

Figure 5.6(a) displays different jobs in the 18th iteration. As one can see, only one of the curves is applicable (purple colour). Here, necking occurs at the right location and is used as the optimized curve. Still, it is visible that LS-OPT has had problems fitting to the target curve. It has not been able to capture the slight bend at the end of the curve. However, this curve was the optimal obtained from LS-OPT and its MSE (see Table 5.5) was considered good. Previous work has had MSE within the same range [40].

For the optimization without yield plateau LS-OPT had no problems. Fewer iterations were necessary and a better fit in terms of MSE was obtained. Figure 5.7(a) shows the optimized curve acquired. Similarly, the heat treated materials caused no difficulty for LS-OPT. This is most likely due to the lack of abrupt changes in the target curve since no yield plateau was present for these configurations. When allowing the yield stress to flow in the unhardened direction 2 optimization, LS-OPT converges a lot faster towards a solution since it did not have to consider the yield plateau in the same strict manner as when locking the yield stress. For both heat treated materials, and the unhardened material without yield plateau consideration, 10 iterations were enough to make a good fit.

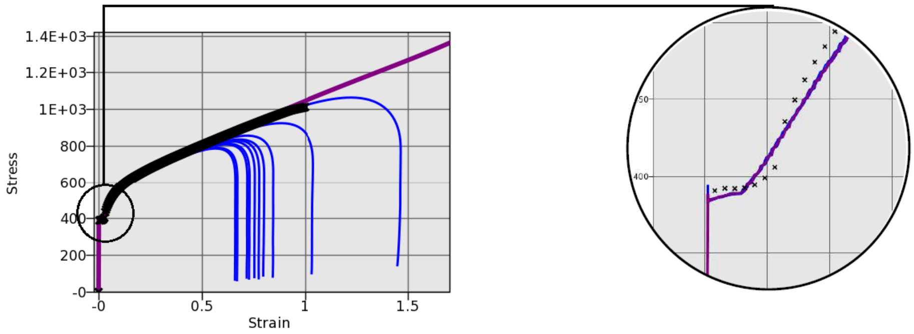

(a) Optimization process for iteration 18.

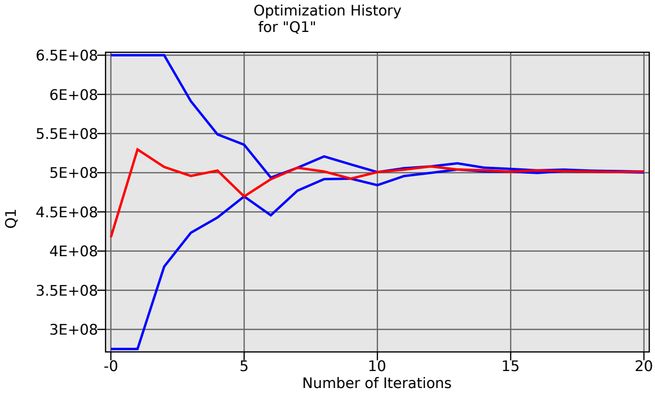

(b) Q1 convergence.

Figure 5.6: Unhardened material with yield plateau: Optimized curve and convergence history for Q_1.

The curves from Figure 5.7 display the convergence history for Q1 and S0, for unhardened direction 2 and hard core. Note that S0 is A in Voce law. For the most part there was little convergence issues for the above parameters. However, one can observe that Q1 has some difficulty for the hard core configuration as it hits the lower bound set by the user. This occurred in the 4th iteration and Q1 remained unchanged in the subsequent iterations. A possible remedy for this would be to increase the bounds, but since LS-OPT gave an overall good estimation (small MSE) this was not pursued. Another observation is that, when optimizing without yield plateau, the Voce parameter, A, hits the lower bound already in the first iteration. But, in the following iterations it finds its place in between the bounds. Of the same reason as described in the former case, an improvement of this was not pursued.

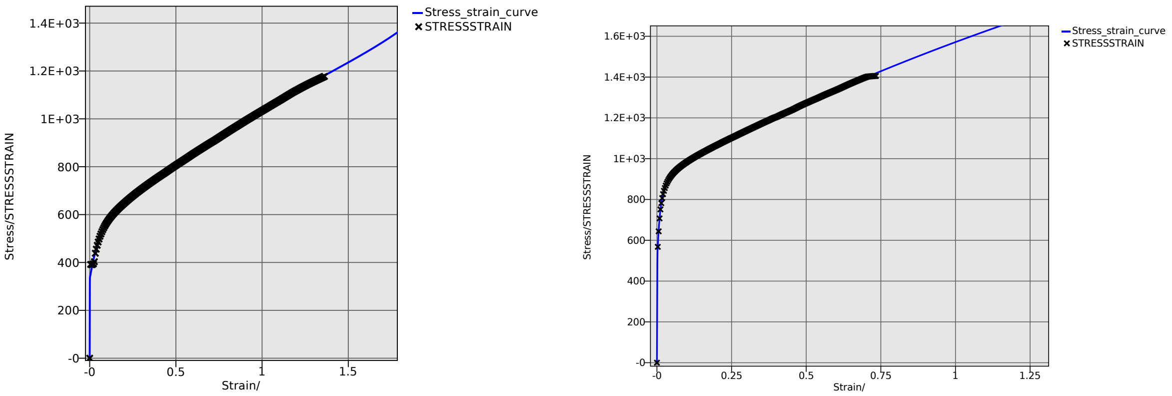

(a) UH2: Optimized curve.

(b) HC: Optimized curve.

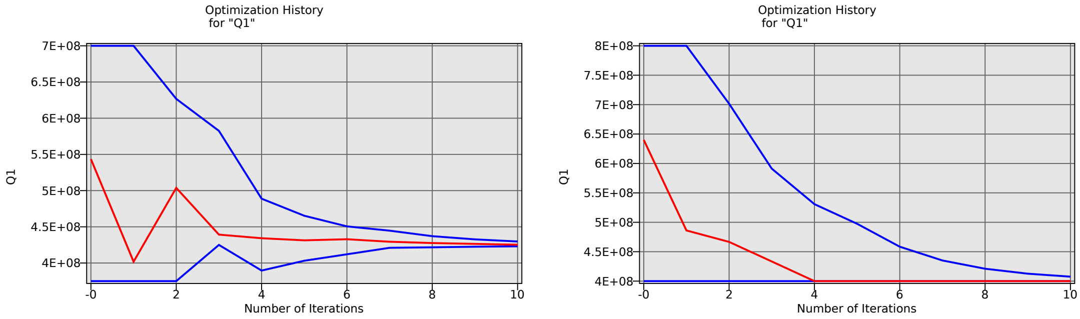

(c) UH2: Q1 convergence.

(d) HC: Q1 convergence.

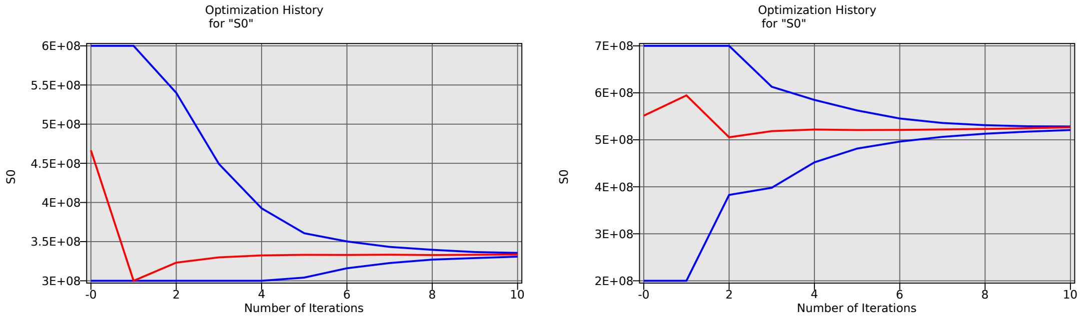

(e) UH2: S0 convergence.

(f) HC: S0 convergence.

Figure 5.7: LS-OPT histories.

Based on the results obtained from LS-OPT, the critical value (W_{cr}) in the CL-criterion was calculated. This was done by considering the innermost element in the necking region (Figure 5.8). The calculated values are presented in Table 5.3. A general observation is that the computed values of W_{cr} are higher than the ones obtained from the experiment. This is as expected since the stress measured in the experiment only is a mean value, while the stress from the innermost element at necking is the location of where one can expect the highest triaxiality, thereby increasing the value of W_{cr} [10].

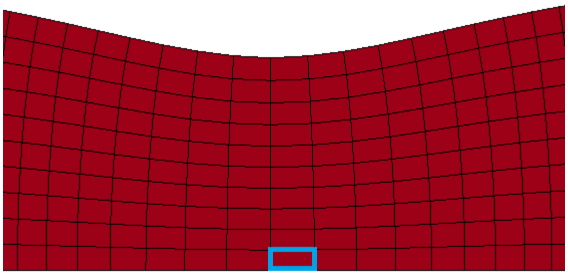

Figure 5.8: Innermost element during necking.

Table 5.3: W$_{cr}$ obtained from LS-OPT compared with experiment.

Configuration	ε_f	W_{cr}[MPa] Experiment	LS-OPT	Difference	Percentage
Unhardened, yield plateau	0.978	791	834	43	+ **5.4 %**
Unhardened, no yield plateau	1.349	1187	1322	135	+ **11.4 %**
Soft core	0.7182	871	956	85	+ **9.8 %**
Hard core	0.719	857	925	68	+ **7.9 %**

Also, due to the aforementioned parameter study on the ballistic effect of yield plateau, W_{cr} was computed for the unhardened material in direction 2 up to plastic failure in direction 1 (Table 5.4).

Table 5.4: W$_{cr}$ obtained from LS-OPT for unhardened material.

Configuration	ε_f	W_{cr}[MPa] Experiment	LS-OPT	Difference	Percentage
Unhardened, yield plateau	0.978	791	834	43	+ **5.4 %**
Unhardened, no yield plateau	0.978	N/A	848	57	+ **7.2 %**

Figure 5.9 displays the optimized curves based on the Voce-parameters obtained from LS-OPT, together with the Bridgman corrected curves. One can see that the curves are rather similar. This is especially the case for the hard core and soft core configuration. Most likely due to the absence of a yield plateau. However, the unhardened case does not

differ significantly from the Bridgman correction. A possible explanation for this is that Bridgman's assumptions when deriving his correction was isotropy, which applies to steel [27]. Due to the similarities and that LS-OPT correctly generates a higher W_{cr}, the data obtained from LS-OPT was used in the numerical analysis.

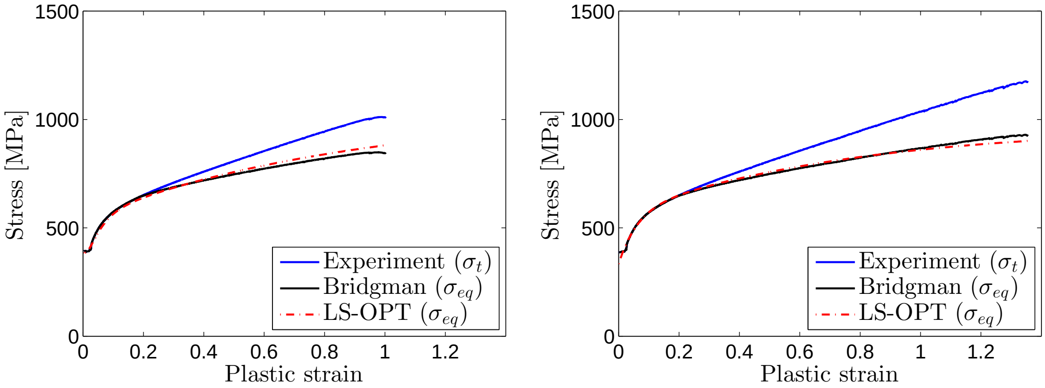

(a) UH1: yield plateau.

(b) UH2: no yield plateau.

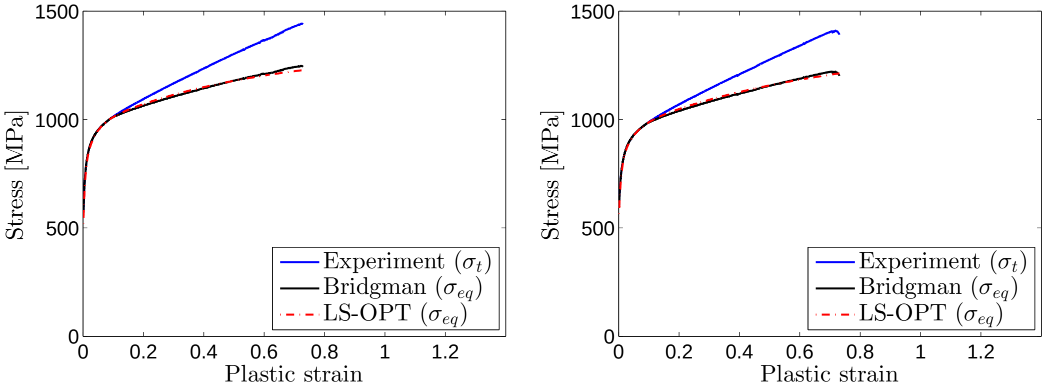

(c) Soft core.

(d) Hard core.

Figure 5.9: σ_{eq} obtained from LS-OPT.

Table 5.5 shows the obtained Voce parameters calibrated in LS-OPT. Here, the MSE is provided from the true stress-strain curves. Also, since the SMM is used as material card, θ_i is provided instead of C_i.

Table 5.5: Obtained Voce parameters from LS-OPT.

	A [MPa]	Q_1 [MPa]	θ_1 [MPa]	Q_2 [MPa]	θ_2 [MPa]	Q_3 [MPa]	θ_3 [MPa]	MSE
Unhardened, Direction 1	391.23	502.61	566.25	301.93	6846.09	-152.50	-9735.95	1.27E-4
Unhardened, Direction 2	333.64	425.29	597.46	255.18	4000.00	-50.00	-254.92	9.87E-6
Soft core	461.29	360.60	689.90	295.72	53200.70	199.68	6406.38	5.39E-7
Hard core	526.71	400.00	607.20	247.28	34247.70	170.72	4325.41	1.68E-6

LS-OPT has numerous algorithms and possibilities with respect to optimization. All of these have not been employed. Further investigation and tweaking in LS-OPT might have given better results than the ones presented above. However, this would have been time consuming and the impact on the numerical analysis of the penetration process would most likely be negligible [40]. Also, difficulties running the above model due to compatibility issues between LS-DYNA and SMM, and usable solvers on Snurre, a significant amount of time had already been spent. Furthermore, another possibility with respect to capturing the yield plateau could have been used by employing a method presented by Kjølseth and Karlsen [47]. But, the results using three term Voce law with SMM as material card in LS-DYNA deemed sufficient.

5.3 Summary of Material Data

Table 5.6 shows a summary of the LS-OPT obtained material parameters that will be used in the numerical study in Chapter 6. Due to the difficulties when modelling a yield plateau in LS-OPT, the Voce parameters from direction 2 will be used for the unhardened material. However, the strain at failure for direction 1 will be applied. This was done because LS-OPT gave the lowest MSE value when not considering a yield plateau, and an overall best fit to the target curve. Additionally, W_{cr} = 848 MPa is in good agreement with the obtained W_{cr} values for the hardened configurations.

Table 5.6: Material parameters that will be used in numerical base model.

	Voce parameters									
	A [MPa]	Q_1 [MPa]	θ_1 [MPa]	Q_2 [MPa]	θ_2 [MPa]	Q_3 [MPa]	θ_3 [MPa]	C	m	W_{cr} [MPa]
UH	333.64	425.29	597.46	255.18	4000.00	-50.00	-254.92	0.0114	0.94	848
SC	461.29	360.60	689.90	295.72	53200.70	199.68	6406.38	0.0114	0.94	956
HC	526.71	400.00	607.20	247.28	34247.70	170.72	4325.41	0.0114	0.94	925

5.4 From Micro Hardness to Yield Stress

The obtained hardness values from Table 3.9 will, together with the measurements from Table 3.7, be used to obtain the varying yield stress over the thickness needed for the numerical analyses. The monolithic values are used because the tension tests were only conducted on monolithic 12 mm plates.

A relationship between the core hardness and the ultimate tensile strength was obtained, and is shown in Table 5.7. From literature [30], this ratio should be approximately 3. Furthermore, this ratio can then be used to obtain a relationship between the hardness and the yield stress.

Table 5.7: Relationship from hardness to yield stress.

	$\sigma_u/HV_{12,c}$	$\sigma_u/\sigma_{0.2}$	$\sigma_{0.2}/HV_{12,c}$
As-received	2.80	1.36	2.06
Soft core	2.78	1.56	1.78
Hard core	2.63	1.44	1.82

where $HV_{12,c}$ is the average core hardness for the different monolithic plates.

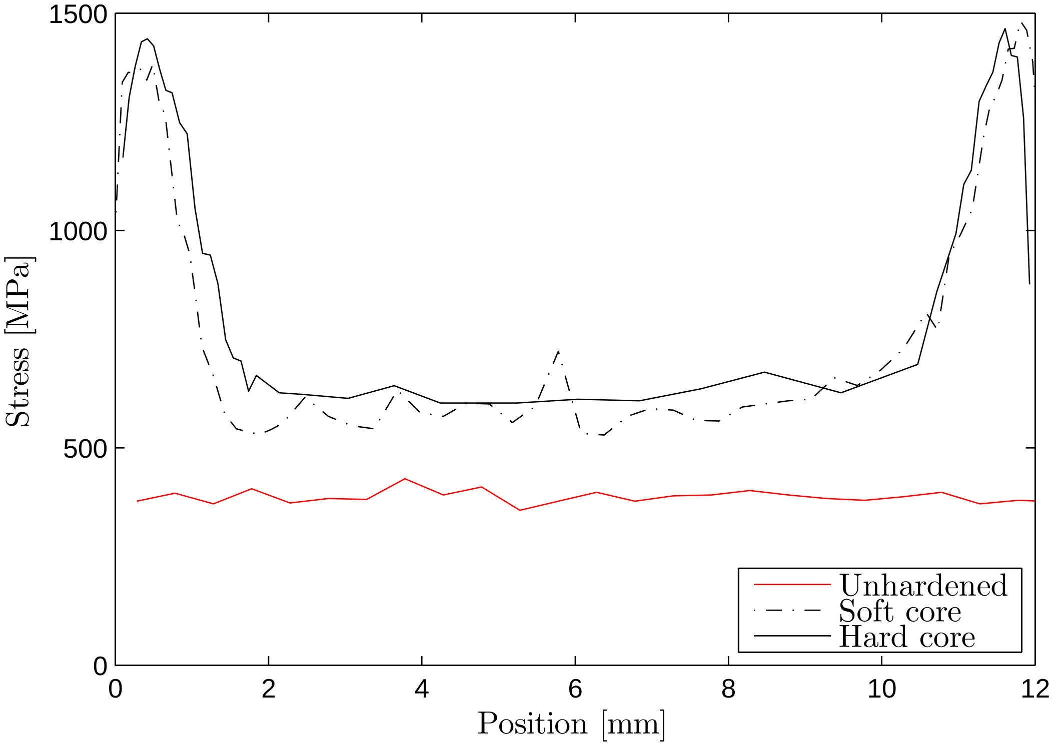

Figure 5.10: $\sigma_{0.2}$ yield stress over the thickness for 12 mm plates.

Figure 5.10 shows how the offset yield stress, $\sigma_{0.2}$ would have varied over the thickness, based on the hardness measurements. However, since the numerical model uses the MJC constitutive relation with a Voce hardening constant A ($\neq \sigma_{0.2}$), a correction must be performed. Hence, the strain hardening will start at wanted value, A.

$$\tilde{A}(z) = HV(z)\left(\frac{\sigma_{0.2}}{HV_{12,c}}\right)\left(\frac{1}{\sigma_{0.2}}\right)A = HV(z)\frac{1}{HV_{12,c}}A = \alpha(z)A$$

where $\alpha(z)$ is the scaling factor (ratio) between the varying hardness, HV(z), and average core hardness, HV$_{12,c}$, while z denotes the thickness variable (Figure 5.11). All scaling factors used in the numerical analyses are presented in Appendix F.

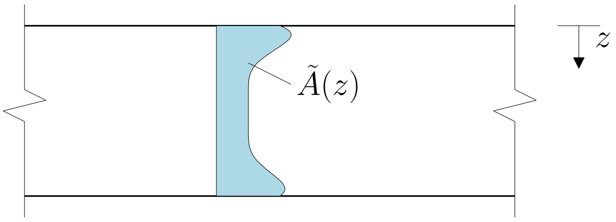

Figure 5.11: Illustration of varying $\tilde{A}$ over plate thickness.

Thus, the MJC constitutive relation (Eq. 2.22) can be extended:

$$\sigma_{eq}(z) = \left[\tilde{A}(z) + \sum_{i=1}^{n} Q_i(1 - e^{-C_i p})\right]\left[1 + \frac{\dot{p}}{\dot{p}_0}\right]^C \left[1 - \left(\frac{T - T_r}{T_m - T_r}\right)^m\right] \tag{5.2}$$

This modified constitutive relation takes the varying yield stress over the thickness into account, and will be used in the numerical analyses. Note that $\mathrm{HV}_{12,c}$ will also be used for the layered plates since no tension tests were performed on these.

Furthermore, we observe a small spread in the ratio, $\sigma_u/HV_{12,c}$, of the different heat treated configurations in Table 5.7. This is because different plates were used for tensile test and hardness measurements. Hardness measurements were performed in Plate 1 while tension tests were conducted on separate plates (Plate 3) for the different configurations. However, Appendix E shows the hardness measurements for Plate 3. If these values were to be used, the relationship would have become

Table 5.8: Relationship from hardness to yield stress for Plate 3.

	$\sigma_u/HV_{12,c}$	$\sigma_u/\sigma_{0.2}$	$\sigma_{0.2}/HV_{12,c}$
As-received	2.80	1.36	2.06
Soft core	2.83	1.56	1.81
Hard core	2.79	1.443	1.93

Table 5.8 shows that the ratio, $\sigma_u/HV_{12,c}$, is almost constant at 2.8. The ratio between $\sigma_{0.2}/HV_{12,c}$, however, shows higher spreads. This can be explained by the offset yield stress from Table 3.7, where the soft core $\sigma_{0.2}$ is lower than hard core $\sigma_{0.2}$.

Furthermore, observations from conversion tables suggest that this relationship decreases proportionally with increased hardness [75]. Since our scaling factors does not take this into account, a possible non conservative yield strength may be used in the numerical analyses. This applies both for the increased hardness in the surfaces, as well for the higher core values in the layered plates. Unfortunately, Table 5.8 was not used in the numerical analyses, because the hardness measurements of Plate 3 did not arrive the authors before mid May.

Chapter 6

Numerical Design

This chapter will establish a numerical base model and investigate how different parameters influence the given impact problem in a sensitivity study. All numerical analyses were executed using IMPETUS Afea Solver on a computer with specifications shown in Table 6.1. The analyses were run using a combination of GPU and CPU, and a representative input file for IMPETUS is given in Appendix F.

Table 6.1: IMPETUS Computer/server configurations.

Component	Description	Quantity
Memory(RAM)	SM Hynix 4 GB DDR3-1866MHz	4
CPU	Intel Xeon E5 quadcore, 3.70 GHz 10 MB cache	1
GPU	Nvidia GPU Tesla Kepler K20C, 5 GB GDDR5 w/2496 cores	2
Motherboard	PNY Quadro NVS 300 512 MB DDR3	1

Most of the sensitivity study will be performed on the unhardened monolithic configuration because this material exhibited a stable hardness profile over the thickness, and a well known failure mode was observed in the experiments (ductile hole growth). However, since the hardened materials experienced fracture and fragmentation, an investigation of the node splitting technique will also be carried out.

All the analyses will be checked for energy balance. When nonlinear dynamic problems are solved by an explicit method, an important task is to perform an energy balance check to detect possible numerical instability [58]. The total energy balance is only approximately constant for an explicit method, however, it should not deviate more than 5% [10]. The energy balance will only be presented for the base model unless some analyses fail this check.

6.1 As-received

6.1.1 Base Model: Establishment

The numerical base model consists of two parts; the monolithic target plate and the projectile. Symmetry of the problem has been employed by only modelling half of the plate and projectile. Furthermore, only a partition of the plate was modelled (80x80 mm^2).

The plate was modelled with the MJC constitutive relation with Voce-law hardening obtained from Chapter 5. A summary of the used calibrated parameters are given in Table 5.6. Only the steel core of the projectile was employed, and modelled as rigid to save computational time. Based on the experimental results, this assumption seems to be valid since the core remained mostly undeformed. The region of the target plate undergoing large deformation (impact region) was modelled using fully integrated 3rd order 64-node hexahedron elements within a 16 mm radius from the impact point. Outside this region, linear elements were applied. The element size was set to 1x1x1 mm^3, i.e. 12 elements over the thickness. Time erosion was set to Δt_{erode}=1E-9, and the default value for deviatoric geometric strain increment, $\Delta \varepsilon_{erode}$ =1E20, was used. A general contact algorithm (penalty) was applied between all parts, and the friction coefficient between all surfaces was set to zero. This is considered conservative. The penalty number was set to -1e15 and was obtained from Holmen and Johnsen [40]. No boundary conditions were introduced, i.e. the plate edges were free. Holmen and Johnsen [40] found that the boundary conditions did not influence the results significantly, and therefore a sensitivity study on this have not been performed.

The base model has been created without a yield plateau, using the LS-OPT obtained value for W_{cr}, see Table 5.6. When the CL-criterion is reached in an integration point the deviatoric stresses in this point are set to zero [60]. However, the integration point is still able to take compressive hydrostatic stresses until the time step size drops below a critical level, i.e. Δt_{erode} (element erosion) [41]. Furthermore, a linear equation of state (EOS) has been applied. Zukas [69] found that nonlinear EOS are of secondary importance when impact velocities are in the range 500 - 2000 m/s. Additionally, when the material's melting temperature (T=1800 K for steel) is reached, the yield strength drops to zero.

A summary of relevant material properties for the base model is given in Table 6.2, while a visualization of the base model and its dimensions can be seen in Figure 6.1.

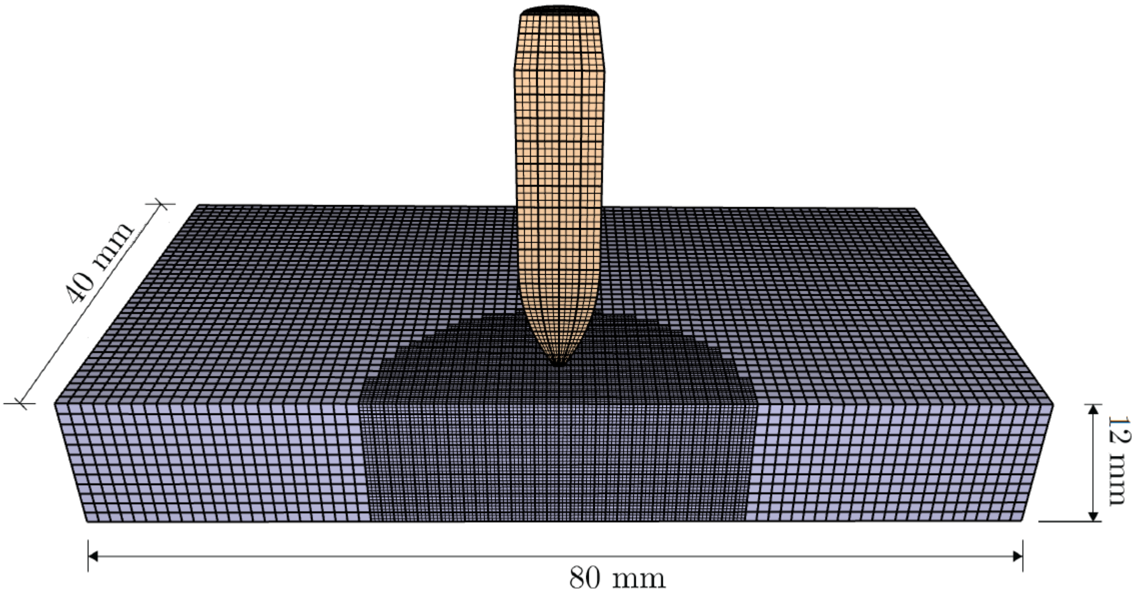

Figure 6.1: Base model of monolithic as-received configuration.

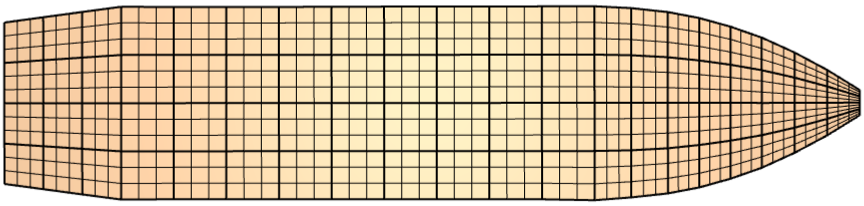

Figure 6.2: Rigid steel core. Mesh provided by Holmen [39].

Table 6.2: Material properties for the base model.

E [MPa]	ν	ρ [kg/m^3]	$\dot{\varepsilon}_0$ [1/s]
212379	0.33	7800[1]	5E-4

In addition, all thermal properties are given in Table 6.3.

Table 6.3: Thermal properties for the base model [12].

α_T [1/K]	C_p [J/KgK]	χ	T_{ref} [K]	T_0 [K]	T_m [K]
1.2E-5	452	0.9	293	293	1800

---

[1] Taken from Kjølseth and Karlsen [47].

6.1.2 Base Model: Results

A Recht-Ipson curve fit has been made for the base model and compared with the experimental result, see Table 6.4. Figure 6.3 shows the obtained ballistic limit curves.

Table 6.4: Recht-Ipson constants for the as-received base model.

	a	p	v_{bl} [m/s]	Deviation
Experiment	1.0	2.21	587.50	-
Base model	1.0	1.93	478.36	-18.6%

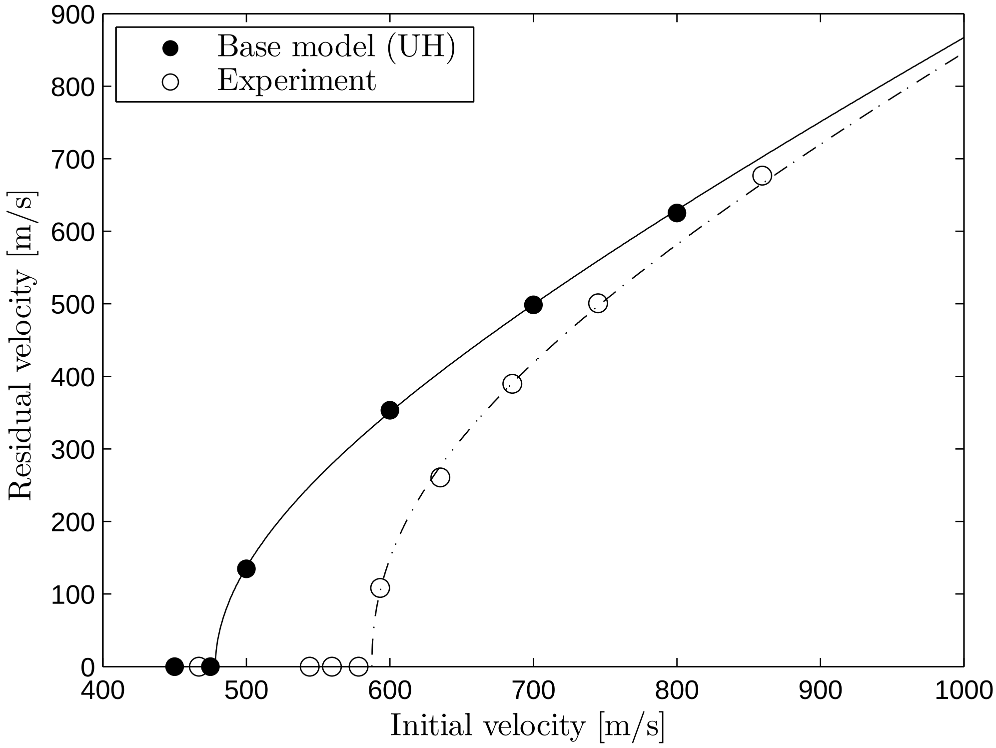

Figure 6.3: Ballistic limit curve for as-received base model.

The base model underestimates the ballistic limit velocity by 18.6%. Thus, the numerical model is conservative with respect to the experimental results.

The total energy balance for v_i=700 m/s is shown in Figure 6.4. A deviation of less than 2% is observed, which is within the criterion of 5%. The two main contributions come from the kinetic energy of the rigid projectile and from the plastic dissipation of the plate. The internal energy and the contact energy can be divided into different parts, see Figure 6.5. Internal elastic energy shows to be very small compared with the internal plastic

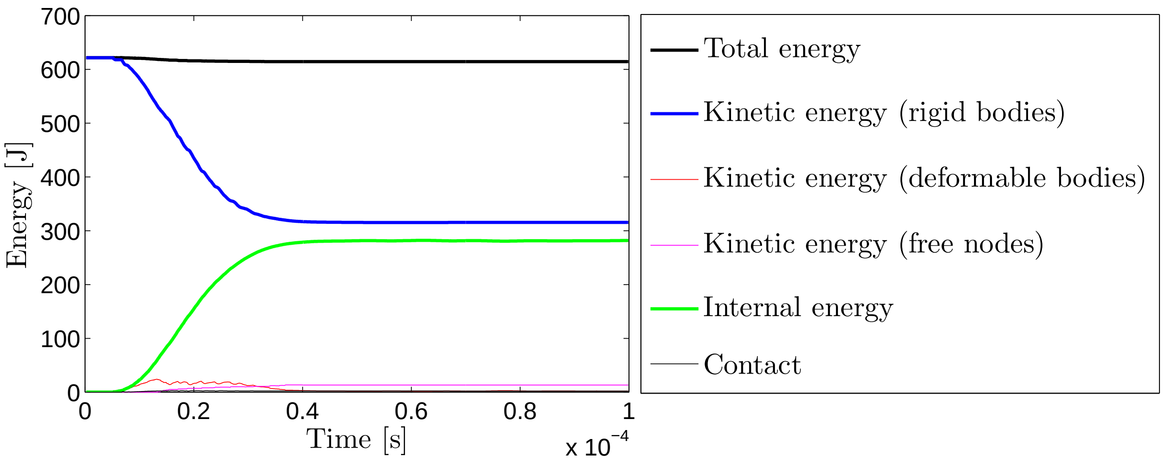

Figure 6.4: Total energy balance for the as-received base model. v_i=700 m/s.

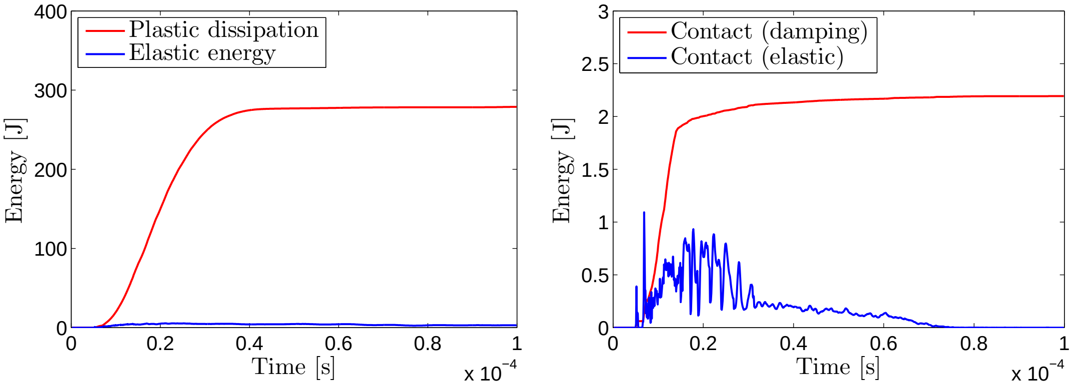

(a) Internal energy.

(b) Contact energy.

Figure 6.5: Internal and contact energy for the as-received base model. v_i=700 m/s.

dissipation. This is in good agreement with the ballistic theory described in Chapter 2. In addition, the contact energy may be neglected in the total energy balance.

Figure 6.6 shows how the damage parameter, D, evolves throughout the analysis for two selected elements. Two elements close to the impact point are chosen. At a certain time, the element 19484 reaches the CL criterion from Eq. 2.23 and fracture occurs, while element 19460 never reaches the criterion.

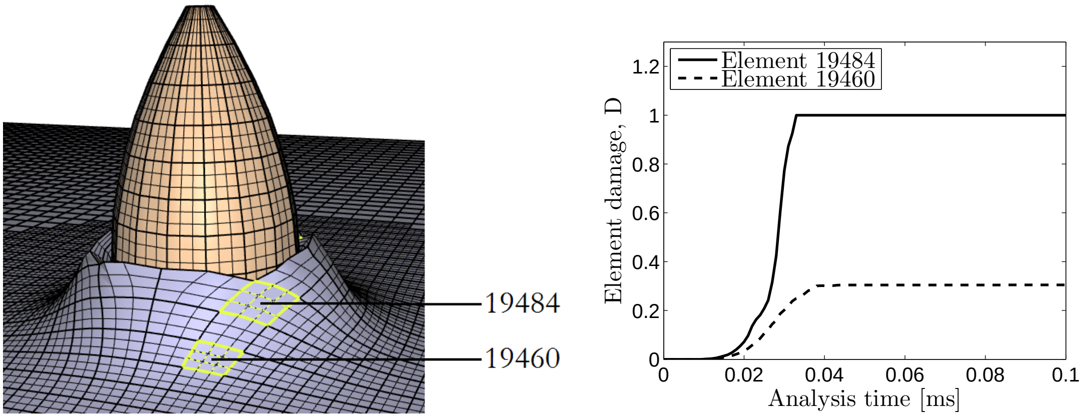

(a) Chosen elements.

(b) Damage evolution.

Figure 6.6: Damage evolution in the as-received base model. $v_i = 700$ m/s.

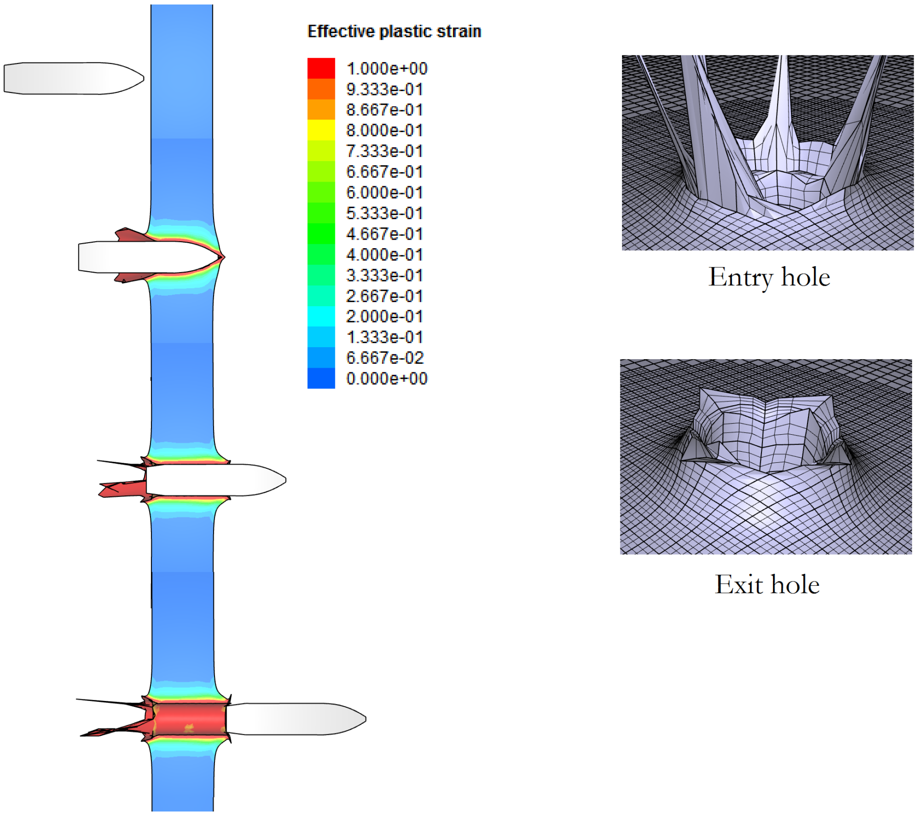

Figure 6.7: Entry and exit holes for as-received base model. $v_i = 700$ m/s.

6.1.3 Sensitivity Study

6.1.3.1 Influence of a Yield Plateau

The tension tests described in Chapter 3 revealed that the unhardened material exhibits a yield plateau in its stress-strain curve. Hence, a parameter study was performed to see the effects of this behaviour. The LS-OPT obtained Voce and W_{cr} values were applied, see Table 5.4. Figure 6.8 displays the obtained ballistic limit curves from IMPETUS. The study showed a relative difference of less than 1% for the ballistic limit velocity (Table 6.5), implying that the yield plateau is of minor importance.

Table 6.5: Sensitivity study: Yield plateau.

	v_{bl} [m/s]	Deviation
Without yield plateau (Base model)	478.36	-
With yield plateau	477.88	-0.1%

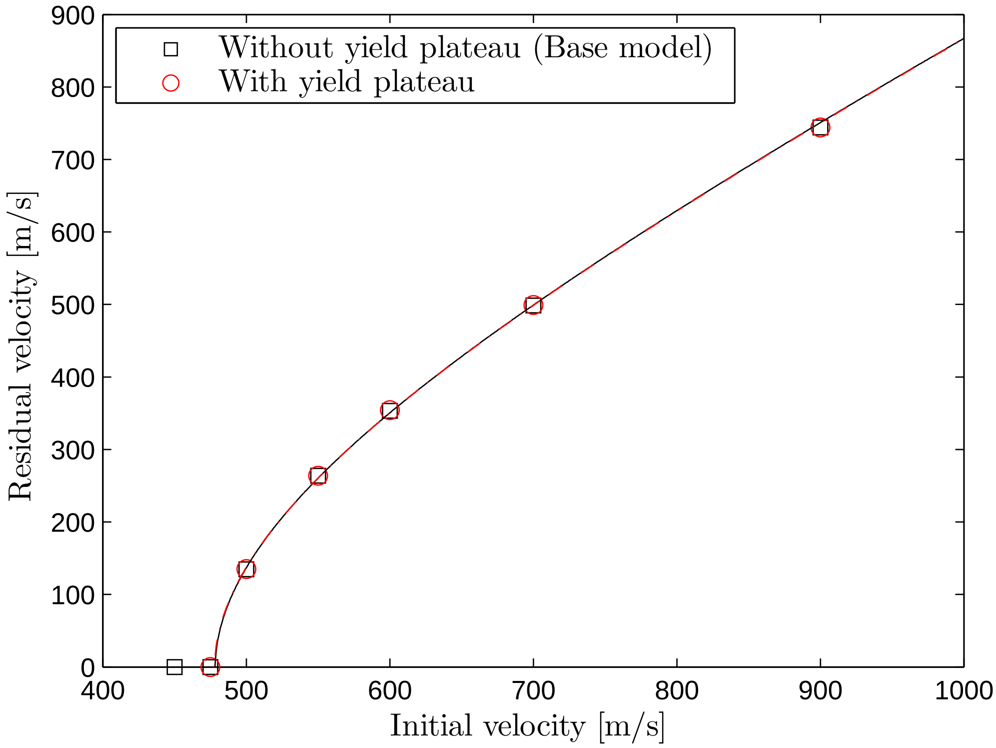

Figure 6.8: Base model of monolithic as-received configuration.

6.1.3.2 Critical Plastic Work Values

Another observation from the tension tests was that direction 1 and 2 differed by approximately 40% in failure strains. Therefore, a study was conducted to see the effects on the ballistic response. Only the LS-OPT obtained values for W_{cr} in direction 2 were used, since direction 1 was calibrated with a yield plateau. Hence, the only difference between the models was the critical value in the CL-criterion. Figure 6.9 shows the obtained ballistic limit curves from IMPETUS, and Table 6.6 shows the obtained ballistic limit velocities.

Table 6.6: Sensitivity study: Critical plastic work.

W_{cr} [MPa]	v_{bl} [m/s]	Deviation
848 (Base model)	478.36	-
1322	483.55	+1.1%

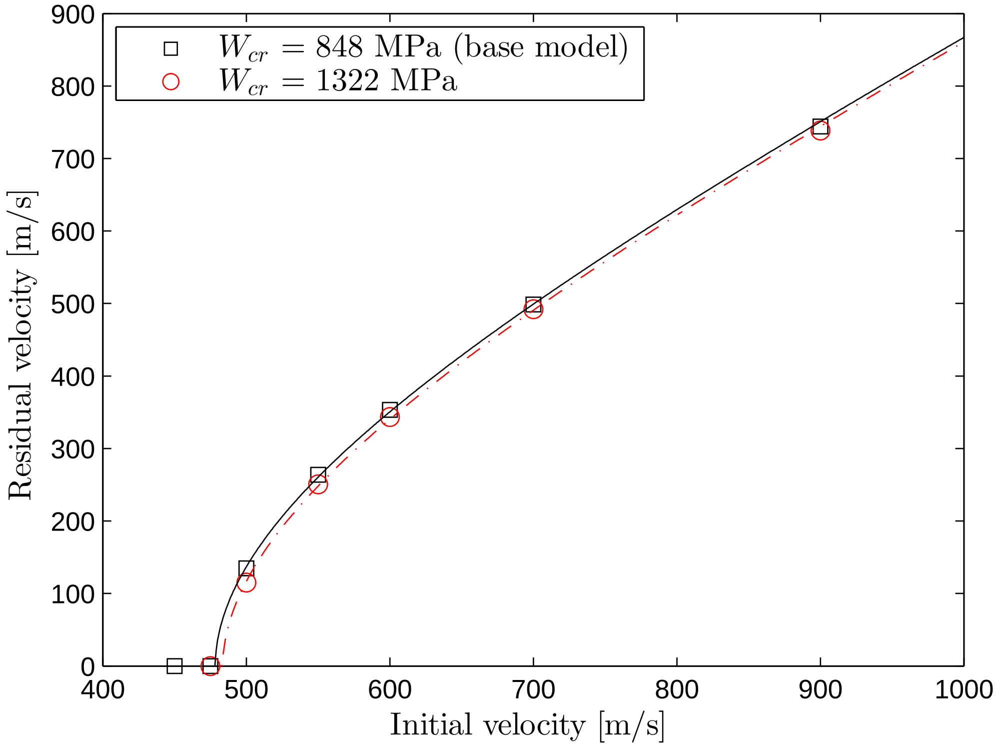

Figure 6.9: Base model of monolithic as-received configuration.

The study showed that the increased value of W_{cr} did not influence the ballistic limit curve significantly. The ballistic limit velocity was only increased by 1.1%.

6.1.3.3 Element Erosion

The base model was established with a time erosion criterion of Δt_{erode} = 1E-9 s. This value was chosen in discussion with Holmen [39]. An investigation of the effects different time erosion values had on the analysis was conducted. Table 6.7 display the various time erosion values and GPU/CPU computational time for an analysis run with initial velocity of v_i=500 m/s and termination time t_{term} = 2E-4 s. Additionally, the obtained ballistic limit velocities are given.

Table 6.7: Sensitivity study: Time erosion.

	Δt_{erode} [s]	GPU/CPU time, v_i=500 m/s [h:min]*	v_{bl} [m/s]	Deviation
Base model	1E-9	[05:28]	478.36	-
Lower limit [0.5x]	5E-10	[17:59]	500.00	+4.5%
Upper limit [2x]	2E-9	[04:15]	474.03	-0.9%
Zero	0	[–:–]**	-	-

*Note that the GPU/CPU times are somewhat affected by the workload on the server. Hence, only general trends of computational time are outlined.
**Analysis caused error. Time erosion criterion must be applied.

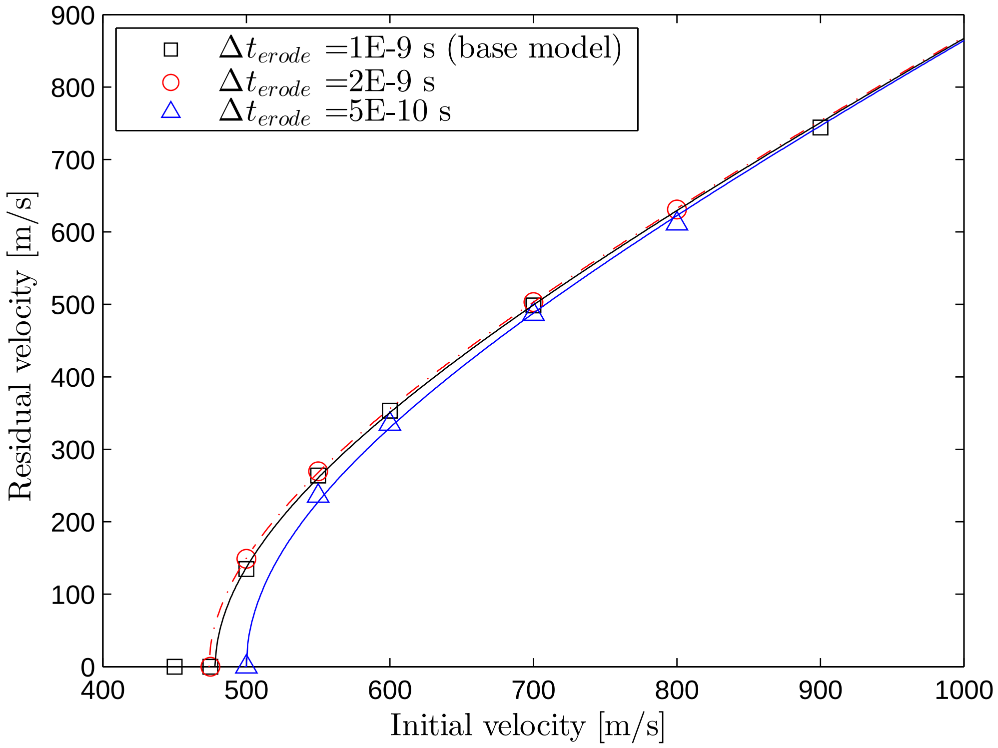

Figure 6.10: Base model of monolithic as-received configuration.

Figure 6.10 shows the ballistic limit curves obtained in the study. The lower limit gives a 4.5% higher ballistic limit velocity than the base model, while the upper limit gave a 0.9% decrease. This is as expected since the time erosion criterion is purely a numerical aid. When reducing the time erosion criterion, elements will remain longer in the analysis, and therefore be able to exercise resistance for a longer period of time. The opposite effect occurs when the critical time step is increased.

Although the lower limit gave a somewhat better result with regards to the experiment, the improvement was deemed insufficient compared to the high computational costs.

6.1.3.4 Modelling the 7.62 mm APM2 Bullet

The base model used only a rigid steel core as the projectile. Since the actual bullet includes brass jacket, sabot, and lead filling, a sensitivity study to see the effects of the initial simplification was done. Material constants for the whole APM2 projectile are given in Table 4.2 in Chapter 4. A MJC constitutive relation with Power law strain hardening and CL-criterion was applied for the different projectile parts. These parameters were obtained from Børvik et al. [18] and are presented in Table 6.8. The mesh for the entire APM2 bullet was provided by Holmen [39] and shown in Figure 6.11.

Table 6.8: MJC parameters for whole APM2 7.62 mm bullet.

Material	A [MPa]	B [MPa]	n	$\dot{\varepsilon}_0$ [1/s]	C	T_r [K]	T_m [K]	m	W_{cr} [MPa]
Steel core	1200	50000	1.0	5E-4	0	293	1800	1.0	N/A
Lead filling	24	300	1.0	5E-4	0.1	293	760	1.0	175
Brass jacket	206	505	0.42	5E-4	0.01	293	1189	1.68	914

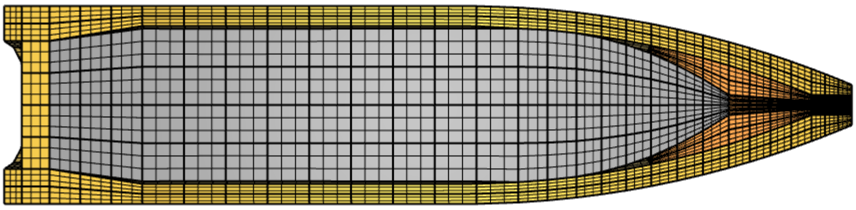

Figure 6.11: The whole APM2 bullet modelled with MJC equation.

Rigid Steel Core vs. Whole Bullet

A comparison between the base model, i.e. only rigid steel core, and a model with the whole bullet was done. However, when modelling the whole projectile, the steel core was still modelled as rigid.

Figure 6.12 shows the whole bullet before and during perforation of the plate. Notice that IMPETUS is able to recreate the peeling of the brass jacket. Furthermore, Figure 6.13 displays a visual comparison between an experimental and a numerical cross section. Although the initial velocities are slightly different, IMPETUS is able to capture the crater caused by the brass jacket giving a similar appearance as the experiment. The residual velocities from the study are presented in Figure 6.14.

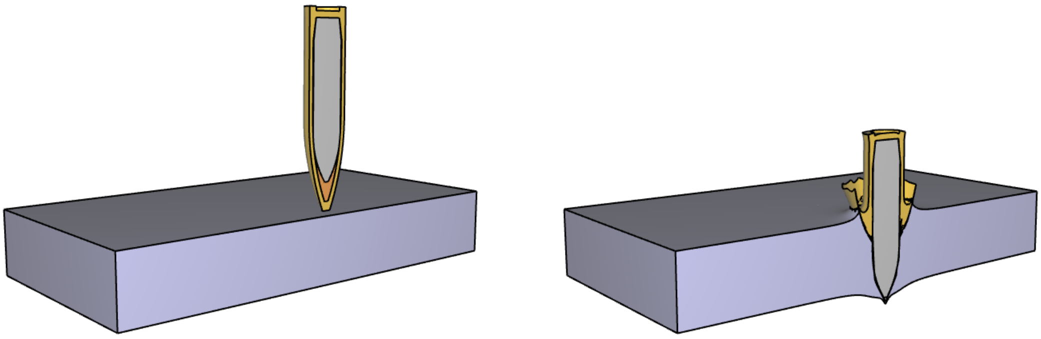

Figure 6.12: The whole APM2 bullet modelled with MJC equation.

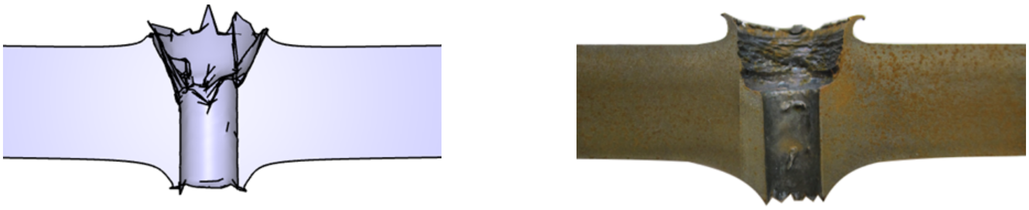

(a) IMPETUS: v_i=700 m/s, v_r=518.08 m/s.

(b) Experiment: v_i=745.10 m/s, v_r=500.60 m/s.

Figure 6.13: Cratering caused by brass jacket.

Rigid steel core vs. MJC steel core

A study on the effects of using only the steel core, but with a MJC constitutive relation, has also been performed. The results are presented in Figure 6.14.

Results

From Figure 6.14 we observe that the difference is not significant between the rigid core and whole bullet. However, the rigid steel core seems to provide overall lower residual velocities. This is as expected since the whole bullet has an increased mass, resulting in more kinetic energy. Børvik et al. [13] also found that the entire bullet had relatively small effect on the perforation process. Additionally, the core with MJC constitutive relation did not alter the results significantly.

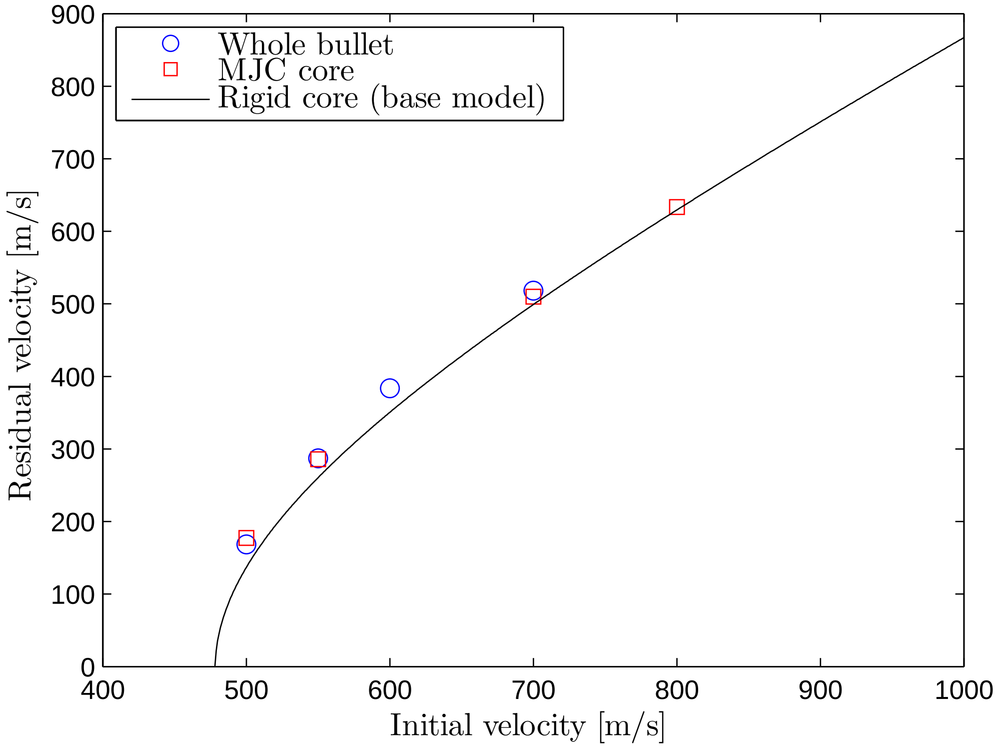

Figure 6.14: Ballistic limit curves for different bullet models.

6.1.3.5 Mesh Study

The base model consisted entirely of solid elements with size 1x1x1 mm^3. This gave a total of 12 elements over the thickness. A study has been performed where the number of cubic elements in the impact region is altered. When changing the mesh size the entire model was scaled accordingly. This was done in order to keep the uniformity of the mesh and better compare it with the base model. Keeping the mesh somewhat uniform has it advantageous as described by Zukas and Scheffler [72]. Abrupt changes in mesh may reflect the stress waves and cause unwanted effects [72]. However, when applying 24 cubic elements over the thickness within the impact region there was not enough resources on the IMPETUS server to run the analysis. Therefore, the impact region was reduced to a radius of 8 mm.

Since the analyses with finer mesh than the base model were computationally expensive, only an initial velocity of $v_i = 700$ m/s was conducted.

Table 6.9: Residual velocities when v_i=700 m/s for different mesh sizes.

Elm. size [mm]	# elm. over thickness	Time [h:min:s]*	v_{bl}** [m/s]	v_r [m/s]	Rel. Diff.
1 (base)	12	[11:38:46]	478.36	498.70	-
0.5	24	[18:22:53]***	493.61	484.00	-3.0%
0.66	18	[18:02:16]	502.46	474.83	-4.8%
2	6	[01:00:19]	556.62	410.87	-17.6%
3	4	[00:20:38]	646.51	254.89	-48.9%
Experiment (fit)	-	-	587.50	418.62	-

*Note that the GPU/CPU times are somewhat affected by the workload on the cluster. Hence, only general trends of computational time are outlined.
**Estimated ballistic limit curves with Recht-Ipson (base model) based on v_r.
***Impact zone with cubic elements has decreased to 8 mm in radius.

From Table 6.9, we see that a coarser mesh causes the residual velocity to decrease compared to the base model, and the estimated ballistic limit velocity to increase. This is as expected since larger elements sizes stiffens the response. However, the same occurs when the mesh is refined. Although, only by approximately 3-5%. Thus, it appears that the finite element analysis has not converged the solution completely. This observation was also found by Holmen and Johnsen [40]. Although the finer mesh gave a somewhat better result with regards to the experiment, the improvement deemed insufficient compared to the high computational costs. Figure 6.15 displays how the residual velocity varies with number of elements over the thickness with an initial velocity of v_i=700 m/s.

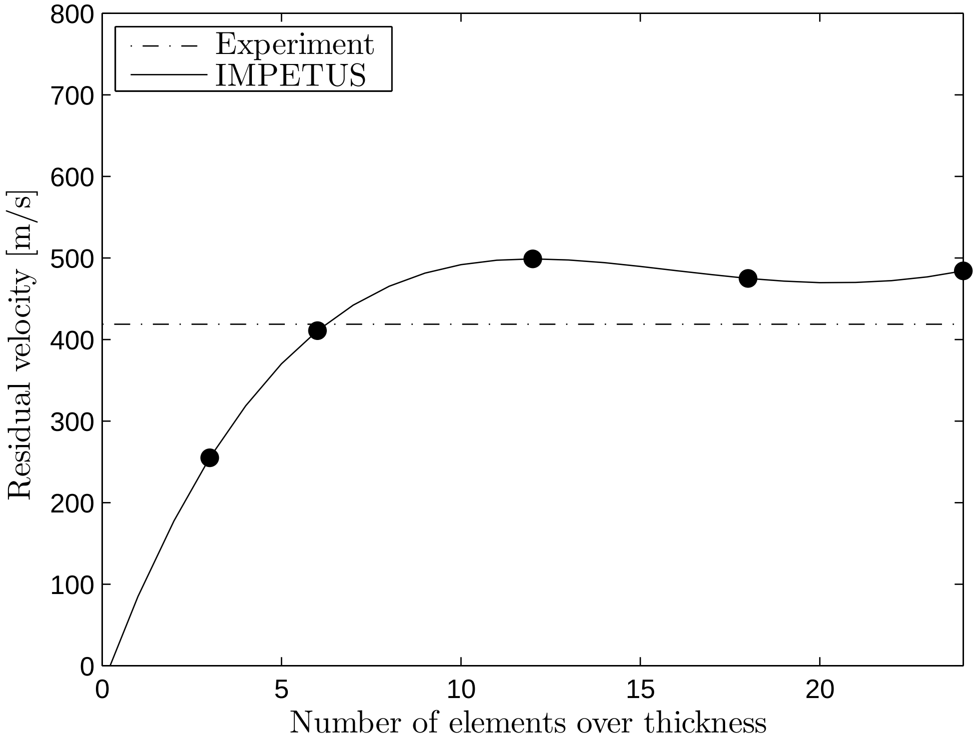

Figure 6.15: Residual velocities for different element sizes over thickness. v_i=700 m/s.

Furthermore, a mesh with 36 linear elements (8 node hexahedron) over the thickness has been studied to compare it with the 12 cubic elements from the base model. Only an initial velocity of v_i=700 m/s was checked. The results can be seen in Table 6.10.

Table 6.10: Cubic vs. linear elements v_i=700 m/s.

Element type	# elm. over thickness	v_{bl}* [m/s]	v_r [m/s]	Rel. Diff.
Cubic (base)	12	478.36	498.70	-
Linear	36	497.92	479.58	-3.8%

*Estimated ballistic limit curves with Recht-Ipson (base model) based on v_r.

The linear analysis provided a better visual impression (Figure 6.16) of the analysis compared with the cubic elements (Figure 6.7). It shows a smoother appearance, and the model better visualise the failure mode as ductile hole growth. This can be explained by the reduced element size. Furthermore, when a larger cubic element erodes, it creates a larger hole than a smaller linear element does. Hence, the residual velocity reduces.

Although the linear elements appear to give somewhat better results, the cubic element will be used in this thesis. The advantage of using the 64-node cubic element is its ability to represent plastic behaviour excellently, according to IMPETUS Afea [61].

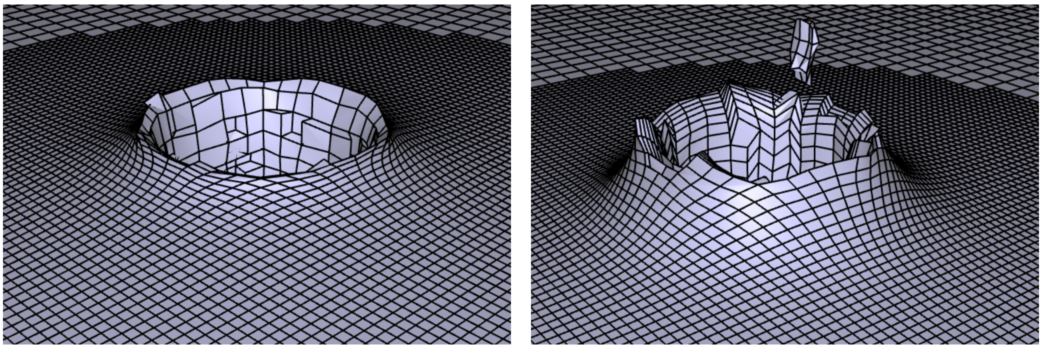

(a) Entry hole. (b) Exit hole.

Figure 6.16: Entry and exit holes for linear elements.

6.1.3.6 Pinhole Model

A short sensitivity study was done where the impact problem was modelled by a pinhole model (PM). The only difference between the base model and the PM was that the PM consisted of a 1/12 ”slice” of the base model (Figure 6.17(a)) and the CL-criterion was not used. Furthermore, at the point of impact there was a small hole, i.e. pinhole, with radius r=0.1 mm. The study was performed because pinhole models has shown to be good for simulating ductile hole growth [10]. Figure 6.17(b) displays the results.

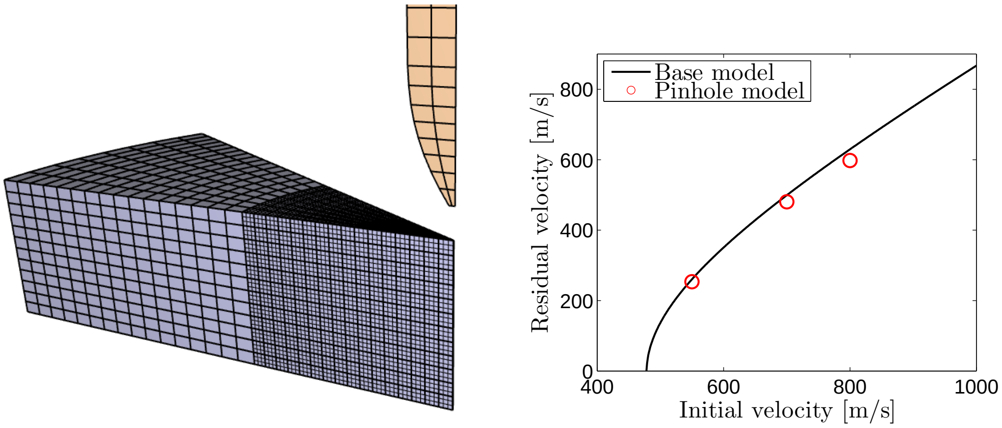

(a) Pinhole model. (b) Pinhole results.

Figure 6.17: Pinhole study.

The PM did not deviate significantly from the base model for the tested initial velocities, see Figure 6.17(b).

6.1.3.7 Strain Rate Hardening

The strain rate hardening constant in MJC was taken from literature. Therefore, a small sensitivity study was conducted to see its effect on the analysis. A value of C=0.005, and C=0.02 was checked against the base model. The results are given in Figure 6.18.

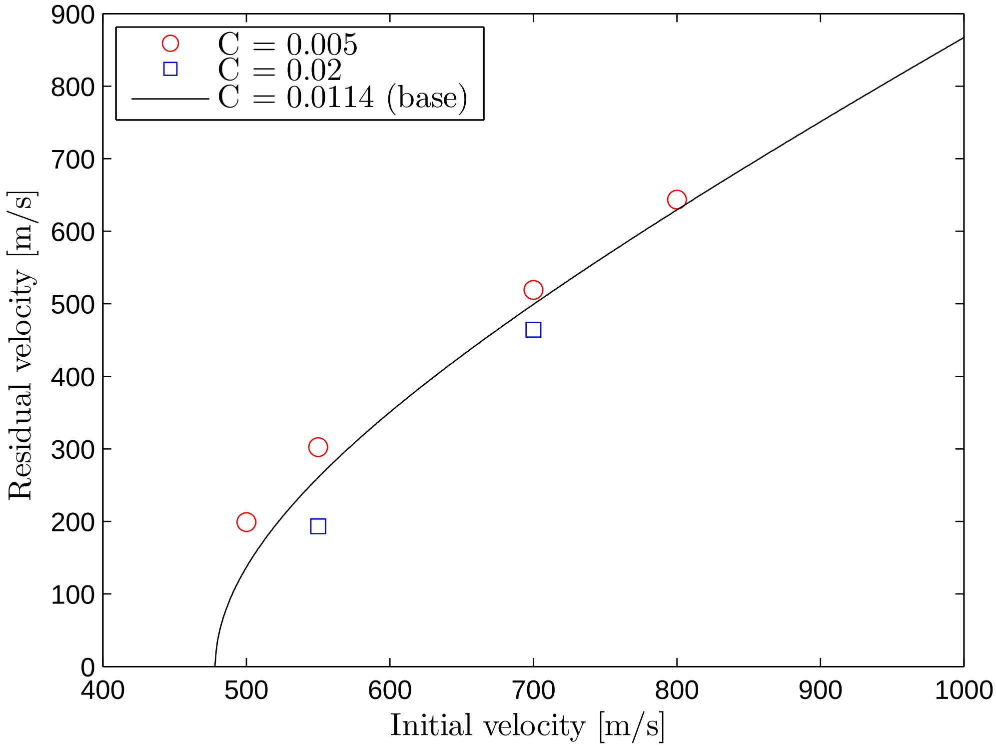

Figure 6.18: Ballistic limit curve for strain rate hardening study.

The MJC constitutive relation states that an increased value of C causes an increased strain rate dependency. Thus, the results from Figure 6.18 are as expected. Using C=0.02 gave a closer value with respect to the experiment, suggesting the material is strain rate sensitive. However, this value is considered too high for the unhardened material and will therefore not be used [10]. Contrary, C=0.005 gave a more conservative solution. However, it is reasonable to assume that a value of C=0.0114 is already conservative since this value was calibrated for Weldox 460 E which has higher yield stress than unhardened NVE36. Also, Børvik et al. [12] observed that the strain rate hardening parameter reduced when increasing the yield strength.

6.2 Soft Core and Hard Core

6.2.1 Base Model: Establishment

Since the soft core and hard core plates showed very similar material behaviour in Chapter 3, only a soft core base model is created in this section. However, the results from this section will be applied to the numerical hard core model in Chapter 7.

Besides the calibrated material constants from Table 5.6, the soft core base model has the same material properties and geometry as the unhardened base model. Additionally, the soft core base model was made with a varying yield stress over the thickness. This varying yield stress was obtained in Section 5.4, and tabulated in IMPETUS using the *CURVE command (see Appendix F). Figure 6.19 shows the varying yield stress over the thickness of the plate. Only the hardness profile from Plate 1 was modelled.

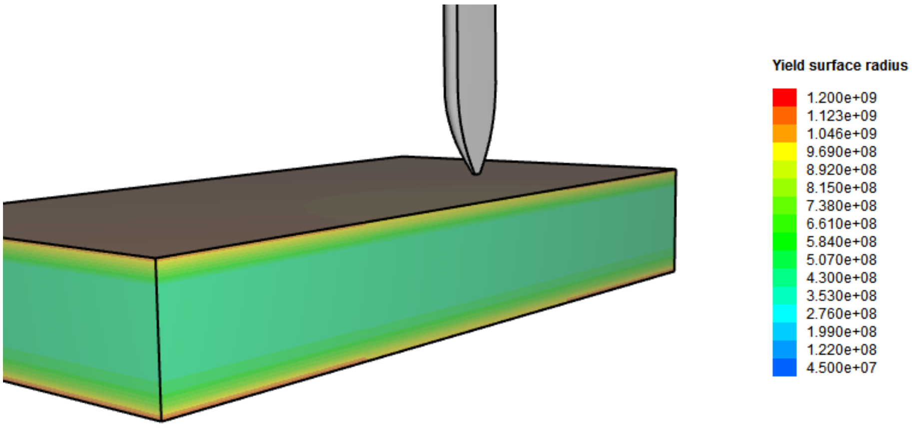

Figure 6.19: Varying yield stress over thickness. Mesh not included for better visuals.

6.2.2 Base Model: Results

A Recht-Ipson curve fit has been made for the base model and compared with the experimental result, see Table 6.11. Figure 6.20 shows the obtained ballistic limit curves.

Table 6.11: Recht-Ipson constants for soft core base model.

	a	p	v_{bl} [m/s]	Deviation
Experiment	1.0	1.88	720.00	-
Base model	1.0	1.96	666.40	-7.4%

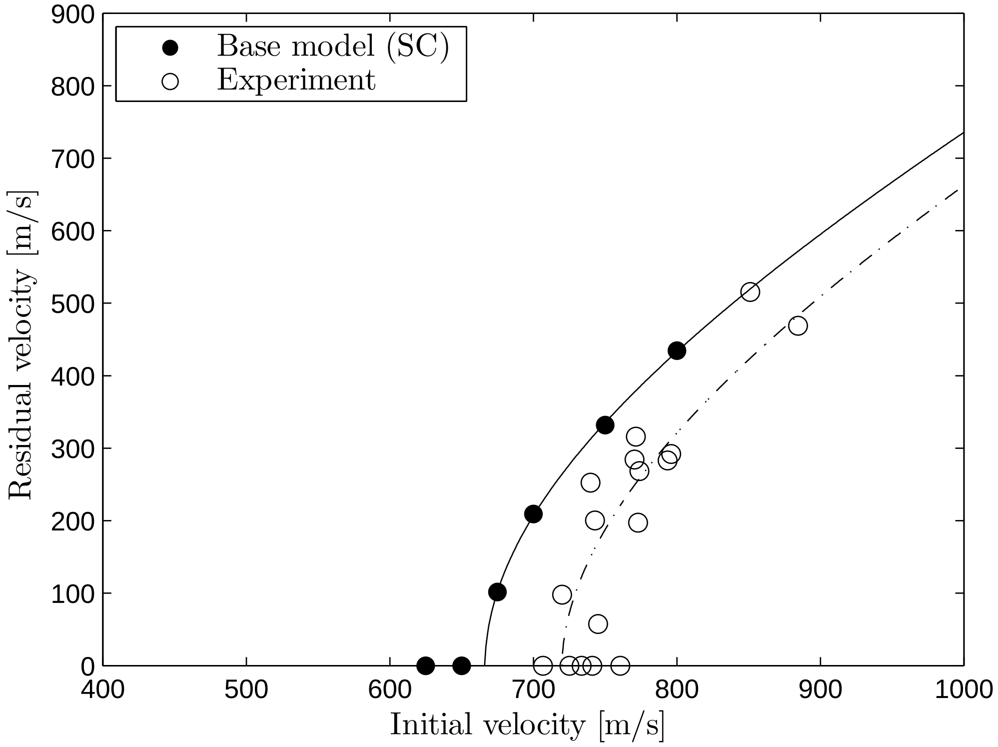

Figure 6.20: Ballistic limit curves for 12 mm soft core plate.

The base model underestimates the ballistic limit velocity by 7.4%. Hence, the numerical model is conservative with respect to the experimental results. Note that the deviation is less than that obtained from the unhardened base model.

NOTE: *Unfortunately, it was discovered that the soft core base model employed a 25% too high yield stress over the thickness because of wrong scaling factor used. More on this in a discussion at the end of this chapter. However, further study in this section will continue to use the overestimated yield stress, due to lack of time. The main trends from the sensitivity study will still apply. In the next chapter (Chapter 7), the correct scaling factors have been used.*

The total energy balance for v_i=700 m/s is shown in Figure 6.21(a). The energy balance satisfies the criterion as described earlier since the deviation in total energy is less than 2%. Furthermore, the figure shows the same energy absorption pattern as the unhardened base model. However, it is apparent that the soft core model absorbs more energy due to higher resistance. Figure 6.21(b) and Figure 6.21(c) shows the contributions to the internal and contact energy, respectively.

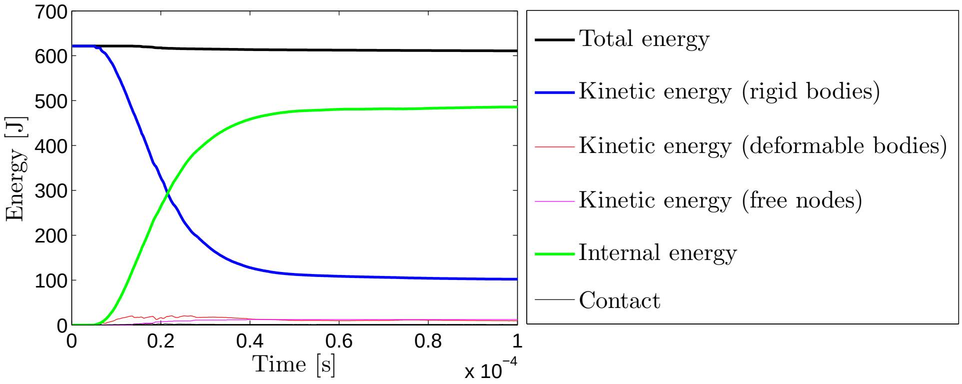

(a) Total energy balance for the soft core base model. v_i=700 m/s.

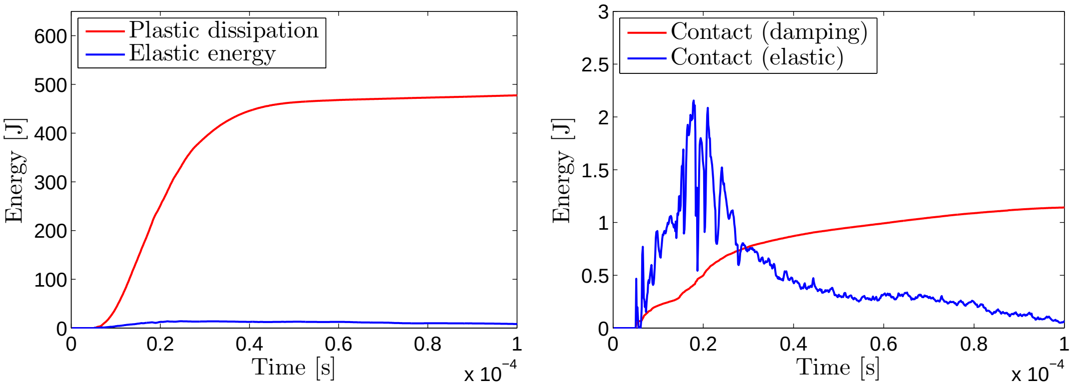

(b) Internal energy.

(c) Contact energy.

Figure 6.21: Energy control. Soft core base model. v_i=700 m/s.

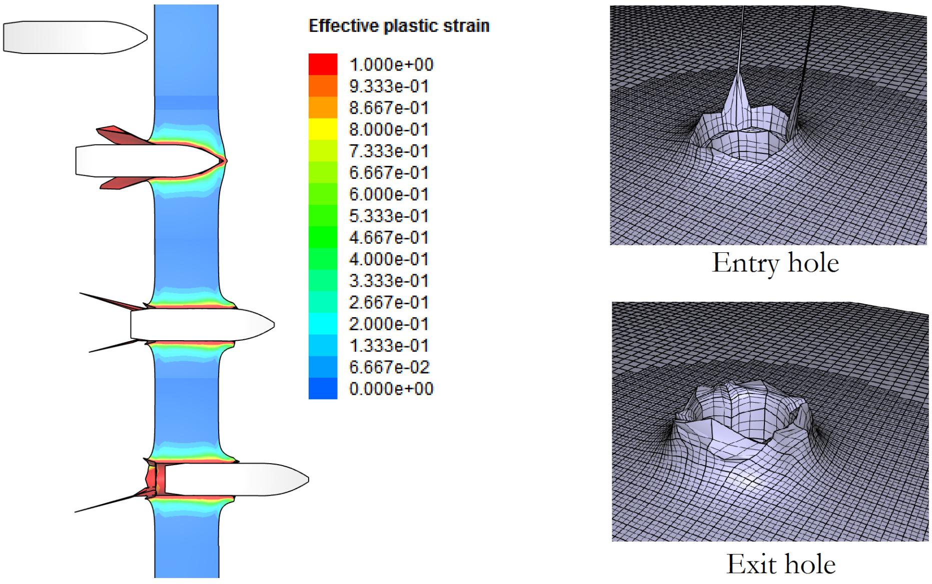

Figure 6.22: Entry and exit holes for soft core base model. v_i = 700 m/s.

6.2.3 Sensitivity Study

6.2.3.1 Node Splitting

The base model did not employ the node splitting technique described in Chapter 2. Therefore, the base model did not display fragmentation or cracking which was observed in the experiments. Instead, it failed by ductile hole growth. Hence, a sensitivity study was conducted to see if node splitting was able to better represent the brittle material response during impact.

Four different energy release rates, G_I, have been studied. Figure 11-18 in Dieter [27] shows a relation between the stress intensity factor, K_I, and the yield strength for brittle materials. Since the soft core material had a surface yield strength of approximately 1400-1500 MPa, this was applied in combination with Eq. 2.32.

Table 6.12: From yield strength to G_I.

σ_0 [MPa] at surface	K_I [MPa/m$^{1/2}$]	G_I [Pa/m]
ca. 1400	80	30135

Extreme values of $G_I = 0$ and $G_I = W_{cr}$ were also studied[2]. In addition, since the core is ductile, a varying G_I was also modelled. This model consisted of $G_I = 30135$ Pa/m on the brittle surfaces (1 mm depth) and G_I=0 in the ductile core.

Figure 6.23 shows time-lapses of simulations where different G_I values are investigated. Setting G_I=0 means that crack propagation is entirely driven by W_{cr} and the scaling function, f, described in Chapter 2, is not used [60]. This gives a good visual representation of the failure mode observed in experiments. Fragmentation and cracking on the surface occur and the core seems ductile.

When G_I varies over the thickness, the analysis was able to obtain a ductile core combined with a more brittle surface. Delamination and cracking occur at the surface while the fracture pattern in the core is limited due to ductility. However, when applying G_I=30135 Pa/m, over the entire thickness, the material response appears to be too brittle, as expected. Large pieces delaminate at the surface and an increased crack propagation in the core compared to the other G_I values was observed. Hence, brittleness in IMPETUS seems to be driven by the strain energy release rate.

Applying node splitting seems to better capture the fracture pattern observed in the ballistic experiments compared to the base model. Hence, the node splitting technique will be employed.

---

[2] G_I and W_{cr} units are not the same, but the value of W_{cr} is adopted

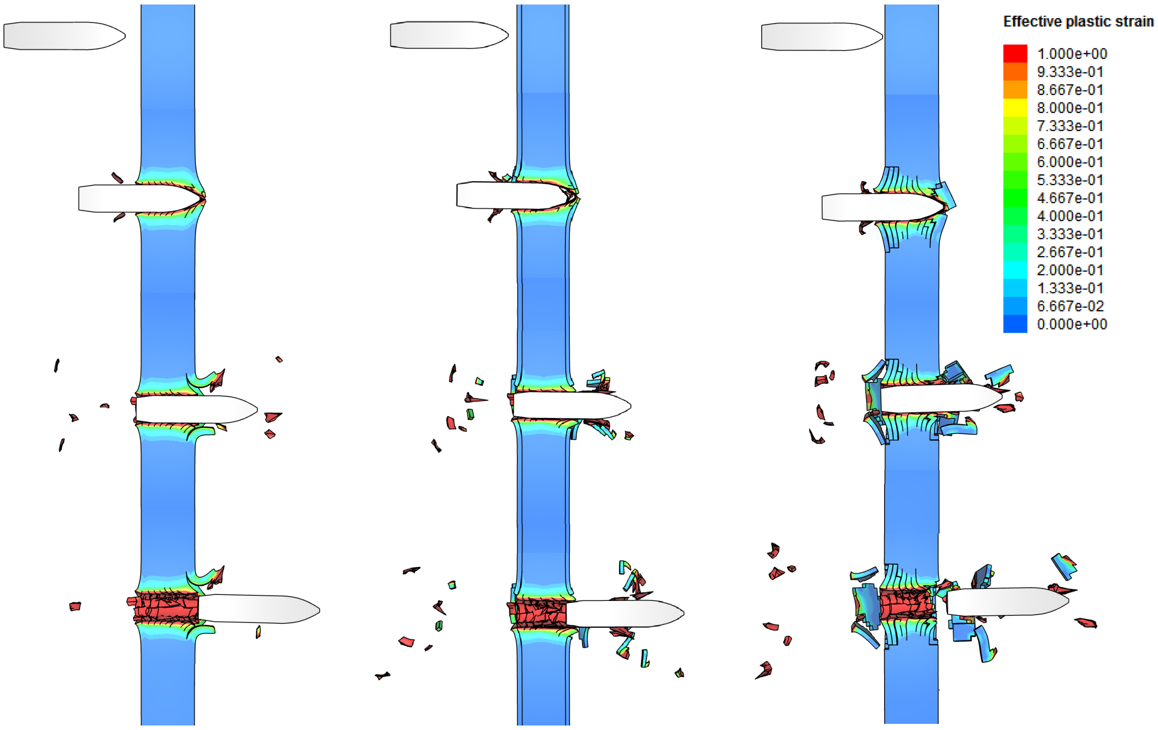

(a) $G_I = 0$ Pa/m. (b) Varying G_I. (c) $G_I = 30135$ Pa/m.

Figure 6.23: Different strain energy release rates. $v_i = 750$ m/s.

The residual velocities obtained from the different G_I values are shown in Table 6.13. The initial velocity was set to $v_i = 750$ m/s.

Table 6.13: Residual velocities when v_i=750 m/s for different strain energy release rates.

	Base model	$G_I = 0$ Pa/m	$G_I = 30135$ Pa/m	Varying G_I	$G_I = 956E6$ Pa/m
v_r [m/s]	331.74	313.30	417.40	337.81	319.58
v_{bl}* [m/s]	666.40	677.24	617.03	664.98	674.20

*Estimated ballistic limit curves with Recht-Ipson (base model) based on v_r.

Except from the brittle G_I value, the residual velocities did not deviate significantly from the base model. The same applies for the estimated ballistic limit velocities. Even though the varying G_I produced a better visualization, it predicted a similar ballistic limit velocity when comparing with $G_I = 0$.

Furthermore, the ballistic limit curves for G_I=0 and $G_I = W_{cr}$ are plotted in Figure 6.24. The difference is small, and the curves almost coincide.

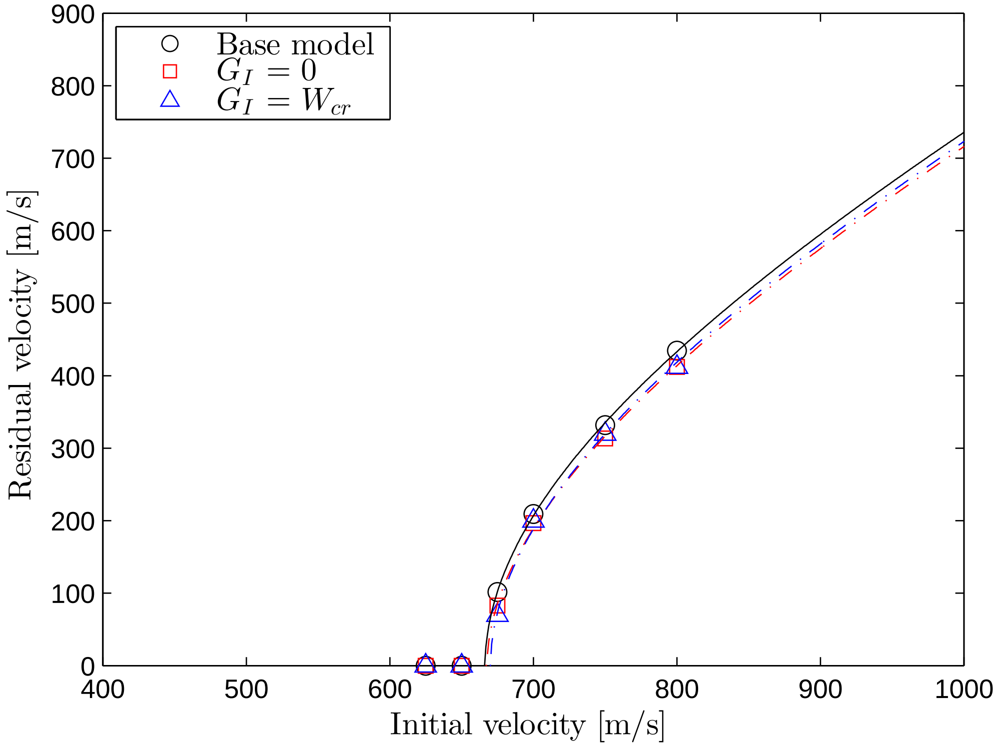

Figure 6.24: Ballistic limit curves for different values of G$_I$.

Figure 6.25 shows the entry and exit holes from the analysis for G$_I$=0, with an initial velocity of v_i=700 m/s.

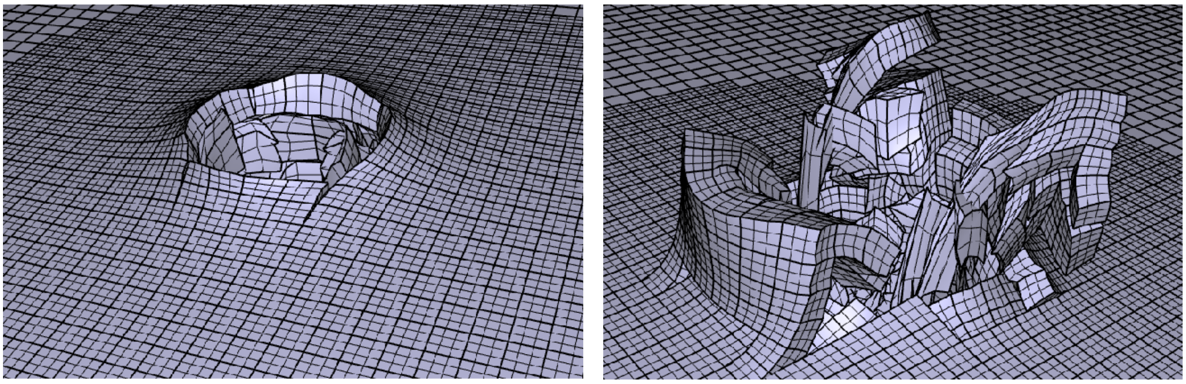

(a) Entry hole.

(b) Exit hole.

Figure 6.25: Entry and exit holes for G$_I = 0$, $v_i = 700$ m/s.

Note that node splitting is dependent on the mesh size. The size of the fragment is bounded from below by the smallest element size in the model. A combination of smaller mesh size and node splitting could have produced a better fragmentation pattern, but was not investigated in this thesis.

Since the authors knowledge on the node splitting technique in IMPETUS is limited, G_I = 0 Pa/m was chosen. This is also the default value in IMPETUS when applying node splitting.

6.2.3.2 Strain Rate Hardening

Since the soft core material exhibited a higher strength than the unhardened material, a different strain rate constant was investigated. A value of C=0.001 was taken from the Domex Protect 500 steel in Børvik et al. [12] for comparison. Note that the Domex Protect 500 has a yield strength of 1592 MPa. In addition, a value of C=0.01 was checked.

The results are given in Table 6.14 and plotted in Figure 6.26.

Table 6.14: Residual velocities [m/s] for different strain rate hardening.

v_i [m/s]	C=0.0114 (base model)	C=0.01	C = 0.001
800	434.48	440.90	501.50
700	209.23	227.37	324.47
675	101.52	123.91	267.58

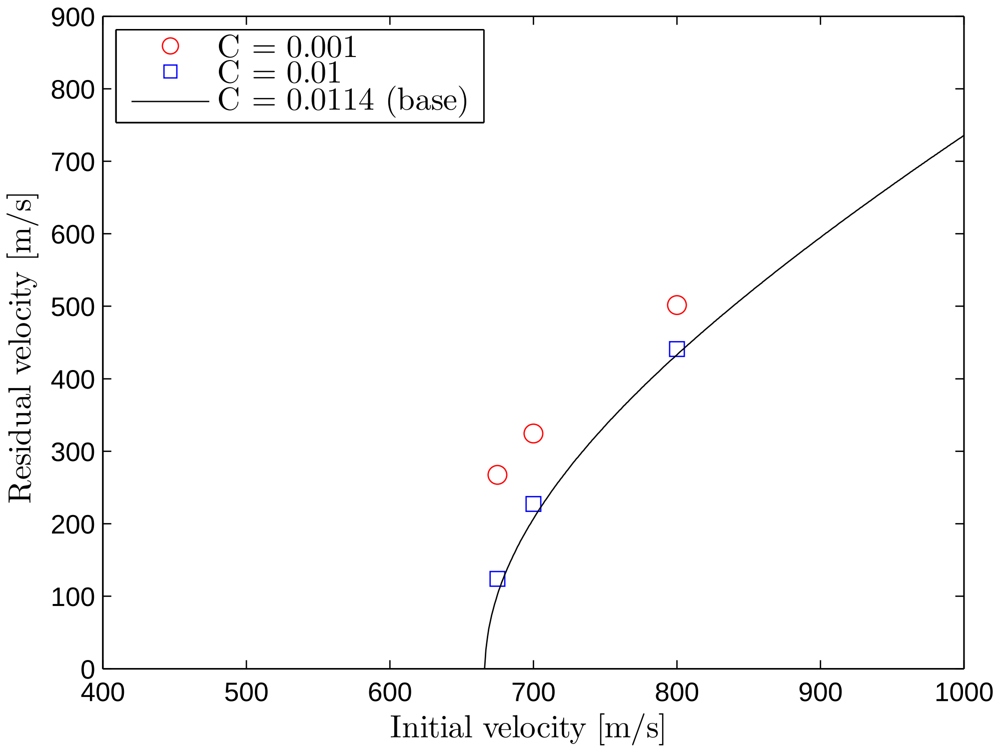

Figure 6.26: Ballistic limit curves for different values of C.

Table 6.14 and Figure 6.26 shows that a smaller strain rate hardening gives a lower ballistic resistance. However, a strain rate hardening of C=0.001 is very conservative for our soft core material which has a yield strength of approximately 600 MPa (much less than 1592 MPa). Yet, since soft core is in fact stronger than the unhardened material, a value of C=0.01 will be used instead of C=0.0114. This value is 12.3% lower than the base model.

6.3 Discussion and Remarks

This chapter established numerical base models for both the unhardened (as-received) material and the soft core material. A sensitivity study was done on both base models. However, the bulk of the sensitivity study was performed on the unhardened material due to a well known failure mode. Also, more reliable material properties were obtained due to constant hardness over the thickness. A short summary follows

- Both base models produced a conservative result compared to the experiment. The ballistic limit velocity decreased by 18.6% and 7.4% for the unhardened and the soft core base model, respectively.
- The soft core base model gave a less conservative ballistic limit velocity than the unhardened base model. The reasons are
    1. It is often seen that a numerical model becomes more ductile than the experiment for high strength steel [10].
    2. Unfortunately, wrong scaling factor was used when obtaining the varying yield stress over thickness. The Voce parameter, $A = 461.29$ MPa, was accidentally interchanged with the offset yield stress of $\sigma_{0,2} = 585$ MPa. Hence, an overestimation of the equivalent stress by approximately 25% was made. Consequently, the soft core base model gave a higher ballistic resistance. In Chapter 7, this has been taken into account and the correct scaling values are used.

A numerical model which implements the parameters chosen from the sensitivity study will be investigated and compared with the experiments in the next chapter.

Chapter 7

Numerical Results

The best suited parameters, chosen from the sensitivity study in Chapter 6, have been implemented to create numerical models for all target configurations. The soft core and hard core models use the same strain rate hardening and strain energy release rate. Results from the numerical analyses will be compared with the ballistic experiments.

Note that the material investigation in Section 3.6 showed that the soft core plates were hardened too much. This caused the soft core and hard core plates to exhibit almost the same core hardness. This indicates that the soft core and hard core results will be similar.

A summary of the different input parameters chosen from the sensitivity study is shown below. These are valid for all layering configurations.

Table 7.1: Numerical model input.

	C	m	Δt_{erode}	Elm. size	Elm. type*	GI [Pa/m]	Bullet	W_{cr} [MPa]	PM?***
UH	0.0114	0.94	1E-9	1 mm	Cubic	Not used	RSC**	848	No
SC	0.01	0.94	1E-9	1 mm	Cubic	0	RSC**	956	No
HC	0.01	0.94	1E-9	1 mm	Cubic	0	RSC**	925	No

*In impact region. Linear used outside

** RSC: Rigid Steel Core

*** PM: Pinhole Model

7.1 Establishing Layered Numerical Models

The list below shows additional information on how the layered configurations were established.

- All the applied scaling factors, α, were derived for the monolithic configuration[1]. Since the laminated plates showed an overall higher hardness than the monolithic, the predicted yield strength will be also be higher.
- The distance between plates was set to 0.1 mm to avoid potential numerical problems.
- 6 and 4 elements over thickness in each plate for the 2x6 and 3x4 configuration, respectively.
- Triple layered model used ONLY the hardness profile for Plate 1 (front plate), since the hardness measurements were similar for each plate, see Section 3.6.3. Due to already present uncertainties regarding the scaling factors, a more detailed model was not pursued. Also, this simplified the IMPETUS input file.

Figure 7.1 shows the appearance of the layered soft core configurations. Notice how the yield strength varies over the thickness. Especially, note that the backplate of the double layered configuration has lower strength reflecting the properties observed from the hardness tests in Section 3.6

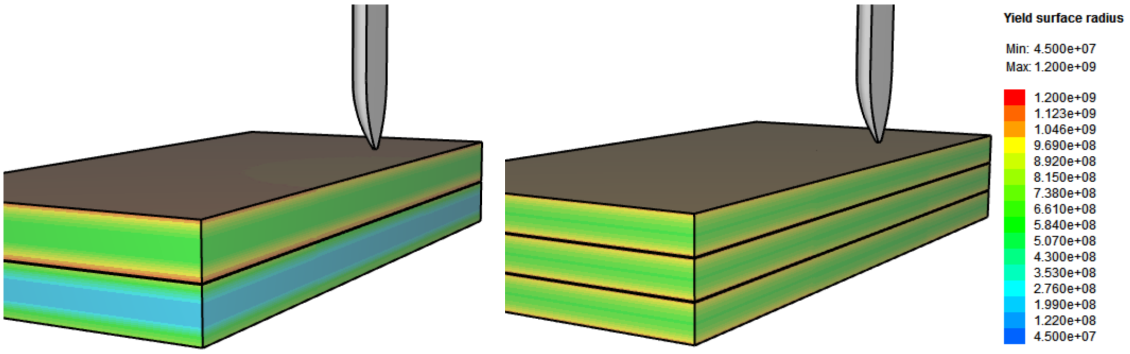

(a) Double layered.

(b) Triple layered.

Figure 7.1: Layered soft core configurations.

---

[1] Can not be emphasized enough.

7.2 12 mm Plates

The ballistic limit curves from the numerical analyses and the experiments are shown in Figure 7.2.

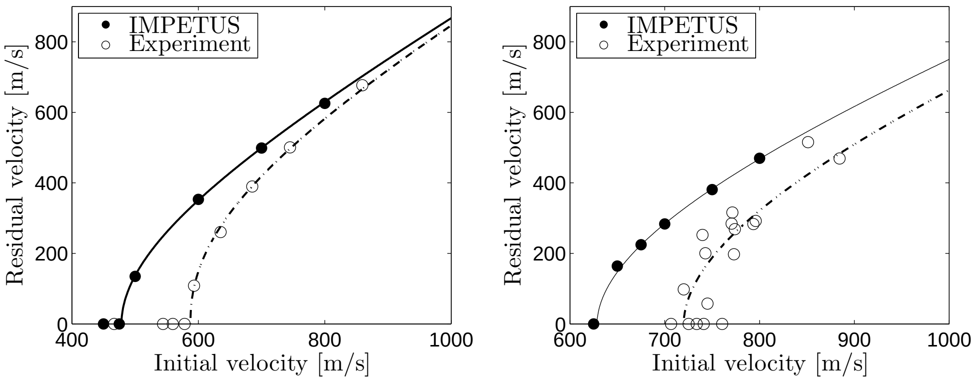

(a) As-received. (b) Soft core.

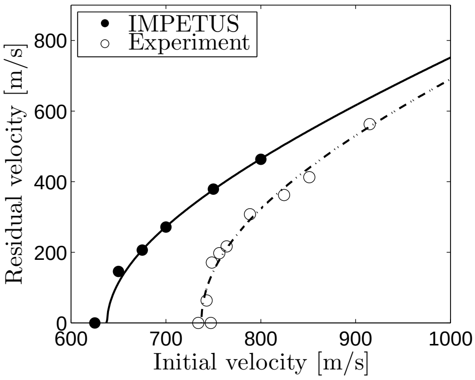

(c) Hard core.

Figure 7.2: The ballistic limit curves for 12 mm plates.

The numerical results are conservative compared to the experimental results for all hardening configurations. The Recht-Ipson parameters are given in Table 7.2, including the difference in ballistic limit velocities between the analyses and the experiments.

Table 7.2: Monolithic: Numerical analysis vs. experiment.

	Numerical model			Experiment				
Heat treatment	a	p	v_{bl} [m/s]	a	p	v_{bl} [m/s]	Diff. [m/s]	Rel. diff.
As-received	1.0	1.93	478.36	1.0	2.21	587.50	109.14	-18.6%
Soft core	1.0	1.88	628.56	1.0	1.88	720.00	91.44	-12.7%
Hard core	1.0	1.92	637.92	1.0	2.06	737.40	99.48	-13.5%

The relative difference between the analysis and the experiment is in the range 12-14% for the surface hardened plates, and 18.6% for the unhardened plate. However, the absolute difference between all the analyses and the experiments are approximately the same.

Figure 7.3 compares the different hardening configurations against each other.

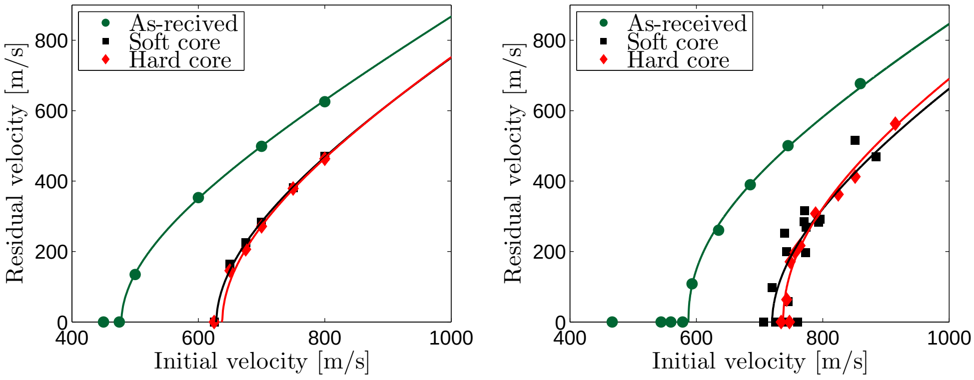

(a) Numerical analysis.

(b) Experiment.

Figure 7.3: The ballistic limit curves for 12 mm plates.

IMPETUS is able to capture the main trends observed in the experiments. Namely, that hardening has a positive effect on the ballistic resistance. Additionally, IMPETUS predicts almost the same ballistic limit curves for the soft core and hard core plates. This is in agreement with the ballistic experiments, and reflects the similar hardness profiles obtained earlier.

The numerical analyses give a somewhat larger relative difference between the different hardening configurations compared to the experiments. This is presented in Table 7.3. However, the absolute difference does not differ significantly.

Table 7.3: Monolithic: Effect of surface hardening.

	Numerical model			Experiment		
Heat treatment	v_{bl} [m/s]	Diff. [m/s]	Rel. diff.	v_{bl} [m/s]	Diff. [m/s]	Rel. diff.
As-received	478.36	-	-	587.50	-	
Soft core	628.56	150.2	+31.4%	720.0	132.5	+22.6%
Hard core	637.92	159.56	+33.4%	737.40	149.9	+25.5%

Time-lapse of different analyses are shown in Figure 7.4.

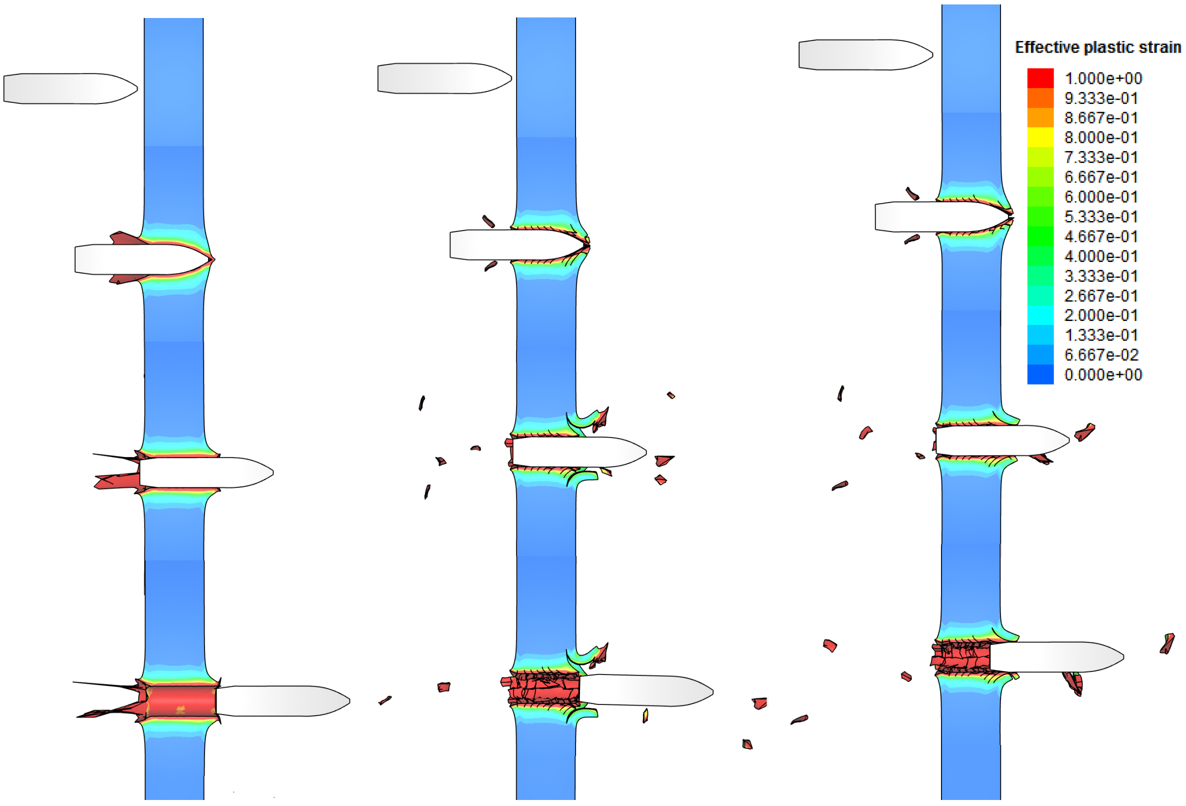

(a) UH, v_r=498.70 m/s. (b) SC, v_r=283.49 m/s. (c) HC, v_r=271.56 m/s.

Figure 7.4: IMPETUS analyses for different 12 mm plates with $v_i = 700$ m/s.

7.3 2x6 mm Plates

The ballistic limit curves from the numerical analyses and the experiments are shown in Figure 7.5.

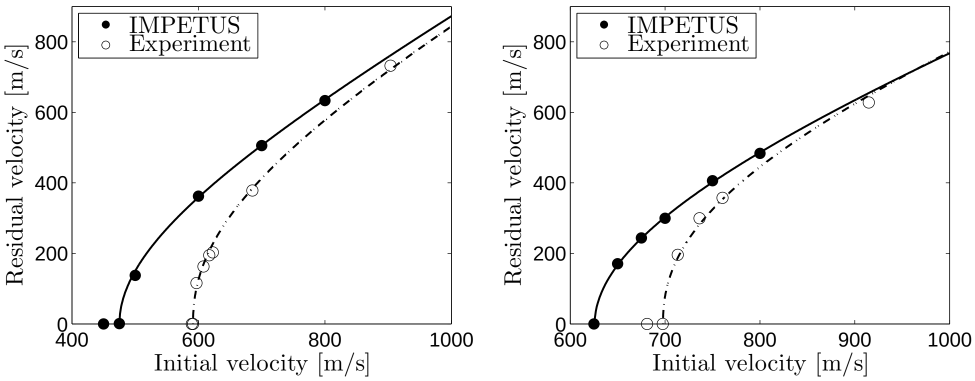

(a) As-received. (b) Soft core.

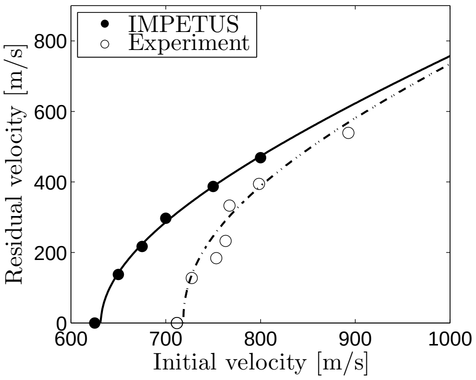

(c) Hard core.

Figure 7.5: The ballistic limit curves for 2x6 mm plates.

The double layered numerical results are conservative compared to the experimental results for all hardening configurations. Table 7.4 summarizes.

Table 7.4: Double layered: Numerical analysis vs. experiment.

	Numerical model			Experiment				
Heat treatment	a	p	v_{bl} [m/s]	a	p	v_{bl} [m/s]	Diff. [m/s]	Rel. diff.
As-received	1.0	1.95	475.00	1.0	2.21	591.50	121.50	-20.5%
Soft core	1.0	1.94	625.75	1.0	2.26	697.80	72.05	-10.3%
Hard core	1.0	1.92	631.45	1.0	2.17	718.50	87.05	-12.1%

The relative difference between the analyses and the experiments is in the range of 10-12% for the surface hardened plates. The unhardened material on the other hand exhibits a relative difference of approximately 21%. The reason for the spread in the relative difference may be explained by the scaling factors used to simulate a varying yield stress, or the numerical model does not capture the brittleness correctly.

A comparison between the different hardening configurations is displayed in Figure 7.6.

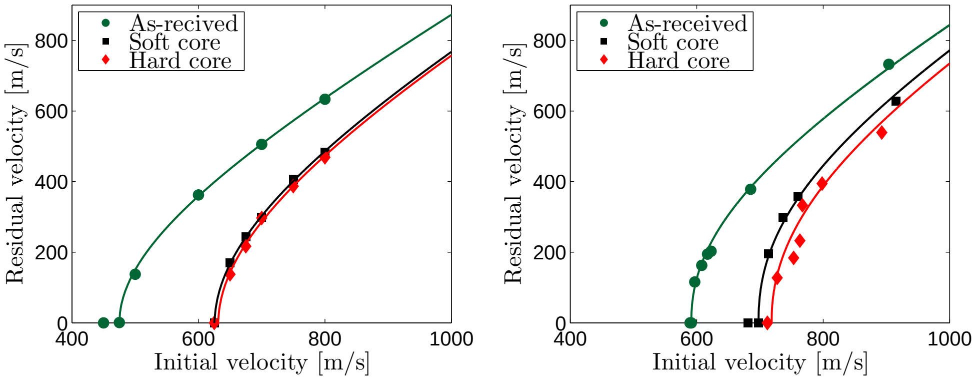

(a) Numerical analysis.

(b) Experiment.

Figure 7.6: The ballistic limit curves for 2x6 mm plates.

IMPETUS is able to capture the main trends found in the experiments, i.e. that hardening has a positive effect on the ballistic perforation resistance. This is shown in Table 7.5.

Table 7.5: Double layered: Effect of surface hardening.

	Numerical model			Experiment		
Heat treatment	v_{bl} [m/s]	Diff. [m/s]	Rel. diff.	v_{bl} [m/s]	Diff. [m/s]	Rel. diff.
As-received	475.00	-	-	591.50	-	
Soft core	625.75	150.75	+31.7%	697.80	106.3	+18.0%
Hard core	631.45	156.45	+32.9%	718.50	127	+21.5%

Time-lapse of the analyses run with v_i=700 m/s are shown in Figure 7.7. Notice that the backplate of the soft core configuration does not fragment, but cracking occurs. However, fragmentation appears at the front plate. This was also observed for the 2x6 mm experiments as explained in Section 4.2.2.2

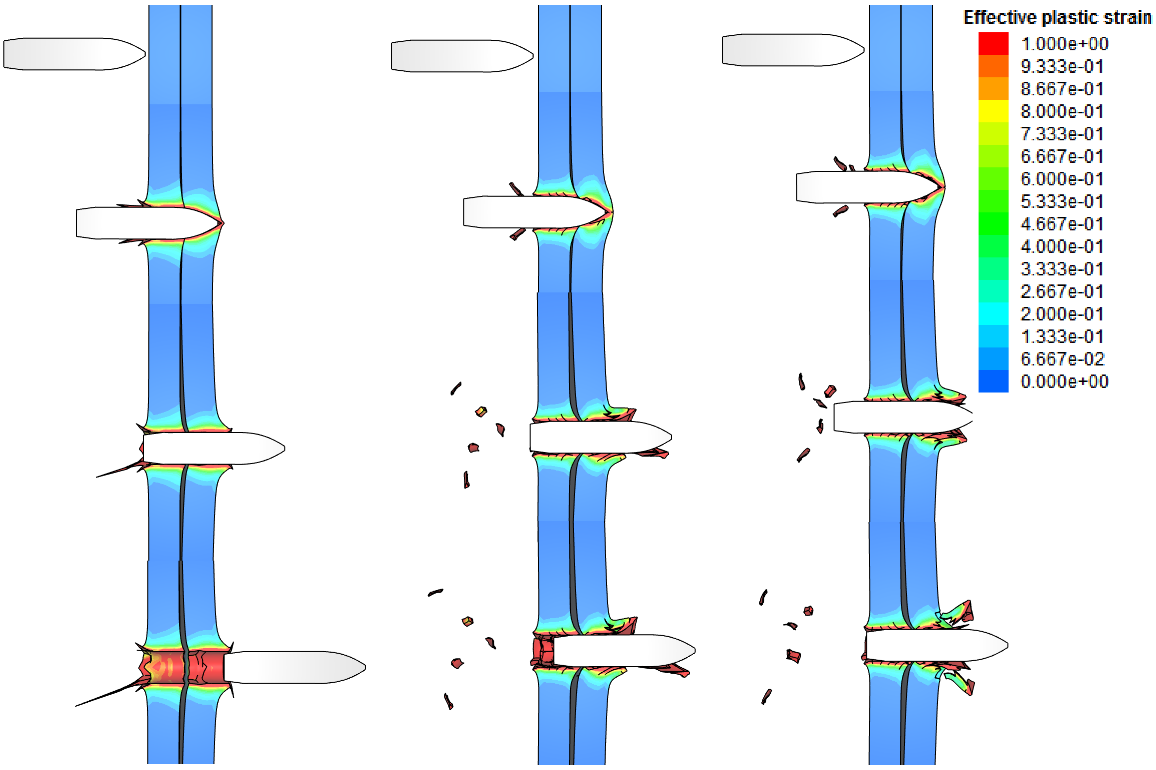

(a) UH, v_r=505.58 m/s. (b) SC, v_r=299.38 m/s. (c) HC, v_r=297.03 m/s.

Figure 7.7: IMPETUS analysis of the different 2x6 mm plates with v_i = 700 m/s.

7.4 3x4 mm Plates

The ballistic limit curves from the numerical analyses and the experiments are shown in Figure 7.8.

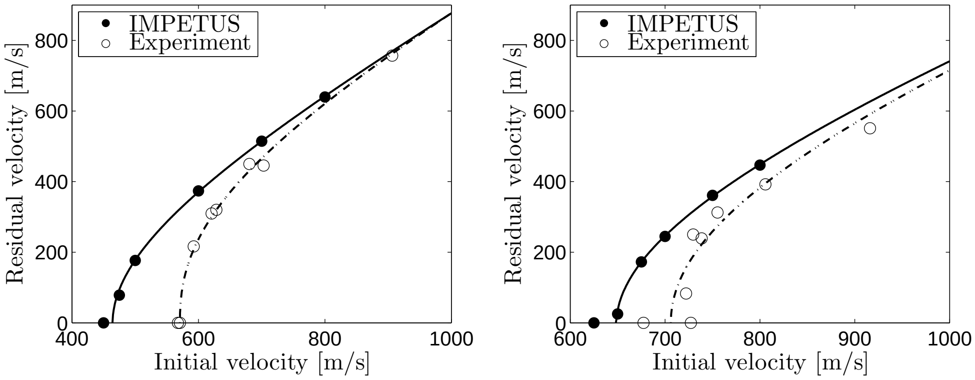

(a) As-received. (b) Soft core.

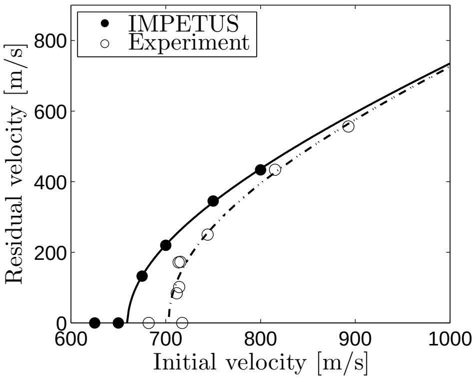

(c) Hard core.

Figure 7.8: The ballistic limit curves for 3x4 mm plates.

The numerical results are conservative compared to the experimental results for all hardening configurations. A comparison is tabulated in Table 7.6.

Table 7.6: Triple layered: Numerical analysis vs. experiment.

	Numerical model			Experiment				
Heat treatment	a	p	v_{bl} [m/s]	a	p	v_{bl} [m/s]	Diff. [m/s]	Rel. diff.
As-received	1.0	1.94	464.29	1.0	2.36	570.80	106.51	-18.7%
Soft core	1.0	1.91	648.74	1.0	2.22	706.10	57.36	-8.1%
Hardcore	1.0	1.93	659.66	1.0	2.05	703.20	43.54	-6.2%

The relative difference between the analyses and the experiments is in the range 6-8% for the surface hardened plates, while the unhardened material has a relative difference of 18.7%. We notice that the relative difference for the hardened materials becomes smaller for the triple layered plates than for the double and monolithic. Generally, we observe that the numerical analyses come closer to the experimental results when the core hardnesses increase. This might be due to the scaling factors, or by the model's limited ability of capturing brittleness.

A comparison between the different hardening configurations is displayed in Figure 7.9.

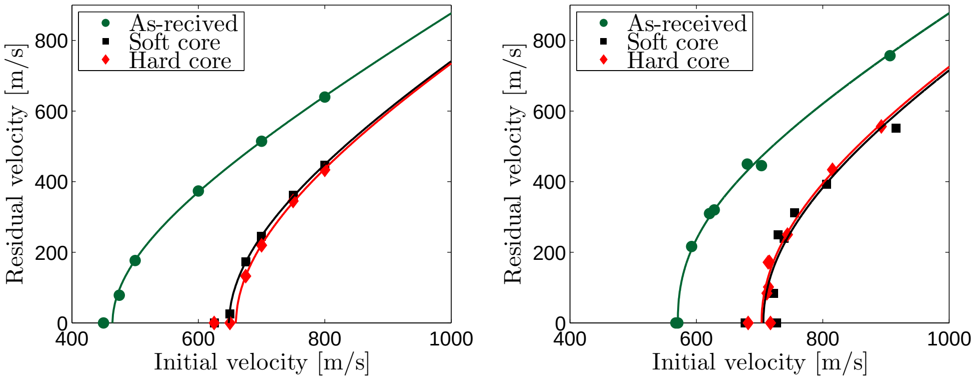

(a) Numerical analysis.

(b) Experiment.

Figure 7.9: The ballistic limit curves for 3x4 mm plates.

The numerical model predicts the same trends as the experiment does. That is, surface hardening improves the ballistic limit velocity. The numerical analyses gave an increased v_{bl} of 39.7% and 42.1% for the soft core and hard core plates, respectively. However, the experiment found only a relative difference of approximately 23% for both hardened configurations. The comparison is shown in Table 7.7.

Table 7.7: Triple layered: Effect of surface hardening.

	Numerical model			Experiment		
Heat treatment	v_{bl} [m/s]	Diff. [m/s]	Rel. diff.	v_{bl} [m/s]	Diff. [m/s]	Rel. diff.
As-received	464.29	-	-	570.80	-	
Soft core	648.74	184.45	+39.7%	706.10	135.30	+23.7%
Hard core	659.66	195.37	+42.1%	703.20	132.40	+23.2%

Time-lapse of the analyses with initial velocity v_i=700 m/s are shown in Figure 7.10. Notice that the plates get spaced during perforation. Figure 7.11 plots the velocity of the back plate for the hard core configuration. At the end of the analysis, the back plate exhibits a velocity of approximately 16 m/s. This effect is also seen in the experiment, where the plates wobble after the perforation.

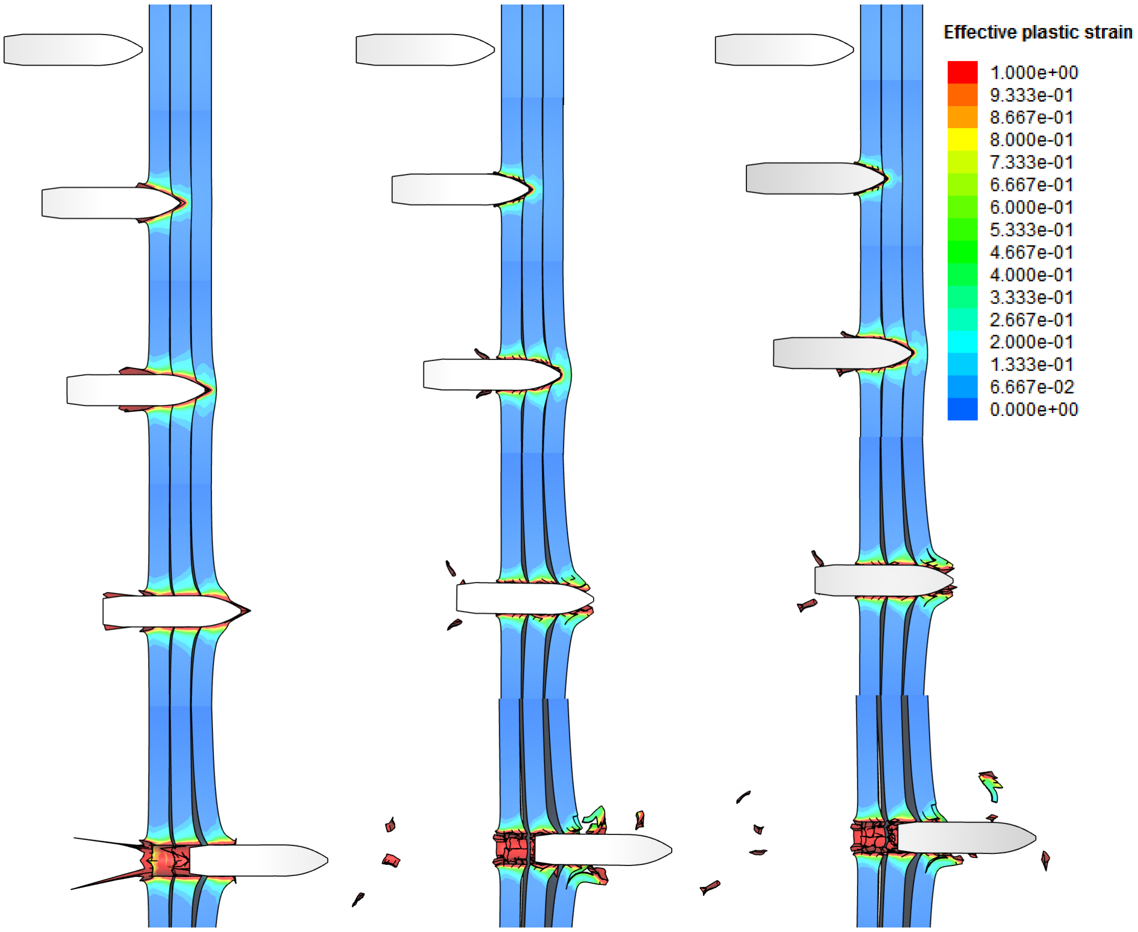

(a) UH, v_r=514.31 m/s. (b) SC, v_r=244.61 m/s. (c) HC, v_r=219.92 m/s.

Figure 7.10: IMPETUS analysis of the different 3x4 mm plates with v_i = 700 m/s.

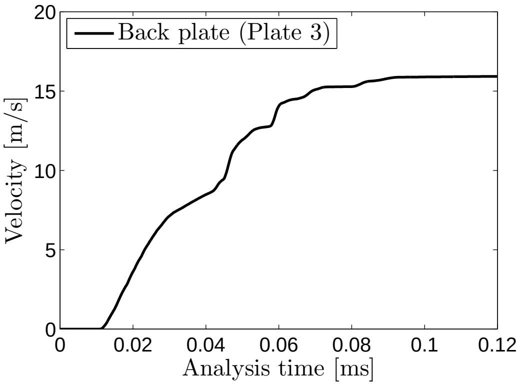

Figure 7.11: Velocity of the back plate for the 3x4 hard core analysis. v_i=700 m/s.

7.5 Monolithic vs Layered Plates

In this section, a comparison between the numerical model and the experiment with respect to different layer configurations will be done.

Note, however, since the hardness profile between the different layer configurations differed from each other, a comparison between the layering effect for the surface hardened plates may not be representative. Nonetheless, the ballistic limit curves will still be displayed and compared with the experimental results. Furthermore, a case study will be performed in Chapter 8 were nominal soft core and nominal hard core configurations are obtained and compared numerically.

7.5.1 As-received Plates

The ballistic limit curves from the numerical analyses and the experiments are shown in Figure 7.12.

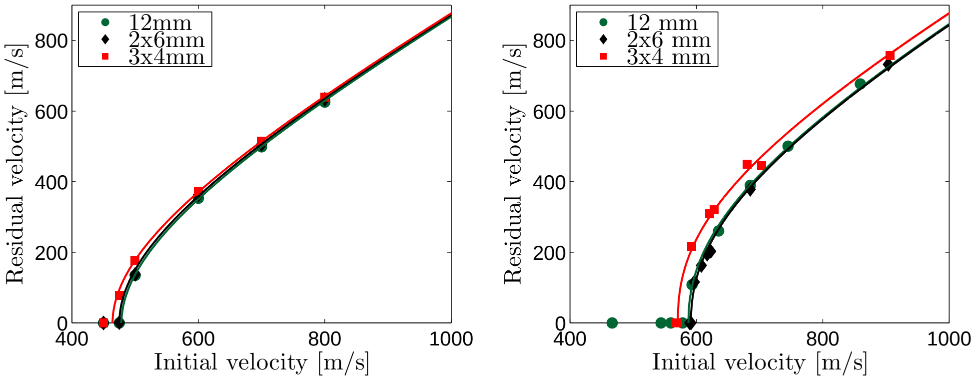

(a) Numerical analysis.

(b) Experiment.

Figure 7.12: The ballistic limit curves for the layered as-received plates.

From the experiment (Figure 7.12(b)), we observed that layering of unhardened plates did not increase the overall ballistic limit velocity. The same tendency is predicted by the numerical model, as seen in Figure 7.12(a). Table 7.8 summarizes the results.

Table 7.8: As-received: Effect of layering.

	Numerical model			Experiment		
Lamination	v_{bl} [m/s]	Diff. [m/s]	Rel. diff.	v_{bl} [m/s]	Diff. [m/s]	Rel. diff.
12 mm	478.36	-	-	587.50	-	
2x6 mm	475.00	3.36	-0.7%	591.50	4.00	+0.7%
3x4 mm	464.29	14.07	-2.9%	570.80	16.70	-2.8%

Figure 7.13 displays the deformation pattern from the different layered as-recived plates. We observe that more layering increases the global deformation, as seen in the experimental results.

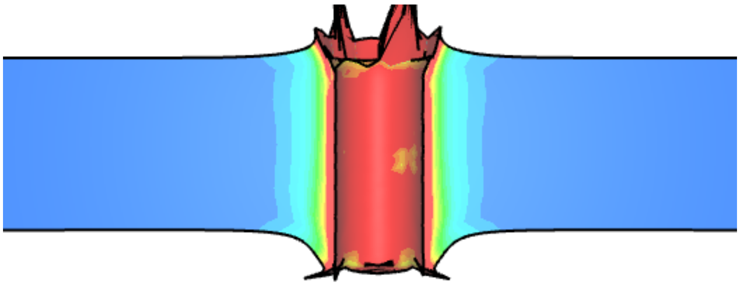

(a) 12 mm. v_r = 498.7 m/s.

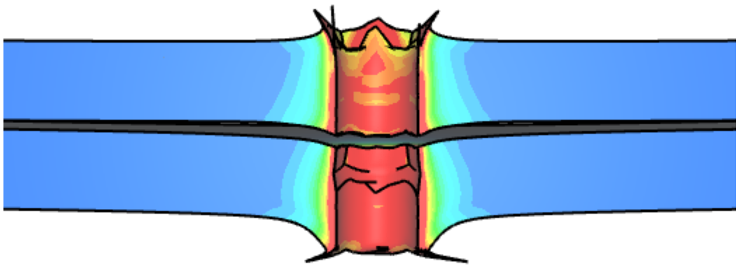

(b) 2z6 mm. v_r = 505.58 m/s.

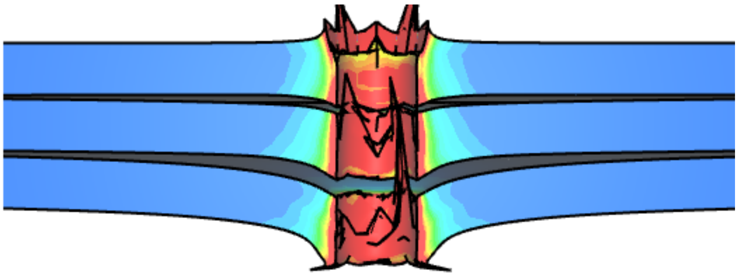

(c) 3x4 mm. v_r = 514.31 m/s.

Figure 7.13: Deformation for different layered configurations in as-received target. v_i= 700 m/s.

7.5.2 Soft Core Plates

The ballistic limit curves from the numerical analyses and the experiments are shown in Figure 7.14.

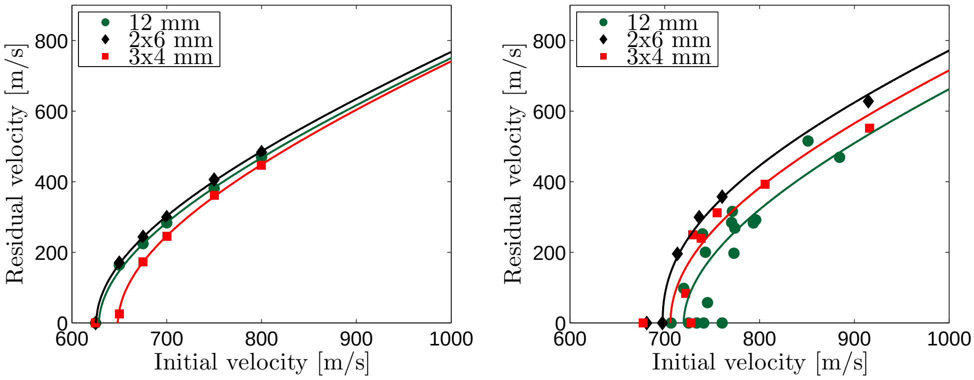

(a) Numerical analysis.

(b) Experiment.

Figure 7.14: The ballistic limit curves for the laminated soft core plates.

From the ballistic experiments, large spread was observed in the data. Hence, conclusions are hard to draw. However, the monolithic plate gave a ballistic limit velocity only 2-3% higher than the laminated configurations.

The numerical model, however, predicted the highest perforation resistance for the triple layered plates, but only by 3.2%. This may be explained by either the model only using the hardness profile from Plate 1 (which was the highest), the applied scaling factor, or the limited ability to capture brittleness numerically.

Table 7.9: Soft core: Effect of layering.

	Numerical model			Experiment		
Lamination	v_{bl} [m/s]	Diff. [m/s]	Rel. diff.	v_{bl} [m/s]	Diff. [m/s]	Rel. diff.
12 mm	628.56	-	-	720.00	-	
2x6 mm	625.75	2.81	-0.4%	697.80	22.20	-3.1%
3x4 mm	648.74	20.18	+3.2%	706.10	13.90	-1.9%

7.5.3 Hard Core Plates

The ballistic limit curves from the numerical analyses and the experiments are shown in Figure 7.15.

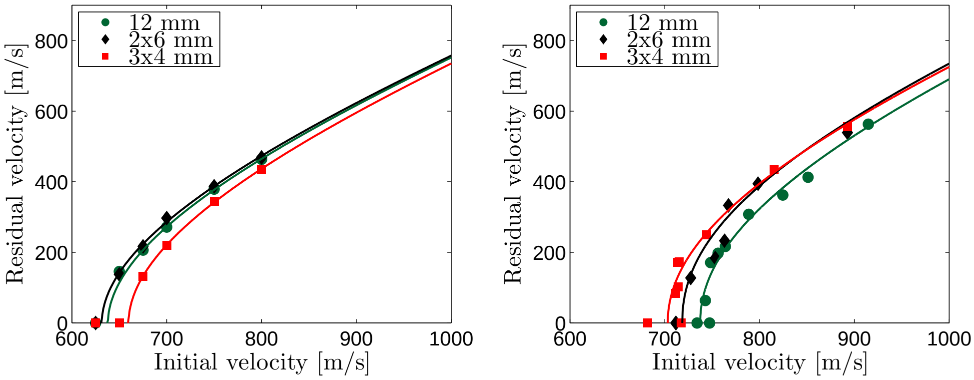

(a) Numerical analysis.

(b) Experiment.

Figure 7.15: The ballistic limit curves for the laminated soft core plates.

The experiments found that layering had no positive effect on the ballistic limit velocity. The monolithic hard core plate was found to be approximately 2-5% better than layered configurations.

The numerical model for the hard core configuration predicts the same tendency found in the numerical soft core from the previous section. Namely, that the triple layered plates exhibited the highest ballistic resistance. This resemblance is due to the similarity in the material properties.

Table 7.10: Hard core: Effect of layering.

	Numerical model			Experiment		
Lamination	v_{bl} [m/s]	Diff. [m/s]	Rel. diff.	v_{bl} [m/s]	Diff. [m/s]	Rel. diff.
12 mm	637.92	-	-	737.40	-	
2x6 mm	631.45	6.47	-1.0%	718.50	18.90	-2.6%
3x4 mm	659.66	21.74	+3.4%	703.20	34.20	-4.6%

7.6 Summary and Discussion

A short summary of the observations and results presented in this chapter will be given. The same notation which was used in Section 4.3 applies.

Table 7.11 gives a summary of the ballistic limit velocities obtained, in IMPETUS, for the different heat treated plates within each layer configuration. Additionally, a relative difference between the hardened configurations with respect to the unhardened is presented for each thickness.

Table 7.11: IMPETUS summary - heat treatment in each plate configuration.

Thickness [mm]	Heat treatment	v_{bl} [m/s]	Rel. diff.	Failure modes
12	As-received	478.36	-	DHG
	Soft core	628.56	+31.4%	RC, F, DHG
	Hard core	637.92	+33.4%	RC, F, DHG
2x6	As-received	475.00	-	DHG
	Soft core	625.75	+31.7%	RC, F, DHG
	Hard core	631.45	+32.9%	RC, F, DHG
3x4	As-received	464.29	-	DHG
	Soft core	648.74	+39.7%	RC, F, DHG
	Hard core	659.66	+42.1%	RC, F, DHG

Table 7.12 summarizes and compares monolithic vs. layered plates for each heat treatment configuration.

Table 7.12: IMPETUS summary - plate layering in each heat treatment.

Heat treatment	Thickness [mm]	v_{bl} [m/s]	Rel. diff.	Failure modes
As-received	12	478.36	-	DHG
	2x6	475.00	-0.7%	DHG
	3x4	464.29	-2.9%	DHG
Soft core	12	628.56	-	RC, F, DHG
	2x6	625.75	-0.5%	RC, F, DHG
	3x4	648.74	+3.2%	RC, F, DHG
Hard core	12	637.92	-	RC, F, DHG
	2x6	631.45	-1.0%	RC, F, DHG
	3x4	659.66	+3.4%	RC, F, DHG

Figure 7.16 compares the experiments with the numerical results. The ballistic limit velocities have been plotted against the different average hardnesses over the entire thickness for each configuration. It illustrates many of the observations given below. Notice that the experimental 12 mm HC and SC has a higher average hardness than the numerical 12 mm HC and SC. This is because only Plate 1 was used in the numerical analysis. However, the ballistic experiments were performed on both Plate 1 and Plate 2. Later, it was observed that Plate 2 had a slightly higher hardness profile than Plate 1 (see Appendix E).

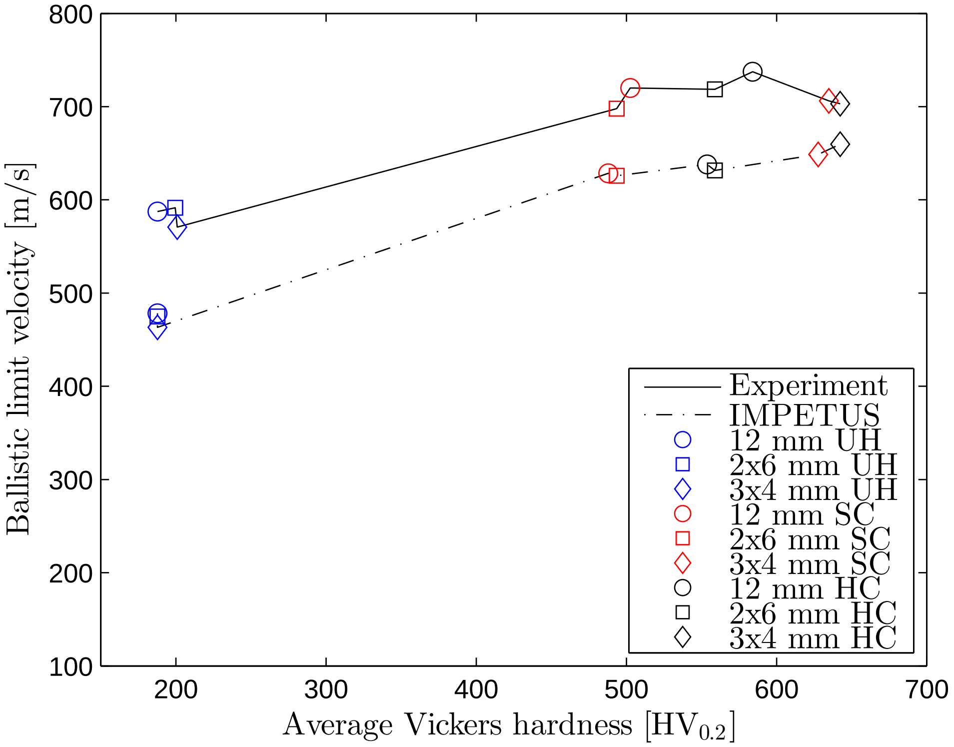

Figure 7.16: Ballistic limit velocities vs. average hardness [$HV_{0.2}$].

Observations from the numerical analyses are listed below.

- Numerical analyses were able to capture the main trends from the experiment. Namely, the positive effect from surface hardening.
- Surface hardened plates increased the ballistic limit velocity approximately 30-40%. The experiments showed an increase of 18-26%.
- No significant difference between soft core and hard core configurations. Also observed for the experiments.
- Ductile hole growth captured. Fragmentation and cracking was observed when the node splitting technique was applied.

- Numerical analyses predicted consistently a conservative result of approximately 20% for the unhardened targets vs. the experiment. For the hardened configurations, this was between 6-13%.
- Monolithic plates showed an absolute difference between the numerical analyses and the experiment of approximately 100 m/s (Table 7.2).
- Relative difference reduced for the hardened configurations. Observation made: Generally, the numerical analyses come closer to the experimental results when the core hardnesses increase (Figure 7.16). This might be due to the scaling factors, or by the model's limited ability of capturing brittleness.
- Lamination did not increase the overall ballistic limit velocity for the unhardened material. Also found in the experiments.
- Triple layered hardened plates showed a slight increase in ballistic limit velocities compared to the monolithic plates. This may be explained by the increased hardness measurements investigated earlier. The results differed from the experiment. However, the spread for both the experiments and the numerical analyses was between 0-5%. Furthermore, for the triple layered plates, only the front plate (Plate 1) was modelled. Also, the uncertainties from the scaling factors (and the brittleness) must be highlighted.
- When layering, the surface hardened configurations tends to give a larger gap between plates during analysis compared to unhardened plates.
- It is, however, important to note that fragmentation is hard to model accurately. This has also been seen in previous work by Børvik et al. [17].

Chapter 8

Numerical Case Study: Nominal Surface Hardening

The microhardness measurements in Section 3.6 revealed that the soft core and hard core configurations were not hardened to their intended (nominal) values. Therefore, numerical models with nominal soft core and nominal hard core hardness profiles will be obtained. A more relevant comparison between soft core and hard core can then be performed.

Different Hardness Depth

A short study was conducted were the surface hardness depth varied. The hardness depth will be defined as the distance from the surface exhibiting a hardness of 800 $HV_{0.2}$. Only the monolithic soft core configuration was considered. The different depths investigated were; 0.5 mm, 0.75 mm and 1.0 mm. Figure 8.1 shows the different hardness profiles examined.

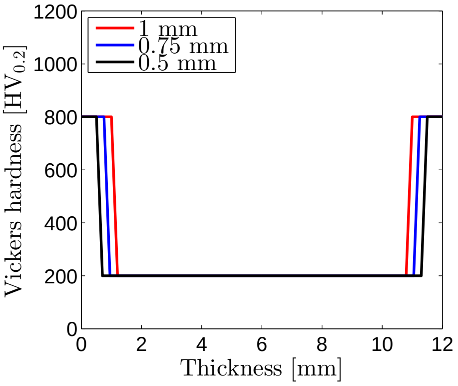

Figure 8.1: Three different hardness depths.

An increased hardening depth is assumed to give an increased perforation resistance, due to higher material strength. However, the material may become too brittle, which might result in a poorer resistance and unwanted fragmentation. Analyses with initial velocity of v_i = 700 m/s were conducted, giving residual velocities as presented in Table 8.1. Figure 8.2 shows a visual representation of the entry and exit holes from the study.

Table 8.1: Residual velocities when v_i=700 m/s for different hardness depths.

	1.0 mm	0.75 mm	0.5 mm
v_r [m/s]	355.48	360.13	375.96
v_{bl}* [m/s]	598.54	595.70	585.66

*Estimated ballistic limit velocity based on Recht-Ipson parameters for nominal soft core (Table 8.5).

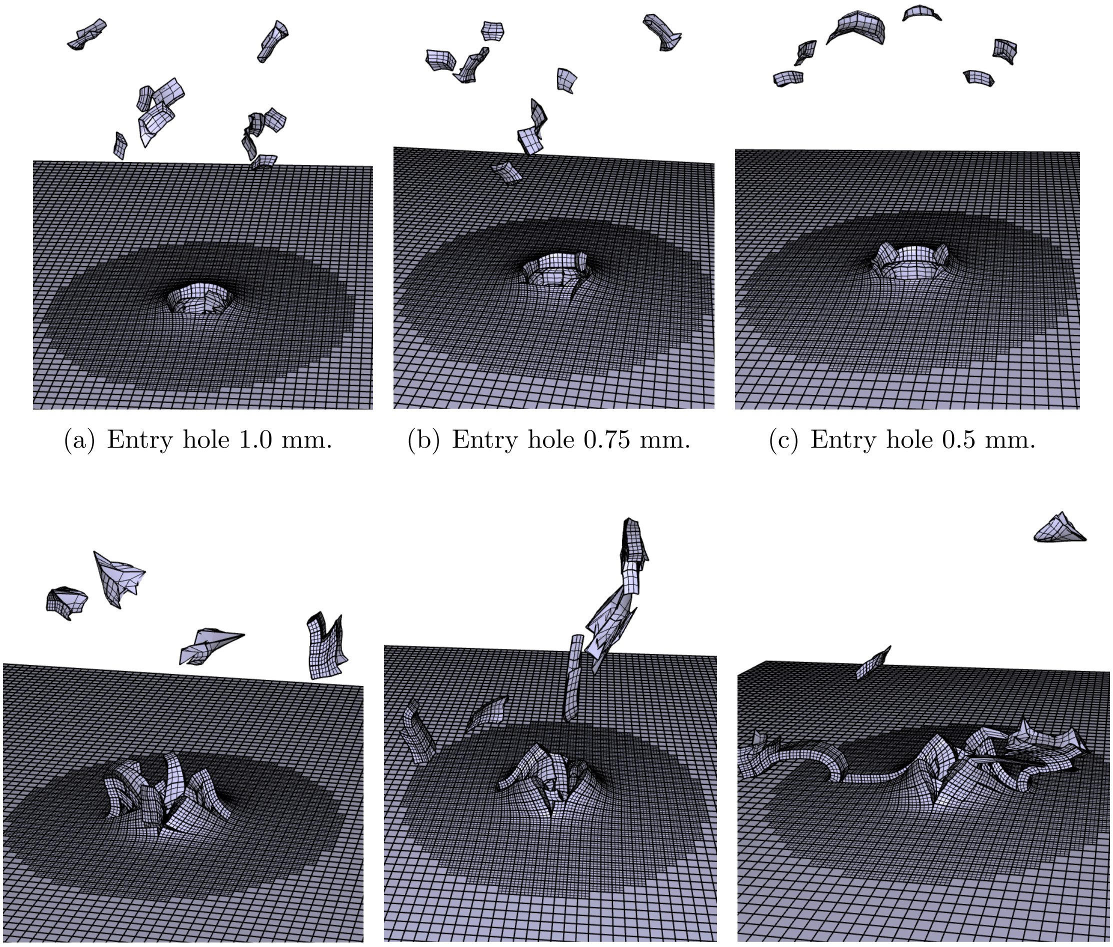
(a) Entry hole 1.0 mm. (b) Entry hole 0.75 mm. (c) Entry hole 0.5 mm.

(d) Exit hole 1.0 mm. (e) Exit hole 0.75 mm. (f) Exit hole 0.5 mm.

Figure 8.2: Entry and exit holes for different hardness depths, v_i =700 m/s.

As expected, the hardness depth of 1 mm gave the lowest residual velocity. Furthermore, Figure 8.2 shows that all the different depths exhibited fragmentation. Since the numerical model consisted of elements with size 1.0x1.0x1.0 mm^3, fragments could not be smaller than this. From Figure 8.2(f), we see that the 0.5 mm depth exhibited both petaling and fragmentation. The petaling effect was not observed for the other depths. This may be because half of the element displays ductile behaviour when the depth is 0.5 mm.

Hardness depths of 1.0 mm and 0.75 mm showed almost the same behaviour. Further in this case study, a hardness depth will be set to 1.0 mm for the monolithic configuration.

A small study with a hardness depth of 1.0 mm was performed on laminated 2x6 mm and 3x4 mm plates as well. The initial velocity was v_i =700 m/s and Table 8.2 displays the different residual velocities.

Table 8.2: Residual velocities when v_i=700 m/s for different layered plates. Constant hardness depth of 1 mm.

	12 mm	2x6 mm	3x4 mm
v_r [m/s]	355.48	308.69	291.84
v_{bl}* [m/s]	598.54	619.27	628.74

*Estimated ballistic limit velocity based on Recht-Ipson parameters for nominal soft core (Table 8.5).

We observe that the residual velocity decreases with number of layers. The 2x6 mm laminated plates reduce the residual velocity by 46.79 m/s which equals a drop of 13.2%. This is due to the increasing average hardness. However, notice that the 3x4 mm plates only drop 16.85 m/s (5.45%) compared to the 2x6 mm. This might be because of the lower bending stiffness which somewhat counteracts the increasing hardness. To exclude the effect from the increased average hardness over the total thickness, it is reasonable to create a hardness profile for each layer configuration with equal average hardness.

Nominal Hardness Profiles

A transition from the brittle surface to the ductile core has been modelled with a distance of 0.2 mm for the monolithic plates. This gradient was included in order to make a valid tabulated function in IMPETUS. Then, an average hardness was calculated and used to obtain a hardness depth for the layered plates (Table 8.3). Consequently, new transitions were acquired. Note that the depths and transition values are the same for both nominal soft core and nominal hard core.

The results are summarized in Table 8.4. Figure 8.3 shows the calculated hardness profiles for all configurations.

Table 8.3: Average hardness for nominal hardness profiles.

	Soft core	Hard core
Average hardness [$HV_{0.2}$]	310.00	473.33

Table 8.4: Different hardness depths and transitions for laminated plates [mm].

Lamination	Depth	Transition
12 mm	1.0	0.2
2x6 mm	0.5	0.1
3x4 mm	0.33	0.067

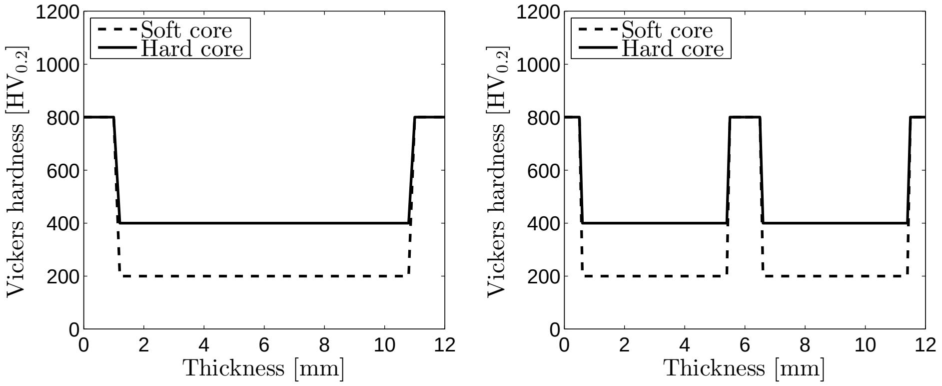

(a) Monolithic.

(b) Double layered.

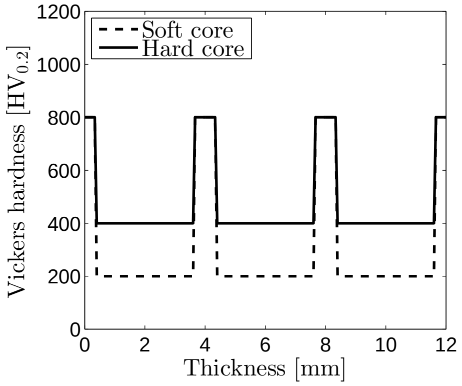

(c) Triple layered.

Figure 8.3: Varying hardness over the thickness.

8.1 Nominal Soft Core

Figure 8.4 shows the ballistic limit curves for the nominal soft core configurations compared with the numerical as-received results. The ballistic limit velocities with the fitted Recht-Ipson parameters are given in Table 8.5.

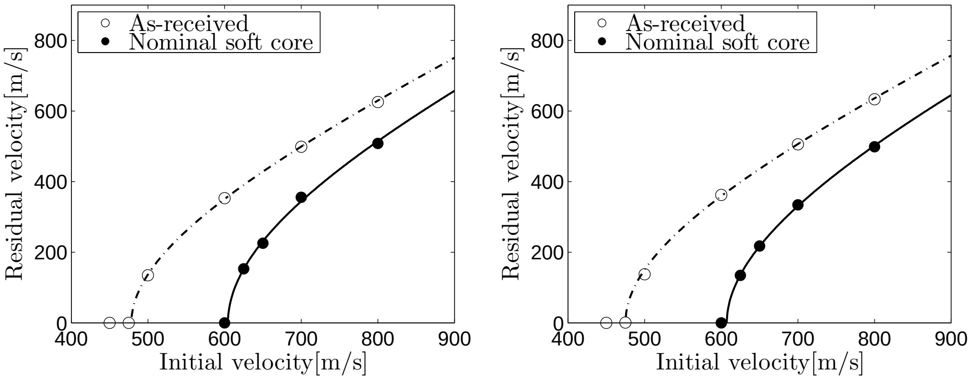

(a) 12 mm.

(b) 2x6 mm.

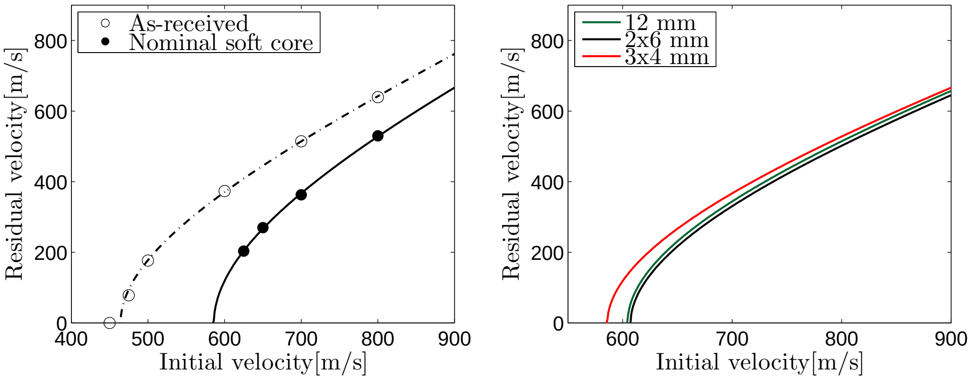

(c) 3x4 mm.

(d) Layering effect.

Figure 8.4: The ballistic limit curves for the different nominal soft core configurations.

Table 8.5 shows an increase in the ballistic limit velocity of approximately 27% for all layer configurations. Hence, nominal soft core hardening has a positive effect on the ballistic resistance.

Table 8.5: Nominal soft core: Effect of surface hardening.

	Soft core			As-received				
Lamination	a	p	v_{bl} [m/s]	a	p	v_{bl} [m/s]	Diff. [m/s]	Rel. diff.
12 mm	1.0	1.96	605.33	1.0	1.93	478.36	126.97	+26.5%
2x6 mm	1.0	1.91	607.15	1.0	1.95	475.00	132.15	+27.8%
3x4 mm	1.0	1.92	585.93	1.0	1.94	464.29	121.64	+26.2%

Table 8.6 shows how layering affects the response when applying a nominal soft core.

Table 8.6: Nominal soft core: Effect of layering.

	Soft core			As-received		
Lamination	v_{bl} [m/s]	Diff.[m/s]	Rel. diff.	v_{bl} [m/s]	Diff. [m/s]	Rel. diff.
12 mm	605.33	-	-	478.36	-	
2x6 mm	607.15	1.82	+0.3%	475.00	3.36	-0.7%
3x4 mm	585.93	19.40	-3.2%	464.29	14.07	-2.9%

Based on the results, a layered nominal soft core configuration does not better the ballistic resistance compared to a pure monolithic configuration. It predicts almost the same layering effect as for the unhardened numerical results. However, both results suggest that a double layered target does not decrease the ballistic limit velocity compared to the monolithic.

8.2 Nominal Hard Core

Figure 8.5 shows the ballistic limit curves for the nominal hard core configurations compared with the numerical as-received results. The ballistic limit velocities with the fitted Recht-Ipson parameters are given in Table 8.7.

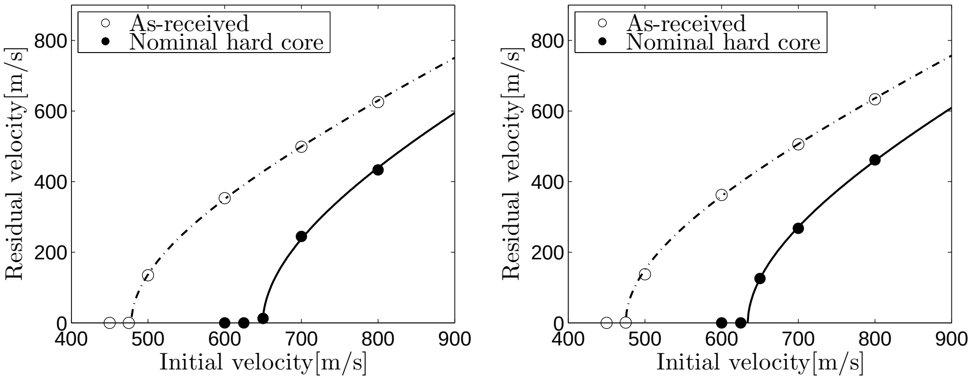

(a) 12 mm.

(b) 2x6 mm.

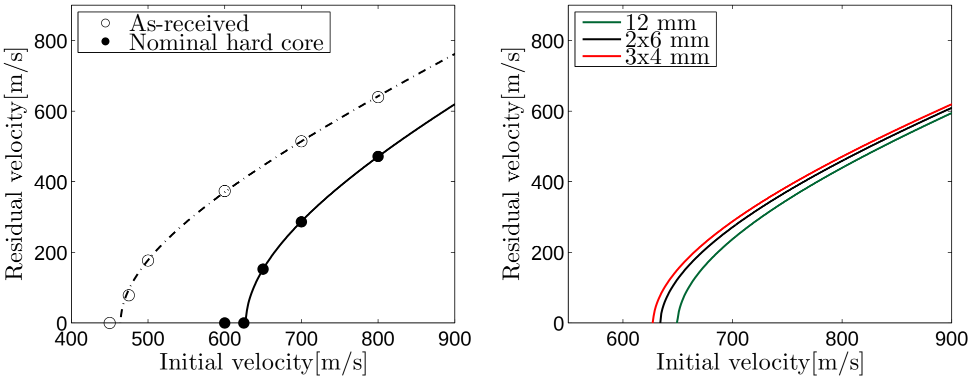

(c) 3x4 mm.

(d) Layering effect.

Figure 8.5: The ballistic limit curves for the different nominal hard core configurations.

Table 8.7 shows an increase in the ballistic limit velocity of approximately 35% for all layer configurations. Hence, nominal hard core hardening has a positive effect on the ballistic resistance.

Table 8.7: Nominal hard core: Effect of surface hardening.

	Hard core			As-received				
Lamination	a	p	v_{bl} [m/s]	a	p	v_{bl} [m/s]	Diff.[m/s]	Rel. diff.
12 mm	1.0	1.88	649.78	1.0	1.93	478.36	171.42	+35.8%
2x6 mm	1.0	1.87	634.10	1.0	1.95	475.00	159.10	+33.5%
3x4 mm	1.0	1.88	627.54	1.0	1.94	464.29	163.25	+35.2%

Table 8.8 shows how layering affects the response when applying a nominal hard core.

Table 8.8: Nominal hard core: Effect of layering.

	Hard core			As-received		
Lamination	v_{bl} [m/s]	Diff. [m/s]	Rel. diff.	v_{bl} [m/s]	Diff. [m/s]	Rel. diff.
12 mm	649.78	-	-	478.36	-	
2x6 mm	634.10	15.68	-2.4%	475.00	3.36	-0.7%
3x4 mm	627.54	22.24	-3.4%	464.29	14.07	-2.9%

The nominal hard core configuration shows no improvement of the ballistic limit velocity in terms of layering. This was also observed for the unhardened and the nominal soft core configurations.

Furthermore, the ballistic limit velocity of the double layered plates was 2.4% lower than the monolithic. This relative difference is larger than what was seen for the as-received and the nominal soft core configurations.

8.3 Nominal Soft Core vs. Nominal Hard Core

The nominal soft core and nominal hard core have been compared in Figure 8.6.

The results are as expected, resulting in the highest ballistic limit velocities for the nominal hard core targets. The monolithic nominal hard core plates seems to be preferable when it comes to perforation resistance of surface hardened plates. Table 8.9 summarizes.

Table 8.9: Comparing nominal soft core and nominal hard core.

	Soft core			Hard core				
Lamination	a	p	v_{bl} [m/s]	a	p	v_{bl} [m/s]	Diff. [m/s]	Rel. diff.
12 mm	1.0	1.96	605.33	1.0	1.88	649.78	44.45	+7.3%
2x6 mm	1.0	1.91	607.15	1.0	1.87	634.10	26.95	+4.4%
3x4 mm	1.0	1.92	585.93	1.0	1.88	627.54	41.61	+7.1%

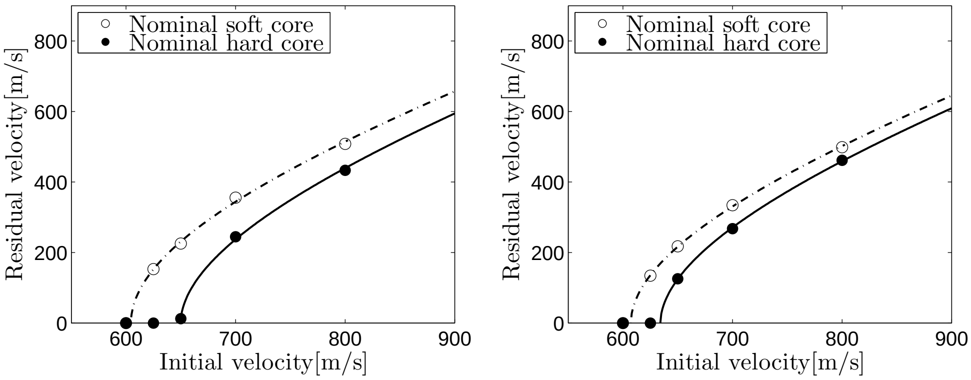

(a) 12 mm.

(b) 2x6 mm.

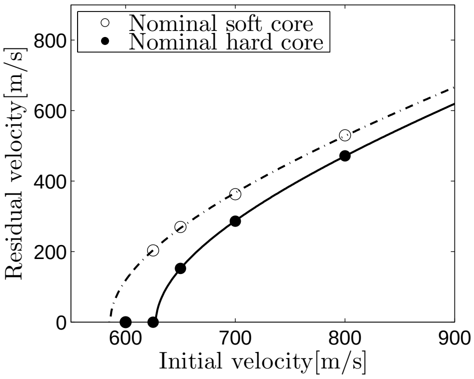

(c) 3x4 mm.

Figure 8.6: The ballistic limit curves for nominal soft core vs. nominal hard core configurations.

For further comparison, the 12 mm soft core plate from Coucheron [24] exhibited a ballistic limit velocity of 684 m/s, i.e. 7.2% less than the experimental monolithic hard core results in this study, see Table 4.4. This is in good agreement with the results from the numerical case study in Table 8.9. However, note that the hardness in Coucheron's study and the hard core plates in this thesis were hardened to approximately 250 $HV_{0.2}$ and 340-370 $HV_{0.2}$ (Appendix E), respectively, i.e. not nominal hardness values.

Figure 8.7 shows the deformation pattern for the triple layered plates. From this figure, there are no noticeable differences between the nominal soft core and the nominal hard core with regards to global deformation.

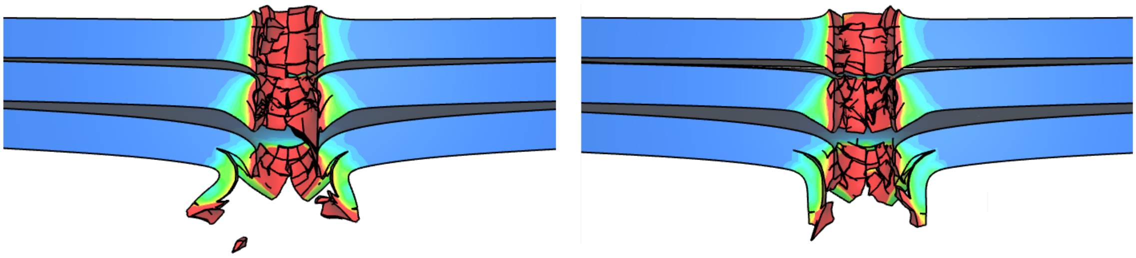

(a) Nominal soft core. v_r = 362.86 m/s.

(b) Nominal hard core. v_r = 286.37 m/s.

Figure 8.7: The deformation pattern for the triple layered plates. v_i = 700 m/s.

8.4 Constant Hardness Over the Thickness

A short study with a constant hardness of 800 $HV_{0.2}$ over the thickness has been performed. Projectiles were shot at all the layering configurations with a velocity of v_i = 800 m/s. Two different strain energy release rates were considered; $G_I = 0$ Pa/m and $G_I = 30135$ Pa/m. More about these values are given in Section 6.2.3.1. Table 8.10 shows the different residual velocities obtained. Nominal hard core is included for further comparison.

Table 8.10: Comparing nominal soft core and nominal hard core.

	Hardness: Constant 800 $HV_{0.2}$		Hardness: Nominal hard core
	G_I=0 Pa/m	G_I=30135 Pa/m	G_I=0 Pa/m
Lamination	v_r [m/s]	v_r [m/s]	v_r [m/s]
12 mm	272.84	403.11	433.15
2x6 mm	291.96	423.10	461.36
3x4 mm	331.25	423.45	471.70

Table 8.10 suggests that a monolithic plate exhibits higher resistance than the laminated plates when the hardness is 800 $HV_{0.2}$. For $G_I = 0$ Pa/m, the model predicts an increase in the ballistic resistance compared to the nominal hard core. The two analyses showed a somewhat similar failure pattern (Figure 8.8).

However, it is clear that IMPETUS does not capture the brittle behaviour when increasing the yield strength. Instead, brittleness in IMPETUS is dependent on the strain energy release rate. This is as expected, since a numerical software tool needs the correct parameters in order to control the material behaviour. Hence, a fracture mechanical test should be performed before the node splitting technique is applied. If this value is put to $G_I = 30135$ Pa/m, the residual velocities drops due to severe delamination of the plate (Figure 8.9). Additionally, we observe that the double and triple layered configuration gave almost the same residual velocities.

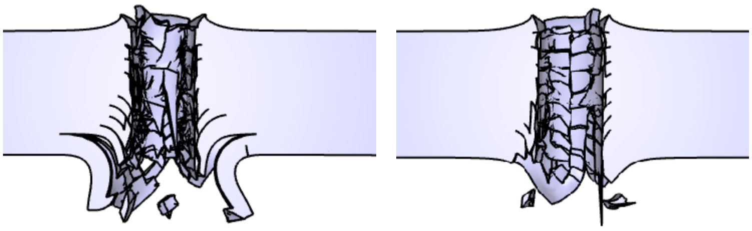

(a) 800 $HV_{0.2}$. v_i=800 m/s. (b) Nominal hard core. v_i=700 m/s.

Figure 8.8: Failure patterns when G_I=0 Pa/m.

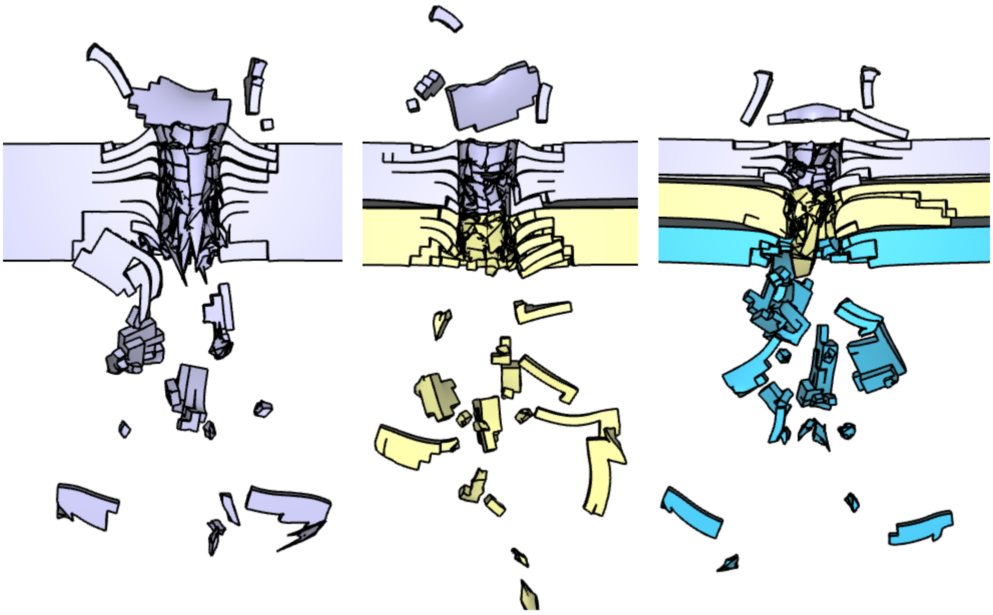

(a) 12 mm. (b) 2x6 mm. (c) 3x4 mm.

Figure 8.9: Delamination of plates when G_I = 30135 Pa/m. v_i=800 m/s.

8.5 Summary and Discussion

A summary of the observations made in the case study will be presented in the following. Note that the observations are based on numerical analyses.

- Increasing hardness depth reduces residual velocity for v_i=700 m/s.
- Constant hardness depth decreased the residual velocity when layering due to increased average hardness.
- Nominal soft core and nominal hard core configurations increased the ballistic limit velocities by approximately 27% and 35%, respectively.

- Layering of plates does not seem to improve the overall ballistic resistance for both nominal hardness profiles.
- Nominal hard core configurations gave 4-7% higher ballistic limit velocity than nominal soft core. Similar results were seen experimentally when comparing Coucheron's [24] monolithic soft core plate with the monolithic hard core from this thesis.
- Brittleness in IMPETUS appears not to be sensitive for increasing yield strength. Instead it is driven by strain energy release rate. This was especially observed when the hardness was constant 800 $HV_{0.2}$ over the thickness. Hence, fracture mechanical tests should be performed beforehand.

Figure 8.10 displays many of the aforementioned observations, e.g. effect of surface hardening and layering.

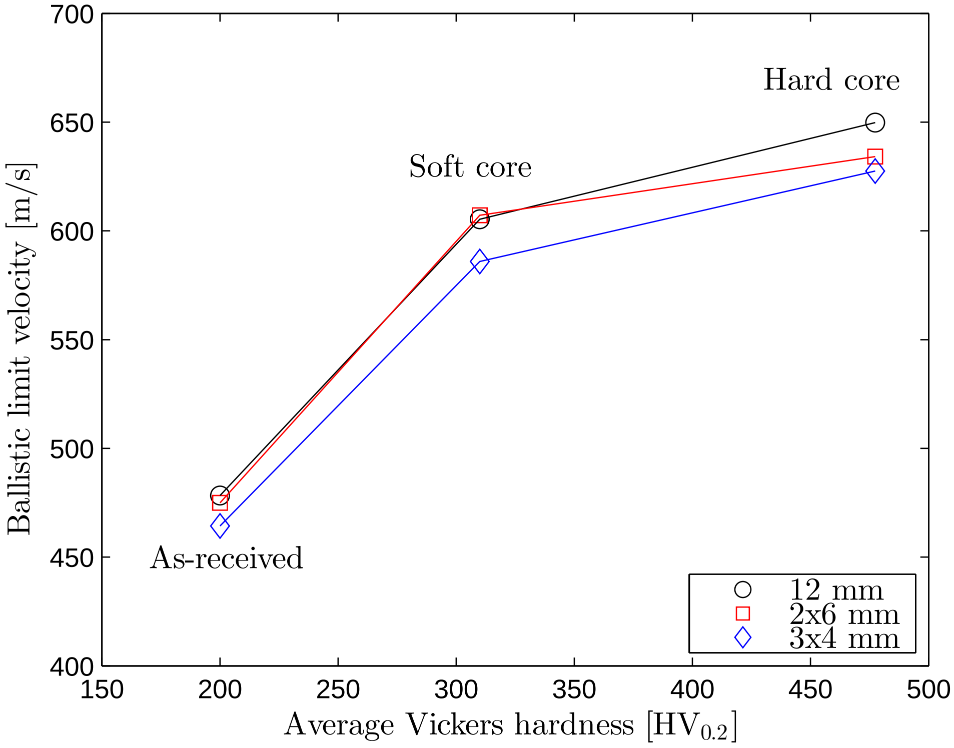

Figure 8.10: Nominal surface hardening: Ballistic limit velocities vs. average hardness [$HV_{0.2}$].

Chapter 9

Concluding Remarks

In this thesis the effects surface hardening have on the ballistic properties for NVE36 steel plates have been investigated. The plates were impacted by 7.62 mm APM2 projectiles. Nine target configurations were considered, see Table 9.1.

Table 9.1: Target configurations.

Layer configuration	Case	Heat treatment
12 mm	#1	As-received
	#2	Soft core
	#3	Hard core
2x6 mm	#4	As-received
	#5	Soft core
	#6	Hard core
3x4 mm	#7	As-received
	#8	Soft core
	#9	Hard core

Ballistic impact experiments were conducted at SIMLab, NTNU. The experiments revealed how the different target configurations responded, and ballistic limit curves were obtained. Quasi-static tension tests and hardness measurements were performed in order to acquire the material properties. A numerical study using IMPETUS Afea Solver was conducted to obtain a numerical model which could capture the same trends observed from the ballistic experiments.

A summary is presented in the following.

Material properties

- All the quasi-static tensions tests were only performed in the core of separate monolithic plates for the respective hardening configurations; as-received, soft core, and hard core.
- In this thesis, it was apparent that the surface hardening process was non deterministic and caused issues. The microhardness measurements revealed that the plates had not obtained their expected hardness.
- The average core hardness of the monolithic plates was between 290-370 $HV_{0.2}$.
- For both the soft core and the hard core, the doubled layered plates exhibited major difference in average hardness in the core. The front plates were hardened to values of 400-500 $HV_{0.2}$, while the back plates had a hardness of 150-170 $HV_{0.2}$. Indicating that either the plates were wrongly marked or incorrectly surface hardened.
- Both soft core and hard core triple layered plates showed an average core hardness of 450-500 $HV_{0.2}$.
- Scaling factors which connected the results from the tensions tests and hardness tests were acquired. These scaling factors were used to create a varying yield strength over the thickness of the plates. Tensile strength and hardness measurements were obtained from different monolithic plates, causing uncertainties in the scaling factors for layered plates.

Experimental results

- Ballistic experiments suggested that surface hardening had a positive effect on the target resistance, for all layering configurations. The ballistic limit velocity was increased between 18-26% compared to the as-received plates.
- No noticeable difference between soft core and hard core was observed. This may be contributed to their similar material behaviour. However, conclusions are hard to draw due to large spread in data.
- Layering of plates did not increase the overall ballistic limit velocity. However, for the as-received material, the double layered plates were comparable with the monolithic plates. Furthermore, the as-received triple layered target decreased the ballistic limit velocities by approximately 3%. Additionally, for layered surface hardened plates, the ballistic limit velocities decreased, but not more than 5%.
- The hardened surface caused radial and circumferential cracks, and fragmentation to occur. All plates experienced ductile hole growth, especially the unhardened targets.

- Layered plates showed more global deformation than monolithic plates. However, surface hardened target materials exhibited less global deformation than as-received materials.

Numerical results

- The surface hardened plates were modelled with varying yield strength over the thickness. These stresses were obtained by employing scaling factors derived from the material investigation. The scaling factors were calculated by considering material tests performed on monolithic plates. However, they were also employed for the laminated configurations.
- IMPETUS Afea Solver was able to capture the positive effect from surface hardening. The numerical analyses predicted an increased target resistance between 31-42% compared to the as-received configurations. Possibly due to shortcomings in the numerical models ability to predict fragments correctly.
- By applying the node splitting technique, IMPETUS was able to model fragmentation and cracking of the surface, to some degree. However, the numerical model appeared to be more ductile than the experiment. The fragment size was bounded by the size of the mesh.
- Layering of plates did not increase the ballistic limit velocity for the as-received material. Furthermore, the double layered plates were comparable with the monolithic plates. However, a small increase of approximately 3.5% was observed for the triple layered plates when surface hardened.
- All the numerical analyses gave conservative results with respect to the experiments. This was between 18-22% for the as-received configurations and between 6-14% for the surface hardened targets.
- The numerical as-received model captured the same layering effect as the experiment.
- The relative difference between the numerical model and the experimental results decreased proportionally with the increased material hardness. This may be contributed to the uncertainty of the employed scaling factors, or limitations in the brittle behaviour of the obtained numerical model.

Case study

- A numerical case study with nominal hardness values for the soft core and the hard core configurations was conducted.

- Surface hardening of plates still increased the ballistic impact resistance compared to the as-received plates. The increase was approximately 27% and 35% for nominal soft core and nominal hard core, respectively.
- Nominal hard core configurations were 4-7% better than nominal soft core in terms of obtained ballistic limit velocities.
- The study showed that lamination did not increase the overall ballistic impact resistance. However, the double layered soft core plates were comparable to the monolithic plates. This was not seen for the nominal hard core lamination. Furthermore, triple layered plates decreased the ballistic limit velocities by approximately 3%.

Uncertainties

Some of the uncertainties and challenges encountered in this thesis is given in the following

- Ballistic Experiments: Impact ballistics involve many complex mechanisms which are hard to catch. Large spread in experimental data makes ballistic limit curves somewhat uncertain, e.g. two projectiles with the same initial velocity may give different residual velocities. Furthermore, dynamic impact conclusions are based on ”one-shot statistics”, meaning that results are often not statistically significant [72].
- Idealization of material behaviour: Many assumptions regarding constitutive relation, fracture criterion, contact algorithms, numerical discretization, and complex failure modes make an accurate numerical model hard to obtain.
- Material properties: Microhardness measurements revealed that variations in the core of the plates were present.
- Scaling factors: The relationship between hardness and tensile strength is only approximate. Especially since two different plates were used to calculate the respective values.

Chapter 10

Further Work

Suggestions for further work will be listed in this chapter. The list contains both experimental and numerical proposals.

- **Better controlled surface hardening process.** The surface hardened plates investigated in this thesis did not obtain their expected hardness profiles. This influenced the conclusions for the layering effect of surface hardened configurations. Hence, the surface hardening process should be investigated more thoroughly before, possibly, applied in industry.
- **New experimental tests.** If the plates had obtained nominal hardness profiles, new ballistic experiments should have been conducted.
- **Fracture mechanical tests.** Relevant fracture mechanical tests should be performed to determine additional material properties before applying node splitting in IMPETUS.
- **More consistent material investigations.** In this study, the tensile tests and microhardness measurements were not performed on the same plates, which led to uncertainties. Furthermore, tension tests were only performed on the monolithic plates, resulting in scaling factors which were also employed on the layered configurations. Therefore, tensions tests should be performed on all plates.
- **Tensile tests of various parts.** Since the target plates were surface hardened, tensile tests of the various parts of the specimen with transformed microstructure could have been investigated in order to obtain better material properties. More suitable scaling factors could then be derived.
- **More comprehensive sensitivity study.** Since each ballistic limit curve requires 4-5 initial shots in order to be obtained, more than 150 analyses were run in this study. With more time available, a more thorough sensitivity study could have been performed. For instance investigation of friction coefficients, boundary conditions,

space between layered target plates, mesh refinement, and G_I values. Also, a 2D axisymmetric model could have been obtained in order to compare the numerical results.

- **Capture fragmentation.** Fragmentation is hard to accurately capture numerically. However, fragments are bounded by the smallest elements in a numerical model. Since the surface hardened plates exhibited somewhat brittle behaviour in the experiments, smaller elements close to the surface could have captured fragmentation better.
- **Strain energy release rate, G_I study.** The strain energy release rate, G_I, was observed to influence the node splitting technique in IMPETUS Afea Solver. Hence, obtaining a suited G_I value should have been investigated further. In addition, a varying strain energy release rate over the thickness should be examined in more detail. The authors were not able to obtained a continuous varying function for this value, which could have been beneficial.
- **Cavity Expansion Theory.** Cavity Expansion Theory with respect to surface hardened materials could have been interesting to implement. This, in order to compare an analytic method with the experimental and numerical results.
- **More comprehensive calibration of constitutive relation.** Since only quasi-static tension tests were performed, the strain rate hardening and temperature softening constants were not calibrated. Tensile tests with different strain rates, and at elevated temperatures, could have been performed in order to obtain these constants.

Bibliography

[1] Almohandes AA, Abdel-Kader MS, Eleiche AM. Experimental investigation of the ballistic resistance of steel-fiberglass reinforced polyester laminated plates. *Composites Part B: Engineering* , 27(5):447-458, 1996.

[2] Andersen KH, Hernandez FB. Numerical simulations of Docol 600 DL Steel Plates Subject to Blast Loading. Master's Thesis, Norwegian University of Science and Technology, 2013.

[3] Anderson TL. *Fracture Mechanics: Fundamentals and Applications.* CRC Press, 2004.

[4] Ashby MF, Jones DRH. *Engineering Materials 2: An Introduction to Microstructures, Processing and Design.* Elsevier Butterworth-Heinemann, 3rd edition, 2006.

[5] Backman EM, Goldsmith W. The Mechanics of Penetration of Projectiles Into Targets. *International Journal of Engineering Science*, 16:1-99, 1978.

[6] Ben-Dor G, Dubinsky A, Elperin T. About effect of layering on ballistic properties of metal shields against sharp-nosed rigid projectiles. *Engineering Fracture Mechanics*, 102:358-361, 2013.

[7] Ben-Dor G, Dubinsky A, Elperin T. Effect of layering on ballistic properties of metallic shields against sharp-nosed rigid projectiles. *Engineering Fracture Mechanics*, 77(14):2791-9, 2010.

[8] Bridgman, PW. Trans Am. Soc. Met, vol. 32:553, 1944.

[9] Børvik T. An Introduction to Impact and Penetration Dynamics. *SIMLAB/Department of Structural Engineering*, NTNU.

[10] Børvik T. Oral discussions in his office, 2014.

[11] Børvik T. Structural Impact. *Lecture in TKT4135 Material Mechanics*, 2014.

[12] Børvik T, Dey S, Clausen AH. Perforation resistance of five different high-strength steel plates subjected to small-arms projectiles. *International Journal of Impact Engineering*, 36:948-964, 2009.

[13] Børvik T, Forrestal MJ, Warren TL. Perforation of 5083-H116 Aluminium Armor Plates with Ogive-Nose Rods and 7.62 mm APM2 Bullets. *Experimental Mechanics*, 50:969-978, 2010.

[14] Børvik T, Hopperstad OS, Berstad T, Langseth M. A computational model of viscoplasticity and ductile damage for impact and penetration. *European Journal of Mechanics - A/Solids*, 20(5):685-712, 2001.

[15] Børvik T, Hopperstad OS, Berstad T, Langseth M. Numerical simulations of plugging failure in ballistic penetration. *International Journal of Solids and Structures*, 38(34-35):6241-6264, 2001.

[16] Børvik T, Hopperstad OS, Langseth M, Malo KA. Effect of target thickness in blunt projectile penetration of Weldox 460 E steel plates. *International Journal of Impact Engineering*, 28(4):413-464, 2003.

[17] Børvik T, Hopperstad OS, Pedersen KO. Quasi-brittle fracture during structural impact of AA7075-T651 aluminium plates. *International Journal of Impact Engineering*, 37:537–551, 2010.

[18] Børvik T, Olovsson L, Dey S, Langseth M. Normal and oblique impact of small arms bullets on AA6082-T4 aluminium protective plates. *International Journal of Impact Engineering*, 37:537-551, 2010.

[19] Cockcroft MG, Latham DJ. Ductility and the Workability of Metals. *Journal of the Institute of Metals*, 96:33-39, 1968.

[20] Corran RSJ, Shadbolt PJ, Ruiz C. Impact loading of plates-an experimental investigation. *International Journal of Impact Engineering*, 1(1):3-22, 1983.

[21] Cook RB, Malkus DS, Plesha ME, Witt RJ. *Concepts and applications of finite element analysis.* John Wiley & Sons, Inc, fourth edition, 2002.

[22] Corbett GG, Reid SR, Johnson W. Impact Loading of Plates and Shells by Free-Flying Projectile. *International Journal of Impact Engineering*, 18(2):141-230, 1996.

[23] Coucheron A. Stål i beskyttelseskonstruksjoner. Project Thesis, Norwegian University of Science and Technology, 2012.

[24] Coucheron A. Stål i beskyttelseskonstruksjoner - Settherdet NVE36 konstruksjonsstål til beskyttelsesformål. Master's Thesis, Norwegian University of Science and Technology, 2013.

[25] Dey S, Børvik T, Teng X, Wierzbicki T, Hopperstad OS. On the ballistic resistance of double-layered steel plates: An experimental and numerical investigation. *International Journal of Soilds and Structures*, 44:6701-6723, 2007.

[26] Dey S. High-strength steel plates subjected to projectile impact. PhD thesis, Norwegian University of Science and Technology, 2004.

[27] Dieter GE, *Mechanical metallurgy*. McGraw-Hill Book Co, 1988.

[28] Flores-Johnson EA, Saleh M, Edwards L. Ballistic performance of multilayered metallic plates impacted by a 7.62 mm APM2 projectile. *International Journal of Impact Engineering*, 38:1022-1032, 2011.

[29] Fourmeau M. Characterization and modelling of the anisotropic behaviour of high-strength aluminium alloy. PhD thesis, Norwegian University of Science and Technology, 2014.

[30] François D, Pineau A, Zaoui A. *Mechanical Behaviour of Materials - Volume I: Micro- and Macroscopic Constitutive Behaviour*. Springer, 2012.

[31] François D, Pineau A, Zaoui A. *Mechanical Behaviour of Materials - Volume II: Fracture Mechanics and Damage*. Springer, 2012.

[32] Goldsmith W. Non-ideal projectile impact on targets. *International Journal of Impact Engineering*, 22:95-395, 1999.

[33] Gruben G. Oral presentation for SIMLab. 3rd of April, 2014.

[34] Gruben G, Fagerholt E, Hopperstad OS, Børvik T, Langseth M. Numerical simulation of ductile fracture in modified Arcan test. *20th European conference on Fracture(ECF20)*, 2014.

[35] Gupta NK, Iqbal MA, Sekhon GS. Effect of projectile nose shape, impact velocity and target thickness on the deformation behaviour of layered plates. *International Journal of Impact Engineering*, 35:37-60, 2008.

[36] Gupta NK, Madhu V. An experimental study of normal and oblique impact of hard-core projectiles on single and layered plates. *International Journal of Impact Engineering*, 19:395-414, 1997.

[37] Hill R. *The Mathematical Model of Plasticity*. Oxford University Press, 1998.

[38] Hodowany J, Ravichandran G, Rosakis A, Rosakis P. Partition of plastic work into heat and stored energy in metals. *Experimental Mechanics*, 40:113-123, 2000.

[39] Holmen JK. Oral discussions in his office. 2014.

[40] Holmen JK, Johnson J. Effects of Heat Treatment on the Ballistic Properties of AA6070 Aluminium Plates. Master's Thesis, Norwegian University of Science and Technology, 2013.

[41] Holmen JK, Johnsen J, Jupp S, Hopperstad OS, Børvik T. Effects of heat treatment on the ballistic properties of AA6070 aluminum alloy. *International Journal of Impact Engineering*, 57:119-133, 2013.

[42] Hopperstad OS. Theory Manual: Models for metals and alloys. Still in progress at SIMLab/Department of Structural Engineering, NTNU.

[43] Hopperstad OS, Børvik T. *TKT4135 Material Mechanics - Lecture Notes Part 1*, NTNU 2014.

[44] Hopperstad OS, Langseth M, Børvik T. Analysis of the Cockcroft-Latham and maximum shear stress criteria for ductile fracture of metals. SINTEF REPORT, 2006.

[45] Johnson GR, Cook WH. A constitutive model and data for metals subjected to large strains, high strain rates and high temperatures. *Proceedings of the 7th International Symposium on Ballistics*, 547(11):541-547, 1983.

[46] Kane A, Børvik T, Berstad T, Hopperstad OS. Failure criteria with unilateral conditions for simulation of plate perforation. *European Journal of Mechanics - A/Solids*, 30:468-76, 2011.

[47] Kjølseth AB, Karlsen T. Fragmentation of Metallic Materials During Impact. Master's Thesis, Norwegian University of Science and Technology, 2012.

[48] Larsen PK, *Dimensjonering av stålkonstruksjoner.* Tapir Akademiske Forlag. 2nd edition. Trondheim 2010.

[49] Larsen T. Stål i beskyttelseskonstruksjoner. Project Thesis, Norwegian University of Science and Technology, 2011.

[50] Le Roy G, Embury JD, Edwards G, Ashby MF. A model of ductile fracture based on the nucleation and growth of voids. *Acta Metallurgica*, 29(8):1509-1522, 1981.

[51] Liang CC, Yang MF, Wu PW, Teng TL. Resistant performance of perforation of multi-layered targets using an estimation procedure with marine application. *Ocean Engineering*, 32:441-468, 2005.

[52] Lou DC, Solberg JK, Børvik T, Aunestad T. Investigation on the ballistic perforation resistance of case hardened monolithic and lamelled steel plates. Unpublished work.

[53] Lou DC, Solberg JK, Børvik T. Surface strengthening using a self-protective diffusion paste and its application for ballistic protection of steel plates. Unpublished work.

[54] Lou DC, Solberg JK, Børvik T. Surface strengthening using a self-protective diffusion paste and its application for ballistic protection of steel plates. *Materials and Design*, 30:3525-3536, 2009.

[55] Marais A, Mazière M, Forest S, Parrot A, Delliou PL. Identification of a strain-aging model accounting for Lüders behaviour in a C-Mn steel. *Philosophical Magazine*, 92(28-30):3589-3617, 2012.

[56] Marom I, Bodner SR. Projectile perforation of multilayered beams. *International Journal of Mechanical Sciences*, 21(8):489-504, 1979.

[57] Mathisen KJ. Lecture 7: Solution of the Dynamic Equilibrium Equations by Explicit Direct Integration. *Lecture notes in TKT4197 - Nonlinear Finite Element Analysis*, 2013.

[58] Mathisen KJ. Lecture 9: Solution of the Nonlinear Dynamic Equilibrium Equation. *Lecture notes in TKT4197 - Nonlinear Finite Element Analysis*, 2013.

[59] Nixdorff K. Some Application of The Impact Theory of J. Awerbuch and S.R. Bodner. *Trans. CSME*, 8(1):16-20, 1984.

[60] Olovsson L. Discussions via mail. May 2014.

[61] Olovsson L. *IMPETUS AFEA SOLVER - An introduction*. September 13th 2013.

[62] Radin J, Goldsmith W. Normal projectile penetration and perforation of layered targets. *International Journal of Impact Engineering*, 7(2):229-259, 1988.

[63] Rakvåg KG. Combined blast and fragment loading on plates. Master's thesis, Norwegian University of Science and Technology, 2009.

[64] Recht RF, Ipson TW. Ballistic Perforaion Dynamics. *Internationl Journal of Applied Mechanics(Trans. ASME)*, 30:384-390, 1963.

[65] Rosenberg Z, Dekel E. Revisiting the perforation of ductile plates by sharp-nosed rigid projectiles. *International Journal of Solids and Structures*, 47(22-23):2022-33, 2010.

[66] Solberg JK. Discussions via mail. May 2014.

[67] Solberg JK. *Teknologiske metaller og legeringer*, Norwegian University of Science and Technology, 2013.

[68] Voce E. *Journal of the Institute of Metals*, 74:537, 1948.

[69] Zukas JA. *High Velocity Impact Dynamics.* John Wiley & Sons, Inc., first edition, 1990.

[70] Zukas JA. *Impact Dynamics.* John Wiley & Sons, Inc., 1982

[71] Zukas JA, Scheffler DR. Impact effects in multilayered plates. *International Journal of Solids and Structures*, 38:3321-3328, 2001.

[72] Zukas JA, Scheffler DR. Practical aspects of numerical simulations of dynamic events: effects of meshing. *International Journal of Impact Engineering*, 24:925-945, 2000.

[73] Engineering Toolbox. http://www.engineeringtoolbox.com/poissons-ratio-d_1224.html. Obtained May 2014.

[74] IMEPTUS Afea Solver. www.impetus-afea.com/solver. Obtained in April 2014.

[75] Steel Express. http://www.steelexpress.co.uk/steel-hardness-conversion.html. Obtained May 2014.

[76] Wikipedia on stress intensity factor. http://en.wikipedia.org/wiki/Stress_intensity_factor. Obtained in May 2014.

Appendix A

Entry and Exit Holes From Ballistic Experiments

In this appendix all the entry and exit holes from the ballistic experiments are presented.

A.1 12 mm Plates

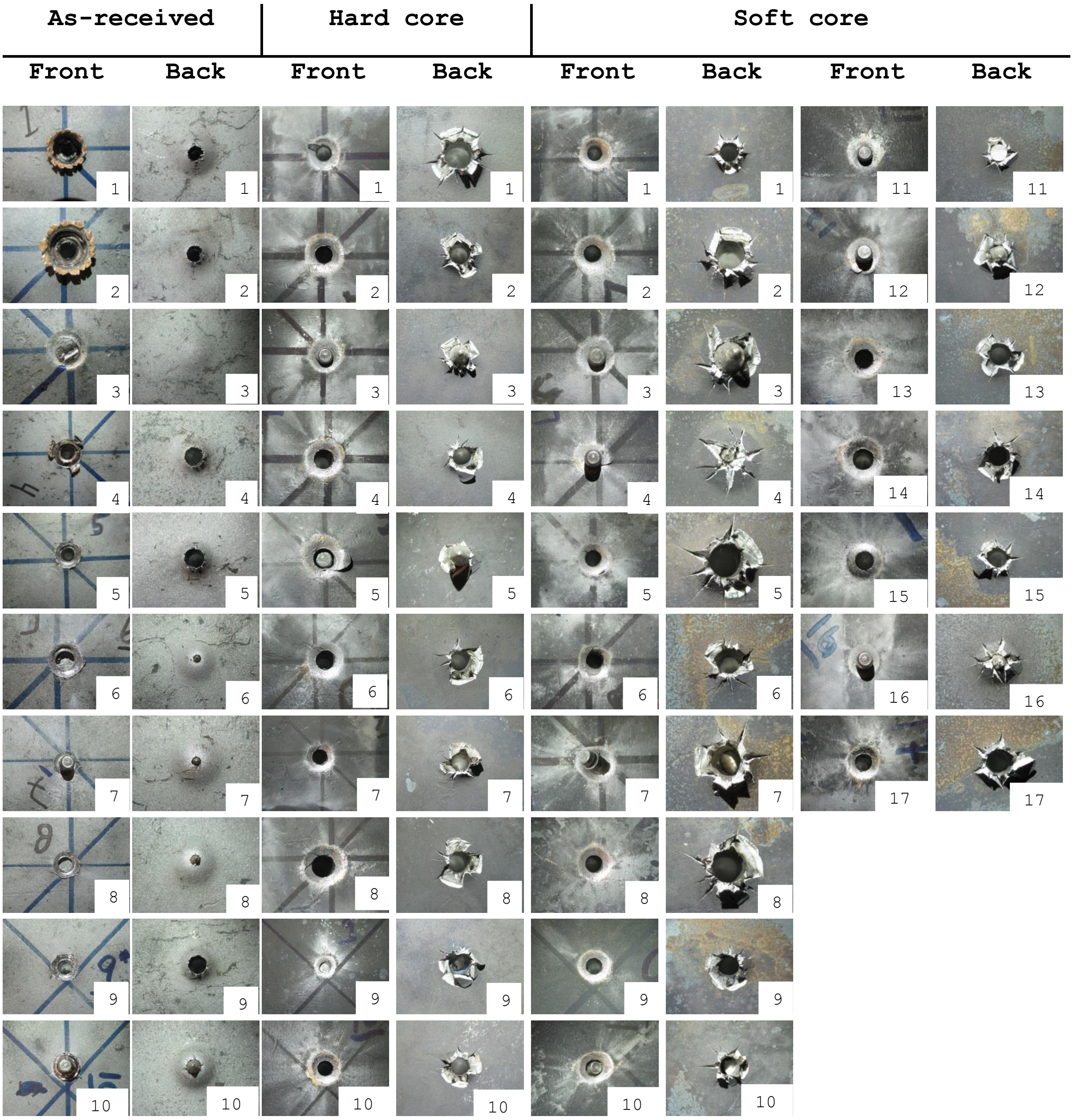

Figure A.1: Bullet holes - 12 mm plates.

A.2 2x6 mm Plates

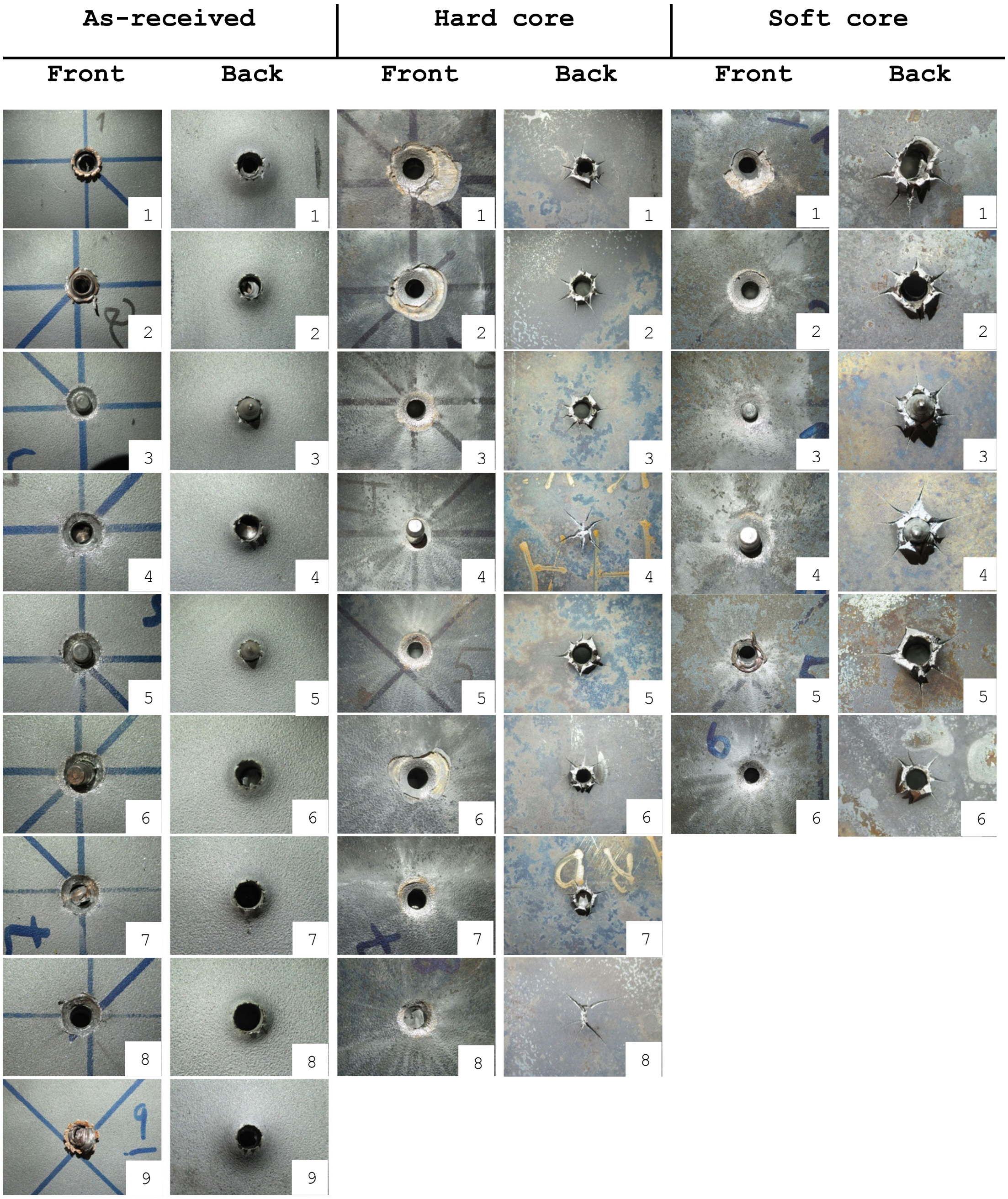

Figure A.2: Bullet holes - 2x6 mm plates.

A.3 3x4 mm Plates

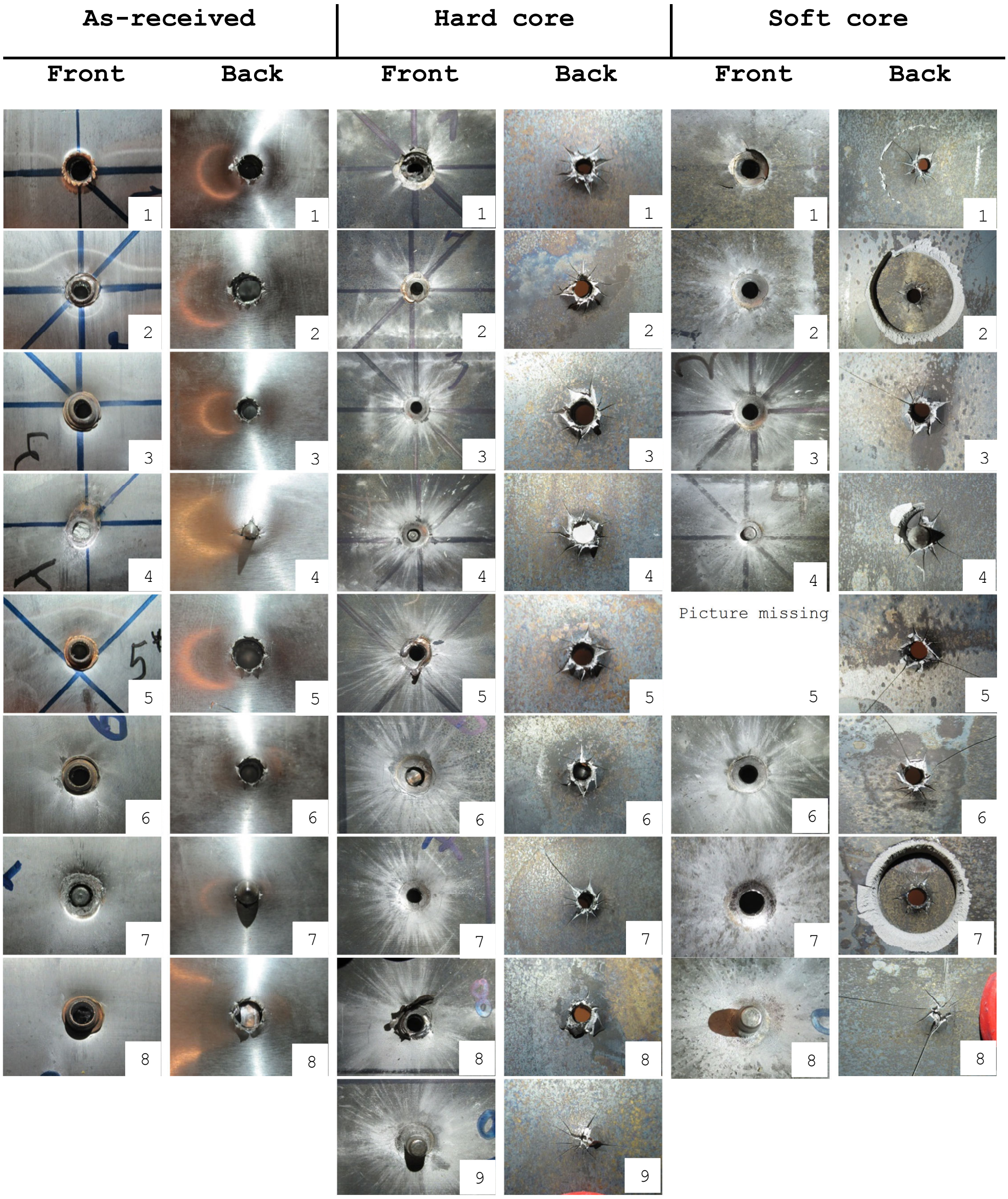

Figure A.3: Bullet holes - 3x4 mm plates.

Appendix B

Front and Backside of All Plates

B.1 12 mm Plates

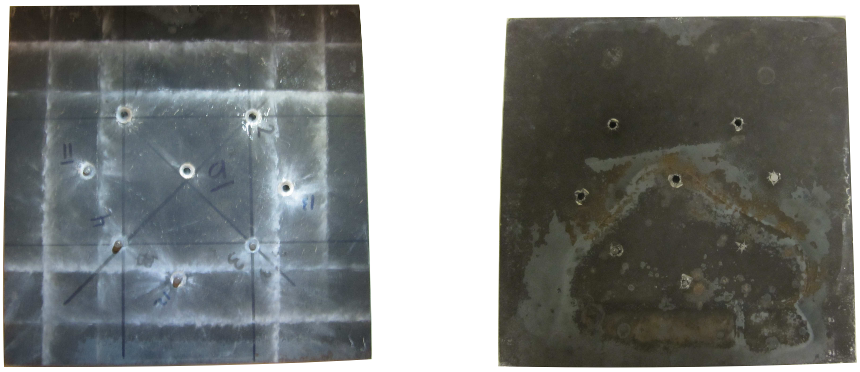

(a) Front-Plate 1. (b) Back-Plate 1.

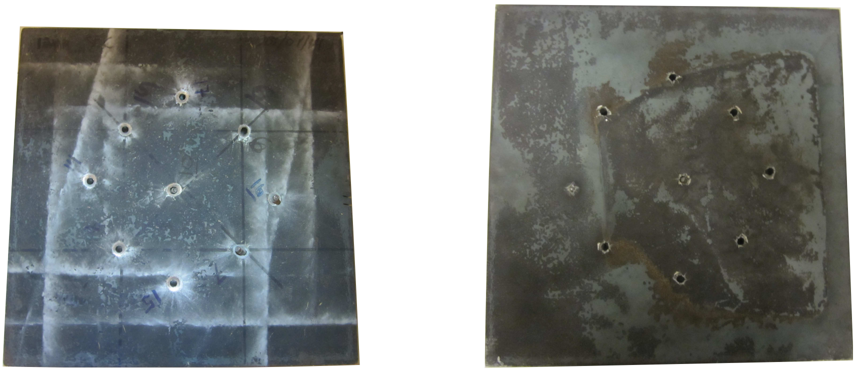

(c) Front-Plate 2. (d) Back-Plate 2.

Figure B.1: Impacted plates: 12 mm as-received.

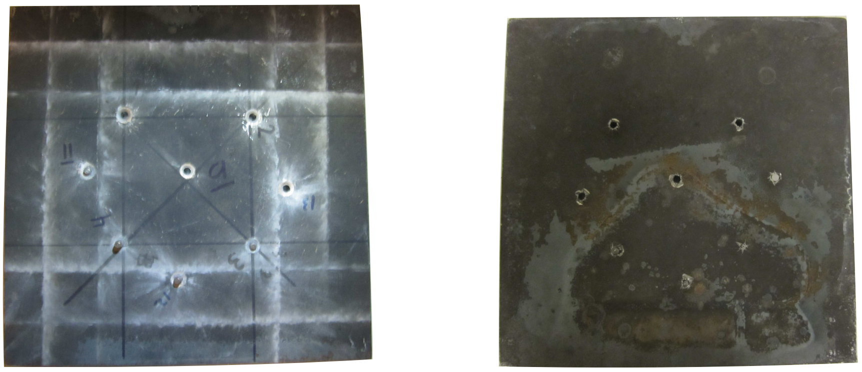

(a) Front-Plate 1.

(b) Back-Plate 1.

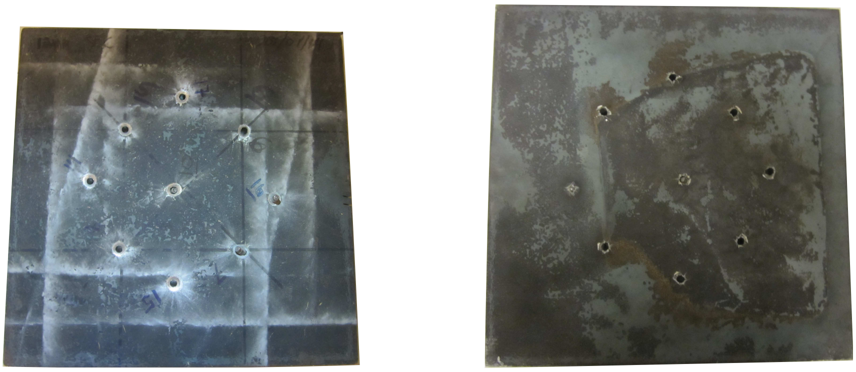

(c) Front-Plate 2.

(d) Back-Plate 2.

Figure B.2: Impacted plates: 12 mm soft core.

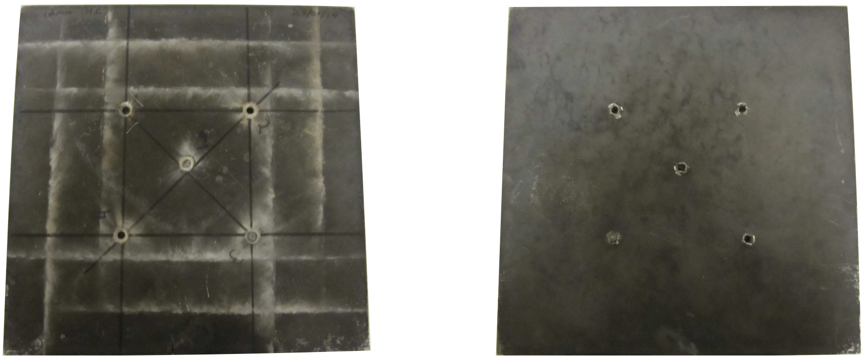

(a) Front-Plate 1.

(b) Back-Plate 1.

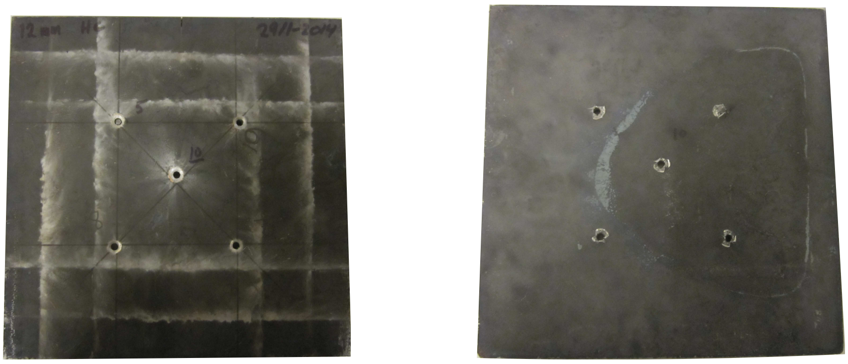

(c) Front-Plate 2.

(d) Back-Plate 2.

Figure B.3: Impacted plates: 12 mm hard core.

B.2 2x6 mm Plates

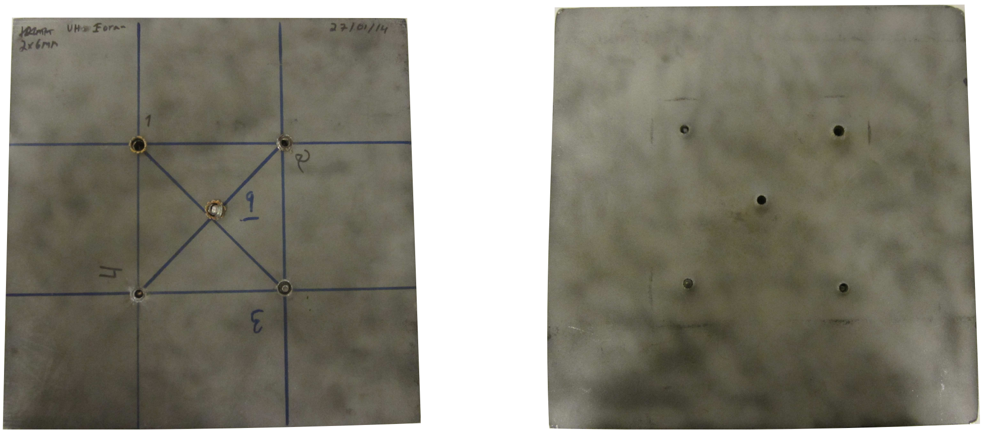

(a) Front-Plate (Plate 1).

(b) Back-Plate (Plate 2).

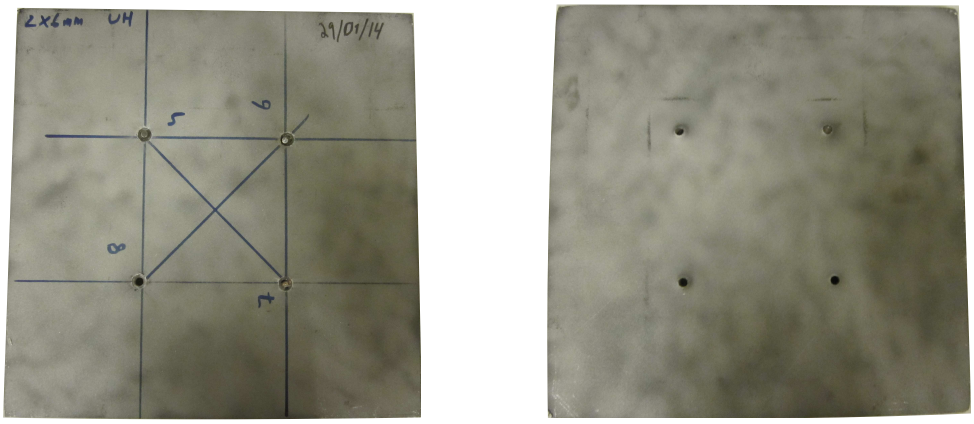

(c) Front-Plate (Plate 1).

(d) Back-Plate (Plate 2).

Figure B.4: Impacted plates*: 2x6 mm as-received.

*For the as-received 2x6 mm plates, two target set-up's were made, and shot 9 times (5+4).

(a) Front-Plate (Plate 1). (b) Back-Plate (Plate 2).

Figure B.5: Impacted plates: 2x6 mm soft core.

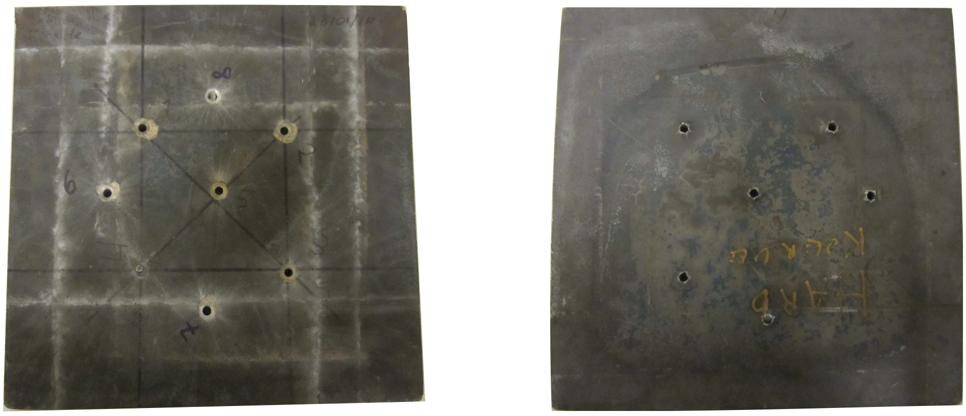

(a) Front-Plate (Plate 1). (b) Back-Plate (Plate 2).

Figure B.6: Impacted plates: 2x6 mm hard core.

B.3 3x4 mm Plates

(a) Front-Plate (Plate 1).

(b) Back-Plate (Plate 3).

Figure B.7: Impacted plates: 3x4 mm as-received.

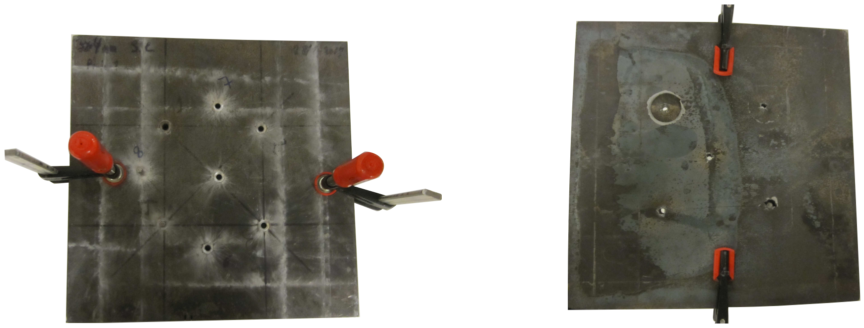

(a) Front-Plate (Plate 1).

(b) Back-Plate(Plate 3)[1]

Figure B.8: Impacted plates: 3x4 mm soft core.

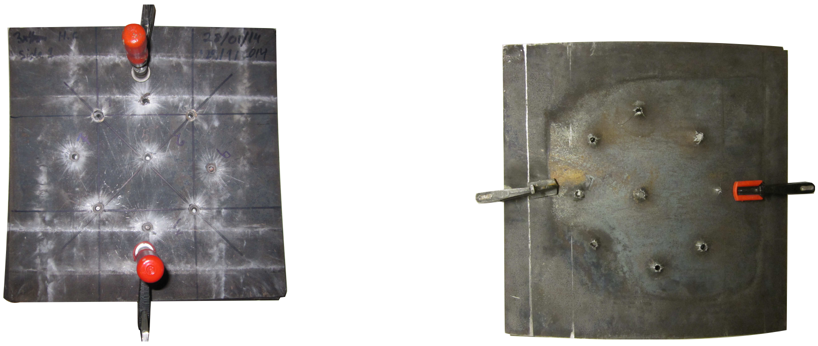

(a) Front-Plate(Plate 1)

(b) Back-Plate (Plate 3).

Figure B.9: Impacted plates: 3x4 mm hard core.

---

[1] Picture taken after the first 5 tests.

Appendix C

Tensile Specimens

C.1 As-received

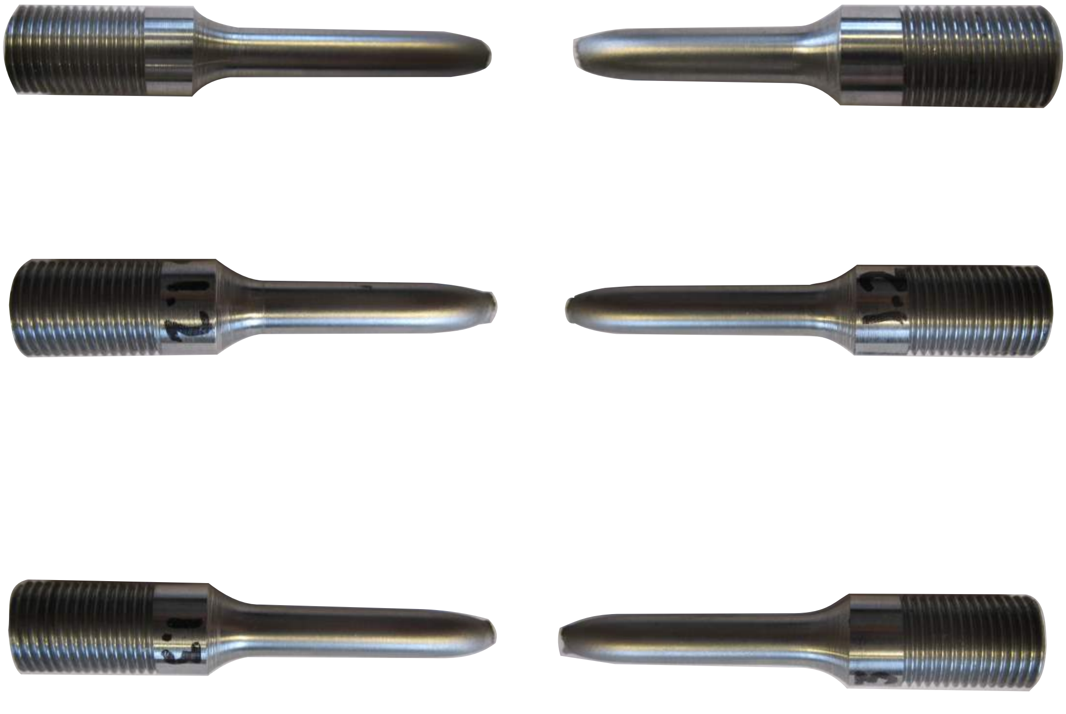

Figure C.1: Tensile specimens: As-received direction 1.

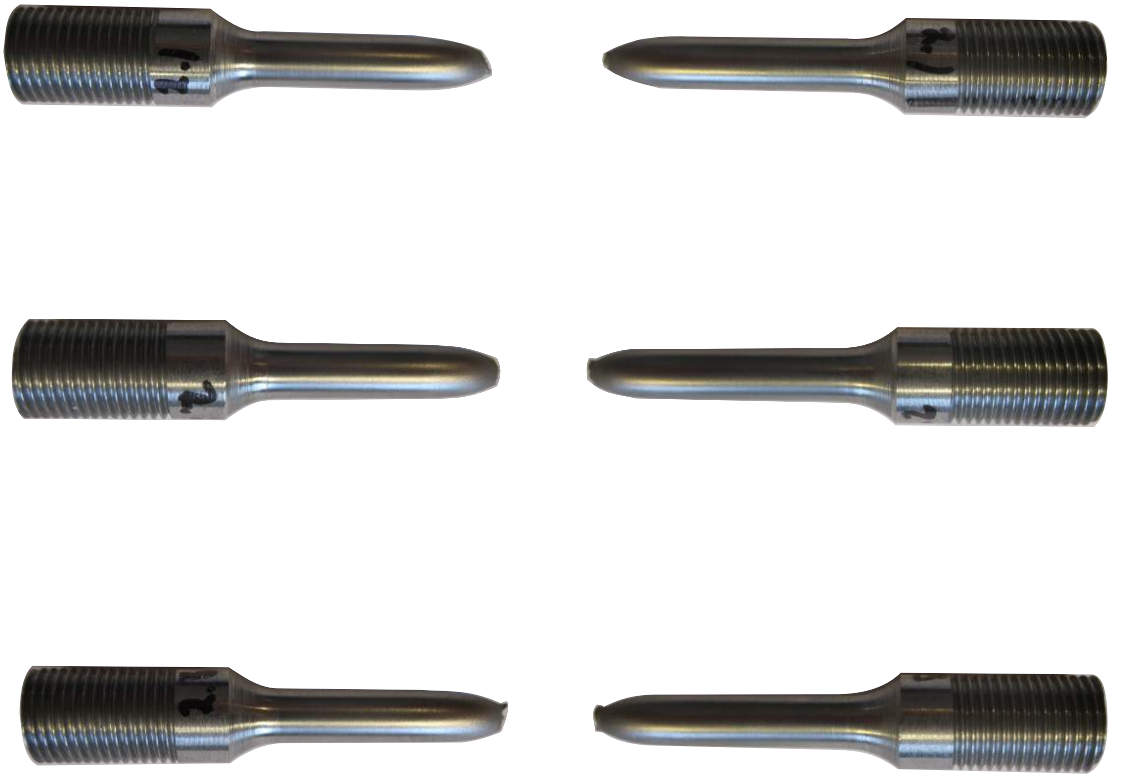

Figure C.2: Tensile specimens: As-received direction 2.

C.2 Soft Core

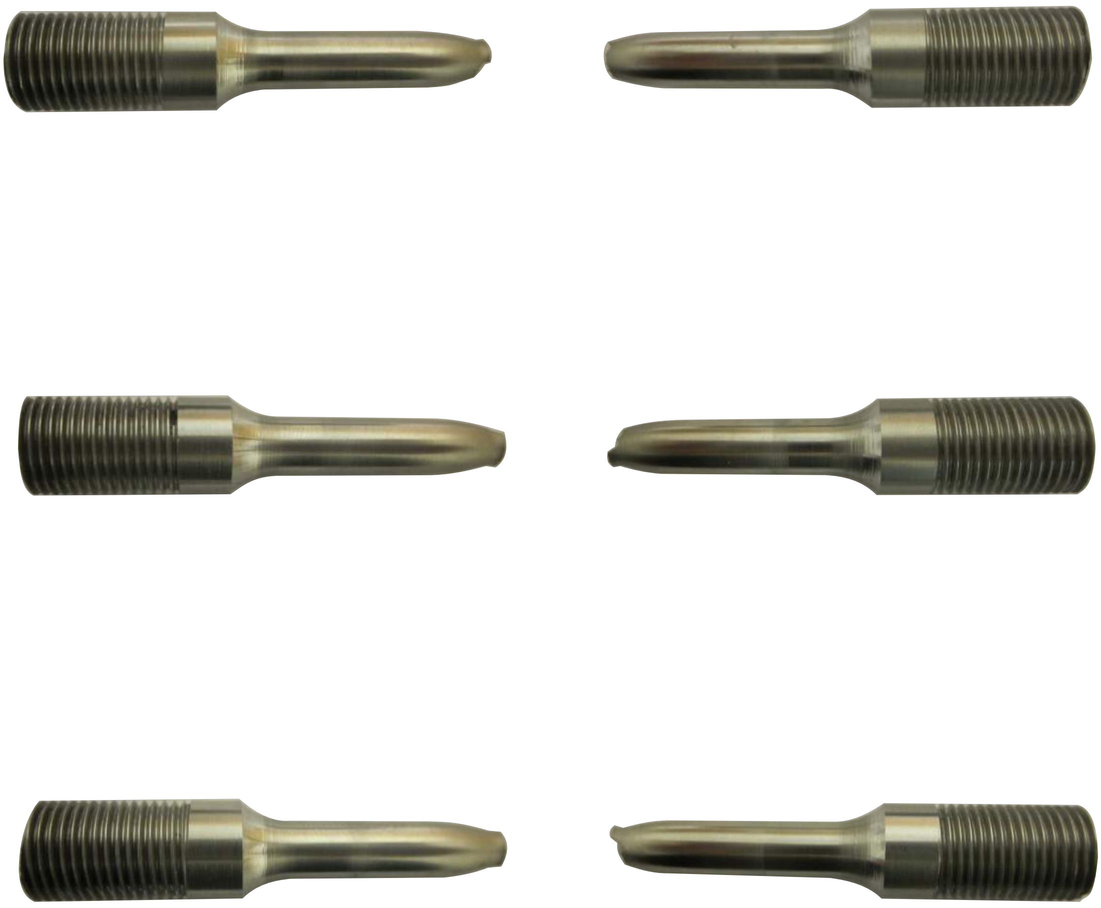

Figure C.3: Tensile specimens: Soft core.

C.3 Hard Core

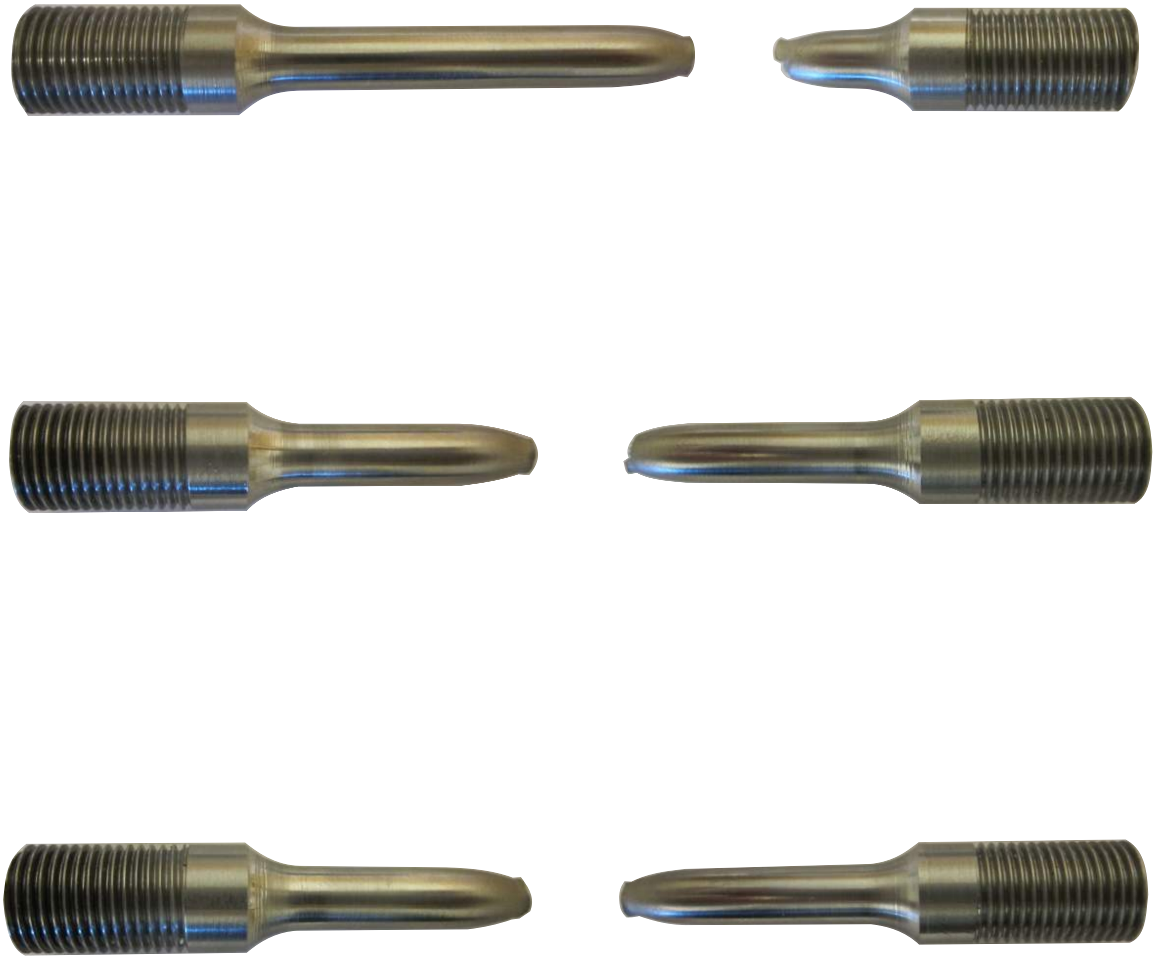

Figure C.4: Tensile specimens: Hard core.

Appendix D

MATLAB Code

MATLAB script for deciding necking and equivalent stress using Bridgman's analysis. In addition, direct calibration with Voce Law is performed on the equivalent stress. The script calibrates the as-received material in direction 1.

```
%------------------------------------------------------
%--- MATLAB script for calibrating materialdata -------
%------- 12mm Unhardened plates Direction 1 -----------
%--- Necking values, stress strain and Voce Law -------
%------------------------------------------------------
% By: Henrik Thorsen and Erlend Orthe

clear all;
clc; clf; close all;

%Plot settings for 0.5x figures
fz=12;
lz=10;
az=10;
lw=1.3;
font_size = fz*1.5;
leg_size = lz*1.5;
ax_size=az*1.5;
line_width=lw/0.8;

%Material constants
E = 212379; %MPa
v = 0.33;
%% Reading Excel files
disp('Start reading Excel files');
excelfile='Staalproveresultater.xlsx';
rows = {'6106' '5581'};
direction = {'retning1_nr1'  'retning2_nr1'};
r1_Sigma_t = xlsread(excelfile,direction{1},strcat('P15:P',rows{1}));
r1_Epsilon_p = xlsread(excelfile,direction{1},strcat('Q15:Q',rows{1}));
```

```
r1_Epsilon_l = xlsread(excelfile,direction{1},strcat('R15:R',rows{1}));
disp('Finish reading Excel file');

%% Deciding necking by the Considere criterion direction 1
N = length(r1_Sigma_t);
%Voce Law with 3 terms (7 unknowns):
Voce_fit_neck = @(x, epsilon) x(1)+x(2)*(1-exp(-x(3)*epsilon))+x(4),...
    *(1-exp(-x(5)*epsilon))+x(6)*(1-exp(-x(7)*epsilon));
Voce_fit_der = @(x, epsilon) x(3)*x(2)*exp(-x(3)*epsilon)+x(5)*x(4),...
    *exp(-x(5)*epsilon)+x(7)*x(6)*exp(-x(7)*epsilon);
x0 = [250, 1270, 0.5, 60, 64, 220, 21]; %A, C1,Q1,C2,Q2,C3,Q3

%Dont need the total range for curve fitting
Stress = r1_Sigma_t(2000:N-200);
Strain = r1_Epsilon_l(2000:N-200);
%Fitting parameters in x
opts = optimset('Algorithm', 'levenberg-marquardt','MaxFunEvals',5000,...
    'MaxIter',1000,'TolFun',1e-20);
[x,resnorm,~,exitflag,output] = lsqcurvefit(Voce_fit_neck,x0,Strain,...
    Stress,[],[],opts);
stress_necking = 0;
log_strain_necking = 0;
for i = 1:length(Strain)
    if Voce_fit_neck(x,Strain(i)) > Voce_fit_der(x,Strain(i))
        stress_necking = Stress(i);
        log_strain_necking = Strain(i);
        break;
    end
end
plastic_strain_necking = log_strain_necking-stress_necking/E;

% Engineering values
epsillon_e = exp(log_strain_necking)-1;
sigma_e = stress_necking/(1+epsillon_e);

%Plot necking point
figure(1)
plot(r1_Epsilon_l, r1_Sigma_t,'k','linewidth',1.5)
hold on
plot(Strain,Voce_fit_neck(x,Strain),'r','linewidth',1.5)
hold on
plot(Strain,Voce_fit_der(x,Strain),'-.','color','r','linewidth',1.5)
leg1=legend('Experiment ($\sigma_t$)','Curve fit',...
    'Differentiated curve fit');
set(leg1,'Location','SouthEast')
axis([0 1.4 0 1500])
box on
set(gcf,'position',[80, 80, 600, 400])
set(gcf,'PaperPositionMode','auto')
set(leg1,'Interpreter','latex','fontsize',font_size)
xlabel('Logarithmic strain','interpreter','latex','fontsize',font_size)
ylabel('True stress [MPa]','interpreter','latex','fontsize',font_size)
set(gca,'fontsize',ax_size)
```

```matlab
print(gcf,'-depsc','NeckingUH1')


%% Fitting Voce Law to Bridgman Criterion (equivalent stress)  direction 1
% A constant at 391.23
Voce_fit = @(x, epsilon) x(1)+x(2)*(1-exp(-x(3)*epsilon))+x(4),...
    *(1-exp(-x(5)*epsilon))+x(6)*(1-exp(-x(7)*epsilon));

%Remove zeros in plastic strain
start = 0;
for i = 1:length(r1_Epsilon_p)
   if r1_Epsilon_p(i) > 0.001
       start = i;
       break
   end
end
True_Stress = r1_Sigma_t(start:N);
Plastic_Strain = r1_Epsilon_p(start:N);
Bridgman_stress = zeros(length(True_Stress),1);
W_cr1 = 0; %"Plastic Work"
sigma_f = 0;
epsilon_f = 0;
for i = 1:length(Bridgman_stress)
    if Plastic_Strain(i) > plastic_strain_necking
        a_R = 1.1*(Plastic_Strain(i) - plastic_strain_necking);
        Bridgman_stress(i) = True_Stress(i)/((1+2/a_R)*log(1+0.5*a_R));
    else
        Bridgman_stress(i) = True_Stress(i);
    end
    if i > 1 %Calculate plastic work
        W_cr1 = W_cr1 + (Plastic_Strain(i)-Plastic_Strain(i-1)),...
            *(True_Stress(i-1)+True_Stress(i))/2;
    end
    if True_Stress(i) >= sigma_f
        sigma_f = True_Stress(i);
        epsilon_f = Plastic_Strain(i);
    end
end

%Fitting Voce law
we = ones(1,length(Plastic_Strain));
we(1:80) = 15*we(1:80); %15 times more
x0 = [391.23, -127, 120, 415, 1.25, 290, 23]; %sigma0, C1,Q1,C2,Q2,C3,Q3
opts = optimset('Algorithm', 'levenberg-marquardt','MaxFunEvals',5000,...
    'MaxIter',1000,'TolFun',1e-20);
[x,resnorm,~,exitflag,output] = lsqcurvefit(Voce_fit,x0,Plastic_Strain,...
    Bridgman_stress,[],[],opts)


% LS-OPT data
xOPT_UH1 = [400, 502.61, 566.25/502.61, 301.93, 6846.09/301.93,...
    -152.50, 9735.95/152.497];
LS_OPT_Sress = Voce_fit(xOPT_UH1,Plastic_Strain);
```

```

%Plot Bridgman equivalent stress
figure(2)
plot(Plastic_Strain,True_Stress,'b','linewidth',1.5)
hold on
plot(Plastic_Strain,Bridgman_stress,'k','linewidth',1.5)
hold on
plot(Plastic_Strain,Voce_fit(x,Plastic_Strain),'-.','color','r',...
    'linewidth',1.5)
leg1 = legend('Experiment ($\sigma_t$)','Bridgman ($\sigma_{eq}$)',...
    'Voce ($\sigma_{eq}$)');
set(leg1,'Location','SouthEast')
axis([0 1.4 0 1500])
box on
set(gcf,'position',[80, 80, 600, 400])
set(gcf,'PaperPositionMode','auto')
set(leg1,'Interpreter','latex','fontsize',font_size)
xlabel('Plastic strain','interpreter','latex','fontsize',font_size)
ylabel('Stress [MPa]','interpreter','latex','fontsize',font_size)
set(gca,'fontsize',ax_size)
print(gcf,'-depsc','BridgmanUH1')

%Plot LS-OPT equivalent stress
figure(3)
plot(Plastic_Strain,True_Stress,'b','linewidth',1.5)
hold on
plot(Plastic_Strain,Bridgman_stress,'k','linewidth',1.5)
hold on
plot(Plastic_Strain,LS_OPT_Sress,'-.','color','r','linewidth',1.5)
leg1 = legend('Experiment ($\sigma_t$)','Bridgman ($\sigma_{eq}$)',...
    'LS-OPT ($\sigma_{eq}$)');
set(leg1,'Location','SouthEast')
axis([0 1.4 0 1500])
box on
set(gcf,'position',[80, 80, 600, 400])
set(gcf,'PaperPositionMode','auto')
set(leg1,'Interpreter','latex','fontsize',font_size)
xlabel('Plastic strain','interpreter','latex','fontsize',font_size)
ylabel('Stress [MPa]','interpreter','latex','fontsize',font_size)
set(gca,'fontsize',ax_size)
print(gcf,'-depsc','LSOPT_UH1')
```

Appendix E

Microhardness

Additional microhardness measurements for 12 mm plates.

Table E.1: Average hardness for plate cores ($HV_{0.2}$) of the 12 mm plates.

	Plate 1	Plate 2	Plate 3
Soft core	328.10	294.70	322.82
Hard core	338.71	372.17	319.10

The hardness profiles from Plate 3 were not available before mid May. Therefore, they were not used in this thesis.

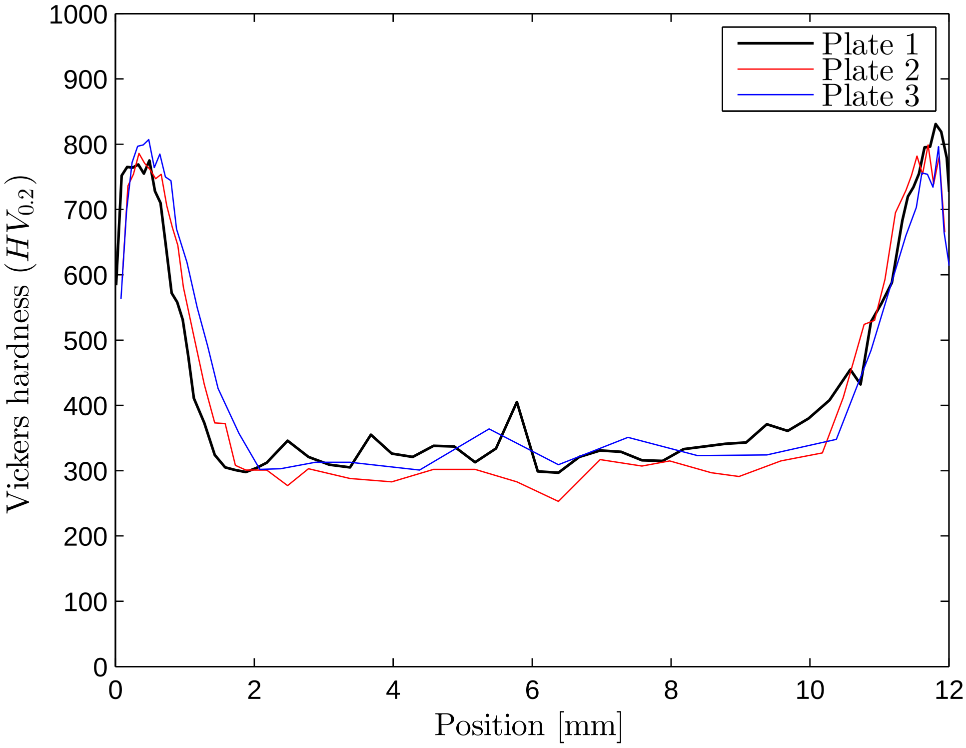

(a) Soft core

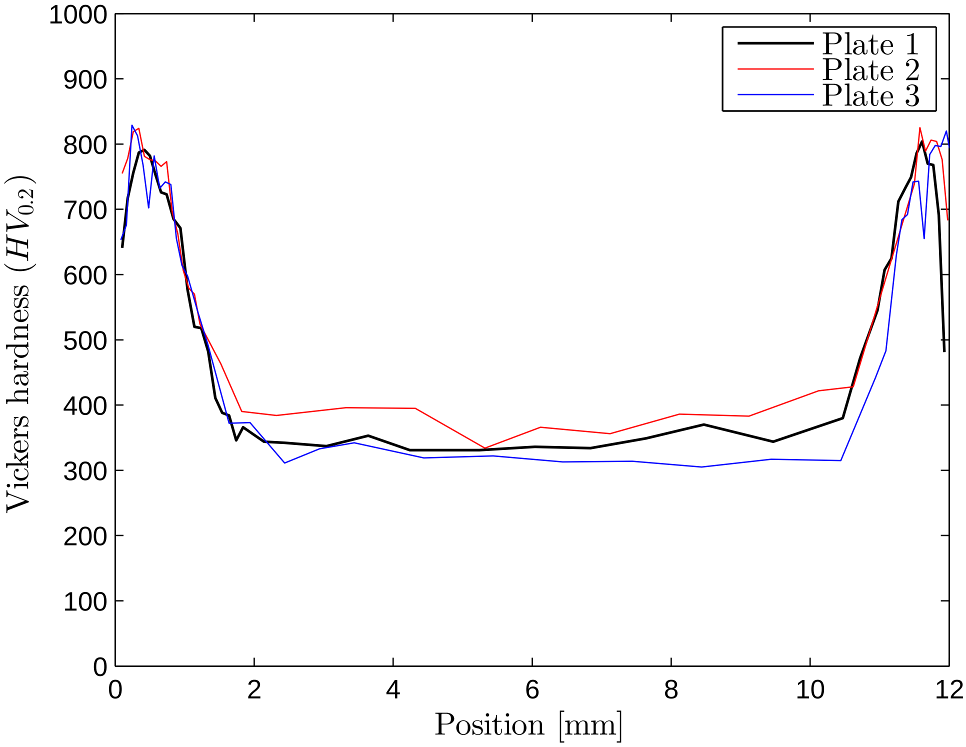

(b) Hard core

Appendix F

IMPETUS Afea Solver Input

IMPETUS input file is provided for the double layered soft core configuration. This script is given as an example of the IMPETUS input files used in this thesis. The only difference between soft core and hard core is the material constants, and the scaling factors in *CURVE. For the as-received material, this is unity. All scaling factors are shown in F.2.

F.1 2x6 mm Double Layered Soft Core

```
*UNIT_SYSTEM
SI
*PARAMETER
%term = 1.2e-4
%Wc   = 956.21E6
%Vi   = 700
%A    = 461.29E6
%Q1   = 360.60E6
%TH1  = 689.90E6
%C1   = %TH1/%Q1
%Q2   = 295.72E6
%TH2  = 53200.70E6
%C2   = %TH2/%Q2
%Q3   = 199.68E6
%TH3  = 6406.38E6
%C3   = %TH3/%Q3
%c    = 0.01
%m    = 0.94
%E    = 212379E6
%nu   = 0.33
*TIME
[%term]
*COMPONENT_BOX
1, 1, 6,40,80
0,-40E-3,-40E-3,6E-3,0,40E-3
```

```
*COMPONENT_BOX
2, 2, 6,40,80
61E-4,-40E-3,-40E-3,121E-4,0,40E-3
*INCLUDE
#Add 2 to the part ids in the included file:
#Hence, part id 2,3,4 in bullet_half.k becomes 4,5,6 here
core.k
0,0,0,0,0,2
0,0,0,10e-3,0,0,0
0,0,0, 0,0,0
*PART
"Plate1"
1,1, , , , 1E-9
"Plate2"
2,3, , , , 1E-9
"Steel core"
5,2
*SET_PART
123
1,2
*CHANGE_P-ORDER
P,5,3
*GEOMETRY_PIPE
1
-1,0,0,1,0,0,16E-3
*CHANGE_P-ORDER
PS,123,3,1
*MAT_METAL
#Plate 1
1,7800,[%E],[%nu],1,1
111,0,0,[%c], 5E-4, [%m], 293,  1800
*MAT_METAL
#Plate 2
3,7800,[%E],[%nu],1,1
112,0,0,[%c], 5E-4, [%m], 293,  1800
*MAT_RIGID
#Steel core
2,7850.0
*FUNCTION
111
fcn(10)+%Q1*(1-exp(-%C1*epsp))+%Q2*(1-exp(-%C2*epsp))+%Q3*(1-exp(-%C3*epsp))
*FUNCTION
112
fcn(11)+%Q1*(1-exp(-%C1*epsp))+%Q2*(1-exp(-%C2*epsp))+%Q3*(1-exp(-%C3*epsp))
*PROP_DAMAGE_CL
1,2
[%Wc],0
*PROP_THERMAL
1,1.2e-5, 452, 0, 0.9, 293
*BC_SYMMETRY
Y
*INITIAL_VELOCITY
P,5,[%Vi],0,0,
```

```
*CONTACT
"General contact"
1
ALL,0,ALL,0,0,-1E15
2
*FUNCTION_STATIC
10
%A*crv(12,dist_surf(-1,0,0))
*FUNCTION_STATIC
11
%A*crv(13,dist_surf(-1,0,0))
*CURVE
#Here are the scaling factors.
12
0,2.143
1.90E-04,2.451
5.90E-04,2.213
1.36E-03,1.256
4.51E-03,1.274
5.59E-03,2.667
6.00E-03,2.277
*CURVE
13
0,1.082
2.60E-04,2.015
6.60E-04,1.631
1.19E-03,0.564
2.09E-03,0.433
4.49E-03,0.503
4.79E-03,0.738
5.40E-03,2.204
6.00E-03,1.433
*END
```

F.2 Scaling Factors Used in *CURVE for All Configurations

Note that the layered plates do not have $\alpha(z) = 1.0$ in their core. This is because they either have a higher or lower hardness compared to the monolithic plates.

Table F.1: Scaling factors α over the thickness, z. Soft core configurations.

Soft core configurations							
12 mm Plate 1		2x6 mm Plate 1		2x6 mm Plate 2		3x4 mm Plate 1	
z [mm]	$\alpha(z)$	z [mm]	$\alpha(z)$	z [mm]	$\alpha(z)$	z [mm]	$\alpha(z)$
0	1.779	0	2.143	0	1.082	0	2.204
90	2.292	190	2.451	260	2.015	260	2.280
490	2.362	590	2.213	660	1.631	890	1.643
1430	1.000	1360	1.256	1190	0.564	1490	1.329
9000	1.000	4510	1.274	2090	0.433	2090	1.277
10730	1.317	5590	2.667	4490	0.503	2690	1.457
11810	2.533	6000	2.277	4790	0.738	2990	1.472
12000	1.990			5400	2.204	3840	2.350
				6000	1.433	4000	1.805

Table F.2: Scaling factors α over the thickness, z. Hard core configurations.

Hard core configurations							
12 mm Plate 1		2x6 mm Plate 1		2x6 mm Plate 2		3x4 mm Plate 1	
z [mm]	$\alpha(z)$	z [mm]	$\alpha(z)$	z [mm]	$\alpha(z)$	z [mm]	$\alpha(z)$
0	1.893	0	1.863	0	1.305	0	2.350
340	2.324	166	2.606	240	2.134	510	2.214
500	2.308	566	2.518	400	2.105	990	1.603
1740	1.000	1346	1.479	1250	0.658	1590	1.458
9540	1.000	4646	1.494	1550	0.522	2790	1.429
11680	2.374	5246	1.677	3950	0.520	3390	1.768
12000	1.420	5546	2.482	4550	0.590	3870	2.311
		5706	2.615	5600	2.072	4000	2.075

Appendix G

Stress-Strain Curves

Stress-strain curves for soft core and hard core material.

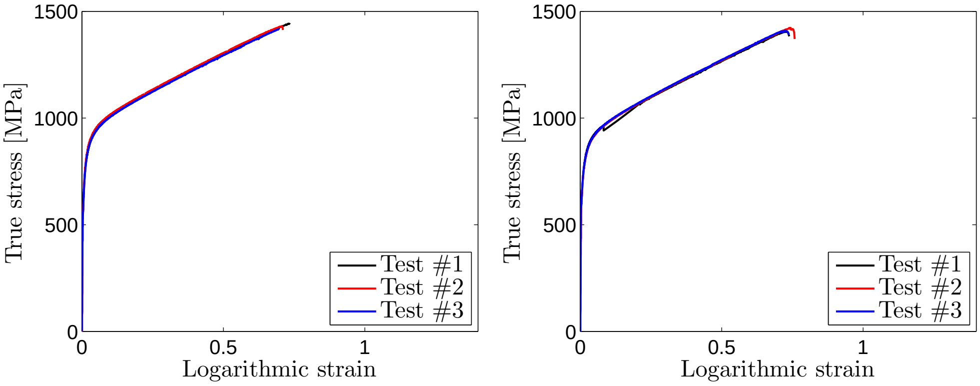

(c) Soft core.

(d) Hard core.

Figure G.1: Stress-strain curves.